Dielectric properties on the insulating side of the superconductor-insulator transition

Von der Fakultät Mathematik und Physik der Universität Stuttgart zur Erlangung der Würde eines Doktors der Naturwissenschaften (Dr. rer. nat.) genehmigte Abhandlung vorgelegt von

Nikolaj Gabriel Ebensperger
aus Kirchheim unter Teck

Hauptberichter: Prof. Dr. Martin Dressel
Mitberichter: Prof. Dr. Jörg Wrachtrup

Tag der mündlichen Prüfung: 22.10.2021
Prüfungsvorsitzende: Prof. Dr. Maria Daghofer

1. Physikalisches Institut
Universität Stuttgart

2021

Contents

Publications

Publications related to this thesis

- **Nikolaj Gabriel Ebensperger**, Benedikt Ferdinand, Dieter Koelle, Reinhold Kleiner, Martin Dressel and Marc Scheffler.
  "Characterizing dielectric properties of ultra-thin films using superconducting coplanar microwave resonators"
  Rev. Sci. Instrum., **90**, 114701 (2019) [1]

Further publications

- Lars Wendel, Vincent T. Engl, Gabriele Untereiner, **Nikolaj Gabriel Ebensperger**, Martin Dressel, Ahmed Farag, Monika Ubl, Harald Giessen and Marc Scheffler.
  "Microwave probing of bulk dielectrics using superconducting coplanar resonators in distant-flip-chip geometry"
  Rev. Sci. Instrum., **91**, 054702 (2020) [2]

- Vincent T. Engl*, **Nikolaj G. Ebensperger***, Lars Wendel and Marc Scheffler.
  "Planar GHz Resonators on SrTiO3: Suppressed Losses at Temperatures below 1 K"
  submitted to Phys. Rev. Lett.
  ArXiv: 1911.11456 (2019) [3]

*authors contributed equally

- **Nikolaj Gabriel Ebensperger**, Markus Thiemann, Martin Dressel and Marc Scheffler.
  "Superconducting Pb stripline resonators in parallel magnetic field and their application for microwave spectroscopy"
  Supercond. Sci. Technol., **29**, 115004 (2016) [4]

- Manfred H. Beutel, **Nikolaj Gabriel Ebensperger**, Markus Thiemann, Gabriele Untereiner, Vincent Fritz, Mojtaba Javaheri, Jonathan Nägele, Roland Rösslhuber, Martin Dressel and Marc Scheffler.
  "Microwave study of superconducting Sn films above and below percolation"
  Supercond. Sci. Technol., **29**, 085011 (2016) [5]

List of abbreviations

a Suppression factor

AC Alternating current

AFM Atomic force microscopy or atomic force microscope

$\alpha_{\mathbf{scr}}$ Thomas-Fermi screening length

BCS-theory Bardeen-Cooper-Schrieffer theory

BKT Berezinskii-Kosterlitz-Thouless

CP Cooper-pair

CPW Coplanar waveguide

d Sample thickness

D_2 Fractal dimension

DC Direct current

δ Energy level splitting

Δ (Superconducting) energy gap

Δ_C Coulomb-gap

Δ_p Parity/pseudo-gap

DOS Density of states

ES Efros-Shklovskii

ε Dielectric constant

J Superconducting stiffness

JJA Josephson-junction array

ν_0 Density of states at Fermi energy

ω_D Debye frequency

Q Quality factor

QCP Quantum critical point

QPT Quantum phase transition

ρ Resistivity

R_s Sheet resistance

SC Superconductivity or superconducting

σ_1 (Microwave-)conductivity

SIT Superconductor-insulator transition

T_c Critical temperature

$T_{\mathbf{CO}}$ Crossover temperature between Mott VRH and ES VRH

$T_{\mathbf{VBKT}}$ Vortex BKT transition temperature

T_0 Activation temperature

$T_{0,\mathbf{ES}}$ ES activation temperature

$T_{0,\mathbf{Mott}}$ Mott activation temperature

VRH Variable range hopping

VTI Variable temperature insert

ξ Localization length

$\xi_{\mathbf{sc}}$ Superconducting coherence length

1. Introduction

1.1. Abstract

Amorphous indium oxide is the prime example of strongly disordered superconductors showing a quantum phase transition at strong levels of disorder, where a disorder-driven superconductor-insulator transition (SIT) is found. While there are studies focusing on the superconducting side, the insulating side is much less explored because experimental means are lacking. In this work an experimental approach is presented, employing coplanar microwave resonators in GHz frequency range and down to mK-temperatures, giving access to dielectric properties and the finite-frequency conductivity of amorphous indium oxide as a function of temperature, frequency and disorder. It is found that depending on disorder, indium oxide has a large dielectric constant with a critical value of $\varepsilon_1 \approx 100$, separating samples with and without localized Cooper-pairs. From scaling, the fractal nature of electronic eigenstates is inferred. Strong effects of a gap are found, giving direct evidence for a finite pairing pseudogap even in the insulating phase, perfectly matching fractal Anderson localization theory.

1.2. Motivation

The quantum breakdown of superconductivity has been of prominent interest in solid state research for several decades already [6–8]. The peculiar phenomenon is the immediate transition from a superconductor to a non-

superconducting state, such as a metal state (SMT) or even a completely insulating state (SIT). Although experimental access to these transitions is naturally limited to finite temperatures, the transition between the two ground states are expected to occur even at $T = 0$, reminiscent of quantum-phase-transitions (QPT) [8, 9]. In particular the direct transition to an insulator, the superconductor-insulator transition (SIT) has attracted large interest, both experimentally [10, 11] and theoretically [12–14]. SIT has been found in several materials and compounds, such as e.g. granular materials [15], but also most prominently in homogeneously disordered amorphous thin-films such as e.g. indium oxide [10, 11, 16] or TiN [17]. Amorphous materials pose important and fundamental questions, as by their homogeneous nature, they do not show any grain boundaries or inherent structure [10, 11, 18–20], which might otherwise play a role in the suppression of superconductivity and charge transport.

There are several possibilities known to drive an initially superconducting system to an insulating state. Most attack an intrinsic material parameter, such as the charge carrier density, disorder, dimensionality or by the application of strong external magnetic field. It has been found that by changing a thin-film's thickness [21], applying magnetic field [22–25] or inducing disorder [10, 11, 26], superconductivity is gradually suppressed until at the QPT the insulating state is reached. In particular the disorder-driven SIT is a paramount example of such a transition. While small amounts of disorder should not disturb superconductivity [27], strong amounts of disorder strongly suppress T_c [28] and even inhibit superconductivity altogether [10].

There are numerous theories on the fundamental principles governing this phenomenon, but there are still many unresolved questions and challenges [8]. While suppression of superconductivity by the means of reduction of the energy gap (Fermionic mechanism [29, 30]) is given in certain materials (e.g. in MoGe [7, 29, 31]), in amorphous thin-film samples the underlying principles have to be of a more complex nature, since a (pseudo-) gap is still found with finite value at temperatures exceeding T_c [17, 28, 32] in samples

where superconductivity is already strongly suppressed. Even in insulating samples fingerprints of a gap can be inferred from resistivity scaling [10, 12, 19, 33]. It has been suggested that superconductivity only survives on a *local* scale, with the emergence of spatially separated pockets or "puddles" of superconductivity [17, 28], with the length-scale of these inhomogeneities found to be on the nanometer scale.

The remaining energy gap and the structure of the insulating state raises fundamental questions on the nature of the underlying electronic eigenstates and the role of Coulomb interactions [8]. It has been established that the intricate interplay between Cooper-attraction and Anderson-localization, which plays an important role in the formation of pseudo-gaped insulators [8], however, it has not been clear yet as to how Coulomb interactions participate in its formation [8]. Two main questions arise:

- Why is superconductivity not suppressed completely but possibly remains locally (finite pseudogap), even though bare electron-electron repulsion should be large?
- What is the driving mechanism for localizing Cooper-pairs?

Answering these questions has not been possible to full extend yet [8]. To answer the first, it is speculated, that while the bare Coulomb repulsion between electrons in theory is large [29, 30, 33], it might be effectively screened to negligible size [33]. For this to happen however, the polarization and the dielectric constant would need to be rather large [33]. Answers to the second question are quite debated and while some theories exist, hard evidence is still sparse. Localization similar to the Coulomb blockade in Josephson-Junction Arrays (JJA) following Berezinsky-Kosterlitz-Thouless-physics seems possible at first glance due to the emergent superconducting granularity [14, 34]. For this to be the sole reason, however, the Cooper-pairs would have to interact repulsively themselves by Coulomb interactions [35, 36]. Additionally the large inter-site distance necessary in JJAs, seems to

not be given in the amorphous thin-films [8] as superconducting granularity is on the nanometer scale [17, 28], making BKT-physics improbable. The most advanced theory describing the processes in homogeneously disordered, amorphous thin-film samples, has been derived mostly by M. V. Feigel'man [12, 33] and relies purely on fractal Anderson localization of charge carriers. It predicts for the electronic eigenstates to be of fractal nature, meaning that they occupy less volume than a delocalized eigenstate [37]. With this mechanism single-electrons are localized on nanometer length-scale, yet they still are able to interact attractively and form Cooper-pairs within their given volume [33]. This is suggested, since Cooper-pairs form in k-space, meaning that only the momenta of the individual electrons and their spins set the base for singlet-pairing enabled by BCS-type effective phonon-mediated attraction, but not their confinement to small extensions in real space, as long as the energy level splitting of the small confinement-droplet does not exceed phonon energies [12, 33] (for coherent superconductivity this must not exceed the superconducting gap [27]). This necessitates large polarization and a large dielectric constant, because the relation between Coulomb interaction strength and Cooper-attraction has to allow for attractive electron interaction [33]. Withing this framework, several predictions for the influence of localized Cooper-pairing and their evoked pseudogap on the dynamical polarization and the conductivity at finite frequencies have been made [38, 39], however until now no direct experimental evidence could be presented.

The prime material showing this peculiar SIT is disordered, amorphous indium oxide. It has been object of many studies over a broad range of disorders [8, 10, 11, 26, 28, 32, 40–42]. It has repeatedly been found to be homogeneous in disorder [10, 20] but inhomogeneous in superconductivity with superconducting granularity [28]. Since it is the most studied material of SIT-physics, it is also the most important to the scientific community and will therefore be the prime candidate in this work.

Both of the above burning questions could be answered by investigating the polarization, the dielectric constant, and the finite-frequency conduc-

tivity of insulating amorphous thin-film samples [14, 33, 38, 39]. However, measurements on the insulating side of SIT other than simple transport measurements [10, 11] are particularly rare, since experimental challenges are huge. The enormous resistivity of the samples at low temperatures inhibits any kind of tunneling experiments and the very small thickness impedes traditional measurements of polarization, e.g. by dielectric resonators. Additionally, two crucial requirements for successful investigations into the dielectric properties and the finite-frequency conductivity emerge, which are the very small excitation energies and the very low temperatures that are needed, in order to not break possible localized Cooper-pairs. The gap found in the single-particle density of state of amorphous indium oxide, suspected to be the pairing gap of localized Cooper-pairs, has been found to have a size of about $\Delta_p \sim 0.5 - 1\,\mathrm{meV}$ as determined by tunneling experiments [26, 28]. These energies translate to frequencies in the range of about $100 - 200\,\mathrm{GHz}$. Finite-frequency experiments, which do not break possible localized Cooper-pairs, would therefore necessarily have to be performed below these upper limits, making experimental methods in the microwave regime the most suited candidates. Additionally, very low temperatures are necessary, because on the one hand, the gap has to be fully developed [28], and on the other hand, any residual conductivity (via hopping) has to be strongly suppressed such that emergent granularity is fully established [8] and dissipation does not hamper measurements via strong losses. In this regime, thermal excitations are entirely suppressed (zero-phonon regime [43, 44]) making excitations by phonons the dominating contribution if the condition $\hbar\omega > k_b T$ is met, thus enabling frequency-dependent measurements of the parameters under study. The latter requirement again poses GHz-frequencies as the optimal means, because phonon energies exceed thermal energies in the mK-regime within a well-accessible temperature range.

Fulfilling all of the mentioned requirements (low frequencies, temperatures and ultra thin samples) with an experimental method studying dielectric properties, could not be done until now, since traditional methods each fall

short on at least one of the requirements. In this work, an experimental approach is detailed, which overcomes these challenges and is able to measure very thin films in the nanometer regime at frequencies below corresponding gap energies at very low temperatures in the mK-regime. For this, highly sensitive coplanar microwave waveguide resonators are applied, which allow to determine dielectric properties and the finite-frequency conductivity in insulating amorphous indium oxide. This is done over a broad frequency range of up to $\sim 25\,\mathrm{GHz}$, corresponding to maximum excitation energies of $0.1\,\mathrm{meV} \ll \Delta_p$. The dielectric constant is determined with both its absolute value and its scaling with disorder over a very broad range of disorders on the insulating side of SIT. Two regimes are found, one where local pairing is present and one where even local pairing is suppressed. Evidence for the suppression of Coulomb interactions is found in samples showing local pairing. Here a critical value of $\varepsilon_1 \approx 100$ is established, separating samples with and without localized Cooper-pairs. From scaling with disorder, the fractal nature of the electronic eigenstates is inferred and characteristic effects of the pairing energy gap are found. The latter are reflected in a suppression of both finite frequency conductivity and dielectric constant and give direct evidence for the existence of a finite-size pseudogap evoked by Cooper-pairing [38, 39], perfectly fitting to the theory of Anderson localization being the main mechanism driving the samples insulating [12, 33].

This work is structured as follows. In chapters 2 and 3 some theoretical background is given concerning superconductivity in disordered thin-films with the theoretical concepts of e.g. Finkel'stein mechanism and fractal Anderson localization. In chapter 4 a detailed explanation of the developed experimental method concerning resonator design, optimization and the analysis procedure is given. The feasibility of this procedure is verified and demonstrated on known thin-film samples as demonstration experiments in chapter 5. In chapter 6 disordered thin-film samples of amorphous indium oxide are investigated and interpreted in the context of fractal Anderson

localization for samples without local pairing (electron glass samples) and for samples with local pairing (local pairing samples).

1.3. Deutsche Kurzfassung

Diese Arbeit befasst sich mich dünnen Schichten amorphen, ungeordneten Indium Oxids. Bei amorphem Indium Oxide handelt es sich um eine Dünnschichtprobe, welche einen Supraleiter-Isolator Übergang aufweist [8]. Sie besteht aus einer zufälligen Verteilung von Indium und Sauerstoff in einer glasartigen, amorphen Struktur [10, 19] mit vielen mikroskopischen Fehlstellen [45]. Trotz dessen, dass diese starke Unordnung vorherrscht, sind Indiumoxidproben komplett homogen [10, 11, 18–20], ohne etwaige Einschlüsse von z.B. reinem Indium. Mit zunehmender Unordnung kommt es zu einem Quantenphasenübergang (Übergang auch bei 0 K) von einer makroskopisch supraleitenden Phase zu einer isolierenden Phase, ohne dabei eine dazwischenliegende beispielsweise metallische Phase zu durchqueren [6, 8]. Beteiligt an der Unterdrückung der Supraleitung sind Phasenfluktuationen zwischen Bereichen mit hohem und niedrigem supraleitenden Ordnungsparameter [17, 28]. Hier wurde gefunden, dass die große Unordnung zu einer inhärenten elektronischen Granularität führt, welche sich in der Entstehung von supraleitenden Bereichen getrennt von nicht-supraleitenden Bereichen manifestiert [17, 28, 46, 47]. Letztere können nicht kohärent miteinander interagieren, um ein Kondensat zu bilden und Supraleitung auszubilden und trotz dessen, dass Cooperpaare vorhanden sind, können diese keinen globalen, makroskopischen Zustand einnehmen [32]. Mit zunehmender Unordnung kondensieren immer weniger Cooperpaare und die kritische Temperatur wird unterdrückt [28]. Während die supraleitende Phase im Hinblick die inhomogene, nicht kohärente Supraleitung experimentell vor allem mit Rastertunnelmikroskopie untersucht ist [26, 28, 32, 48], gibt es auf der isolierenden Seite nur sehr wenige experimentelle Befunde, die hauptsächlich auf Gleichstrommessungen

beruhen [10, 41]. Dennoch wird davon ausgegangen, dass sich hier ebenfalls ein Regime befindet, bei dem es trotz hoher Unordnung und einem isolierenden Grundzustand zur Cooperpaarung von Elektronen kommt, welche Paare bilden, die sich nicht bewegen können und damit lokalisiert sind [8, 12, 33]. Alle vermuteten Phasen sind ersichtlich in einem schematischen Phasendiagramm, dargestellt in Abb. 1.1. Die horizontale Achse bezeichnet die Energieleve-

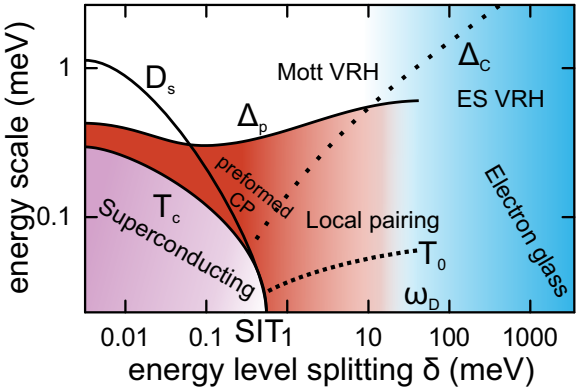

Abbildung 1.1.: Phasendiagramm isolierenden amorphen Indiumoxids als Funktion von δ, der Energielevelaufspaltung (δ steigt mit größerer Unordnung). Supraleitung ist unterdrückt aufgrund der Reduktion der supraleitenden Steifigkeit D_s. Die Paarungs-/Pseudolücke Δ_p bleibt endlich und existiert ebenfalls auf der isolierenden Seite, wo lokalisierte Cooperpaare vermutet werden. Oberhalb der Debyeenergie können diese nicht mehr existieren und Elektronen werden einzeln lokalisiert.

laufspaltung δ, welche sich direkt aus der Lokalisierung von Ladungsträgern ergibt mit $\delta \propto 1/\xi^3$ [33] mit ξ dem Radius auf welche ein Ladungsträger in seiner Ausdehnung beschränkt ist. Mit steigender Unordnung ist eine Unterdrückung der kritischen Temperatur T_c zu sehen [28, 32], welche durch die sinkende Kohärenz, die supraleitenden Steifigkeit D_s, beschränkt wird und im Übergang zum Isolator endet. Die anschließende Phase ist die Lokal-

paarungsphase, bei der Elektronen zwar zu Cooperpaaren binden können [12, 33], diese allerdings kein Kondensat mehr bilden können. Bei noch höherer Unordnung können selbst Cooperpaare nicht mehr gebildet werden, da δ die Debyeenergie übersteigt und Phononen keine attraktive Interaktion mehr vermitteln können [33]. Dieses Regime ist das Elektronenglasregime, in dem Elektronen vereinzelt lokalisiert werden [49]. Die bisher fortgeschrittenste Theorie, welche die gefundenen Befunde am besten beschreibt, beruht auf der fraktalen Andersonlokalisationstheorie mit fraktalen Eigenzuständen der lokalisierten Elektronen, die größtenteils von M. H. Feigel'man et al. entwickelt und beschrieben wurde [12, 33, 38, 39, 50]. Da die Elektronen fraktale Eigenzustände einnehmen sind sie stark in ihrer Ausdehnung eingeschränkt und lokalisieren. Dennoch können sie aufgrund von paarweiser Wechselwirkung im Impulsraum (k-Raum) Cooperpaare ausbilden, trotz dessen, dass die Cooperpaare im Ortsraum lokalisiert sind. Die Wechselwirkung wird hierbei von Phononen, analog zur BCS-Theorie [51] vermittelt, woraus sich der kritische Wert der Debyeenergie $\hbar\omega_D$ im Phasendiagramm (Abb. 1.1) ergibt. Die fraktale Andersonlokalisationstheorie beschreibt erfolgreich das Vorhandensein einer harten Energielücke in Gleichstrommessungen und einige Befunde in Tunnelexperimenten (z.B. das Verschwinden von sogenannten Kohärenzpeaks [28]), allerdings gibt es vor allem in isolierendem Indiumoxid bisher wenige weiterführende Befunde, die die Theorie unterstützen.

Ladungsträgertransport kann in einem solch ungeordneten System nur über Hüpf-Vorgänge vermittelt werden, bei dem einzelne Elektronen von einem Lokalisationsbereich zum anderen springen können [41, 43, 52–54] (das Hüpfen von Cooper-Paaren kann aufgrund derer erhöhten Masse vernachlässigt werden [55]). Dies wurde in der vorliegenden Arbeit bestätigt, wobei gefunden wurde, dass alle untersuchten Indium Oxid Proben in einem bestimmten Temperaturbereich Mott variable range hopping (VRH) $R_s(T) \propto \exp\left[(T_{0,\mathrm{Mott}}/T)^{1/4}\right]$ aufweisen, welches teilweise in Efros-Shklovskii VRH $R_s(T) \propto \exp\left[(T_{0,\mathrm{ES}}/T)^{1/2}\right]$ [53] übergeht unterhalb einer gewissen

Übergangstemperatur. Für Proben in der Lokalpaarungsphase geht der Widerstand bei Unterschreiten von etwa $\sim 4\,\mathrm{K}$ über in ein aktiviertes, Arrhenius-Verhalten mit $R_s(T) \propto \exp(T_0/T)$. Dies deutet auf eine harte Energielücke hin [12, 33], die als Paarungslücke oder Pseudolücke bezeichnet Δ_p wird und durch das Paaren von Elektronen zu Cooperpaaren entsteht.

Generell gilt, dass Supraleiter zwar einen gewissen Grad an Unordnung verkraften ohne ihre supraleitenden Eigenschaften zu verlieren [27], bei sehr hoher Unordnung jedoch wird erwartet, dass die Diffusionsgeschwindigkeit der Elektronen sehr weit reduziert wird und die abstoßenden Coulombkräfte zwischen den Elektronen die Überhand gewinnen [33], sodass anziehende Cooperkräfte übertroffen werden und eine Cooperpaarung nicht mehr möglich ist. Eine Reduktion der Übergangstemperatur T_c mit steigender Unordnung wird in diesem Zusammenhang vom Finkel'stein Mechanismus beschrieben [29, 30]. Dass in schwach supraleitenden bzw. isolierendem Indium Oxid dennoch eine Paarungslücke gefunden wird, spricht vermutlich dafür, dass die Coulombkräfte selbst bei starker Unordnung noch immer sehr stark abgeschirmt werden [33]. Abschirmung führt dazu, dass die elektromagnetischen Potentiale der Elektronen von den umliegenden Ladungen reduziert werden und sich deren effektive Ausdehnung verkleinert [56]. Dadurch kann die attraktive Cooperanziehung erneut die Oberhand gewinnen und einzelne Elektronen können zu Cooperpaaren paaren. Eine solche Abschirmung wird primär durch eine hohe Polarisierbarkeit der Ladungen im System verstärkt [33, 56]. Eine Größe dafür ist die dielektrische Konstante ε_1. Für Indium Oxide Proben ergibt sich ein kritischer Wert von etwa $\varepsilon_{1,\mathrm{c}} \approx 100$. Ist $\varepsilon_1 > \varepsilon_{1,\mathrm{c}}$, so ist die Abschirmung groß genug, dass eine Attraktion der Elektronen zueinander erwartet wird und lokalisierte Cooperpaare gebildet werden könnten.

Um ε_1 und die Mikrowellenleitfähigkeit σ_1 messen zu können, bedarf es eines einzigartigen experimentellen Ansatzes. Da es sich bei den Proben um sehr dünne Filme handelt, welche bei sehr niedrigen Temperaturen und mit relativ niedrigen Frequenzen gemessen werden müssen, um die Verluste durch Hüpfprozesse zu minimieren bzw. eventuell vorhandene lokalisierte Cooper-

paare nicht zu zerstören, sind konventionelle Methoden (z.B. Ellipsometrie, dielektrische Resonatoren) ungeeignet. Der in dieser Arbeit vorgestellte und eingesetzte Ansatz, verwendet koplanare Mikrowellenresonatoren, welche bei GHz-Frequenzen arbeiten, bei mK-Temperaturen eingesetzt werden können und hochsensibel für ε_1 und σ_1 von Dünnschichten sind [1]. Im Rahmen dieser Arbeit wurde der Ansatz entwickelt und optimiert und mit verschiedenen Simulationen, sowie Demonstrationsexperimenten verifiziert. Das Grundprinzip besteht auf der Störung der Mikrowelleneigenschaften der Resonatoren durch die Probe, welche direkt auf den koplanaren Resonator abgeschieden wird. Die Störung wirkt sich auf die Resonanzfrequenz und die Güte der Resonanzen aus, welche folglich als Messgrößen dienen und die Bestimmung von ε_1 und σ_1 erlauben.

ε_1 wurde für sieben isolierende Indiumoxidproben unterschiedlicher Unordnung bestimmt. Die gemessenen Daten sind in Abb. 1.2 dargestellt. Für jede Probe wurden mehrere Messreihen durchgeführt, bei verschiedenen Unordnungszuständen. Ausgehend von der maximalen Unordnung einer Probe, verringert sich deren Unordnung mit der Zeit oder durch gezieltes Tempern hin zu geringerer Unordnung [10, 45]. Dies wurde sich zu nutze gemacht, um einen sehr breiten Bereich an Unordnungen abzudecken, welcher einige Größenordnungen der Variation von δ umfasst. Die beiden oben genannten Regime, das Elektronenglasregime und das Lokalpaarungsregime, wurden dabei abgedeckt, wobei sich herausstellt, dass sowohl maximale ε_1-Werte im Elektronenglasregime, als auch minimale ε_1-Werte im Lokalpaarungsregime etwa $\varepsilon_1 \sim \varepsilon_{1,\mathrm{c}} \approx 100$ betragen und somit der kritische Wert von $\varepsilon_{1,\mathrm{c}}$ experimentell bestätigt wird. Unterhalb dessen gibt es keine lokalen Cooperpaare, wohingegen oberhalb dessen die Voraussetzungen für deren Bildung gegeben sind.

Die Skalierung von $\varepsilon_1(\delta)$ mit der Unordnung zeigt im Elektronenglasregime eine gute Übereinstimmung zu theoretischen Vorhersagen, die extrem lokalisiertes amorphes Indiumoxid als Andersonisolator beschreiben [39], wobei gilt $\varepsilon_1 \propto \xi^2$. Der gefundene Vorfaktor ist dimensionsabhängig, wobei den

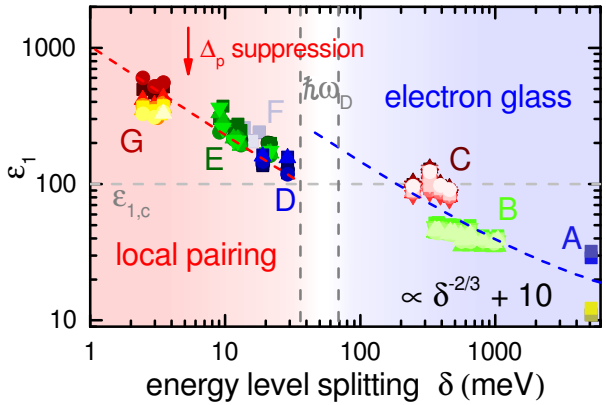

Abbildung 1.2.: Dielektrische Konstante ε_1 als Funktion von δ. Das Elektronenglasregime und das Lokalpaarungsregime liegen zu beiden Seiten der Debyeenergie $\hbar\omega_D$. Ein kritischer Wert von $\varepsilon_{1,c} \approx 100$ wird gefunden, welcher die beiden Regimes voneinander trennt, in guter Übereinstimmung mit theoretischen Vorhersagen. Im Lokalpaarungsregime ist ε_1 teilweise unterdrückt aufgrund der Paarungslücke.

untersuchten Proben ein dreidimensionales Verhalten gefunden wurde [39]. Im Lokalpaarungsregime zeigt die Skalierung von ε_1 und σ_1 mit der Unordnung, dass die zugrundeliegenden Eigenzustände der Elektronen in der Tat fraktal sind. Dies schlägt sich in der Skalierung von ε_1 mit der Aktivierungstemperatur T_0 des Arrheniusverhaltens nieder, mit $\varepsilon_1 \propto T_0^{-2/D_2}$, wobei $D_2 \approx 1.3$ die fraktale Dimension ist und perfekt mit der Theorie übereinstimmt [33].

In Messungen der Mikrowellenleitfähigkeit wurde als Funktion der Frequenz $\sigma_1(\omega) \propto \omega^2 \ln(\text{const.}/\omega)$-Verhalten gefunden, was auf Mott-Resonanzen basierende Mott-Verhalten hindeutet [38, 43, 57]. Die Leitfähigkeit wird durch die eintreffenden Mikrowellen sehr stark erhöht (thermische Aktivierung spielt bei mK-Temperaturen keine Rolle mehr) welche mit zunehmender Mikrowellenfrequenz weiter steigt. $\sigma_1(T)$ wurde zusätzlich auch als Funktion der

Temperatur gemessen, wobei ein Austin-Mott-Verhalten mit linearer Temperaturabhängigkeit gefunden wurde [43]. Aus der gefundenen Steigung kann die Lokalisationslänge bestimmt werden, welche gut mit der Lokalisationslänge bestimmt aus Gleichstrommessungen übereinstimmt. Es zeigt sich, dass die Ausdehnung der Ladungsträger auf wenige Nanometer beschränkt ist.

Im Lokalpaarungsregime ist zusätzlich eine Unterdrückung des Absolutwerts von ε_1 zu finden, welche sich in einem mit Faktor $1/a_\varepsilon \sim 2-4$ kleineren Wert zeigt, wie angedeutet in Abb. 1.2. Quantitativ ist der Unterdrückungs-Vorfaktor dargestellt in Abb. 1.3. Elektronenglasproben zeigen keine redu-

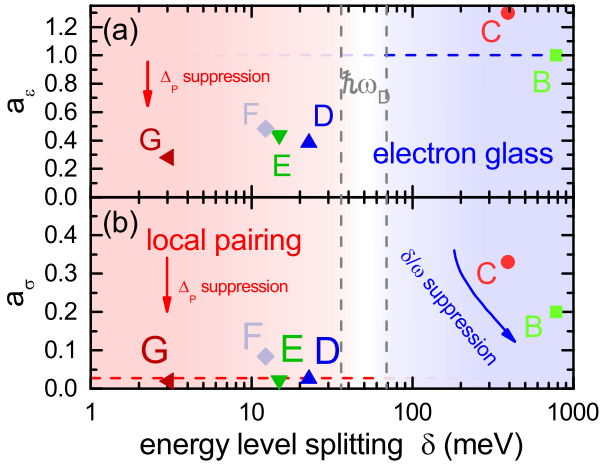

Abbildung 1.3.: Vorfaktor (a) a_ε von $\varepsilon_1(\delta)$ und (b) a_σ von $\sigma_1(\omega)$. Eine Reduktion von sowohl ε_1 als auch σ_1 wird gefunden für Proben im Lokalpaarungsregime. Dies ist in sehr guter Übereinstimmung mit theoretischen Vorhersagen. Im Elektroglasregime wird keine (ε_1) oder schwächere (σ_1) Unterdrückung gefunden.

zierten Werte, wohingegen Lokalpaarungsproben unterdrückte Werte zeigen. Ähnlich verhält es sich bei Betrachtung von $\sigma_1(\omega)$, der frequenzabhängigen

Mikrowellenleitfähigkeit, deren Absolutwerte im Lokalpaarungsregime auf etwa $a_\sigma \approx 0.03$ des aufgrund von simplen Mott-Argumenten erwarteten Wertes unterdrückt wird (im Elektronenglasregime gibt es ebenfalls eine, verglichen mit dem Lokalpaarungsregime schwächere Unterdrückung aufgrund der sehr starken Unordnung und der Reduktion der Beiträge von Mottresonanzen [33, 39]). Beide Reduktionen, a_ε und a_σ im Lokalpaarungsregime lassen sich perfekt mit der Existenz einer Pseudoenergielücke Δ_p erklären, wie dies im Rahmen der fraktalen Andersonlokalisationstheorie möglich ist [38, 39] und liefern daher Hinweise darauf, dass selbst in komplett isolierenden Indiumoxidproben noch eine Paarungslücke vorhanden ist, welche wahrscheinlich durch lokalisierte Cooperpaare hervorgerufen wird [12, 33].

Zusammenfassend konnten in dieser Arbeit die drei folgenden Hauptergebnisse erzielt werden

- In der Nähe des Supraleiter-Isolator-Übergangs sind Coulombinteraktionen zwischen Elektronen in isolierendem, amorphen Indiumoxid stark abgeschirmt und damit Unterdrückt. ($\varepsilon_1 > \varepsilon_{1,c} \approx 100$)
- Die elektronischen Eigenzustände sind fraktal in der Nähe des SIT. (Skalierung von $\varepsilon_1(T_0)$ und $\sigma_1(T_0)$ mit der fraktalen Dimension $D_2 \approx 1.3$)
- Selbst in komplett isolierendem, amorphen Indiumoxid existiert eine Pseudoenergielücke, welche auf lokalisierte Cooperpaare hindeutet. (Unterdrückung von ε_1 und σ_1)

2. Theory

2.1. Superconductivity

A microscopic theory of superconductivity has been developed by Bardeen, Cooper and Schrieffer in 1957 [51], which has been dubbed the BCS-theory. Its key points are the formation of so-called Cooper-pairs consisting of two electrons [58] at the Fermi-level which attractively interact via the exchange of a phonon. This can be understood visually by the deformation of the lattice by the negative potential of the first electron leading to a positively charged cloud, which produces an attractive force on a second electron. In this regard it is important, that electrons move faster than the lattice is able to relax back to its initial state. This is given in a typical conductor since the Fermi-energy is typically larger than the Debye energy. The attractive interaction is characterized by the Cooper-interaction constant λ, leading to electron-pairs even for arbitrarily low λ [58].

The resulting superconducting state can be characterized by the (simplified) Hamiltonian [33]

$$\mathcal{H} = \sum_{j\sigma} E_j c^\dagger_{j\sigma} c_{j\sigma} + \sum_{j,k} V_{jk} c^\dagger_{j\uparrow} c^\dagger_{j\downarrow} c_{k\uparrow} c_{k\downarrow} \,, \tag{2.1}$$

with E_j the energy of a single electron, V_{jk} the interaction potential and $c_{j\sigma}$, $c^\dagger_{j\sigma}$ the annihilation and creation operators of single electrons with spin state σ. The first term is the kinetic energy of the electrons, while the second term is the interaction of two electrons. Here, it is assumed that always

two electrons of opposite spin interact attractively. This is required, since electrons are Fermions and their total wavefunction has to have antisymmetric character even in the paired state. Since their spatial wavefunction typically is symmetrical, their spin functions have to be antisymmetrical, leading to opposing spins in the pair. This also defines the total spin of a Cooper-pair in a simple BCS-superconductor to $S = 0$. This in turn makes Cooper-pairs Bosons, which can form a macroscopically coherent ground-state ψ of defined amplitude Δ and phase ϕ, $\psi = \Delta \cdot \exp(i\phi)$ [56]. The superconducting energy gap Δ arises due to the energy gain by pairing electrons to pairs and consequently leads to a suppression of the density of states ν_0 at the Fermi energy E_F. The states suppressed at E_F shift to $E_F - \Delta$ and $E_F + \Delta$, giving a spectral energy gap of 2Δ.

If the temperature is below a certain critical temperature T_c the missing ν_0 states at E_F evoked by the formation of the macroscopic ground-state lead to completely suppressed scattering-possibilities, giving a perfect conductor with zero DC-resistivity. At finite frequencies $0 < \hbar\omega < \Delta$ and at temperatures $0 < T < T_c$, in-gap states, meaning unpaired quasi-particles lead to a finite frequency-dependent resistivity [56]. At $\hbar\omega > \Delta$ the Cooper-pairs are broken and normal-conducting behavior is restored at high enough ω. T_c stands in close relation to the gap Δ and by deriving the temperature-dependent gap $\Delta(T)$ it can be found [56]

$$\frac{2\Delta(T=0)}{k_B T_c} \approx 3.53\,. \tag{2.2}$$

For the theory of simple BCS-superconductivity this ratio is universal and independent of the material. However, if values are found which are vastly different from (2.2) it is a strong indicator that more complex mechanisms are at play such as non-BCS superconductivity [59] or strong influences of disorder [8].

Apart from zero DC-resistivity, superconductivity is also characterized by perfect diamagnetism [56]. When situated in an external magnetic field, surface currents are established, which themselves create an antagonistic magnetic field in the interior of the bulk superconductor, which in turn cancels the exterior magnetic field. This leads to an exponential decay of the external magnetic field at the surface of the superconductor. In this area also the surface currents run. For this decay the characteristic decay depth can be found with the London equations (cgs-units) [56, 60]

$$\lambda = \sqrt{\frac{mc^2}{4\pi e^2 N_s}}\,, \tag{2.3}$$

with m and e the electron mass and charge and N_s the superfluid density. This is the London penetration depth with its empirical temperature-dependence found as the Gorter-Casimir equation [61]

$$\lambda(T) = \frac{\lambda(T=0)}{\sqrt{1-\left(\frac{T}{T_c}\right)^4}}\,, \tag{2.4}$$

with T_c the critical temperature of the superconductor.

2.2. Thomas-Fermi screening

A solid metal consists of a lattice and electrons. Free electrons can rearrange freely depending on external stimuli (electric/magnetic field, current) and on the crystal structure. When adding an additional charge $-e$ into a metal, the conduction electrons rearrange and shield the electronic Coulomb potential of the additional charge. This process is called screening. In the static case ($\omega = 0$) this can be described by the Thomas-Fermi screening [56, 62]. In a classical, microscopic model, the screening is caused by repelling the

conduction electrons. This leads to an effective positive charge density around the charge directly counteracting the negative charge potential.

To find the characteristic length scale on which the Coulomb potential of the charge $-e$ is suppressed, the Poisson equation will be used following [56, 63]

$$\nabla(\varepsilon\nabla\Phi(\mathbf{r})) = -4\pi\rho = -4\pi(\rho_{\text{ind}} + \rho_{\text{ext}}) \tag{2.5}$$

$$\nabla^2\phi(\mathbf{r}) = -\frac{4\pi}{\varepsilon}\left(\delta N(\mathbf{r}) + \rho_{\text{ext}}\right) , \tag{2.6}$$

with $\rho = \rho_{\text{ind}} + \rho_{\text{ext}}$ the sum of the external and the induced charge density, ε the isotropic dielectric constant and a deviation $\delta N(\mathbf{r})$ from the homogeneous charge density N_0 as

$$\delta N(\mathbf{r}) = N(\mathbf{r}) - N_0 \, . \tag{2.7}$$

The potential ϕ adds energy to the kinetic energy of the system as [56]

$$E(\mathbf{r}) = E_F - e\phi(\mathbf{r}) = \frac{\hbar^2}{2m}\left(3\pi^2 N(\mathbf{r})\right)^{2/3} , \tag{2.8}$$

with E_F the Fermi energy. Solving (2.8) for $N(\mathbf{r})$ and expanding it around E_F leads to only a small change as (2.7) becomes $\delta N(\mathbf{r}) = -\frac{3N_0 e}{2E_F}\phi(\mathbf{r})$. Putting this into (2.6) one finds

$$\nabla^2\phi(\mathbf{r}) = -\frac{\alpha_{\text{scr}}^2}{\varepsilon}\phi(\mathbf{r}) - \frac{4\pi}{\varepsilon}\rho_{\text{ext}} \, . \tag{2.9}$$

with α_{scr} the Thomas-Fermi screening length, which can be derived in a general form as (SI-units) [62]

$$\alpha_{\text{scr}} = \frac{v_F}{\omega_P} = v_F\sqrt{\frac{m\varepsilon_0}{N_0 e^2}} \, , \tag{2.10}$$

with $\omega_P = \sqrt{N_0 e^2/\varepsilon_0 m}$ the plasma frequency [56] and v_F the Fermi-velocity. Solving (2.9) in three dimensions for a point charge $-e$ at $\mathbf{r} = 0$ with $\rho_{\text{ext}} = -e\delta(\mathbf{r})$ one finds the Yukawa potential as the solution [63]

$$\phi(r) = \frac{e}{\varepsilon r} e^{-\alpha_{\text{scr}} r}\,, \tag{2.11}$$

where r now is the distance from the additional charge. It can be seen, that the potential takes on the form of a Coulomb potential $\propto 1/r$ with an additional exponential suppression. Schematically the change between the regular Coulomb potential and the screened Yukawa potential is shown in Fig. 2.1 (a). For two electrons close to each other the overlap of the potentials

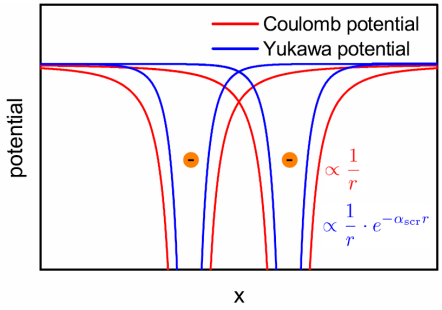

Fig. 2.1.: (a) Schematic potential in the unscreened case (Coulomb potential) and the screened case (Yukawa potential) for two point-charges close to each other. Their overlap reduces, meaning less Coulomb interaction between the charges. (b)Schematic depiction of a two-dimensional conductor and the surrounding dielectrics.

reduces and Coulomb interactions diminish.

Screening can also be mapped as a function of a wavevector-dependent dielectric function. By Fourier transforming (2.11) and taking ε as a function of the charge distribution it is found $\varepsilon_1(q) = 1 + \frac{\lambda^2}{q^2}$ [56], showing that far away from the additional charge, where $q \to 0$, ε_1 diverges, meaning that here the charge is perfectly screened and the electron states are not perturbed.

3. Superconductivity in disordered thin-films

3.1. Hopping conductivity

In disordered conductors charge carriers can be localized strongly. Typically charge transport is then mediated by variable range hopping (VRH). Originally the simplest model for VRH has been proposed by Mott [52], which focuses on non-interacting electrons. This so-called [56] Fermi-glass shows thermally assisted DC-conductivity in d dimensions following [41, 56, 64, 65]

$$\sigma_{\mathrm{DC}}(T) \propto \exp\left(-\left(\frac{T_{0,\mathrm{Mott}}}{T}\right)^{\frac{1}{d+1}}\right), \tag{3.1}$$

where [41, 52, 56, 65]

$$T_{0,\mathrm{Mott}} \propto \frac{1}{k_B \nu_0 \xi^d} \tag{3.2}$$

is the characteristic Mott-temperature with ν_0 the density of states (DOS) at the Fermi-energy and ξ a typical localization length-scale defining the localization radius. When including long-range electron-electron interactions,

meaning Coulomb repulsion, it follows the Efros-Shklovskii-type behavior for all dimensions [53, 54, 56, 65]

$$\sigma_{\mathrm{DC}}(T) \propto \exp\left(-\left(\frac{T_{0,\mathrm{ES}}}{T}\right)^{1/2}\right) \tag{3.3}$$

where [53]

$$T_{0,\mathrm{ES}} \propto \frac{e^2}{k_B \varepsilon_0 \varepsilon_1 \xi}\,, \tag{3.4}$$

with ε_1 the dielectric constant. This behavior emerges due to the opening of the so-called Coulomb-gap Δ_C [53, 56, 66], which suppresses the DOS at the Fermi-energy due to Coulomb-interactions, leading to the Coulomb-glass state. For Δ_C it holds [54, 67]

$$\Delta_C \approx \frac{e^3 \nu_0^{1/2}}{(\varepsilon_0 \varepsilon_1)^{3/2}} = k_B \left(\frac{T_{0,\mathrm{ES}}^3}{T_{0,\mathrm{Mott}}}\right)^{1/2}. \tag{3.5}$$

The soft gap (3.5), however, vanishes for large temperatures, if the temperature-assisted hopping energy exceeds Δ_C. Then the conductivity crosses over from ES-behavior (3.3) back to Mott-behavior (3.1) [66, 68].

The above formulae were derived for DC-conductivity. To find σ as a function of frequency the pair approximation is used, which is based on the probability of photon-assisted single-electron hopping between localized sites [69]. In this regard two localized states Ψ_a and Ψ_b are looked at, which are spatially separated $|x_a - x_b| > 0$ but energetically close $E_a - E_b = \hbar\omega$, so that incoming photons with frequency ω can induce the transition from one state to the other. Schematic wave functions for two such states are shown in Fig. 3.1 (a) [57]. Ψ_a and Ψ_b are localized, meaning that they are not extended across large distances but are limited to a length scale of the order of the

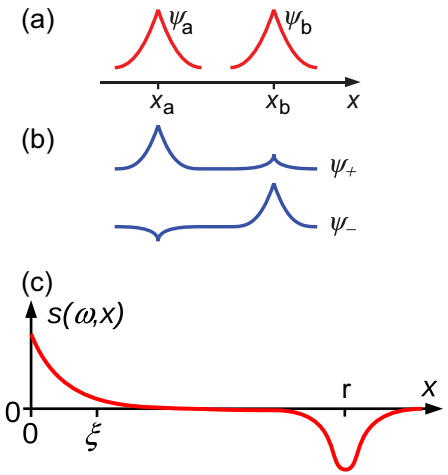

Fig. 3.1.: (a) Schematic depiction of the wave functions Ψ_a and Ψ_b of two localized single-electrons at locations x_a and x_b. (b) Hybridization of the two individual wave functions to a combination. (c) Dynamical density response function $s(\omega, x)$. ξ denotes the localization length, r the most effective hopping distance. (a) and (b) with modifications from [57], (c) with modifications from [38].

localization length ξ [57, 70, 71]. Such pairs of states can now be understood as two states hybridizing to combined states Ψ_+ and Ψ_- [57], see Fig. 3.1 (b).

An incoming photon can now excite the transition from Ψ_a to Ψ_b, which is why this excitation mechanism is founded on so-called Mott resonances. In the following only frequencies $\omega \ll \delta$ with the energy splitting $\delta \propto 1/\xi^3$ are taken into account. To find quantitative details about dynamic properties of such Mott resonances, correlation functions between the two states can be

calculated. In particular the disorder-averaged dynamical density response function is useful with [57]

$$s(\omega, |x_\alpha - x_\beta|) = 2 \left\langle \sum_{n,m} \delta(E_m - E_n - \hbar\omega) \times \Psi_n^*(x_\alpha)\Psi_n(x_\beta)\Psi_m^*(x_\beta)\Psi_m(x_\alpha) \right\rangle , \tag{3.6}$$

where the sum over all eigenstates m and n with energies E_m and E_n is taken and averaged over disorder $\langle \dots \rangle$ [38]. The factor 2 stems from spin degeneracy [38]. The general form of $s(\omega, x)$ is found as schematically shown in Fig. 3.1 (c) (where $x_\alpha = 0$ and $x_\beta = r$). The region close to 0 is dominated by the statistics of a single wave function [57], whereas at r there is a negative hump [38, 57]. r in this case is the most effective distance for hopping between two wave functions and has been found by Mott to [38, 43, 57, 65, 71]

$$r = \xi \ln\left(\frac{2I_0}{\hbar\omega}\right) , \tag{3.7}$$

with I_0 the pre-exponential factor of the overlap-integral between the states [43].

$s(\omega, |x_\alpha - x_\beta|)$ is related to several physical quantities such as the frequency-dependent conductivity σ_1 and the static polarizability χ with [38]

$$\sigma_{1,\alpha\beta}(\omega) = -\frac{\pi}{2}\omega^2 \int d\mathbf{x} x_\alpha x_\beta s(\omega, |x_\alpha - x_\beta|) \tag{3.8}$$

$$\chi_{\alpha\beta} = \frac{2}{\pi} \int_0^\infty \frac{d\omega}{\omega^2} \sigma_{1,\alpha\beta}(\omega) , \tag{3.9}$$

where (3.9) is the Kramers-Kronig relation to calculate χ from σ_1. From equation (3.8) the well-known Mott behavior $\sigma_1(\omega) \propto \omega^2 \ln^{d+1}(\text{const.}/\omega)$ [38, 71] is found.

In general, quantitatively for interacting electrons including long-range Coulomb repulsion $e^2/\varepsilon r$ it follows [43, 71]

$$\sigma(\omega) = \frac{\pi^2}{3} e^2 \xi \nu_0^2 \omega r^{d+1} \left(\hbar\omega + \frac{e^2}{\varepsilon r} \right) . \tag{3.10}$$

ν_0 is the DOS at the Fermi-energy assumed to be constant. In the two limiting cases, the case where the exciting frequency is larger than the Coulomb-interaction and the opposite case it follows

$$\sigma(\omega) = \begin{cases} \frac{\pi^2}{3} e^2 \xi^{d+2} \nu_0^2 \hbar\omega^2 \ln^{d+1}\left(\frac{2I_0}{\hbar\omega}\right) & \hbar\omega \gg \frac{e^2}{\varepsilon r} \quad (3.11) \\ \frac{\pi^2}{3\varepsilon} e^4 \xi^{d+1} \nu_0^2 \hbar\omega \ln^{d}\left(\frac{2I_0}{\hbar\omega}\right) & \hbar\omega \ll \frac{e^2}{\varepsilon r} . \quad (3.12) \end{cases}$$

Equation (3.11) is the typical Mott-behavior of the Fermi-glass [71]. Here, apart from a logarithmic correction it is $\sigma(\omega) \propto \omega^2$. In the second case, the Coulomb-glass in equation (3.12) a linear behavior is found $\sigma(\omega) \propto \omega$ in first approximation. Consequently a crossover from Coulomb-glass at low frequencies to Fermi-glass at high frequencies can be found [65, 72]. Equation (3.12) has been found assuming constant DOS ν_0 at the Fermi-level. This is given if $e^2/\varepsilon r \gg \Delta_C$, meaning that only states outside the gap contribute to the conductivity and occupation numbers are not much altered [43, 65]. However, if states inside the gap $\hbar\omega < e^2/\varepsilon r < \Delta_C$ contribute, it follows for the conductivity $\sigma(\omega) \propto \omega / \ln\left(\frac{2I_0}{\hbar\omega}\right)$ [43], meaning $\sigma(\omega)$ shows sub-linear behavior.

In the case of localized Anderson insulators, where an energy splitting $\delta \propto 1/\xi^3$ with the localization length ξ is found (see later section 3.5.2), the argument of the logarithm in equations (3.11) and (3.12) can be identified with $\ln(\delta/\hbar\omega)$ [33, 38, 39].

Above formulas are only applicable if the system is in the zero-phonon regime [43, 44]. This is the case if $k_B T \ll \hbar\omega$, meaning that here the phonon-

assisted conductivity is small compared to the photon-assisted conductivity. In this case $\sigma(\omega)$ is temperature-independent [56, 65]. It's possible, that in this regime the conductivity is many orders of magnitude larger than at zero frequency [65, 73] even at still relatively low frequencies (e.g. $1 \times 10^2 - 1 \times 10^3$ Hz [73]). If the temperature is larger however, electrons can move in the system by absorbing and emitting phonons leading to relaxation processes with their corresponding energy dissipation. The characteristic hopping distance then changes to the order of $r' = \xi/2 \ln(\nu_{\mathrm{ph}}/\omega)$ [43], with a frequency ν_{ph} on the order of phonon frequencies (typically $\sim 1 \times 10^{12} - 1 \times 10^{13}$ Hz) [43]. $\sigma(\omega)$ is found as the Austin-Mott behavior following [43, 74, 75]

$$\sigma(\omega, T) = \frac{\pi^4}{24} e^2 \xi \nu_0^2 k_B T \omega r'^{d+1} = \frac{\pi^4}{384} e^2 \xi^{d+2} \nu_0^2 k_B T \omega \ln^4\left(\frac{\nu_{\mathrm{ph}}}{\omega}\right). \quad (3.13)$$

3.2. Suppression of the superconducting wavefunction

For disordered materials the superconducting order parameter found in section 2.1 becomes highly complex, meaning that the order parameter [6, 56]

$$\psi(\mathbf{r}) = \Delta(\mathbf{r}) e^{i\phi(\mathbf{r})} \quad (3.14)$$

is strongly dependent on the underlying material properties with spatial variance both in the amplitude $\Delta(\mathbf{r})$ and the phase $\phi(\mathbf{r})$. Any suppression of the order parameter can now be driven by either part, $\Delta(\mathbf{r})$ and $\phi(\mathbf{r})$, were each mechanism is fundamentally different. Usually both mechanisms occur at the same time [8, 76] although with varying magnitude [77]. The two pathways are sometimes called the fermionic pathway (attacking $\Delta(\mathbf{r})$) and the bosonic pathway (attacking $\phi(\mathbf{r})$) [8, 77, 78]. The dimensionality of the systems which exhibit the these mechanisms are usually reduced, meaning

that the mechanisms are prominent in quasi-two-dimensional thin films [6, 8, 29, 30, 36].

A schematic phase diagram of a disordered superconductor is shown in Fig. 3.2 [8, 36]. The critical temperature as a function of disorder is depicted with the two pathways in red (bosonic) and blue (fermionic). In the fermionic

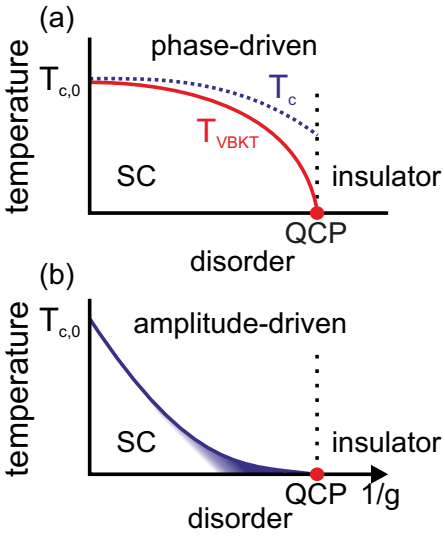

Fig. 3.2.: (a) Phase diagram of a superconductor (SC) with the critical temperature as a function of disorder. At the quantum critical point (QCP) the transition from SC to insulator happens. T_{VBKT} denotes a critical temperature at which phase-coherence and superconducting stiffness are established and macroscopic SC is formed. $T_{c,0}$ is the critical temperature from BCS-theory, which is suppressed by the Finkel'stein mechanism (T_c) shown in (b). Close to QCP fluctuations give rise to uncertainties in T_c. Modeled after [8] and [36].

case any effective attractive interaction between the electrons in the system is suppressed by increased repulsive interaction [29, 30, 79]. In BCS-type super-

conducting materials the repulsive Coulomb interactions between electrons is effectively screened by Thomas-Fermi-screening [56], see section 2.2, hence the attractive Cooper-attraction mediated by phonons surpasses the Coulomb interaction and Cooper-pairs can form [51]. Intuitively, increasing disorder in the system deceases the ability of electrons to move freely, since now the scattering rate is enhanced strongly [80, 81]. This in turn leads to less diffusive motion of the electrons and weakens screening [81]. Weakened screening however, enhances Coulomb repulsion which overcomes Cooper attraction and leads to destruction of all Cooper-pairs [30], meaning that here $\Delta(\mathbf{r}) = 0$. In Fig. 3.2 the suppression of the critical temperature by this mechanism is shown in blue. Since the fermionic mechanism applies to the formation of the Cooper-pairs themselves on a fundamental level, its corresponding critical temperature, simply called T_c in the figure, might be different from a global superconducting transition, which only occurs at T_{VBKT} [82, 83], the critical temperature of the vortex-Berezinskii–Kosterlitz–Thouless transition (explained below and in section 3.4). The suppression of T_c with disorder has been described by Finkel'stein [29, 30] and will be explained in further detail in section 3.3.

The bosonic pathway at first seems less intuitive. Here, the Cooper-pairs are not destroyed, but still remain in the system [8, 17, 28, 33, 36]. However, their long-range phase coherence, the superconducting stiffness, is lost, so they do not form a global phase coherent macroscopic state [36]. While the amplitude $\Delta(\mathbf{r})$ can still be finite, the phase $\phi(\mathbf{r})$ is not well-defined anymore and varies in space. This leads to a scenario, where the localization of electronic states due to disorder, inhibits the formation of macroscopic superconductivity, but still enables local one [17, 46, 84]. As a function of disorder this pathway leads to a reduction of the Berezinskii–Kosterlitz–Thouless (BKT) transition temperature T_{VBKT}, which is the characteristic quantity denoting the temperature below which phase-coherent superconducting stiffness is established [82, 83]. In Fig. 3.2 (a) this is shown in red. Note that in the area $T_{\mathrm{VBKT}} < T < T_c$ Cooper-pairs without phase-coherence can exist

[28, 32]. The bosonic pathway is made possible by the reduced dimensionality in thin-film systems. The quasi-2D character enhances fluctuations and generates topological defects [8]. These defects come in the form of vortices, which play a major role in the suppression of the superconducting stiffness, giving rise to the BKT-transition [82, 83].

There are two possible mechanisms which could drive the suppression of superconductivity within the bosonic pathway, depending on whether Coulomb interactions are considered to be large or negligible [33]. In the first case it is assumed, that Cooper-pairs interact with each other via Coulomb interaction, repelling each other [36, 85]. It is assumed that there are areas, where superconductivity exist locally, which are separated by insulating tunnel barriers. This is analogous to an array of Josephson-junctions, where the Coulomb charging energy E_C competes with Josephson energies E_J [14, 33]. Depending on the energy ratio E_J/E_C, the ground state is either superconducting ($E_J/E_C \gg 1$) or insulating with Mott-Hubbard localization ($E_J/E_C \ll 1$) [36, 86]. This will be explained in more detail in section 3.4.

The other possible mechanism in the bosonic pathway neglects Coulomb interactions between Cooper-pairs completely. In this case, the localization of single electron states are the main reason for suppression of macroscopic superconductivity and directly lead to an insulating ground state [33, 87]. It is suggested [33] that this mechanism is a third alternative to fermionic and bosonic and should be called the "fractal pseudo-spin scenario", since the (fractal) superconductivity emerging in this scenario can be described using Anderson's reformulation of the BCS-theory with pseudo-spins [33, 88]. The detailed mechanisms at play will be explained further in section 3.5.

While the first bosonic pathway with the interplay of E_J and E_C seems primarily dominant in granular materials [89–91], where the inhomogeneous structure of the films already imposes superconducting granularity with island-like structure that is separated by non-conducting material, the situation is more complicated in homogeneously disordered amorphous thin-films. Here, also a suppression of superconductivity is found [8, 17, 28, 33, 46, 47, 92,

93], with emergent superconducting granularity [17], the underlying physics however, may be more complex [8, 33].

For sufficiently high disorder, at some point a quantum critical point (QCP) is traversed in a continuous quantum phase transition [9]. In the following regime, there is no superconducting stiffness and phase-coherence will not be able to be established even at arbitrarily low temperatures. Typically this regime can either be metallic or an insulating state [8]. In this work, the insulating state will be highlighted, since it is the most peculiar state occurring in some homogeneous amorphous thin-films, in particular in indium oxide [10–12, 33, 48]. The nature of this state still poses many unresolved questions, as it shows strong insulating behavior, sometimes exceeding even simple activated behavior [42, 94], yet Cooper-pair formation still seems possible. This poses the question, whether in this regime with localized single-electron states, also the Cooper-pairs are localized. This would possibly be the case for $T < T_c$ (compare Fig. 3.2), if T_c still remains finite far into the insulating state, yet $T_{\mathrm{VBKT}} = 0$.

Of course it is not always clear cut whether it is only one pathway or the other and the pathways are not entirely separable. In real materials there are often contributions from multiple pathways at the same time [8]. It is also possible that depending on the amount of disorder first the fermionic pathway for medium amounts of disorder will occur to some extend, followed by a bosonic pathway at higher disorder [8]. Current state of the art experiments for thin-films of indium oxide will be shown in section 6.1.

3.3. Finkel'stein mechanism

In the Finkel'stein mechanism Coulomb interactions play a large role [29, 30]. They are the main driving forces inhibiting the formation of Cooper-pairs and ultimately preventing superconductivity. It's possibly applicable to some homogeneously disordered thin-films without any underlying granularity.

While superconductivity is robust when subjected to small amounts of disorder (Anderson theorem) [27], increasing disorder at some point leads to a substantial decrease of the diffusive motion of the electrons, decreasing screening and thus enhancing Coulomb interactions between electrons [81]. To describe superconductivity in such conditions, the BCS-mean field theory [51] is extended to include disorder reduced Cooper-attraction as [33]

$$\lambda(E) = \lambda_0 - \frac{e^2}{3\pi\hbar} R_\square \ln \frac{1}{E\tau}\,, \tag{3.15}$$

with a small energy transfer E, λ_0 the unaltered Cooper-attraction and τ the mean scattering time. $R_\square$ is the normal-state sheet resistance of the thin-film. T_c is directly related to λ and can be found as [29, 30]

$$T_c = T_{c,0}\left[1 - \frac{1}{12\pi g}\ln^3\left(\frac{1}{T_{c,0}\tau}\right)\right]\,, \tag{3.16}$$

with $T_{c,0}$ the unaltered critical temperature, assuming zero disorder ($g \to \infty$). (3.16) is now expressed as a function of $g = \frac{h}{4e^2 R_\square}$, which is the dimensionless film conductance [33]. For strong disorder close to complete suppression of superconductivity it is found with renormalization-group analysis [7, 29, 30]

$$\begin{aligned} T_c &= T_{c,0} e^{-\frac{1}{\gamma}} \left[\frac{\gamma - \rho/4 + (\rho/2)^{1/2}}{\gamma - \rho/4 - (\rho/2)^{1/2}}\right]^{1/\sqrt{2\rho}} \\ \text{with } \gamma &= \left(\ln \frac{T_{c,0}\tau}{\hbar}\right)^{-1}\,, \quad \rho = \frac{e^2}{2\pi^2\hbar} R_\square\,. \end{aligned} \tag{3.17}$$

(3.17) now describes the suppression of T_c with increasing sheet resistance of the thin-film and is shown in Fig. 3.2 (b) as a function of $1/g$ and in Fig. 3.3 as a function of $R_\square \propto 1/g$. Fig. 3.3 shows good agreement with T_c-data from MoGe-films of different disorder [29, 31]. It demonstrates that when increasing disorder, the resistivity of a material increases, meaning reduction of g, and T_c is quickly suppressed. At some point the superconductivity is

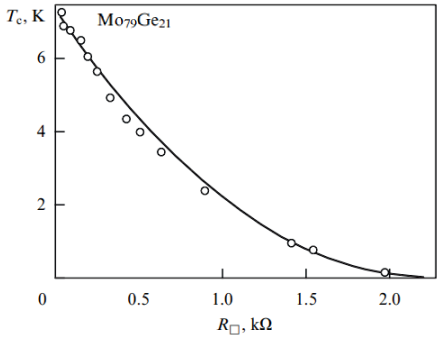

Fig. 3.3.: Critical temperature T_c of MoGe thin-films as a function of disorder, with $R_\square \propto 1/g$ as characteristic quantity. The data is well described by (3.17). From [7] based on [29] with data from [31].

even terminated completely. From (3.17) a critical conductance is found as $g_c = \frac{1}{2\pi} \ln^2 \frac{1}{T_{c,0}\tau}$ [8].

The Finkel'stein mechanism is a valid pathway to describe suppression of superconductivity with disorder and focuses on the suppression of $\Delta(\mathbf{r})$ at all locations $\mathbf{r}$ in the system. However, the number of systems it can describe successfully is limited. In most, g_c is quite large [8, 29, 33] meaning that superconductivity is quickly suppressed at low amounts of disorder. Superconductivity is then terminated by a 'bad metal' regime showing weak localization effects.

An interesting effect that occurs very close to the transition at g_c is the formation of mesoscopic fluctuations of the superconducting state in real space [95–97]. Small spatial variations in the conductance $g(\mathbf{r})$ lead to strong influence on the Cooper-coupling (3.15) and consequently on the local critical temperature $T_c(\mathbf{r})$ (3.16). For nearly critical films $g \approx g_c$ the fluctuations even become as large as T_c itself, $\Delta T_c/T_c \geq 1$, meaning that now the superconducting state has become inhomogeneous. Superconducting islands are separated by poorly metallic barriers [33, 97]. They form weakly

coupled SNS Josephson-junctions, which depending on the competing energies of E_C and E_J can form a non-superconducting state already below g_c [97]. In the systems discussed here, the interplay between E_J and E_C is highly complex due to the fluctuating nature of the superconducting state near g_c. Nevertheless it seems closely related to the suppression of superconductivity with the Coulomb-blockade in Josephson-junction arrays, as will be discussed in section 3.4.1.

3.4. Berezinskii-Kosterlitz-Thouless physics

Opposed to the amplitude-driven pathway of section 3.3, which mainly suppresses Δ in the wavefunction (3.14), the phase-driven pathway focuses on (quantum) fluctuations in the phase $\phi(\mathbf{r})$ that destroy superconductivity [6]. Here, for sufficiently high disorder, $\Delta(\mathbf{r})$ can remain finite, forming superconducting "puddles", that are separated by non-superconducting areas [17, 33], while a global macroscopic superconducting state cannot be established. Depending on whether Coulomb interactions between the charge carriers play a role within the context of this pathway, different mechanisms can be at play, on the one hand based on BKT-physics (including Coulomb interactions) [8, 14, 98], discussed in this section, or on the other hand on localization of single-electron states (neglecting Coulomb interactions) [33], which will be discussed in the next section 3.5.

The Berezinskii-Kosterlitz-Thouless (BKT) transition [82, 83] is based on the topological binding-unbinding phase transition of a pair of vortices and antivortices in a two-dimensional system. It appears in 2D-materials or Josephson-junction (JJ) arrays, where superconductivity is confined to superconducting areas separated by tunneling barriers [99, 100]. For the vortex-BKT transition the system has to be strong-coupling and the Josephson energy has to be larger than the Coulomb charging energy $E_J > E_C$, so the system becomes superconducting at low temperatures [14]. In these

systems vortex-antivortex pairs interact with each other and are able to bind and unbind depending on temperature and properties of the underlying material/array. To conserve flux neutrality there are always equal amounts of vortices and antivortices.

Above the characteristic binding temperature T_{VBKT}, where the system is resistive, the vortex-antivortex pairs are unbound and the vortices as well as the antivortices can diffuse freely [14]. Since every vortex carries a phase of 2π (this can be seen by integration around a vortex, encircling it), their movement in the system leads to phase fluctuation, directly inhibiting global phase coherence, suppressing superconductivity. Below T_{VBKT} however, the vortices and antivortices bind together and form neutral dipoles. These dipoles each consist of one vortex and one antivortex, giving a total phase of zero when encircling the dipole. Since the pair carries no phase, diffusion of the dipole does not cause phase fluctuations and has no influence on the global superconducting phase. Below T_{VBKT}, therefore superconductivity sets in.

The defining parameter for the magnitude of T_{VBKT} is whether it is energetically more favorable to bind vortex-antivortex pairs together or to have them unbound in the system. Two energies play antagonistic roles. The binding energy of the pair is competing with the energy contribution of the entropy. The total energy is found as the Helmholtz free energy consisting of the energy of a vortex-antivortex pair and the product of temperature and entropy. For one vortex-antivortex pair this gives [14, 83]

$$\begin{aligned} F &= E - TS \\ &= E_0 \ln\left(\frac{r}{a}\right) - k_B T \ln\left(\left(\frac{r}{a}\right)^2\right) \\ &= (E_0 - 2k_B T) \ln\left(\frac{r}{a}\right) . \end{aligned} \tag{3.18}$$

Here, E_0 is the energy parameter of the pair, r is their distance and a is a minimum spatial cut-off parameter. In JJ-arrays a is the lattice parameter

with which the number of configurations to place a vortex-antivortex pair at a distance r is $\propto (r/a)^2$, giving the above entropy contribution. From (3.18) it is seen that F can either be positive or negative depending on temperature

$$F = \begin{cases} > 0 & \text{for} \quad T < \frac{E_0}{2k_B} \\ < 0 & \text{for} \quad T > \frac{E_0}{2k_B} \,. \end{cases} \tag{3.19}$$

Therefore, below the critical temperature T_{VBKT}, defined at $F(T_{\mathrm{VBKT}}) = 0 \Rightarrow T_{\mathrm{VBKT}} \approx E/2k_B$, it is energetically favorable to reduce the distance $r \to 0$ between the vortex and antivortex in order to minimize F. The vortex-antivortex pair is consequently bound to a dipole. Above T_{VBKT}, the system reduces energy by placing the vortex and antivortex far apart due to the energy gained by the entropy contribution. The vortex and antivortex are then unbound and free to diffuse.

A crucial requirement for equation (3.18) is the fact that the interaction energy between the vortex and antivortex grows logarithmically with their separation $\propto \ln(r/a)$ and not faster, so it combines exactly with the energy contribution from entropy [83]. This is only given in 2D lattice systems [14]. Another requirement is for the model system to have relatively large superconducting puddles connected by tunneling barriers [8]. This fixes a to be relatively large. This in turn is necessary, since one limiting factor is the vortex-antivortex confinement. The distance of the pair must not exceed the London penetration depth λ_L [14]. The requirement for large superconducting puddles and large values of a is given in artificial JJ-lattice systems. However, in the case of homogeneously disordered systems, it is argued that typical sizes of superconducting puddles might be much smaller than what is required and the tunnel barriers might be too inhomogeneous and inconsistent in coupling strength [8].

3.4.1. Coulomb-blockade in Josephson-junction arrays

The deciding factor, whether a lattice system goes superconducting or if it goes insulating at low temperatures is the competition between Josephson energy E_J and Coulomb charging energy E_C. The latter, the energy needed to add an additional Cooper-pair to a superconducting grain is $E_C = (2e)^2/2C$ [33], C being the capacitance containing contributions from inter-grain coupling as well as the ground capacitance of the grain [98]. If E_C is smaller than E_J, then superconductivity is possible with the mechanism detailed above. However, if $E_C > E_J$ movement of Cooper-pairs from one grain to the other is unfavorable and any conduction is suppressed leading to an insulator. The transition from superconductor to insulator happens at $E_J \approx E_C$ [14, 33]. A model to describe this transition based on superconducting grains has first been proposed by M. P. A. Fisher [35, 36, 85] and proposes the following Hamiltonian

$$\mathcal{H} = \sum_{ij} E_C^{ij} \left(N_i - q_i\right)\left(N_j - q_j\right) - \sum_{ij} E_J^{ij} \cos\left(\phi_i - \phi_j + A_{\text{ext}}^{ij}\right) . \qquad (3.20)$$

The first sum describes charging energies of the grains i and j, while the second term describes Josephson-tunneling energies. In addition to the pure charging energies described by $\sum_{ij}(2e)^2/(2C_{ij})N_iN_j$, an additional contribution q_i is introduced, giving each grain a small random potential to ascribe for conditions in real JJ-arrays [101], where it has been found that random fluctuations occur, although with very slow change. Due to the slow variation, they can be set constant ascribing them to be quenched to a fixed value [33, 36]. Furthermore the second term, the Josephson term includes an additional magnetic vector potential A_{ext}^{ij} (with $\mathbf{B}_{\text{ext}} = \nabla \times \mathbf{A}_{\text{ext}}$) to include a possible contribution from an external magnetic field giving the magnetic-field-driven transition [22, 24, 36]. For the purely disorder-driven transition it is $A_{\text{ext}}^{ij} \equiv 0$.

(3.20) describes hard-core, interacting charge carriers, dubbed "dirty bosons" [8, 102]. The implications of this model are not fully understood yet [33] and

pose several curious properties, which e. g. show glassy features with Cooper-pairs forming a Bose-glass [35, 103]. The transition from superconductor to (possibly) insulator in this mechanism is driven by the competition between Cooper-pairs and vortices wanting to condense. Similar to Cooper-pairs, which condense to a macroscopic state at T_{VBKT}, vortices can also condense to a macroscopic state, since both are bosons. At the critical disorder, where the transition happens, both want to form macroscopic states, which in turn leads to them diffusing at the same time. Here it is therefore predicted that there should exist a universal resistance with the quantum resistance of a Cooper-pair $h/(2e)^2 \approx 6.5\,\mathrm{k\Omega}$ [85, 102, 104]. This metallic behavior at the transition and its scaling [36] close to the transition is debated, yet it could be found in experiments to varying accuracy even in homogeneously disordered thin-film samples such as indium oxide [22, 105].

Another implication of the model (3.20), in particular in dependence of an external magnetic field, is the emergence of negative magnetoresistance in the insulating phase [40, 89, 106, 107]. In the insulating phase, all charge carriers are formed to Cooper-pairs and localized due to Coulomb interactions and random potentials, following (3.20). This means, that there are no single electrons left in the systems, which could contribute to the conductivity via tunneling. Subsequently the insulating phase has large resistance with $R(T) \propto \exp\left(T_0/T\right)$. If a large external magnetic field is applied however, the superconducting gap is suppressed and Cooper-pairs are split up. The single-electrons have a larger tunneling amplitude and lower Coulomb charging energy (due to having a charge of e as opposed to a Cooper-pair with $2e$), which leads to an increase in conductivity, since now single-electrons contribute to transport. This intriguing effect has been found in granular materials [89], as well as in homogeneously disordered thin-films of indium oxide [40, 107].

3.4.2. Superconductor-superinsulator duality

At the beginning of section 3.4 it has been shown that Berezinskii, Kosterlitz and Thouless found a fundamental transition, which is based on the idea that the superconducting transition is explained by the formation of bound vortex-antivortex pairs with total phase zero. Fundamental requirement for this transition is the logarithmic dependence of the binding energy on the distance so it exactly combines with the energy contribution of the entropy (equation (3.18)). This mechanism however, is suggested to not be limited to the superconducting phase alone. Deep in the insulating phase, the attraction between Cooper-pairs and "anti-Cooper-pairs" gains logarithmic character leading to a full duality between superconductor and (super-)insulator [36, 85, 108]. In literature suggesting the presented theory, "Anti-Cooper-pairs" are typically characterized denoted as the "local deficit of a Cooper-pair" [14, 109]. Both Cooper-pairs and anti-Cooper-pairs are suggested to be found in equal amount in these systems to conserve neutrality [14]. Similar to the critical temperature T_{VBKT}, the temperature of the **v**ortex-BKT transition at which vortex-antivortex pairs bind, a critical temperature T_{CBKT} is found at which the **c**harge-BKT transition happens, where Cooper-pairs and anti-Cooper-pairs bind.

The implications of this are a superinsulating state at low temperatures, at which conductivity reaches exactly zero at finite temperatures [34, 42, 94]. Similar to a superconductor where resistivity reaches zero, it is the conductivity which vanishes in the superinsulating state. A phase diagram including all these phases has been proposed [14, 100] and is shown in Fig. 3.4 [14]. The exact shape of the phase-diagram, in particular directly at the QCP at g_c, whether $T_{\mathrm{CBKT}}(g_c) = T_{\mathrm{VBKT}}(g_c) = 0$ or maybe $T_{\mathrm{CBKT}}(g_c) = T_{\mathrm{VBKT}}(g_c) > 0$ is still under debate [14]. g can have two meanings, it can either be the energy ratio $g = E_J/E_C$ with $g_c = E_J \approx E_C$ for JJ-arrays [14, 33], or the dimensionless conductance for homogeneously disordered thin-films. For large g, meaning for disordered thin-films with good conductivity

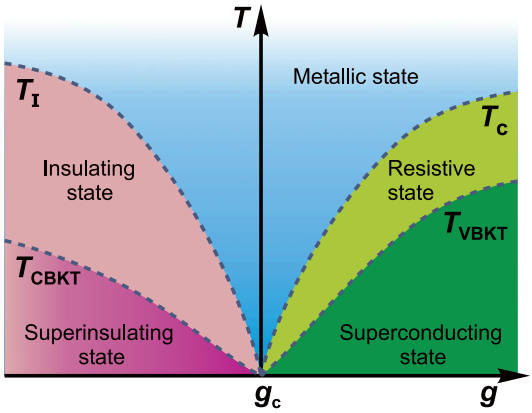

Fig. 3.4.: Proposed phase-diagram for the superconductor-superinsulator duality. For high g (high conductivity for disordered films or large coupling $g = E_J/E_C$ in JJ-arrays) below T_c Cooper-pairs form. Only below T_{VBKT} the vortex-antivortex pairs bind and superconductivity is reached. At $T_{\mathrm{VBKT}} < T < T_c$ the film is still resistive. For low g this is analogous, below T_I the Cooper-pairs form but can still tunnel from site to site, leading to activated insulating behavior. Below T_{CBKT} Cooper-pairs anti-Cooper-pair dipoles bind and true zero is reached in conductivity forming the superinsulator. Taken from [14].

or JJ-arrays with good inter-grain coupling, the system goes from a metallic state via a resistive state with Cooper-pairs to the superconducting state. Below T_c Cooper-pairs form, however no phase coherence is established, which is due to the diffusion of vortices and antivortices. Conduction is still possible driven by inter-grain Josephson-tunneling of Cooper-pairs from one grain to the other [14]. Since the single-electrons pair together, their density decreases and their contribution to conductivity reduces. This can lead to an increase in resistivity at temperatures slightly above T_{VBKT}. Below T_{VBKT} vortices

and anti-vortices bind and macroscopic phase-coherence of the Cooper-pairs is established.

On the insulating side $g < g_c$, the metallic state is terminated at T_I which marks the critical temperature of the insulating state. At temperatures $T_{\mathrm{CBKT}} < T < T_I$ the conductivity has thermally activated behavior [14], where charges are bound to Cooper-pairs, that can tunnel from grain to grain. Since charge transport is mediated by this tunneling, this regime might also be dubbed "Cooper-pair insulator". Below T_{CBKT} Cooper-pairs and their local deficits the "anti-Cooper-pairs" [14, 109] attract due to their logarithmic interaction and Cooper-pair-anti-Cooper-pair dipoles are formed, which do not carry any charge and are therefore neutral [14, 109]. Naturally, any charge transport is inhibited, which thus leads to the superinsulator. As a consequence, the resistivity increases (conductivity decreases) much faster with T [42] in a double-exponential fashion $\rho \propto \exp\left[\exp a\,(b/T)\right]$ (with a and b some constants) [34].

One fundamental requirement for the superinsulating state is the logarithmic dependence of the Coulomb interactions on the distance r between Cooper-pair and anti-Cooper-Pair, similar to the logarithmic dependence between vortex and anti-vortex in the vortex BKT-transition. It has been found [110] that this interaction indeed becomes $V(r) \approx 2e^2/(\varepsilon_1 d)\,\{\ln\left[2e/(\varepsilon_s+1)\cdot d/r\right]\}$ with d the film thickness, ε_1 its dielectric constant and ε_s the dielectric constant of the substrate below the film (with vacuum/air on top). For this dependence to hold however, the electrostatic screening length $\varepsilon_1 d/(\varepsilon_s+1)$ [14, 110] has to be larger than the Cooper-pair anti-Cooper-pair distance $d \ll r \ll \varepsilon_1 d/(\varepsilon_s+1)$ [34, 94, 110]. For $\varepsilon_1 d/(\varepsilon_s+1) \ll r$ the potential becomes the usual $V(r) \sim 1/r$. The fact that the screening length is larger than the distance, and consequently has to be larger than the total system size [34], requires the dielectric constant ε_1 to be very large (as an order of magnitude example, for a 10 nm-thick sample with size 10 µm and a substrate with $\varepsilon_s = 10$, ε_1 has to be $\varepsilon_1 \approx 10\,000$). In this framework however this is expected, since close to the transition ε_1 should increase strongly.

The network of grains coupled via Josephson junctions behaves similar to a percolative system [14, 34, 111], where disorder breaks connections from one grain to the next. Here, ε_1 is expected to diverge at the transition, see the appendix section A.1. Consequently with large ε_1 logarithmic distance dependence holds and charge BKT-transition can occur. However, when going very deep into the insulating regime at some point for low enough g the electrostatic screening length decreases to smaller than the sample size [14] since ε_1 decreases. At this point the Coulomb interaction is no longer of logarithmic nature and the superinsulator ceases to exist.

Another important consequence is the dependence of the activation energy in the insulating state on the system size [14, 34, 111–113]. In the insulating state, the conductivity follows $\sigma \propto \exp(-\Delta_C/k_BT)$ with the activation energy $\Delta_C = E_C \ln(L/a)$ (for 2D JJ-arrays), with L the linear size of the array and a the grain size [34, 111]. This size-dependent activation energy is a consequence of the macroscopic Coulomb-blockade spanning the whole array. The transport of a cooper-pair along the array therefore not only depends on the capacitance of a single grain, but the total capacitance of the whole system, which scales with $\ln(L/a)$ and results in the above activation energy [14, 34, 111]. For this concept to apply however, the system size has to be smaller than the Coulomb screening length [34], or the screening length has to be larger than the system size respectively, which seems unlikely in disordered superconductors [33]. Nevertheless some size-dependence on the transport has been found in homogeneously disordered indium oxide [112] and TiN [113], but has not been found in JJ-arrays yet [14].

3.5. Fractal Anderson localization

Up to now all mechanisms of superconductivity suppression and insulation in disordered thin-films have included (strong) Coulomb interaction between the charge carriers, being either single electrons (Finkel'stein mechanism,

section 3.3) or Cooper-pairs (BKT-physics, section 3.4). However, mechanisms for localization without Coulomb interactions are also possible. Here, Cooper-attraction as the only form of interaction between electrons is the driving force for localization.

The following mechanism relies on the simple BCS-mean field theory [51], with the addition of strong disorder and combines both analytical and numerical approaches [8, 12, 33]. While weak disorder does not perturb superconductivity in bulk superconductors [27], strong disorder can lead to localization of single-electron states, which in turn leads to destruction of superconductivity. In this context the wavefunctions of the electrons become (multi-)fractal [12, 33, 114]. The emerging superconductivity can be described by Anderson's reformulation of the BCS-theory with pseudo-spin operators, which is why this mechanism can also be called the "fractal pseudo-spin" mechanism [33]. The mechanism assumes the samples to be thick enough for them to be assumed three dimensional [12, 33] as a similar theory for two dimensional systems is not yet constructed [33].

The main parameter determining whether a system is superconducting or insulating with this mechanism is the size of the Fermi-energy E_F compared to the Anderson mobility edge E_m [12, 33]. The mobility edge is the energy of the highest localized state, meaning that E_m separates the localized from the extended states. If E_F lies beyond E_m, the electron states at the Fermi-level are localized and the material is expected to be an insulator, while if E_F lies outside the mobility edge there are mobile electrons resulting in the system being conductive. In the localized state of a highly disordered system, the electrons interacting with each other are electrons of opposite spin (analogous to singlet BCS-theory).

3.5.1. Fractal nature of nearly localized electron wavefunctions

One key element in this mechanism is the (multi-)fractal nature of the electronic eigenstates [12, 13, 33, 37, 114]. Close to the Anderson localization transition the eigenstates of the single-electron wavefunctions become fractal in spatial dimension, meaning that they only occupy a fraction of the given volume a delocalized eigenstate would occupy [37, 114]. A visual representation can be seen in Fig. 3.5 [37]. The implications on the properties of

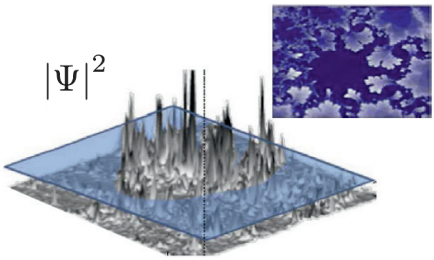

Fig. 3.5.: 3D representation of the spatial intensity $|\Psi|^2$ of a wavefunction of a fractal state close to the transition at the Anderson mobility edge. The inset shows the cut through the blue plane. It is found, that the wavefunction occupies only a fraction of the space. With modifications from [8], data from [37].

the model at hand can be derived starting from the BCS-Hamiltonian (2.1) (section 2.1), since the present theory describes simple BCS-type interaction between single-particle fermionic electrons. Now, for the interaction potential a space-local BCS-type interaction via phonons is assumed $V_{ij} = g\delta(\mathbf{r})$, with g the electron-phonon coupling constant. Only pair-wise terms are taken into account leading to the Hamiltonian [12, 33]

$$\mathcal{H} = \sum_{j\sigma} \mathcal{E}_j c^\dagger_{j\sigma} c_{j\sigma} - \frac{\lambda}{\nu_0} \sum_{j,k} M_{jk} c^\dagger_{j\uparrow} c^\dagger_{j\downarrow} c_{k\uparrow} c_{k\downarrow} \,, \tag{3.21}$$

with $\mathcal{E}_j = E_j - E_F$ the energy of the single-particle in relation to the Fermi-energy. The matrix elements in (3.21) [12],

$$M_{jk} = \int d\mathbf{r} \Psi_j^2(\mathbf{r}) \Psi_k^2(\mathbf{r}) \,, \tag{3.22}$$

play the crucial role, quantifying the interaction between the single-electrons. Here, in particular the diagonal elements $j = k$, describing *local* interaction of two electrons with opposite spin show anomalous scaling. For $j = k$ equation (3.22) becomes one-over the inverse participation ratio (IPR) $\mathcal{N}$ [115, 116]. It has been found that for a fractal system this IPR has an unusual scaling with the localization length following [12, 116]

$$\begin{aligned} \mathcal{N} = M_{jj}^{-1} &= \left(\int d\mathbf{r} \left| \Psi(\mathbf{r}) \right|^4 \right)^{-1} \\ &\propto \xi^{D_2} \,, \end{aligned} \tag{3.23}$$

The IPR gives a quantity for the number of eigenstates a (de-)localized electron is subjected to. A perfectly delocalized electron extends along all eigenstates in the system. Consequently for a large system, $\mathcal{N} \to \infty$, since $\Psi(\mathbf{r}) \sim 1/\sqrt{N}$ (from normalization) and N the number of eigenstates. If an electron is perfectly localized however, $\Psi \sim \delta(\mathbf{r})$ and $\mathcal{N} \to 1$.

The scaling of the IPR in (3.23) as a function of the localization length is attributed to the multifractality of the system. Here D_2 is the correlation exponent or the fractal dimension [12, 33, 116, 117]. For a fully delocalized system $D_2 = d$ with d the dimension of the system (in this case $d = 3$), for a fully localized system $D_2 = 0$. For a multifractal system $0 < D_2 < d$, which means that the multifractal wave is delocalized, but occupies only a fraction of the given space [116]. D_2 can only be found numerically. It has been found

for model systems in $d = 3$ with sizes up to several thousands of calculated states as [116, 117]

$$D_2 \approx 1.29 \pm 0.1\,. \tag{3.24}$$

3.5.2. Localization mechanism

The main concept of the suppression of superconductivity in this mechanism is the competition of several energy scales as well as their corresponding characteristic length scales. On the one hand there are the superconducting gap Δ at the Anderson transition point [12] and the Debye-energy $\hbar\omega_D$ of the phonons mediating the Cooper-attraction between the electrons. On the other hand there is the mean quantum level spacing of the single-electrons δ [118]. In a standard BCS-type superconductor it is $\delta \ll \Delta \ll \hbar\omega_D$. However, when confining the electrons to small localization volumes with the radius ξ, the localization length, the average energy level spacing becomes

$$\delta = \frac{1}{\nu_0 \xi^3}\,, \tag{3.25}$$

with ν_0 the single-particle density of states. If $\delta \ll \Delta$, the level spacing being smaller than the gap, the BCS-theory holds and conventional superconductivity is formed. However if δ gets close to Δ, the BCS-theory fails at some point and localization effects occur. Originally this has been derived for small grains of superconductivity [118] (ξ in this case being the size of the grain), but this mechanism can also be generalized to bulk Anderson insulators [12, 33], where fractality plays an additional role.

The main control parameter of this model is the Fermi-energy E_F [12, 33] in comparison to the Anderson mobility edge E_m. Both of which determine the localization length following [12]

$$\xi = l \left(\frac{E_0}{E_m - E_F} \right)^{\nu} \quad \text{with} \quad E_0 = \frac{1}{\nu_0 l^3} \,. \tag{3.26}$$

l is the minimal length of the fractal structure [12, 33] similar to a "pixel" [33] and its corresponding energy scale is E_0, which can be smaller than E_F [12, 33]. Typically l can be assumed to be of the order of the mean free path [33, 119]. ν_0 is the single-particle density of states at E_F. ν is the localization length exponent [33] which can vary from $\nu \approx 1.57$ (E_F close to E_m) [120] to $\nu \approx 1.2$ (E_F slightly further away from E_m), determined numerically.

A (pseudogapped) insulator is now formed if $\Delta \ll \delta \ll \hbar\omega_D$, meaning the level spacing is larger than the superconducting gap but still smaller than the Debye energy. The superconductive long-range order will not prevail and the macroscopic, coherent superconductivity will not form, however since $\delta \ll \hbar\omega_D$, interaction between electrons can still be mediated by phonons and local pairing between electrons at the same location with opposing spins will occur [12]. In this pseudogapped insulator [33, 39], there are still local areas which are superconducting [13], however, global transport will show that the system stays insulating even at arbitrarily low temperatures. The hallmark result of this localization mechanism is therefore that only the attractive Cooper-interaction between the electrons can already drive localization without the need of a repulsive force such as e. g. the Coulomb repulsion in BKT-physics (section 3.4).

In this insulating regime the remaining conductivity in the system is mediated by unpaired electrons, since conduction mediated by Cooper-pairs is strongly suppressed [33]. The remaining single electrons however, have higher energy due to being unpaired. Any local area in the system (e.g. of

size ξ) carrying an odd number of electrons with a single unpaired electron has a higher energy than that for the closest even number. This leads to the emergence of a parity gap Δ_p [118]. It can be found by adding a single-particle excitation transferring an electron from the m-th state to the $m+1$-th state on an already filled Fermi-sea as [33]

$$\begin{aligned}\Delta_p &= \frac{3}{2}\lambda E_0 \left(\frac{E_m - E_F}{E_0}\right)^{\nu D_2} \\ &= \frac{3}{2}\lambda E_0 \left(\frac{l}{\xi}\right)^{D_2},\end{aligned} \tag{3.27}$$

with ξ from equation (3.26) and λ the Cooper-attraction constant. Equation (3.27) is a single-particle formula, however the corresponding energy scale Δ_p is also the defining quantity of macroscopic transport properties. This is due to the fact that all pairs of electron reduce in energy by the amount Δ_p. Electron-pairs themselves, however, cannot contribute to charge transport when localized sufficiently deep in the insulating regime [55]. The transport is then characterized by the breaking of electron pairs, followed by hopping of individual single electrons. This will further be discussed in section 3.5.5. Consequently Δ_p has to be overcome, meaning that a hard-gap insulator is formed. The resulting DC-conductivity shows activated behavior with [12, 33]

$$\sigma(T) \propto \exp\left(-\frac{T_0}{T\ln\left(T_0/T\right)}\right) \tag{3.28}$$

$$\text{and} \quad T_0 \sim 0.25\Delta_p\,. \tag{3.29}$$

As a function of the localization length ξ, the activation energy T_0 is hence found from equations (3.29) and (3.27) as

$$T_0 \approx 0.5\lambda E_0 \left(\frac{l}{\xi}\right)^{D_2} \tag{3.30}$$

$$= 0.5\frac{g}{l^3}\left(\frac{l}{\xi}\right)^{D_2}, \tag{3.31}$$

with $\lambda = g\nu_0$ where g is the electron-phonon coupling strength [33, 119]. Any remaining conductivity due to VRH of single-electrons is strongly suppressed due to the pairing-induced reduction of the DOS at the Fermi energy. Usually the slightly altered activated behavior in equation (3.28) cannot be distinguished in experiments [33] from a purely activated behavior, hence the latter (see equation (4.89)) is used throughout this work.

The resulting phase diagram found for the fractal Anderson transition is shown in Fig. 3.6 [12]. The superconducting state (SC) is terminated by the hard gap insulator characterized by Δ_p. Inducing an external magnetic field to the system (vertical axis) leads to similar suppression of the superconductivity. High B destroys Cooper-pairs and consequently the SC-phase, as well as the hard-gap insulator phase. However, experiments on films very close to the transition under the influence of B [40, 89, 106, 107] point towards different phenomenology of the transition [8, 33], meaning that they cannot directly be compared to the transition driven by disorder alone. This is an unsolved challenge [8, 33] within the framework of fractal superconductivity on top of Anderson localization, however it will not be the focus of this work.

Coming back to transport by Cooper-pairs in the insulating regime, it is thinkable that although a macroscopic superconducting state is suppressed, very close to the transition transport of charges might still be possible by Cooper-pairs (by tunneling and hopping from one grain to the next). However, since pairing shifts all filled levels down in energy, the total density of states at the Fermi energy is reduced and consequently this tunneling is

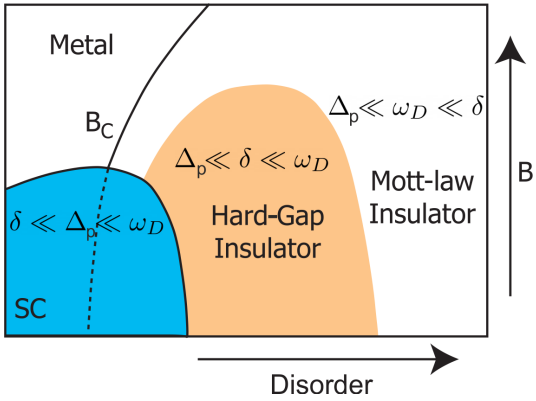

Fig. 3.6.: Phase-diagram of the transition from superconductor (SC) to insulator as a function of disorder and magnetic field. The competing energy scales δ, Δ_p and ω_D drive the transitions. For large disorder SC is terminated by a hard-gap insulator characterized by unpaired-electron conduction with parity gap Δ_p. The hard-gap insulator in turn is terminated by a Mott-law insulator where no pairing happens at all. Increasing B leads to suppression of both SC and hard-gap insulator. With modifications from [12].

strongly suppressed [33]. Nevertheless very close to the transition on the insulating side the small but finite tunneling contribution of the Cooper-pairs is expected to lead to an activated behavior in the transport conductance [55]. This contribution to conductance however is very fragile. When going a little deeper into the insulating regime with higher amounts of disorder, the characteristic gap energy of the activated behavior increases very fast until it becomes infinite a short distance away from the transition where no Cooper-pair transport will prevail [33, 55]. It is therefore safe to neglect the contribution of the Cooper-pairs to the conductivity in almost all realistic cases.

Going deeper into the insulating regime, meaning stronger localization of the charge carriers and a reduction of ξ (equation (3.26)), at some point the

level spacing δ (equation (3.25)) will exceed the Debye energy, $\Delta \ll \hbar\omega_D \ll \delta$. In this case no Cooper-attraction between the electrons can be mediated by phonons and not even local pairing will occur anymore [12]. No Cooper-pairs will exist in the system, no parity/hard-gap Δ_p will form and consequently the system stays a rather regular insulator with full many-body localization [12, 13] giving a Mott law [19] or Efros-Shklovskii type insulation [54, 121]. Fig. 3.6 [12] shows the hard-gap insulator being terminated by a Mott-law insulator when increasing the disorder strongly.

In the superconducting phase but close to the transition, where $\delta \lesssim \Delta$, meaning the level spacing is smaller but in the range of the gap, unusual superconductive states are formed, with the formation of preformed Cooper-pairs (see section 6.1) and an insulating trend above T_c [28, 32]. To find T_c of the superconductor, the interaction matrix element from equation (3.22) is found as a function of the energy levels j and k as $M(\omega) = (E_0/(E_j - E_k))^{1-D_2/3} = (E_0/\omega)^{1-D_2/3}$ [12, 33] with $\omega = E_j - E_k$. With this, solving a modified self-consistent BCS gap equation leads to [8, 33]

$$T_c(\lambda) \sim E_F \lambda^{1/(1-D_2/3)} . \tag{3.32}$$

For constant Cooper-attraction parameter λ this means, that the critical temperature for pairing T_c not only stays constant but even enhances above the bulk BCS value $T_{c,0}$ when approaching the mobility edge [8]. This in turn can lead to a pseudogap opening even above $T_{c,0}$, while the actual temperature, where the system becomes macroscopically superconducting is reduced by fluctuations and the reduction of superfluid density [13, 47]. In the crossover region close to the transition the superconducting pairing amplitude gets very inhomogeneous [13, 46, 47]. This is due to the fact that the disorder in the system leads to a local random potential interacting with the single-electrons, which in turn leads to *emergent superconducting granularity* [8]. The resulting inhomogeneous superconducting state can for example be studied using a negative-U Hubbard model with on-site disorder by the means of an

additional local random potential. What has been found [46, 47] is that an initially homogeneously superconducting state splits up into superconducting islands separated by an insulating sea when increasing the amount of local disorder. The pairing amplitude $\Delta(\mathbf{r})$ of such an island-like state is seen e.g. in Fig. 3.7 (a) [47]. Here, the dispersion of the superconducting amplitude

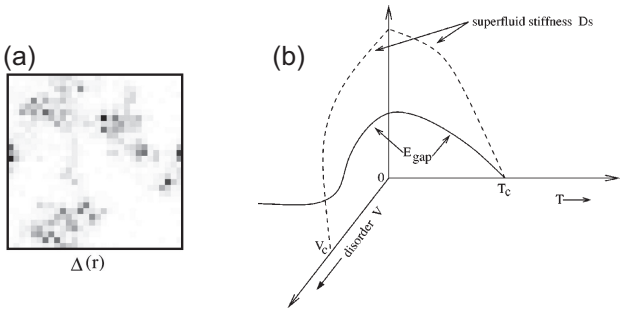

Fig. 3.7.: (a) Gray-scale plot of the spatial distribution of the pairing amplitude $\Delta(\mathbf{r})$ of a very disordered state. Superconductivity splits into superconducting islands (dark) embedded in an insulating sea (white). (b) Phase-diagram of the disorder-driven Anderson localization transition. Opposed to the zero-disorder transition where the gap goes to zero, the disorder-driven transition suppresses superfluid stiffness and retains finite gap. With modifications from [47].

is much larger than its mean value [13]. This state is not only found in the superconducting state close to the transition, where the overlap between islands is still large enough for a macroscopic superconductivity to emerge, but it is also able to survive deep into the insulating regime, where no continuous superconducting path connecting two macroscopically separated points in the conductor exists anymore [13]. At areas where $\Delta(\mathbf{r})$ is large coherence peaks at the edge of the gap in tunneling spectra are expected [33, 47], but not in between at locations of the insulating sea. This splintered state is therefore a direct consequence of the fractal nature of the eigenstates in the

crossover region [8], since disorder makes the eigenstates fractal, limiting the boundaries of electrons to small areas. The defining parameter for the suppression of *global* superconductivity in this inhomogeneous state is the superfluid stiffness D_s. A proposed [47] phase-diagram as a function of disorder and temperature is shown in Fig. 3.7 (b). Upon increasing T for low disorder, superconductivity is suppressed by the vanishing of the gap, in line with regular BCS-like behavior. The disorder-driven transition at $T = 0$ however, is not driven by the gap but by D_s, which decreases with increasing homogeneity of the superconducting phase, ultimately terminating superconductivity at a critical amount of disorder. Here, the gap stays finite throughout the whole transition and even increases slightly in the insulating regime due to the strong localization of the single-particle wavefunctions [47], similar to the enhancement of T_c in equation (3.32).

3.5.3. Scaling of dielectric constant and conductivity in the insulating regime

The dielectric constant in the insulating regime of an Anderson localized system consists of multiple contributions. First there is a contribution by non-mobile electrons, far from the Fermi-energy, which can be of considerable size for systems with large density of states in the valence band close to the Fermi-energy [33, 39]. This will give a constant contribution, an "$\varepsilon_{1,\mathrm{Host}}$", independent of the amount of disorder and the nature of the insulator. However, in this section the focus lies on the main contribution close to the transition, which is the polarizability of conduction electrons getting localized by disorder. Similar to previous results, the scaling of the dielectric constant close to the Anderson localization transition can be found in a combination of analytical and numerical methods [39].

From perturbation methods using a random potential, including disorder, and considering only non-interacting single-electrons, the dielectric constant as a function of localization length ξ in three dimensions is found as [39]

$$\varepsilon_1 = \alpha \frac{e^2 \nu_0}{\varepsilon_0} \xi^2 \,, \tag{3.33}$$

with α a numerical coefficient of order unity depending on the dimension, ν_0 the full density of states of electrons (spins are included in ν_0) and ε_0 the vacuum permittivity. In two and three dimensions α is almost universal with $\alpha \approx 3$ [39]. In one dimension α can be found analytically to about $\alpha \approx 4.8$ [39]. When a system of parallel one-dimensional wires or a stack of two-dimensional layers has to be considered, similar behavior is expected although with more complex prefactors [39, 122]. Note that initially during derivation of equation (3.33) the polarizability χ is found, which is a function of location in the system and can therefore fluctuate substantially depending on the local disorder distribution [39]. The dielectric constant in equation (3.33) is in turn found with the mean-field approximation $\varepsilon_1 = \varepsilon_0 (\chi + 1)$. ε_1 in equation (3.33) should therefore be taken as a figure of magnitude for the average of ε_1, since these fluctuations can become considerable in particular in three dimensions [39]. α is a numerical constant and has been found almost universal independent of disorder and its distribution [39].

To find ε_1 as a function of a well accessible experimental quantity, the activation energy T_0 as a function of localization length ξ, equation (3.31), can be solved for ξ and put into equation (3.33) to arrive at the scaling

$$\begin{aligned} \varepsilon_1 &= \alpha \frac{\nu_0 e^2}{\varepsilon_0} l^2 \left(\frac{g}{2 T_0 l^3} \right)^{2/D_2} \\ \Rightarrow \varepsilon_1 &\propto \nu_0 T_0^{-2/D_2} \approx \nu_0 T_0^{-1.54} \,. \end{aligned} \tag{3.34}$$

At the current state of this theory the scaling of the dielectric constant ε_1 cannot be separated from the single-particle density of states at the Fermi

energy ν_0 [119]. (3.34) predicts, that upon approaching the transition from the insulating side, ε_1 diverges in a power-law fashion. When going deeper into the insulating regime ε_1 is expected to decrease. There are however still the constant contributions from $\varepsilon_{1,\mathrm{Host}}$ (valence electrons far from Fermi-energy and "host" material), which at some point should define ε_1 and lead to a saturation towards very high amounts of disorder.

The conductivity σ_1 of disordered Anderson-localized samples should in general follow variable range hopping behavior, shown already in section 3.1, in particular equation (3.11). Any dependence on the amount of disorder is represented by the localization length ξ, with less disordered samples in general having larger ξ. With this, σ_1 can also be found as a function of T_0 by solving equation (3.31) for the localization length ξ and combining it with (3.11), leading to

$$\sigma_1(\omega) = \frac{\pi^2}{3} e^2 l^5 \left(\frac{g}{2l^3}\right)^{5/D_2} \nu_0^2 \hbar\omega^2 \ln^4\left(\frac{\delta}{\hbar\omega}\right) T_0^{-5/D_2} \tag{3.35}$$

$$\Rightarrow \sigma_1 \propto \nu_0^2 T_0^{-5/D_2} \approx \nu_0^2 T_0^{-3.85}\,, \tag{3.36}$$

in three dimensions $d = 3$ and for a fractal dimension of $D_2 \approx 1.3$ [33].

3.5.4. Frequency-dependent conductivity in very strong localization

The frequency-dependent conductivity in its Mott form, equation (3.11) and (3.35), is most exact if the energy of the frequencies used are roughly similar to or larger than the energy level splitting $\delta \sim \hbar\omega$. If δ exceeds $\hbar\omega$ by a large margin however, the prefactor of equation (3.11) (and (3.35)) is expected to be suppressed to some extent, since then the contributions by Mott resonances are reduced [33, 39, 123]. This is mainly expected to be prominent for samples where $\delta \gg \hbar\omega$ by many orders of magnitude, but not so much in the regime

of $\delta \approx \hbar\omega$ [123]. For $\delta \gg \hbar\omega$ the conductivity in general is expected to follow Mott-Berezinsky law [39]

$$\sigma_1(\omega) = \Sigma_d e^2 \hbar \xi^{2-d} \left(\frac{\omega}{\delta}\right)^2 \ln^{d+1}\left(\frac{c_d \delta}{\hbar\omega}\right) , \tag{3.37}$$

where Σ_d and c_d are numerical factors dependent on dimensionality. In three dimensions $d = 3$, equation (3.37) follows $\sigma_1(\omega) \propto \xi^5 \omega^2 \ln(\delta/\hbar\omega)$, equivalent to equation (3.11). Using Kramers-Kronig relations, equation (3.9), an expression for the product $\Sigma_d c_d$ can be found as [39]

$$\alpha \approx \frac{(2d+1)!}{\pi} \Sigma_d c_d \, . \tag{3.38}$$

For the one-dimensional case $d = 1$ with $\alpha \approx 4.8$ [39] (section 3.5.3) this can be calculated analytically and it is $\Sigma_d c_d \approx 3.8$, which is accurate up to a few percent [39]. For the three dimensional case however, with $\alpha \approx 3$, the numerical coefficients are much smaller $\Sigma_d c_d \approx 0.2$, meaning that here $\sigma_1(\omega)$ is expected to be suppressed [123].

This suppression is also seen when calculating the optimal hopping distance for Mott-hybridized resonance states. This has been performed in the extreme localization regime by Feigel'man et al. [33] and is shown in Fig. 3.8. It is found that the optimal hopping distance R is linear in $\ln(\delta/\hbar\omega)$, meaning that $R(\omega) \propto \ln(\delta/\hbar\omega)$ as it is expected, see equation (3.7). This linear behavior is only found in the regime $R > 2\xi$, which is the logical lower limit where Mott resonance mixing applies [33]. Note that consequently for the parameters assumed in this model of Fig. 3.8 it is not possible to study the region $\hbar\omega \sim \delta$, as here the lower limit $R > 2\xi$ is not met. Only extremely strongly localized systems are studied here.

The linear fit in Fig. 3.8 shows a strong vertical offset, where the fit parameter $B \approx -8$ (for the model values assumed here) [33]. This means that the optimal hopping distance is strongly suppressed and consequently

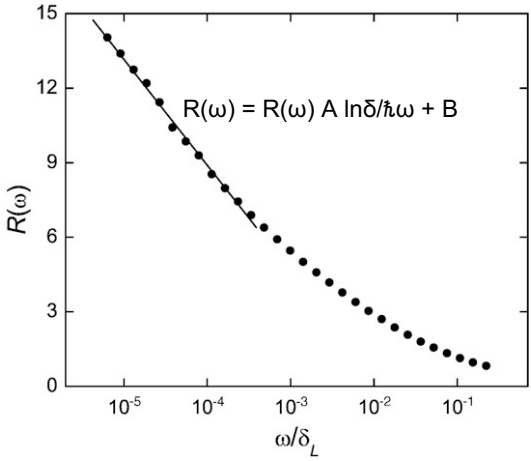

Fig. 3.8.: Optimal hopping distance for Mott resonances of an extremely localized Anderson insulator calculated for a model system by Feigel'man et al. [33]. $R(\omega)$ is found linear in $\ln(\delta/\hbar\omega)$, equivalent to Mott arguments (section 3.1), however a large vertical offset $B < 0$ is found, indicating reduced contributions of Mott resonances. With modifications from [33].

also the contributions by Mott resonances are suppressed [33]. This again demonstrates that the contributions by Mott resonances are in fact smaller than expected from simple Mott arguments when being in the extremely localized regime $\delta \gg \hbar\omega$. This could in turn possibly lead to reduced measured values of $\sigma_1(\omega)$, being smaller than expected from Mott-behavior.

Unfortunately detailed numerical studies are missing [123] and a quantitative analysis of the suppression of $\sigma_1(\omega)$ due to extreme localization cannot be performed. The analysis concerning $\sigma_1(\omega)$ in section 6.4 therefore has to be limited to a qualitative discussion.

3.5.5. Effects of pairing on the dielectric constant and conductivity

Equations (3.33) and (3.36) were derived neglecting any interaction between electrons. However, as seen in previous sections, interactions can become the driving factor for the nature of the resulting state and consequently the non-interacting values of ε_1 and σ_1 should be modified to include interactions. On the one hand Coulomb interactions repelling electrons from each other could be included. However, they are considered to be very small in the systems investigated [33], with their energy scale being two orders of magnitude smaller than the energy scale of the localization [39], so that their contribution can safely be neglected. On the other hand Cooper-attraction, being the driving factor of the suppression of superconductivity in this framework, is considerable and leads to a modification of (3.33) and (3.36).

Starting from the procedure shown in section 3.1, where Mott hybridized resonance states have been investigated, an additional attractive interaction can be introduced. Hopping then follows the schematic shown in Fig. 3.9 (a) [38]. Two possible locations for localized single-electrons separated by spatial distance x with slightly different energy levels $E_1 - E_2 = \hbar\omega$ are shown, occupied by two electrons of opposite spin. If now coupling of two single electrons to a paired state (localized Cooper-pair) leads to an effective gain in energy in the size of the pseudogap Δ_p, then pairing two electrons on a single energy level is favorable, and the lower two states are energetically superior. Note that only singlet states are taken into account, as triplet states (with parallel spins) would have higher energy as unpaired electrons [38]. Transitions from one level to the other can only be done via the intermediate step shown on top in (a), via the Mott hybridized state. The resulting Hamilton operator therefore now has contributions by Δ_p [38] and modifies

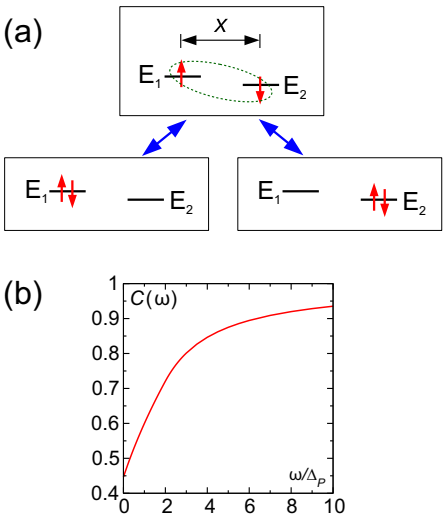

Fig. 3.9.: (a) Schematic showing the three states participating in Mott-resonance conduction including the two possible electron locations separated spatially by x with their corresponding energy levels E_1 and E_2. The dashed line shows the hybridized state, while blue arrows show possible transitions. (b) Numerical factor $C(\omega/\Delta_p)$. It starts from 0.446 at $\omega = 0$ and goes up to 1 somewhere at $\omega > \Delta_p$. (a) and (b) With modifications from [38].

the dynamical density response function $s(\omega, x)$, equation (3.6). Consequently $\sigma_1(\omega)$ is also modified accordingly. For $s(\omega, x)$ and $\sigma_1(\omega)$ it follows [38]

$$s(\omega \ll \delta, x) = C(\omega/\Delta_p) \cdot s\left(\sqrt{\omega(\omega + \Delta_p)}, x\right)_{\text{nonint}} \tag{3.39}$$

$$\sigma_1(\omega \ll \delta) = C(\omega/\Delta_p)\frac{\omega}{\omega + \Delta_p}\sigma_1\left(\sqrt{\omega(\omega + \Delta_p)}\right)_{\text{nonint}} \tag{3.40}$$

with δ the energy level splitting due to the localization length ξ and $s(\omega, x)_{\text{nonint}}$ and $\sigma_1(\omega)_{\text{nonint}}$ the non-interacting dynamical density response function and

conductivity respectively (equations (3.6) and (3.11)). $C(\omega/\Delta_p)$ is a numerical prefactor. It can be calculated and is shown in Fig. 3.9 (b) [38] as a function of the frequency in orders of the pseudogap ω/Δ_p. $C(\omega/\Delta_p)$ starts from the value $C(\omega = 0) = 0.446$ and reaches 1 somewhere above Δ_p. Note that Fig. 3.9 (b) shows $C(\omega/\Delta_p)$ of a model including only one pair of states for simplicity. To describe a large system of many localized states as it would be found in a real disordered conductor, disorder averaging would have to be applied additionally. The general form of $C(\omega/\Delta_p)$ however, would stay roughly the same and can already be seen in Fig. 3.9 (b) with disorder averaging leaving the form mostly unchanged [38].

In the non-interacting limit, meaning either $\omega \gg \Delta_p$ or $\Delta_p = 0$, equation (3.40) reproduces equation (3.11) [38]. If however $\Delta_p > 0$ and $\omega \ll \Delta_p$, the general Mott behavior $\sigma_1(\omega) \propto \omega^2 \ln^{d+1}(\text{const.}/\omega)$ is still preserved, but now the proportionality coefficient is strongly reduced (note that in this work it always holds $\omega \ll \Delta_p$, since maximum photon energies are in the range $\sim 0.1\,\text{meV}$, while Δ_p is several times larger). The proportionality factor then is strongly reduced by the factor of [38]

$$\begin{aligned} \frac{4+\pi}{16}\left(\frac{1}{2}\right)^{d+1} &\approx 0.446\left(\frac{1}{2}\right)^{d+1} \\ &\approx 0.03 \quad \text{for } d = 3\,. \end{aligned} \tag{3.41}$$

The local pairing of electrons with the corresponding reduction in energy, therefore not only leads to the hard gap found in DC-transport, equation (3.28), but also leads to a strong reduction of the photon-induced conductivity $\sigma_1(\omega)$.

Similarly the static polarizability χ is also reduced. This follows from Kramers-Kronig relations, relating σ_1 to χ, equation (3.9). The modification

of χ can be found as the relative change $\delta\chi/\chi$ as a function of the pseudogap Δ_p and the energy level splitting δ_L* as [38, 39]

$$\frac{\delta\chi}{\chi} \propto -\frac{\Delta_p}{\delta_L}\left(\ln\frac{\delta_L}{\Delta_p}\right)^{d+1}, \tag{3.42}$$

up to a numerical proportionality coefficient of order one. For realistic values of $\Delta_p/\delta \sim 0.01 - 0.1$ (insulating regime) this possibly leads to a suppression of a factor of about $2-3$ compared to (3.33) [119]. χ in equation (3.42) is a quantity dependent on local disorder, meaning that both its initial value as well as the predicted suppression possibly vary as a function of location. The dielectric constant can be estimated from χ with $\varepsilon_1 = \varepsilon_0(\chi + 1)$ although this formula is a mean field approximation [39, 56] averaging across disorder variations and might therefore again seen as a figure of approximation. ε_1 is thus equally suppressed with $\frac{d\ln\varepsilon_1}{d\Delta_p} \sim -\frac{1}{\delta}\ln^{d+1}\left(\frac{\delta}{\Delta_p}\right)$ [39]. Equation (3.42) also predicts, that upon subjecting the system to an external magnetic field, reducing Δ_p, a linear increase in ε_1 might be seen [39, 119]. Experiments utilizing magnetic field exceed the scope of the present work but might be relevant in future experiments.

3.6. Summary

In conclusion, several important aspects have been presented in the previous sections, that could profit greatly from experiments on polarization and finite-frequency conductivity. Firstly, knowledge about the absolute value of ε_1 would give crucial insight into the role of Coulomb interactions and their possible suppression in amorphous disordered indium oxide (possibly rendering the Finkel'stein mechanism obsolete). Therefore directly measuring the absolute value of ε_1 would be highly desirable at low temperatures and

*In order to not confuse energy level splitting δ_L to the notation of relative change $\delta\chi/\chi$, the notation of the energy level splitting here reads δ_L, whereas in the rest of this work it will simply be called δ.

with minimal excitation energies, where possible localized Cooper-pairs are undisturbed. Large polarization is suggested to be the main driving parameter for the screening of Coulomb interactions, which upon strong suppression could be weaker than Cooper-attraction, which would in turn allow for pairing of electrons. Putting a number to this polarization is critical to the understanding of these mechanisms. Secondly, in the previous section 3.5 several important predictions in particular for the scaling of ε_1 and σ_1 with disorder as well as a possible suppression in value upon the emergence of a pseudogap were presented. It is thus desired to perform measurements on both ε_1 and σ_1 also as a function of varying disorder. On the one hand, from the change of $\varepsilon_1(T_0)$ and $\sigma_1(T_0)$ as a function of T_0 (representing disorder [33]) the scaling predictions from equation (3.34) and (3.36) could be tested, which could give evidence for the possibility of a (multi-)fractal nature of the electronic eigenstates [12, 33] due to the characteristic fractal dimension $D_2 \approx 1.3$ [33] entering the scaling exponent. On the other hand, comparing the quantitative experimental values of ε_1 and σ_1 to the values of $\varepsilon_1(\xi)$ and $\sigma_1(\omega)$ suggested by simple theoretical considerations including e.g. the localization length ξ (equations (3.11) and (3.33), ξ estimated from transport measurements) would directly show a possible suppression of the type of (3.40) and (3.42) and would therefore allow to infer the presence of a pseudogap even in entirely insulating indium oxide samples, pointing towards the existence of localized Cooper-pairs [39].

4. Experiment

4.1. Microwave resonators

Planar (superconducting) resonators are versatile tools with a multitude of applications [124]. Not only has recent development spiked due to the development of qubits and corresponding readouts with in-plane coplanar structures [125–127] as well as other applications such as single-photon detectors [128] and microwave kinetic-inductance devices (MKID) which allow for the realization of detectors for astronomy [129] and even particle physics [130]. But more importantly, planar microwave devices can conveniently and reliably be applied in solid state research. Here, many applications exist, including but not limited to the determination of complex material parameters of bulk materials [2, 131, 132], of thin-films [1, 5], as well as ESR studies [133, 134]. In most applications the main advantages are the comparably low frequencies and thus excitation energies [132, 134, 135] with the simultaneous investigation of many frequencies by using harmonics [136, 137] or by multiplexing [138, 139]. Many different geometries can be used [140] from stripline [4, 5, 131, 132, 141, 142], microstrip [143], flip-chip [2, 3] to coplanar [1, 133, 134]. Depending on geometry, the frequencies covered range from few 100 MHz up to several 10 GHz [137] and the temperature range that can be covered is from room temperature in the case of metallic resonators [144] or several K in the case of superconducting resonators [4, 5] down to mK [132, 134]. Especially the combination of low frequencies and the possibility to measure at very low temperatures allows for measurements at

$k_B T < \hbar\omega$, giving access to the full electrodynamics even for low-T_c materials [135].

In this work coplanar resonators will be used and their operation will be detailed in the following sections.

4.2. Coplanar Waveguides

Coplanar lines are transmission lines where all parts of the conductor are in the same plane. They usually consist of a dielectric substrate with a thin metallic or superconducting layer on top, which is shaped in a way to guide currents and electromagnetic waves. The conductor can consist of single conductor strips, the microstrips, slotlines with a single slot, coplanar strips with two adjacent strips or coplanar waveguides (CPW) [145–147]. In the following, coplanar waveguides (CPW) will be discussed, as the main experimental approach in this work utilizes CPW resonators. They have first been proposed in 1969 [148] and have since become a major part in technological advances and progress.

CPW have the great advantage, that they are easy to fabricate, as it only takes two steps to produce them: first the deposition of the conductor layer on the substrate and second the shaping of the conductor layer with optical lithography. The general geometry can be described in analogy to a coaxial cable, which is sliced in the center, as depicted in Fig. 4.1 (a). The resulting planar structure is shown in (b) and (c). A center conductor of width S^* is separated by gaps with width W from ground planes to either side. Compared to S and W the ground planes have orders of magnitude larger dimensions and can be assumed infinite in the following. The conductor has a thickness of size t. The similarity to coaxial cables allows for the direct connection of

*The terminology of "S"and "W" for center **S**trip width and gap **W**idth is often used in textbooks [145, 147] and articles. In some occasions the usage of "S"and "W" is inverted (center strip **W**idth and **S**lot width). In this work however, the first is used, since it is more popular.

CPWs to standard microwave equipment with an impedance of 50 Ω, where the center conductor is connected to the inner conductor of a coaxial cable and the ground planes are put to ground potential.

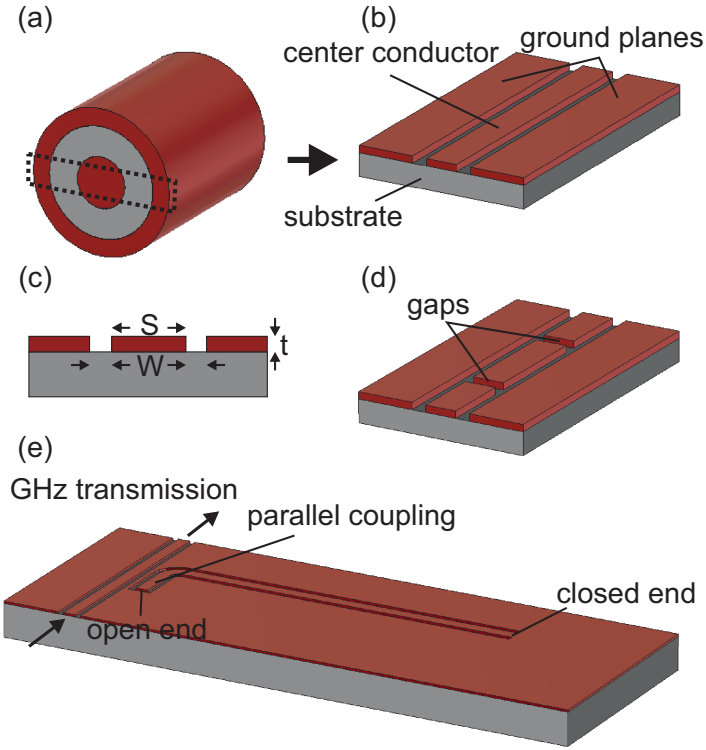

Fig. 4.1.: (a) Model of a coaxial cable with dielectric (gray) and conductors (red). (b) Model of a coplanar waveguide (CPW) transmission line. (c) Crosssection of a CPW with typical magnitudes. (d) Model of a CPW $\lambda/2$-resonator with gaps for capacitive coupling. (e) Model of a $\lambda/4$-resonator with parallel coupling to a CPW transmission line.

In order to match the impedance Z of CPWs to the 50 Ω-standard, the ratio of S and W has to have a fixed value. S/W is the most deciding

parameter for the impedance of CPWs. Since only this ratio defines Z, CPWs can easily be scaled to larger or smaller sizes without altering the impedance. Only the losses might be affected [147]. Z as a function of this S/W for a CPW with Al_2O_3-substrate is displayed in Fig. 4.2, details of the calculation will be shown in section 4.3. The resulting optimal ratio is $S/W \approx 2.2$

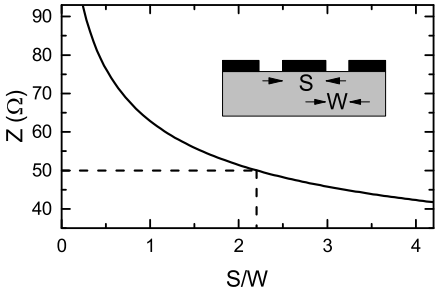

Fig. 4.2.: Impedance Z of a CPW as a function of S/W (compare inset). For Al_2O_3-substrate the optimal value is about $S/W \approx 2.2$.

with an assumed effective dielectric constant of $\varepsilon_{\text{eff}} \approx 5.5$ corresponding to a typical CPW on Al_2O_3-substrate. While a ratio of $S/W \approx 2.2$ matches $Z = 50\,\Omega$, most of the CPW in this work have slightly different $S/W \approx 2.4$. This however, has negligible influence on the results, as the difference in both ratios only leads to a difference in Z of about 2.5 %, which leads to a mismatch loss of about 0.002 dB. This mismatch is certainly much smaller than contributions from other sources (e.g. cables, microwave contacts, etc.).

The electromagnetic waves that are guided by such a CPW are TEM waves. Simulation data of the fields for E and B are shown in Fig. 4.3. The E-field reaches from the center conductor to the ground planes, while the direction, whether the E-field lines are pointing inward or outward, is dependent on the phase and changes with time. The B-field has closed loops of field lines around the center conductor. This configuration of the conductors leads to a strong compression of the B-field lines in the gaps, since all field lines have

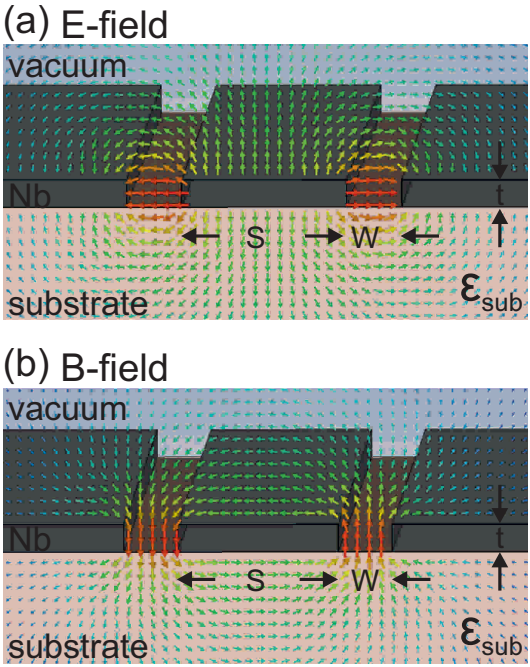

Fig. 4.3.: Simulation data for the distribution of the (a) E- and (b) B-field in a coplanar waveguide. The typical carried wave is TEM-like.

to pass through the opening of width W. This leads to the highest value of B being concentrated in the gap. The E-field is also mostly concentrated in the gap, the finite metallization thickness t making it homogeneous in this area. Further implications of this enhancement due to t will be discussed in section 4.3.1. Similar to the E- and B-field, the surface currents are most dominant close to the gap in the surface of the conductor. Here the CPWs are most vulnerable to imperfections such as unclean edges, surfaces or etching residuals [144].

The E- and B-field distributions of CPWs, shown in Fig. 4.3 are generally much less confined than in other configurations such as microstrips or striplines

[145]. Meaning that in vertical direction the E-field and B-field have much larger extension, while setups such as microstrips or stripline also have ground planes above or below, which confines the fields to a fixed volume. While CPWs can be conductor backed [145, 147, 149, 150] to confine the fields, the typical distance to the grounded back conductors is typically much larger. In our experimental setup it is on the order of several 100 µm. The large extension of the fields makes the CPW much more sensitive to perturbations by additional (sample) materials above or below the conductor [145]. This is particularly useful for the application in this work, since high sensitivity to materials above the conductor plane is desirable when depositing the sample directly on top of the CPW.

CPWs can be directly used in experimental approaches, e.g. for electron spin resonance measurements [133]. However, by using just a broadband transmission line, the fields are usually pretty weak and therefore the sensitivity to perturbations of the microwave properties might be too low to detect the (often weak) influence of the sample. It is therefore desirable to enhance the field strength and the sensitivity in the CPW. This can be done by forming resonators [136, 151].

There are multiple ways to form resonators in CPWs. One of them is to place gaps in the center conductor of the CPW, as can be seen in Fig. 4.1 (d). The gaps act as capacitive coupling. The E-field originating from the microwave lead induces an E-field in the center conductor bridging the gap. This potential then travels along the center conductor until it is reflected again by the impedance mismatch of the opposing gap. If the round-trip time back to the initial gap is equal to the period of the exciting microwave, the wave is constructively enhanced. The resulting pattern is a standing wave with its wavelength twice as long as the resonator ($\lambda/2$-resonator).

Similarly a resonator can also be coupled parallel to a transmission line. This is depicted in Fig. 4.1 (e). Here it is chosen that its ending next to the transmission line is an open end and the opposing ending is a closed end, where the center conductor is connected to the ground planes. This leads to

a standing wave with a wavelength that is four times as long as the resonator ($\lambda/4$-resonator). The distribution of the E-field and the B-field is shown with simulation data in Fig. 4.4. The E-field here has a maximum in the coupling

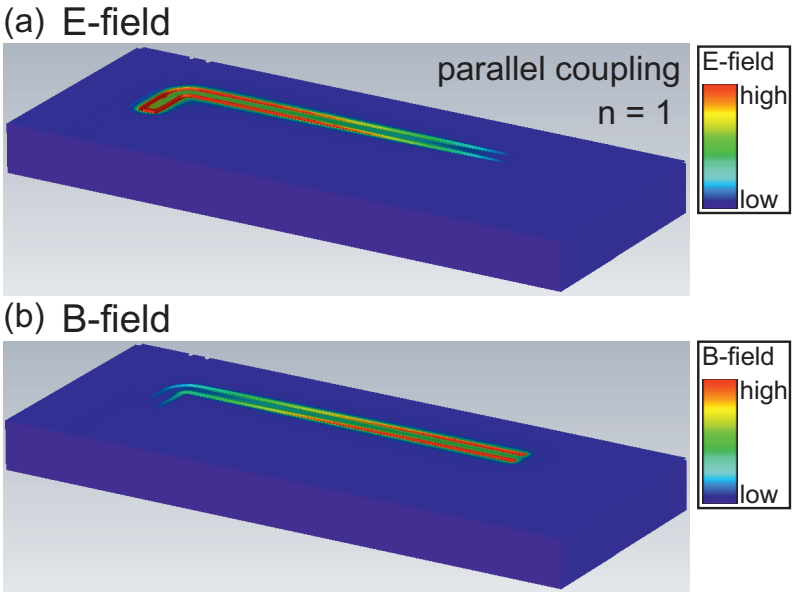

Fig. 4.4.: Contour plot of simulation data of the strength of the (a) E-field and (b) B-field in a $\lambda/4$-resonator with parallel coupling. The E-field is enhanced manifold in the resonator (compare to very low values in the feedline).

arm at the transmission line, where the B-field is zero. At the opposing end the roles reverse and it is $E = 0$, $B = B_{\max}$.

Not only at wavelength of two and four times the resonator length the resonance condition is met, but also at multiples of $\lambda/2$ and $\lambda/4$ respectively. The resonance frequencies therefore are

$$\begin{aligned} \nu_n &= \frac{n}{\tilde{l}} v_{\mathrm{ph}} = \frac{nc}{\tilde{l}\sqrt{\varepsilon_{\mathrm{eff}}}} \\ \text{with} \quad \tilde{l} &= 2l \quad \text{for } \lambda/2\text{-resonators} \\ \text{and} \quad \tilde{l} &= 4l \quad \text{for } \lambda/4\text{-resonators} \end{aligned} \tag{4.1}$$

with v_{ph} the phase velocity, l the length of the resonator, c the vacuum speed of light, and $\varepsilon_{\mathrm{eff}}$ the total effective dielectric constant of the resonator, which will be further discussed in section 4.3. n is the number of the mode with

$$n = 1, 2, 3, \ldots \quad \text{for } \lambda/2\text{-resonators} \tag{4.2}$$

$$n = 1, 3, 5, \ldots \quad \text{for } \lambda/4\text{-resonators}\,, \tag{4.3}$$

where $n = 1$ is the fundamental and $n > 1$ are higher harmonics. Note that for the $\lambda/4$-resonator only odd multiples exist, since the ending opposite of the coupling arm is closed and here it is always $E = 0$ and $B = B_{\max}$. The resonance frequency (4.1) is one of the most important parameters of the resonator under study. Since it is directly dependent on $\propto 1/\sqrt{\varepsilon_{\mathrm{eff}}}$ it will also give direct access to the dielectric properties of the resonator. Details of which will be discussed in the following sections.

Fig. 4.1 (e) and Fig. 4.4 show straight resonators with only one bend between the coupling arm from the majority of the resonator. This geometry can directly be used in experiments if short resonators are useful, in particular when dealing with substrates of exceptionally high ε_1 such as e.g. $SrTiO_3$ [3]. However when using Al_2O_3 as a substrate, the length of a typical $\lambda/4$-resonator with a fundamental frequency of about 2 GHz exceeds 15 mm, which is not feasible in linear geometry, since the dimensions of the substrate chips used in this work are usually < 12 mm. In order to fit a resonator on the

substrate-chip anyways, it is possible to form meander structures, an example of which you can see in Fig 5.3 (section 5.2.1). Here the resonator is bent multiple times to reduce the amount of space the resonator needs. CPW resonators here have the advantage, that the distance between to neighboring lines of the meanders can be spaced much closer than for other types such as microstrips or striplines since the center conductors are surrounded by grounded planes, which will also fill the space between two meander lines. This grounding leads to a much more confined E- and B-field in lateral direction and in turn reduces cross-talk between the lines [147]. A more detailed discussion will follow in section 4.2.1.

Apart from the resonance frequency there is another defining parameter of a microwave resonator, which gives information about how well it oscillates. This so-called quality factor Q is the ratio of the amount of energy that is stored in the resonator over the amount that is lost each cycle

$$Q = \frac{\text{energy stored}}{\text{energy lost per cycle}} . \tag{4.4}$$

In the case of microwave resonators this can be viewed as how long a photon in the resonator will survive. If e.g. $Q \approx 10\,000$, an incoming photon will be reflected on average 10 000 times until it is lost or absorbed. Q therefore directly gives a magnitude about the quality of the resonator.

In order to find a mathematical expression for the calculation of Q it is handy to look at a resonator as an equivalent LRC-model, consisting of an impedance L, a capacitance C and a resistance R, as shown in Fig. 4.5 (a). The energy that is stored in the resonator is $W_m + W_e$, the sum of the energy stored in the inductance and the capacitance. At resonance this energy is equal for both parts $W_m = W_e$. The power dissipated $P_{\text{loss}} = \frac{1}{2}|I|^2 R$ [150] is the energy lost per cycle, which is dissipated in the resistance R with the current being I. Note that all loss mechanisms are included in R, not depending on whether they are truly dissipative in the resistance or if there

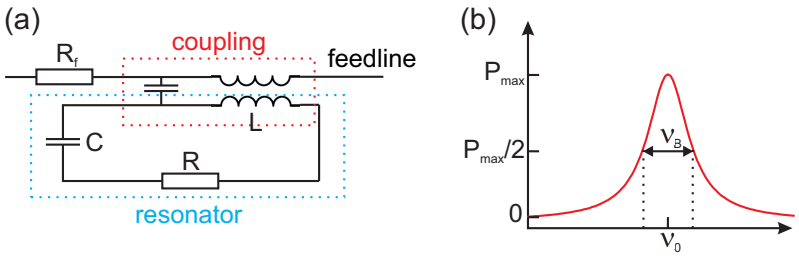

Fig. 4.5.: (a) Equivalent LRC-model of a resonator with parallel coupling to a feedline. (b) Delivered power to the resonator with a resonance frequency ν_0. At half-power the bandwidth ν_B can be accessed.

are other mechanisms at play, such as e.g. radiation losses. It therefore follows for Q [150]

$$Q = \omega_0 \frac{W_m + W_e}{P_{\text{loss}}} = \omega_0 \frac{4W_m}{|I|^2 R} = \omega_0 \frac{4W_e}{|I|^2 R} \tag{4.5}$$

$$= \frac{\omega_0 L}{R} = \frac{1}{\omega_0 RC} \tag{4.6}$$

$$\text{with} \quad W_m = \frac{1}{4}|I|^2 L \quad \text{and} \quad W_m = \frac{1}{4}|I|^2 \frac{1}{\omega_0^2 C}\,, \tag{4.7}$$

with $\omega_0 = \frac{1}{\sqrt{LC}}$ the frequency at resonance. The total input impedance of the circuit is

$$Z = R + i\omega L - i\frac{1}{\omega C} = R + i\omega L \left(1 - \frac{1}{\omega^2 LC}\right) \tag{4.8}$$

$$= R + i\omega L \left(\frac{\omega^2 - \omega_0^2}{\omega^2}\right)\,. \tag{4.9}$$

For small deviations $\Delta\omega$ of the frequency from ω_0 this can be simplified as

$$Z \approx R + i2L\Delta\omega \tag{4.10}$$

$$= R + i\frac{2RQ\Delta\omega}{\omega_0}\,. \tag{4.11}$$

If we look at frequencies where only half the power is transmitted to the resonator, the impedance is $\sqrt{2}$ times the value at resonance frequency $|Z|^2 = 2R^2$ [145]. The frequencies where this happens define the bandwidth with their distance being ω_B, meaning that now $\Delta\omega = \omega_B/2$ and therefore with (4.11)

$$|Z|^2 = \left|R + i\frac{RQ_0\omega_B}{\omega_0}\right|^2 = 2R^2 \tag{4.12}$$

$$\Rightarrow Q = \frac{\omega_0}{\omega_B} = \frac{\nu_0}{\nu_B}\,, \tag{4.13}$$

with $\nu_i = \omega_i/2\pi$. This is the common definition of the quality factor of a microwave resonator. It combines two easily accessible quantities, the resonance frequency ν_0 and the bandwidth at half maximum ν_B, as it is schematically depicted in Fig. 4.5 (b).

From this it is clear, that Q gives some magnitude of the losses in the system. A resonator with small losses will have large Q and therefore sharp resonances with very narrow ν_B, whereas for resonators with higher losses ν_B will be large. The losses which cause Q to shrink can be manifold, but can be generally separated into three parts, the losses due to radiation α_r, due to losses in the conductor α_c and due to losses in the dielectrics α_D. α here is the attenuation constant, which describes how strong a electromagnetic wave

is reduced over length [147]. With this it follows for Q of a $\lambda/4$-resonator [145, 147, 150]

$$\begin{aligned} Q &= \frac{\pi}{4l\alpha} \\ \alpha &= \alpha_r + \alpha_c + \alpha_D \,. \end{aligned} \tag{4.14}$$

4.2.1. Coupling of coplanar waveguides

A free-standing resonator will not oscillate on its own. In order to bring a resonator into oscillation it will have to be driven by an external source. This has been shortly mentioned before as Fig. 4.1 (d) and (e) show capacitive coupling and parallel coupling of CPW resonators, but the influence of the coupling on the parameters such as Q have to be evaluated further.

The quality factor Q in previous equations has been derived purely for the free-standing resonator, e.g. equation (4.7) is only dependent on L, R and C of the resonator. It can therefore be called the internal or unloaded quality factor Q_0. To include effects of the external circuitry, such as a feedline with its resistance, see Fig. 4.5 (a), a new quality factor, the loaded quality factor Q_l is found as the inverse sum of the internal (Q_0) end external quality factor (Q_e) [131, 136, 150, 152]

$$\frac{1}{Q_l} = \frac{1}{Q_0} + \frac{1}{Q_e} \,. \tag{4.15}$$

The loaded quality factor Q_l describes the quality factor of the resonator under influence of the external coupling, e.g. a feedline. By measuring the transmission through the feedline, always Q_l will be measured. Solving for Q_0 gives

$$\frac{1}{Q_l} = \frac{1}{Q_0}\left(1 + \frac{Q_0}{Q_e}\right) \tag{4.16}$$

$$\Rightarrow Q_0 = Q_l(1+g)\,, \tag{4.17}$$

with g the coupling factor, which gives the strength of coupling of the resonator to the external circuitry. g substantially determines the amplitude and the quality factor of a resonance. If g is small, the resonator is called under-coupled. Here, $Q_0 \approx Q_l$, so by measuring the response of the resonator excited by the feedline, it is directly possible to deduce Q_0. However, if $g > 1$ the resonator is over-coupled and Q_l is strongly suppressed, meaning that the quality factor of the resonator itself Q_0 is overshadowed by the influence of Q_e.

The amplitude of the resonance, called the insertion loss IL, on the other hand behaves inversely. For weak coupling ($g < 1$) the amplitude A is small, for strong coupling ($g > 1$) the amplitude is strong. The relation between A and g is [150]

$$A = \frac{g}{1+g}\,. \tag{4.18}$$

The general behavior of both Q_l and A as a function of the coupling coefficient is shown in Fig. 4.6 (with an assumed $Q_0 = 10\,000$). At exactly $g = 1$ the

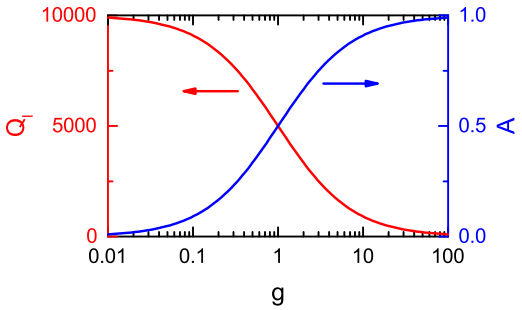

Fig. 4.6.: Loaded quality factor Q_l and insertion loss A of a resonator as a function of coupling strength g. Q_0 has been assumed $Q_0 = 10\,000$. At critical coupling Q_l and A are half.

resonator is critically coupled. Here it holds at the resonance frequency for the

impedance $Z = R$ (from (4.11)) and for optimal coupling the impedance of the feedline $Z_f = R$. It follows with (4.7) for both Q_0 and Q_e, that $Q_0 = Q_e$ [150]. At this critical coupling Q_l and A are exactly half of their maximum values.

Apart from the designed, wanted coupling by a feedline, it is also possible that parts of a resonator unwantedly couple to other parts within the structure of the same resonator. This is called crosstalk and can occur if parts of the resonator come too close to other parts, where they run parallel to each other [153–155]. This can in particular happen, when meandering the resonator. In order to reduce this issue the lines of the resonator have to have large enough distance to each other. As a figure of merit the distance of the center conductors D should be roughly $D > 5 \cdot (S/2 + W)$ [156] (for a crosstalk less than 35 dB). This is fulfilled for all the resonators in this work since the line distance is typically of the order of several 100 µm, whereas S and W are few 10 µm.

4.3. Conformal mapping technique

The conformal mapping technique poses a handy procedure to properly calculate parameters of a coplanar waveguide, such as impedance or effective dielectric constant. In general the geometry of a coplanar waveguide is a complex system with its rigorous solution proving cumbersome, especially if multiple additional layers of finite thickness (substrate, thin-film sample) are included. The conformal mapping technique maps this complex system onto a simpler system, for which solutions readily exist which can straightforwardly be applied [147].

Generally microwave waveguides are made up of a stack of different layers containing conducting layers and dielectric layers. E.g. in the case of coplanar waveguides the layer stack with a sample layer deposited on top looks like Fig. 4.7 (a). In order to find possible solutions for the electric field E and

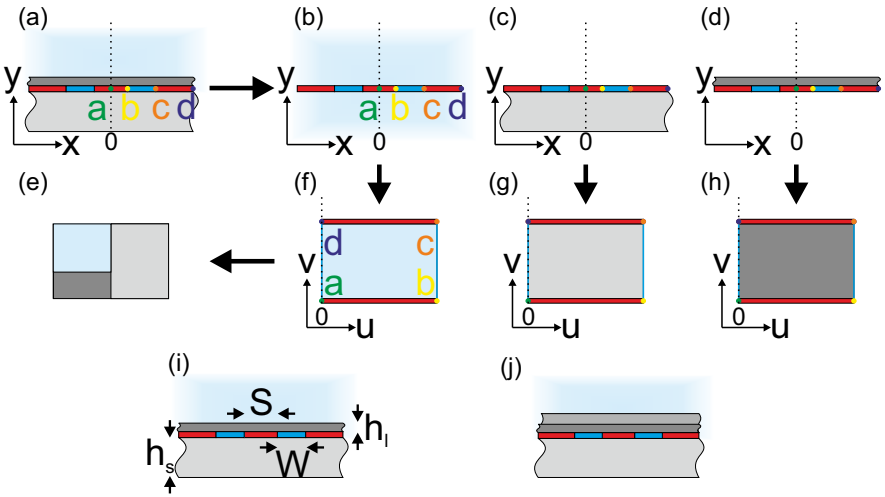

Fig. 4.7.: (a) Schematic crosssection of a coplanar waveguide (CPW) with thin-film layer on top. Points a-d and their colors correspond to other subfigures. (b) - (d) Separation of layer-stack from (a) into sub-layers. (f) - (h) Mapped sub-layers in the w-plane. (e) Layers in the w-plane weighted by their influence on C_{CPW}. (i) CPW crosssection with typical dimensions. (j) Crosssection of CPW with two additional layers on top.

the magnetic field B in the static case, one has to solve the two dimensional Laplace equation

$$\Delta_{x,y}\phi(x,y) = \left(\frac{\partial^2}{\partial x^2} + \frac{\partial^2}{\partial y^2}\right)\phi(x,y) = 0\,, \tag{4.19}$$

with the electrostatic potential function $\phi(x,y)$. Here it is assumed that purely TEM-Modes exist, meaning that there is no longitudinal part of E and B along the waveguide but only transversal parts. In general solving (4.19) for waveguides proves cumbersome and cannot be done analytically. Several possibilities exist ranging from variational approaches [157, 158],

numerical calculations of the Fourier transform [159], Galerkin's method [160], to the determination of an appropriate Green's function [161, 162]. These approaches however, tend to be numerically challenging and do not give any closed-form expressions.

A more convenient way to calculate solutions for (4.19) is the conformal mapping using Schwarz-Christoffel mapping [148, 152, 163]. Here first it is focused on an infinitesimally thin conductor layer. In the next section finite metallization thickness will be taken into account. The coordinates of the geometry in the x, y-system are mapped to new coordinates by going from the complex variable plane to the complex w-plane $z = x + iy \rightarrow w = u(x, y) + iv(x, y)$ leaving (4.19) invariant under this mapping [152]. When looking at a CPW with additional layer as in Fig. 4.7 (a) the lateral symmetry can be utilized and only one half has to be evaluated. The mapping is then done by

$$w = \int_{z_0}^{z} \frac{dx}{\sqrt{(z-b)(z-c)}}\,, \tag{4.20}$$

which is of the form of an elliptical integral [145]. This mapping is illustrated in Fig. 4.7 (b)-(h). Each sub-layer, the conductor layer without dielectrics (b), with substrate (c) and with thin-film (d) is separately mapped into a rectangle, where the upper plate and lower plate are the conductor surfaces and the dielectric fills the space in between. This now has the form of a simple parallel plate capacitor with its capacitance $C = \varepsilon_0 \varepsilon_r A/d$, with the area of the plates A and d their distance. Since the line capacitance of the CPW is investigated, corresponding values are the distance between points c and d, $\overline{cd}$ and distance between b and c, $\overline{bc}$. For the line capacitance it therefore follows

$$C_i = 2\varepsilon_0(\varepsilon_r - 1)\frac{\overline{cd}}{\overline{bc}} = 2\varepsilon_0(\varepsilon_r - 1)\frac{K(k_i)}{K(k_i')}\,, \quad i = s, l, a \quad , \tag{4.21}$$

with the factor 2 from the lateral symmetry consideration. Since layers/substrates of finite thickness are studied, the factor $(\varepsilon_r - 1)$ is introduced here, giving the relative enhancement of the dielectric constant compared to the free-space capacitance [145]. $K(k)$ is the complete elliptical integral of first kind with its modulus k. For the substrate and sample layers (Fig. 4.7 (c) and (d)) the modulus is [149]

$$k_i = \frac{\sinh\left(\frac{\pi S}{4h_i}\right)}{\sinh\left(\frac{\pi(S+2W)}{4h_i}\right)}, \quad i = \mathrm{s,l} \quad , \tag{4.22}$$

with S and W the inner conductor width and distance to ground planes of the resonator and h_i the thickness of the respective layer, compare Fig. 4.7 (i). The modulus for the conductor-backed (brass-box of the setup) surrounding air layer is

$$k_a = \frac{\tanh\left(\frac{\pi S}{4h_a}\right)}{\tanh\left(\frac{\pi(S+2W)}{4h_a}\right)}, \tag{4.23}$$

with h_a a thickness of the air layer, which is set to be rather large (typically a few mm) and symmetric on both sides. The complementary modulus is defined as $k' = \sqrt{1-k^2}$.

In order to find the properties of the whole layer stack system, the total capacitance can now be summed

$$C_{\mathrm{CPW}} = C_s + C_l + C_a \tag{4.24}$$

$$= 2\varepsilon_0(\varepsilon_s - 1)\frac{K(k_s)}{K(k_s')} + 2\varepsilon_0(\varepsilon_l - 1)\frac{K(k_l)}{K(k_l')} + 4\varepsilon_0\frac{K(k_a)}{K(k_a')}. \tag{4.25}$$

The effective dielectric constant ε_{eff} of the system is defined as the ratio between (4.25) and the capacitance of the air layer [145, 147]

$$\varepsilon_{\text{eff}} = \frac{C_{\text{CPW}}}{C_a} \tag{4.26}$$

$$= 1 + q_l(\varepsilon_l - 1) + q_s(\varepsilon_s - 1)\,, \tag{4.27}$$

with the partial filling factors

$$q_i = 2\frac{K(k_i)}{K(k_i')}\frac{K(k_a')}{K(k_a)}\,, \quad i = l, s \quad . \tag{4.28}$$

It follows that the partial filling factor q is defined as the ratio of the area filling up the crosssection of the system in w-plane to the total area [164, 165], the latter being equal to the area of the air layer. This can be visualized as in Fig. 4.7 (e).

Equation (4.27) gives the effective dielectric constant for the typical configuration of resonators in this project. However (4.27) can be extended for an arbitrary number of layers. Here, additional addends are added, each with their filling factor q_i and the relative factor of dielectric constants $(\varepsilon_i - \varepsilon_{i-1})$, where the dielectric constant of the layer ε_i is reduced by the dielectric constant ε_{i-1} of the neighboring layer on the outside with respect to the conductor layer. The last addend being the outermost non-air layer reduced by the air-layer. This is summed for all layers i above and j below the conductor layer. The total effective dielectric constant then gives

$$\varepsilon_{\text{eff}} = 1 + \sum_i q_i(\varepsilon_i - \varepsilon_{i-1}) + \sum_j q_j(\varepsilon_j - \varepsilon_{j-1})\,. \tag{4.29}$$

The dielectric constant of a single layer $k \in i$ is then

$$\varepsilon_k = \frac{1}{q_k}\left(\varepsilon_{\text{eff}} - \sum_{i'} q_{i'}(\varepsilon_{i'} - \varepsilon_{i'-1}) - \sum_{j} q_j(\varepsilon_j - \varepsilon_{j-1}) - 1\right) + \varepsilon_{k-1}\,, \tag{4.30}$$

with $i' \subset i \setminus \{k\}$. In the case of one single layer below and one single layer above the conductor layer, as in Fig. 4.7 (a) and equation (4.27), this gives for the thin-film layer ε_l (with $\varepsilon_{\text{a}} \approx 1$)

$$\varepsilon_l = \frac{1}{q_l}\left(\varepsilon_{\text{eff}} - q_s(\varepsilon_s - 1)\right) + 1\,. \tag{4.31}$$

The impedance of the CPW can be found as [145, 147, 149]

$$Z = \frac{1}{C_{\text{CPW}} v_{\text{ph}}} = \frac{1}{cC_a\sqrt{\varepsilon_{\text{eff}}}} = \frac{30\pi}{\sqrt{\varepsilon_{\text{eff}}}}\frac{K(k_a')}{K(k_a)}\,, \tag{4.32}$$

v_{ph} being the phase velocity. Z as a function of S/W has been shown in Fig. 4.2.

4.3.1. Role of metallization thickness

Above formulae have been derived using an infinitesimally thin conductor layer. In reality however, the conductor layer has finite size of at least several 100 nm. This leads to an increased concentration of the electric field E in the space between center conductor and ground planes, where the highest values of $|E|$ exist. This leads to a decrease both in ε_{eff} and Z [145, 166–168], although significant changes of the line parameters are only expected if the ratio of metallization thickness to conductor width t/S gets close to unity [166].

To account for the concentration of the E-field between center conductors and ground planes, a new effective geometry of the transmission line can be

defined, after which the above formalism for the infinitesimally thin conductor layer can be used. Effective values for the geometry of the resonator can be empirically defined as [145]

$$S_e = S + \Delta \tag{4.33}$$

$$\text{and} \quad W_e = W - \Delta\,, \tag{4.34}$$

where the effective change in width is

$$\Delta = \frac{1.25t}{\pi}\left(1 + \ln\left(\frac{4\pi S}{t}\right)\right)\,. \tag{4.35}$$

The new effective geometry therefore has a wider center conductor S and a reduced gap W. Schematically this can be seen in Fig. 4.8 (a) and (b).

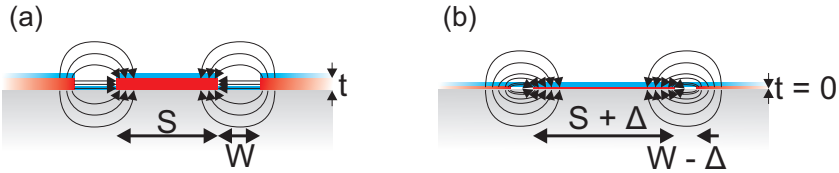

Fig. 4.8.: (a) Schematic crosssection of a CPW with thin-film sample. (b) Altered effective geometry. Here S and W are changed and the conductor metallization is assumed zero.

An altered effective dielectric constant is found as [145, 169]

$$\varepsilon_{\text{eff,e}} = \varepsilon_{\text{eff}} - \frac{0.7(\varepsilon_{\text{eff}} - 1)\frac{t}{W}}{\frac{K(k)}{K(k')} + 0.7\frac{t}{W}}\,, \tag{4.36}$$

and the effective impedance as [145]

$$Z_e = \frac{30\pi}{\sqrt{\varepsilon_{\mathrm{eff,e}}}} \frac{K(k_a')}{K(k_a)} \tag{4.37}$$

$$\text{with} \quad k_e = \frac{S_e}{S_e + 2W_e} \,. \tag{4.38}$$

4.4. Calculation of the complex dielectric constant and the microwave conductivity

In general the permittivity $\hat{\varepsilon}$ is a complex function consisting of a real part ε_1 and an imaginary part ε_2 following

$$\hat{\varepsilon} = \varepsilon_1 + i\varepsilon_2 \,. \tag{4.39}$$

The interaction between materials and electromagnetic waves usually depends on this complex magnitude via a complex refraction index $\hat{n} = n + ik$ consisting of a real part n and an extinction coefficient k [56]. For the real part it holds [56]

$$n^2 = \frac{1}{2}\left(\sqrt{\varepsilon_1^2 + \varepsilon_2^2} + \varepsilon_1\right) . \tag{4.40}$$

This real part of the refractive index is the main quantity determining the electromagnetic propagation speed c' since

$$c' = \frac{c}{\sqrt{\hat{\varepsilon}}} = \frac{c}{\hat{n}} = \underbrace{\frac{c}{n}}_{\text{velocity}} - i \underbrace{\frac{c}{k}}_{\text{extinction}} . \tag{4.41}$$

In many dielectrics the imaginary part of the dielectric constant is much smaller than the corresponding real part $\varepsilon_2 \ll \varepsilon_1$, giving the typical relation $\hat{n} \approx n \approx \sqrt{\varepsilon_1}$. In this thesis, however, materials with non-negligible losses,

meaning finite ε_2, will be investigated. In section 4.3, the conformal mapping technique has been presented, allowing for the calculation of a "dielectric constant" ε_l, see equation (4.31). Its derivation was done on the assumption of a purely real dielectric constant without considering losses ($\hat{\varepsilon} = \varepsilon_1$). In order to now extend this to include contributions by ε_2, the derived ε_l is identified as the squared refractive index $\varepsilon_l = n_l^2$. It can now not only include contributions by ε_1 alone, but also contributions by ε_2, following equation (4.40). This means, that $\varepsilon_l = n_l^2$ determined from conformal mapping consists of contributions of both parts ε_1 and ε_2 of the sample (although $\varepsilon_l = n_l^2$ is entirely real). The aim of this section is to separate ε_1 and ε_2 and to acquire both quantities individually. For this, a second measured quantity determined in experiments, the quality factor Q, has to be included. With both, the resonance frequency ν_0 and the quality factor Q, as well as some knowledge about the sample geometry, individual calculation of ε_1 and ε_2 is possible. In the following, the real part n of the refractive index will primarily be used, in order to point out, that while real, n consists of a combination of both ε_1 and ε_2.

The effective real part of the refractive index $n_{\mathrm{eff},s}^2$ of the resonator under influence of the sample can be directly derived from the resonance frequency of the resonator $\nu_{m,s}$ with equation (4.1),

$$n_{\mathrm{eff},s} = \frac{mc}{4\nu_{m,s}l}\,, \tag{4.42}$$

with l the resonator length. Note that here m is the mode number. Alternatively this can be derived from a relative frequency shift

$$n_{\mathrm{eff},s} = \frac{\nu_{m,e}}{\nu_{m,s}} n_{\mathrm{eff},e}\,, \tag{4.43}$$

with $\nu_{m,e}$ and $n_{\mathrm{eff},e}$ the resonance frequency (fundamentals and harmonics) and the effective real part of the refractive index of the empty resonator.

Here, $n_{\mathrm{eff},s}$ is a quantity which consists of contributions from all layers in the resonator (substrate and sample).

The losses α in the resonator are the sum of different loss mechanisms in the system, namely α_C the conductor losses, α_r radiation losses and α_D the dielectric losses [146]. α_D can be further separated into contributions of the substrate $\alpha_{D,\mathrm{sub}}$ and of the sample α_D. In total this gives

$$\alpha = \alpha_C + \alpha_r + \alpha_{D,\mathrm{sub}} + \alpha_D \,. \tag{4.44}$$

Usually in coplanar waveguides the radiation losses α_r are small and can be neglected. In order to find the losses of a thin-film sample on top of the resonator, losses in the resonator including a sample are compared relative to the empty resonator. Since only the sample is evaporated on top of the resonator, but the conductor is not changed, it is assumed that α_C does not change. Similarly, the substrate is unchanged, so $\alpha_{D,\mathrm{sub}}$ of the substrate is constant. Any difference in α between the resonator with sample (α_s) and without (α_e) is therefore purely dependent on the dielectric losses in the sample

$$\alpha_D = \Delta\alpha = \alpha_s - \alpha_e = \frac{\pi}{4l}\left(\frac{1}{Q_s} - \frac{1}{Q_e}\right) \tag{4.45}$$

$$= \frac{\pi}{c}\nu_{m,s} n_{\mathrm{eff},s}\left(\frac{1}{Q_s} - \frac{1}{Q_e}\right) = \frac{\pi}{c}\nu_{m,s} n_{\mathrm{eff},s}\Delta Q \,, \tag{4.46}$$

with $\alpha = \frac{\pi}{4lQ}$ from equation (4.14), $l = \frac{mc}{4\nu_{m,s} n_{\mathrm{eff},s}}$ from equation (4.1) and

$$\Delta Q = \frac{1}{Q_s} - \frac{1}{Q_e} \,. \tag{4.47}$$

For the loss tangent of the sample layer l it holds [146]

$$\tan\delta = \frac{\varepsilon_{2,l}}{\varepsilon_{1,l}} = \alpha_D \frac{n_{\mathrm{eff},s} c}{\pi q n_l^2 \nu_{m,s}} \,, \tag{4.48}$$

with q the filling factor of the sample (equation (4.28)). n_l is the (real) refractive index of the sample including contributions by $\varepsilon_{1,l}$ and $\varepsilon_{1,l}$ and is derived following conformal mapping, equation (4.31), as

$$n_l^2 = \frac{1}{q}\left(n_{\mathrm{eff},s}^2 - 1 - q_{\mathrm{sub}}(n_{\mathrm{sub}}^2 - 1)\right) + 1\,, \tag{4.49}$$

with $q_{\mathrm{sub}} \approx 0.5$ and $n_{\mathrm{sub}}^2 = \varepsilon_{\mathrm{sub}} \approx 10$ [170, 171] the filling factor and the dielectric constant of the substrate assumed to be purely real, since for Al_2O_3 it is $\varepsilon_2 \ll \varepsilon_1$. Equation (4.49) is similar to equation (4.31), however, n_l now is a combination of ε_1 and ε_2 following equation (4.40).

Solving equation (4.48) for α_D and combining it with (4.46) leads to

$$n_{\mathrm{eff},s}^2 \Delta Q = q n_l^2 \frac{\varepsilon_{2,l}}{\varepsilon_{1,l}}\,. \tag{4.50}$$

From equation (4.40) an expression for $\varepsilon_{2,l}$ can be derived as

$$\Rightarrow \varepsilon_{2,l} = 2n_l\sqrt{n_l^2 - \varepsilon_{1,l}}\,. \tag{4.51}$$

Putting equation (4.51) into (4.50) and solving for $\varepsilon_{1,l}$ with quadratic formula (taking the positive solution) gives

$$\varepsilon_{1,l} = \frac{2n_l^6 q^2}{n_{\mathrm{eff},s}^4 \Delta Q^2}\left(\sqrt{1 + \frac{n_{\mathrm{eff},s}^4 \Delta Q^2}{n_l^4 q^2}} - 1\right) \tag{4.52}$$

$$= \frac{2n_l^6 q^2}{\left(1 + q_{\mathrm{sub}}(\varepsilon_{\mathrm{sub}} - 1) + q(n_l^2 - 1)\right)^2}\left(\frac{1}{Q_s} - \frac{1}{Q_e}\right)^{-2} \left(\sqrt{1 + \frac{\left(1 + q_{\mathrm{sub}}(\varepsilon_{\mathrm{sub}} - 1) + q(n_l^2 - 1)\right)^2}{n_l^4 q^2}\left(\frac{1}{Q_s} - \frac{1}{Q_e}\right)^2} - 1\right)\,. \tag{4.53}$$

After calculating $\varepsilon_{1,l}$ with (4.53), $\varepsilon_{2,l}$ can directly be calculated using equation (4.51). In order to calculate $\varepsilon_{1,l}$ and $\varepsilon_{2,l}$ from measured data ν_0 and Q, first n_l^2 of the sample will be calculated using conformal mapping with equations (4.43) and (4.49), similar to section 4.3. After that, $\varepsilon_{1,l}$ will be calculated using (4.53) and then $\varepsilon_{2,l}$ using (4.51). This procedure will always be performed in this work.

To give an idea how strong the individual contributions of $\varepsilon_{1,l}$ and $\varepsilon_{2,l}$ to the resonance frequency shift and consequently to n_l are and in which parameter regimes the contribution by $\varepsilon_{2,l}$ becomes of similar size to that of $\varepsilon_{1,l}$ (in particular for small Q), in the following some estimations are performed. The general form of $\varepsilon_{1,l}$ and $\varepsilon_{2,l}$ as a function of quality factor and measured n_l^2 is shown in Fig. 4.9. Fig. 4.9 (a) shows $\varepsilon_{1,l}$ and $\varepsilon_{2,l}$ as a function of Q_s. Here, $Q_e = 10000$, which is a typical value of a good empty resonator and $q \approx 0.001\,86$, corresponding to a 30 nm thin-film. n_l^2 has been set exemplary to 50. It is found that over a large range of Q_s, n_l^2 consists mostly of contributions by $\varepsilon_{1,l}$, meaning that $n_l^2 \approx \varepsilon_{1,l}$ and $\varepsilon_{2,l}$ is negligible. In this range it can be assumed, that the shift in resonance frequency when applying the sample is only evoked by $\varepsilon_{1,l}$ and contributions to the resonance shift by $\varepsilon_{2,l}$ can be neglected (although $\varepsilon_{2,l}$ can still have strong effect on Q_s). In this range $\varepsilon_{1,l}$ could therefore also be derived directly from the frequency shift calculated via equation (4.1). Fig. 4.9 (b) shows the same data as a function of $1/Q_s$, where the low-Q_s region is enhanced.

If the measured Q_s is small however, contributions from both $\varepsilon_{1,l}$ and $\varepsilon_{2,l}$ have to be accounted for. As seen in the figure, below $Q_s \approx 400$, the influence of $\varepsilon_{2,l}$ on the measured n_l^2 grows and at some point even overtakes $\varepsilon_{1,l}$. In this regime $\varepsilon_{1,l}$ and $\varepsilon_{2,l}$ have to be calculated explicitly using the above formalism. The point at which the influence of $\varepsilon_{2,l}$ increases and $\varepsilon_{1,l}$ decreases, does not strongly depend on Q_e. From equation (4.47) it is clear, that since always $Q_e > Q_s$, Q_e is only a small correction to ΔQ and therefore in most conditions $\Delta Q \approx 1/Q_s$ in the above calculation.

In Fig. 4.9 (c) and (d) $\varepsilon_{1,l}$ and $\varepsilon_{2,l}$ are shown as a function of Q_s and as a function of n_l^2 up to 100. It is seen that with increasing n_l^2 the calculated $\varepsilon_{1,l}$ increases linearly at high Q_s. When decreasing Q_s the contribution of $\varepsilon_{2,l}$ to n_l^2 increases strongly as seen before. Only at low values of n_l^2 in the range of about $0-10$ does the crossover between $\varepsilon_{1,l}$ and $\varepsilon_{2,l}$ happen at higher values of Q_s, as can be seen with the dashed line in Fig. 4.9 (e) (for a 30 nm thin-film). This means that a simple calculation of $\varepsilon_{1,l}$ from the change in resonance frequency can be done as long as Q_s is still sufficiently large. Only when the calculation of $\varepsilon_{2,l}$ is desired or Q_s is strongly suppressed the above formalism will be needed.

Following the calculation of $\varepsilon_{1,l}$ and $\varepsilon_{2,l}$, the microwave conductivity $\hat{\sigma}(\omega) = \sigma_{1,l}(\omega) + i\sigma_{2,l}(\omega)$ can be calculated. This can directly be derived from the dielectric constant following [56]

$$\hat{\sigma}(\omega) = i\omega\varepsilon_0 \left(1 - \hat{\varepsilon}(\omega)\right) \tag{4.54}$$

$$\Rightarrow \quad \sigma_{1,l}(\omega) = \omega\varepsilon_0\varepsilon_{2,l}(\omega) \tag{4.55}$$

$$\text{and} \quad \sigma_{2,l}(\omega) = \omega\varepsilon_0 \left(1 - \varepsilon_{1,l}(\omega)\right) , \tag{4.56}$$

with ε_0 the vacuum permittivity and ω the probing frequency.

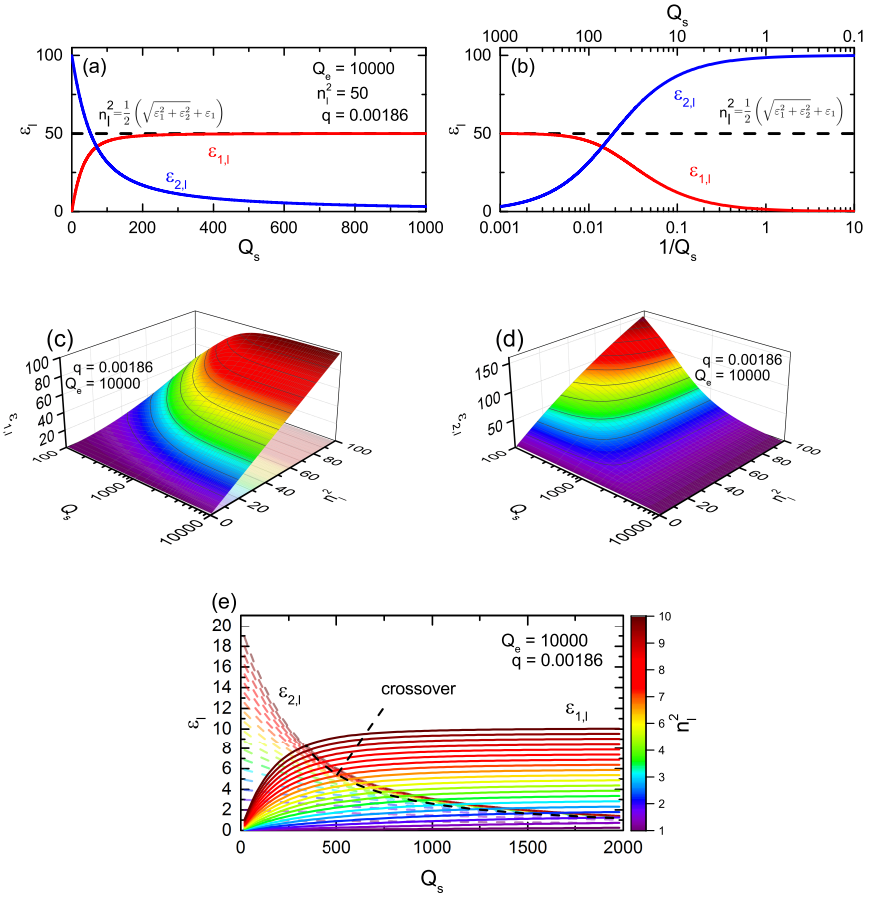

Fig. 4.9.: (a) $\varepsilon_{1,l}$, $\varepsilon_{2,l}$ and n_l^2 as a function of the quality factor Q_s under influence of the sample. The contribution of ε_2 to the measured resonance shift (reflected in n_l^2) is substantial only at low values of Q_s. (b) Same data as a function of $1/Q_s$. (c) $\varepsilon_{1,l}$ and (d) $\varepsilon_{2,l}$ as a function of Q_s and n_l^2. (e) $\varepsilon_{1,l}$ and $\varepsilon_{2,l}$-data from (c) and (d) in the low-n_l^2 regime. The dashed line denotes the crossover $\varepsilon_{1,l} = \varepsilon_{2,l}$.

4.5. Determination of ε in partially covered resonators

Up to now only substrates with isotropic ε have been considered. However, many substrates that are commonly in use for microwave resonators have an anisotropic ε. Especially sapphire-substrates cut in r-plane, which are used in this project, have different values for ε in two different directions between 9 and 11 [170, 171]. Usually this can be neglected, since in most experiments relative resonance frequency changes are used. To consider this more carefully however, in the following section it is shown how to find resonance frequencies and E-field distributions even with anisotropic ε.

If a sample film does not cover the resonator over the whole length but only part of a resonator, the influence of the film is weaker and depends on its location in relation to the electric field distribution of the standing waves. Depending on the harmonic of the resonator, the locations with highest electrical field shifts. This in turn can be used to reduce the influence of the sample on the resonator properties with the idea to reduce sample-induced dielectric losses. However, the problem complicates and the analysis has to be performed in a more rigorous manner. In the following sections a model for the calculation of the electric field distribution in the resonators is introduced and it is shown how this can be solved and used in order to calculate ε of a partially covering sample film.

This procedure has been developed together with Cenk Beydeda, a Bachelor student supervised by the author. Part of this procedure can also be found in his Bachelor thesis [172].

4.5.1. Basics of calculation

In order to calculate solutions for the above mentioned problems numerically, first a model of the resonator has to be assumed and split up into parts with different parameters. This is schematically depicted in Fig. 4.10. (a)

and (b) show the top view on a resonator of length l with parts of different effective ε_{eff} in different colors. In (a) the resonator is covered only partially by a thin film (gray), where in (b) the resonator is located on an anisotropic substrate. (c) and (d) show linear representations of the resonators. Any continuous crossovers in ε_{eff} are approximated with sharp transitions (e.g. from blue to green in the figure). The resonators are split into n parts with their individual lengths l_i adding up to the total length $l = \sum_{i=1}^{n} l_i = s_{n+1}$ and corresponding $\varepsilon_{\text{eff},i}$. The absolute value of $|E|$ of the expected solutions of resonance modes are shown in (e). From this, it is clear that the different modes react differently to the spatial distribution of ε_{eff}, since for each modes the amplitude distribution varies.

The given resonator geometry dictates boundary conditions. Since the ending of the resonator near the feedline (left in the figure) is a closed end, no current is able to run ($B = 0$) and the electric potential has a maximum ($E = E_{\max}$). Analogously at the other end (right in figure) the reverse holds true ($B = B_{\max}$, $E = 0$), since it is an open end.

To calculate the expected solutions of the E- and B-field distributions, a solution to the Helmholtz equation has to be found. The Helmholtz equation describes the distribution of E and B in the stationary resonator under given boundary conditions [147, 150]. In the following only the E-field will be evaluated, since for the measurements and analysis in this project it is usually more convenient to look at E. B can directly be derived from it. Since TEM-waves are considered in our system, the used Helmholtz equation can be assumed one-dimensional

$$\frac{\partial^2 E_i(x)}{\partial x^2} + k_i^2 = 0\,, \tag{4.57}$$

with $E_i(x)$ the E-field distribution. k_i is the wavevector in a given section i and can be written as (v_i being the phase velocity)

$$k_i = \sqrt{\varepsilon_{\mathrm{eff},i}}\frac{\omega}{c} = \sqrt{\varepsilon_{\mathrm{eff},i}}\frac{\pi}{2l} = \sqrt{\varepsilon_{\mathrm{eff},i}}k_0\,, \tag{4.58}$$

with $k_0 = \frac{\pi}{2l}$ the wave vector in vacuum.

The Helmholtz equation (4.57) now has to be solved for each section of the resonator individually with corresponding boundary conditions. The boundary conditions for the first ($i = 1$) and last part ($i = n$) are given by the resonator geometry

$$\begin{aligned} E_1(x = 0) &= E_{\max} \\ E_n(x = l) &= 0\,. \end{aligned} \tag{4.59}$$

The boundaries for all parts have to be consistent with their neighbors in both the absolute value of E_i as well as the first derivative. This gives

$$E_i(x = s_{i+1}) = E_{i+1}(x = s_{i+1}) \tag{4.60}$$

$$\partial_x E_i(x = s_{i+1}) = \partial_x E_{i+1}(x = s_{i+1})\,, \tag{4.61}$$

with s_i the sum $s_i = l_1 + l_2 + \cdots + l_{i-1}$ of the lengths of all parts left of the part i. For the solution of the Helmholtz equation (4.57) an ansatz is chosen as

$$E_i(x) = A_i \sin(k_i \cdot (x - s_i)) + B_i \cos(k_i \cdot (x - s_i))\,. \tag{4.62}$$

with coefficients A_i and B_i.

By looking at the outer boundaries of the entire resonator (equation (4.59)), it can directly be found that

$$B_1 = E_{\max} \tag{4.63}$$

$$B_n = -A_n \tan(k_n l_n)\,. \tag{4.64}$$

A_i and B_i of parts $i = 2 \ldots n-1$ are found in an iterative manner with the boundary condition for the absolute value

$$E_{i+1}(s_{i+1}) \stackrel{!}{=} E_i(s_{i+1}) \tag{4.65}$$

$$\begin{aligned} &A_{i+1}\sin(k_{i+1}(s_{i+1}-s_{i+1})) + B_{i+1}\cos(k_{i+1}(s_{i+1}-s_{i+1})) \\ &\stackrel{!}{=} A_i \sin(k_i(s_{i+1}-s_i)) + B_i \cos(k_i(s_{i+1}-s_i)) \end{aligned} \tag{4.66}$$

$$\Rightarrow B_{i+1} = A_i \sin(k_i l_i) + B_i \cos(k_i l_i)\,, \tag{4.67}$$

and the boundary condition for the first derivative

$$\partial_x E_{i+1}(s_{i+1}) \stackrel{!}{=} \partial_x E_i(s_{i+1}) \tag{4.68}$$

$$\begin{aligned} &k_{i+1}A_{i+1}\cos(k_{i+1}(s_{i+1}-s_{i+1})) - k_{i+1}B_{i+1}\sin(k_{i+1}(s_{i+1}-s_{i+1})) \\ &\stackrel{!}{=} k_i A_i \cos(k_i(s_{i+1}-s_i)) - k_i B_i \sin(k_i(s_{i+1}-s_i)) \end{aligned} \tag{4.69}$$

$$\Rightarrow A_{i+1} = \frac{k_i}{k_{i+1}}\left(A_i \cos(k_i l_i) - B_i \sin(k_i l_i)\right) \tag{4.70}$$

$$\Rightarrow A_{i+1} = \sqrt{\frac{\varepsilon_{\mathrm{eff},i}}{\varepsilon_{\mathrm{eff},i+1}}}\left(A_i \cos(k_i l_i) - B_i \sin(k_i l_i)\right)\,. \tag{4.71}$$

Since the absolute values of E and B are of no interest, A_1 can arbitrarily be set to $A_1 = 1$.

With this iterative procedure, each coefficient for the individual parts is found with a common wavelength. By combining all parts, the solution for the whole resonator follows (compare Fig. 4.10 (e)).

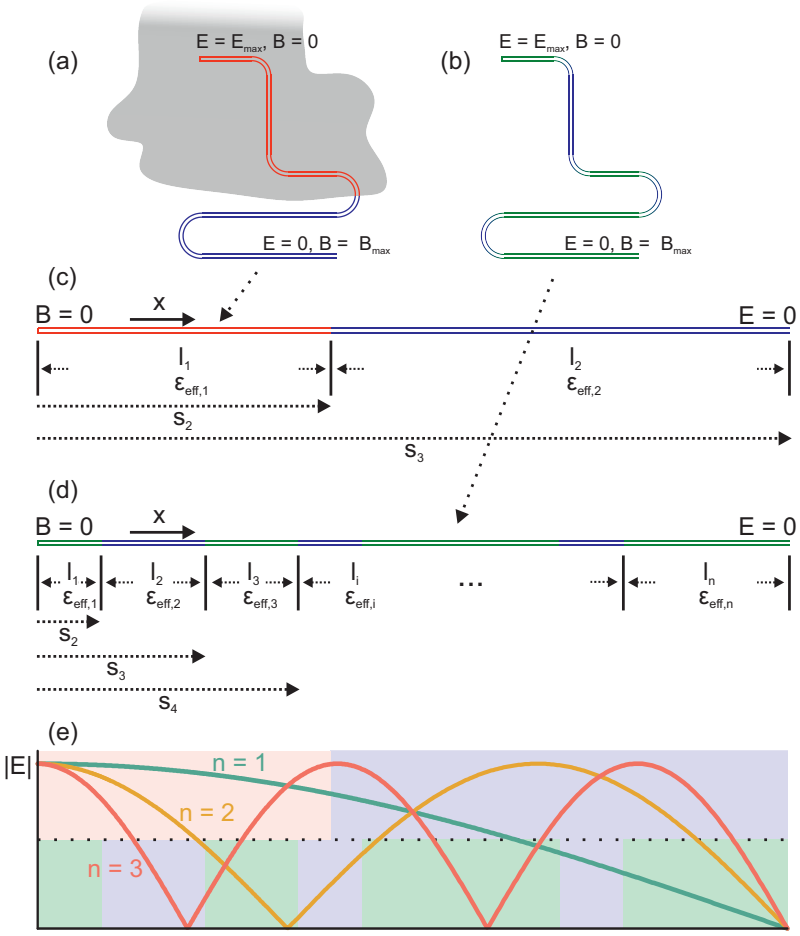

Fig. 4.10.: (a) Schematic depiction of a resonator covered partially with a thin-film. (b) Resonator on an anisotropic substrate. Colors indicated different values of ε. (c) and (d) Linear representation of the resonators split into subsections with different parameters. (e) $|E|$-field distribution of fundamental mode and the first two harmonics. Varying ε is depicted by colors in the background.

4.5.2. Implementation into analysis

The above calculation method can now be used to numerically calculate a solution for a given resonator partially covered with a thin-film. The known parameters are the nominal length of the resonator and ε_{eff} of the empty parts of the resonator, both of which is given by the geometry. Generally these parameters should define the frequency of the empty resonator with $\nu_n = \frac{n \cdot c}{4l\sqrt{\varepsilon_{\text{eff}}}}$ (equation (4.1)). Usually however there is a small mismatch between nominal resonance frequency (from designed geometry) and measured resonance frequency in experiment. This can have various reasons, from slight inaccuracy in production, e.g. due to some scaling of the lithography mask [173], uncertainties in lateral geometry (errors in S and W of the resonator) due to inconsistent etching, uncertainties in the thickness of the conductor layer, or uncertainties in ε of the substrate.

Since the measurement comparing covered resonator to empty resonator is a relative measurement, it does not matter where the mismatch actually comes from. The resulting calculation of ε of the film will still be correct. However it has to be compensated for the above procedure to work. For this the length of the empty resonator l going into the numerical calculation has to be adjusted. This is done by is stretching or compressing each part l_i following

$$l_i = \delta \cdot l_{\text{nom},i}\,, \quad i = 1, \ldots, n \quad \text{with} \quad \delta = \frac{\nu_{\text{nom}}}{\nu_{\text{meas}}}\,, \tag{4.72}$$

with ν_{nom} the nominal resonance frequency and ν_{meas} the measured resonance frequency.

In order to find $\varepsilon_{\text{eff, cov}}$ of the parts covered by the thin-film under study, the resonator is split into parts covered by the film and empty parts. Since the resonance frequency is measured, k_0 (equation (4.58)) can directly be calculated, leaving only $\varepsilon_{\text{eff},i}$ of each part undetermined. For the empty parts $\varepsilon_{\text{eff},i}$ is set to the empty resonator geometry (in a simple model with

an isotropic Al_2O_3 substrate, not considering metallization thickness this is $\varepsilon_{\text{eff}} = 5.5$). For the covered parts $\varepsilon_{\text{eff, cov}}$ is varied, typically in a starting range $4 - 7$ with about 1000 sample points. For each point of $\varepsilon_{\text{eff, cov}}$ the solutions are calculated by iteration of A_i and B_i as above. This $\varepsilon_{\text{eff, cov}}$-sweep leads to a solution, where the wavelength of the resonance fits to the resonator length and hence equation (4.64) is $B_n = 0$, meaning that the E-field has a minimum exactly at the open end of the resonator. The corresponding $\varepsilon_{\text{eff, cov}}$ gives the solution. To reduce the error, this entire procedure is iterated many times, with decreasing starting range of the $\varepsilon_{\text{eff, cov}}$-sweep, depending on the previous solution.

To derive ε_1 and ε_2 from $\varepsilon_{\text{eff, cov}}$ of the sample also the quality factor $Q \propto 1/\alpha$ is needed, as shown in the procedure in section 4.4. However, the measured quality factor of the partially covered resonator Q_{pc} is expected to be substantially larger than for a resonator that was theoretically covered completely by the samples, since the only partially covering sample has overall less impact on the resonator. Analogously α_{pc} is expected to be smaller. The procedure in section 4.4 however, can only be applied if the contributions to α are distributed uniformly along the whole resonator. In order to account for this, the attenuation of the empty resonator α_0, without sample, and of the partially covered resonator α_{pc} are compared and extrapolated to get Q_{cov} and α_{cov} of the resonator with uniform distribution.

To do this, the E-field is integrated along the covered parts and compared to the integral of the E-field along the total length of the resonator. Schematically this is shown in Fig. 4.11 (a). The resulting factor f is

$$f = \frac{\int_0^{l_{\text{pc}}} |E| dl}{\int_0^{l_{\text{cov}}} |E| dl}, \tag{4.73}$$

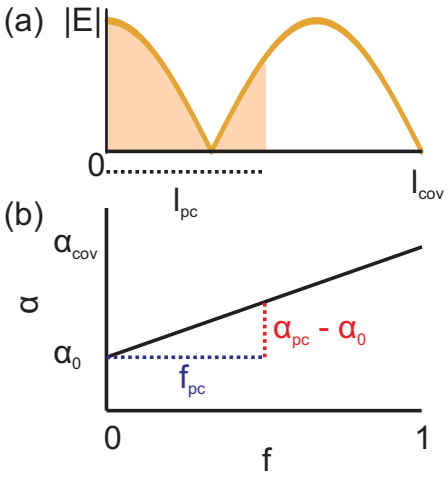

Fig. 4.11.: (a) Absolute value of an exemplary $|E|$-field distribution along a resonator. Shaded area indicates the integral along the length covered by the sample. (b) Attenuation $\alpha(f)$ as a function of the factor f determined from integrals of $|E|$. The linear dependence allows for extrapolation to a theoretically completely covered resonator.

with l_{pc} the length up to which the resonator is covered and l_{cov} the total length of the resonator. f is the quantity which describes the strength of influence of the sample on the resonator. It grows linearly with the amount of E-field that is under the influence of the sample and the attenuation $\alpha(f)$ is therefore a function of f with linear dependence $\alpha(f) \propto f$. Since the attenuation of the empty resonator α_0 is known from Q_{e} of the empty resonator and α_{pc} is known as well, the attenuation for a theoretical completely

covered resonator α_{cov} can now be extrapolated following Fig. 4.11 (b). Q_{cov} is then found as

$$\begin{aligned} \alpha_{\mathrm{cov}} &= \frac{\alpha_{\mathrm{pc}} - \alpha_0}{f_{\mathrm{pc}}} + \alpha_0 \\ \Rightarrow Q_{\mathrm{cov}} &= \left[\frac{\frac{1}{Q_{\mathrm{pc}}} - \frac{1}{Q_0}}{f_{\mathrm{pc}}} + \frac{1}{Q_0} \right]^{-1} . \end{aligned} \tag{4.74}$$

With Q_{cov}, ε_1 and ε_2 can be calculated in regular fashion, as shown in section 4.4.

In general, with the procedures shown in this section other calculations are also possible, e.g. calculating resonance frequency for given ε and l, or calculating l for given ε and ν.

4.6. Temperature dependence of resonator properties

CPW resonators can be used with a superconductor as the conductor material [1–3, 136]. This gives higher Q since the resistance of superconductors is low for microwave frequencies [56]. However, it also introduces substantial temperature dependence. Following the London penetration depth (2.4),

$$\lambda(T) = \lambda_0 \left[1 - \left(\frac{T}{T_c} \right)^4 \right]^{-1/2} , \tag{4.75}$$

electromagnetic waves penetrate the surface of the superconductor at finite temperatures. The depth up to which this happens increases with increasing temperature. This alters the crosssection of a CPW as shown in Fig. 4.12. Here Wheeler's approximation [174] is used, where the effective change in geometry will be approximated by a penetration depth of $\lambda_L/2$ into the superconductor. This new effective geometry has direct influence on

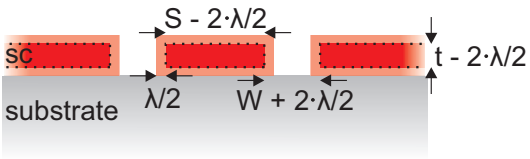

Fig. 4.12.: Schematic crosssection of a CPW with superconducting conductor at finite temperature. The effective geometry of the conductor is altered by the penetration depth λ.

the microwave propagation in the system as the impedance of the CPW, equation (4.32), is altered since S, W and t change. In general this change is approximated well to first extend by

$$\begin{aligned} Z(\lambda) &= Z(0)\left[1+\frac{\lambda}{2}\left(2\left.\frac{\partial Z}{\partial W}\right|_{W_0} - 2\left.\frac{\partial Z}{\partial S}\right|_{S_0} - 2\left.\frac{\partial Z}{\partial t}\right|_{t_0}\right)\right] \\ &= Z(0)\left[1+\frac{\lambda}{2}\Gamma\right], \end{aligned} \tag{4.76}$$

with Z from equation (4.32), S, W, t the characteristic parameters, the partial derivatives evaluated at their values without penetration S_0, W_0, t_0 and Γ a geometric factor combining all partial derivatives. Since Z is inversely proportional to the phase velocity v_{ph}, equation (4.32), and in turn the resonance frequency of the resonator is dependent on v_{ph}, equation (4.1), it directly follows for the resonance frequency in dependence of the temperature

$$\nu(T) = \frac{\nu(0)}{\sqrt{1+\Gamma\frac{\lambda(T)}{2Z(0)}}} = \frac{\nu(0)}{\sqrt{1+\frac{\Gamma}{2Z(0)}\frac{\lambda(0)}{1-\left(\frac{T}{T_c}\right)^4}}}, \tag{4.77}$$

with $\nu(0)$ the resonance frequency without penetration depth and $\lambda(0)$ the penetration depth at $T = 0$. The empirical Gorter-Casimir equation (4.75) is

only valid close to T_c [61], however, experience shows that (4.77) can usually be fitted to temperature-dependent $\nu(T)$ over a large range of temperatures.

4.7. Experimental setup

For the experiments performed in this work, very low temperatures in the mK-regime are necessary[†]. For this, a KelvinoxMX400 dilution refrigerator by Oxford instruments is used, which is a wet dilution refrigerator insert system operated in a stainless steel liquid helium dewar. A photograph of the insert without thermal shielding is shown in Fig. 4.13. The resonator box is placed at the end of the cold finger (shown in more detail in section 5.2.3, Fig. 5.4), which in turn is thermally well connected to the mixing chamber, where ^{3}He/^{4}He-phases are mixed and the system is cooled [175]. The box is connected via coaxial cables, which lead to the top of the insert, where they are connected to external circuitry. Over a short length the coaxial cables are made of NbTiN, which becomes superconducting at low temperatures [176] and therefore inhibits thermal conductance of the coaxial cables and reduces heat load to the cold finger. The DC-cabling ensures the possibility to measure DC-resistance of the samples as well as to read out a temperature sensor, which is mounted directly at the resonator box for a good thermal coupling. With this setup a temperature range from 4 K down to ~ 25 mK can be accessed (DC-measurements can be accessed starting from room temperature), in a frequency range from MHz up to 50 GHz.

Microwave data is acquired with an Agilent Technologies PNA Network Analyzer of type E8364C, allowing for a full complex acquisition of microwave parameters such as S_{12}. DC-measurements are performed with a Stanford Research SR830 Lock-in amplifier and a Femto Variable Gain Low Noise Current Amplifier DLPCA-200, see details in section 4.9.

[†]Note, that samples A and B in section 6.4 have not been measured at mK-temperatures but at temperatures > 1.5 K, for which a VTI and a glass bath cryostat have been used.

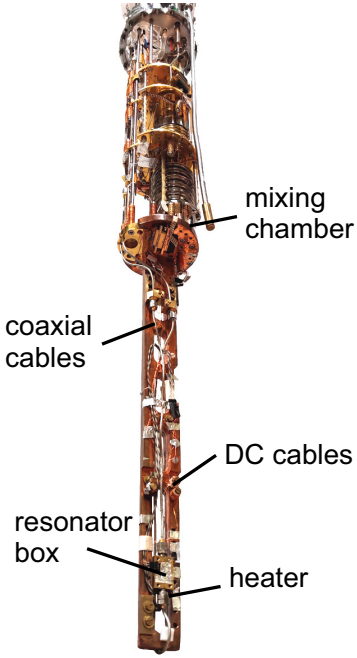

Fig. 4.13.: Photograph of the KelvinoxMX400 dilution refrigerator insert.

4.8. Fitting procedure

The equivalent LRC-model of a microwave resonator from section 4.2 predicts that resonances of the resonator have Lorentzian shape [150]. The power oscillating in the resonator has been shown earlier, in Fig. 4.5 (b) and shows that at resonance frequency ν_0 a maximum of power is oscillating in the resonator, while for off-resonant frequencies $\nu_0 + \Delta\nu$ it quickly diminishes.

Typically the shape of an ideal resonance should follow Lorentzian shape [56] as

$$S_{21} \propto \frac{A\nu_B}{(\nu - \nu_0)^2 + \nu_B^2}\,, \tag{4.78}$$

with S_{21} being the microwave transmission S-parameter, A the insertion loss and ν_B the bandwidth where the power has dropped to half the maximum value. From ν_0, ν_B and the quality factor $Q = \nu_0/\nu_B$, many parameters of the system can be evaluated, as has been seen in previous sections. It is therefore of high interest to determine these resonance parameters precisely.

Depending on the type of coupling, a resonator can enhance the transmission at resonance, i.e. for gapped $\lambda/2$-resonators, or reduce the transmission, e.g. for parallel coupled $\lambda/4$-resonators. Since the latter are the primary probes in this work, the following section will focus on a reduction of transmission.

Due to the experimental setup as well as material parameters, resonances can deviate quite strongly from the ideal Lorentzian shape in (4.78). On the one hand this is influenced by the coaxial cables of the system, which themselves have strong frequency dependence of the transmission due to the frequency-dependent skin effect [174]. This leads to a suppression of overall transmission at higher frequencies, as the microwaves are attenuated stronger the higher the frequency. In the range of 1 GHz to 30 GHz the suppression is in the order of about one magnitude. Additionally, through the finite length of the experimental cabling in the range of several 10 cm to m, standing waves can be induced [177] in the coaxial cables, which can have negative impact in the GHz frequency range.

On the other hand another substantial contribution to the deviation from the ideal Lorentzian shape is the complexity of the resonator design, its coupling and the housing of the microwave-chip. Since there are many bends and transitions in the lines of the CPW it is possible that to a certain extent parasitic resistances, capacitances, inductances and reactances exist [150],

altering the transmission through the feedline. The housing itself is a brass box with dimensions in the cm-regime, which in turn can lead to box modes, similar to microwave cavity modes [150, 178, 179]. These parasitic modes and effects may overlap with resonances and therefore create some offsets or slopes in the transmission spectrum. All of these contributions lead to a nonzero background, which has to be taken into account and corrected.

Another important factor are phase-shifts of the microwave signal, which can strongly alter the resonance shape. These phase-shifts can occur due to the complexity of the coupled and meandered resonator, leading to a shift of the real and imaginary part of the microwave signal in respect to each other, while in the absolute value of the signal this is primarily detected by asymmetry of the resonance. Here, unintuitively it is also possible that $\lambda/4$-resonators show resonances which have partially enhanced transmission signal close to the resonance, where they should only show reduced transmission. Fitting these kind of resonances with an absolute Lorentzian such as (4.78) is insufficient and therefore brings the necessity to analyze the complex response of the resonators. Fortunately the experimental setup with the use of a vector network analyzer enables acquiring complex data directly.

Fig. 4.14 (a) shows such a transmission spectrum of a resonance of a $\lambda/4$-resonator. It is seen that the resonance has some slight asymmetry and is altered from the ideal Lorentzian, mainly due to it sitting on a slope. The absolute value of S_{21}, the real part and the imaginary part are shown. In order to fit the data, the following complex function is used

$$S_{21}(\nu) = \underbrace{e^{2\pi i \tau \nu}}_{\text{phase}} \left[\underbrace{\frac{v_1}{\nu - v_2}}_{\text{Lorentzian}} + \underbrace{v_3 + v_4 \left(\nu - \mathrm{Re}\left(v_2\right)\right)}_{\text{background}} \right] . \tag{4.79}$$

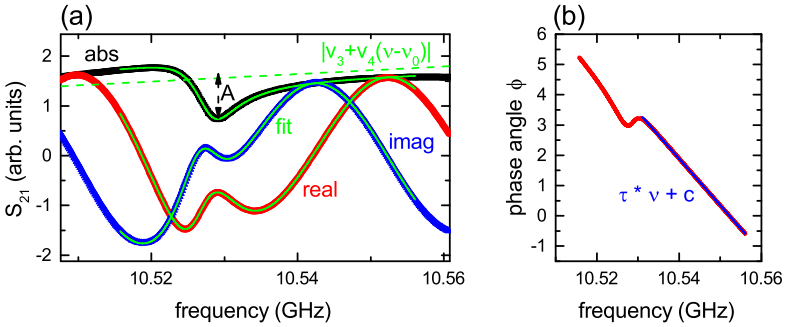

Fig. 4.14.: (a) Transmission spectrum of a resonance frequency of a $\lambda/4$-resonator. Real part, imaginary part and absolute value are plotted with the corresponding (complex) fit. The dashed line shows the first order background approximation. (b) Phase angle ϕ between real and imaginary part.

τ, v_1, v_2, v_3 and v_4 are complex fitting parameters. v_1 and v_2 are combinations of resonance properties as

$$v_1 = \hat{A} \cdot i\frac{\nu_B}{2} \tag{4.80}$$

$$v_2 = \nu_0 + i\frac{\nu_B}{2}\,, \tag{4.81}$$

with ν_0 and ν_B being the absolute value of the resonance frequency and the bandwidth. $\hat{A}$ is the complex insertion loss.

Equation (4.79) consists of three parts. The first part is a global phase that is determined by the phase between real part and imaginary part of S_{21}. τ is determined as a separate fit before the actual fit to the data. This first fit to the phase can be exemplary seen in Fig. 4.14 (b). Finding the phase angle $\phi = \arctan\left(\frac{\mathrm{Im}(S_{21})}{\mathrm{Re}(S_{21})}\right)$ and bringing it from the interval $\left[-\frac{\pi}{2}, \frac{\pi}{2}\right]$ to a larger interval, where all discontinuities are removed, gives a linear regime. The fit is performed off-resonance but close to the resonance and the resulting value for τ will be used in subsequent fittings.

The two parts in brackets of equation (4.79) are expressions for a complex Lorentzian and a complex background model. The background model is a linear approximation with an offset v_3 and a slope v_4, Fig. 4.14 (a) shows the background approximation for the exemplary resonance. Both the Lorentzian and the background model are fitted simultaneously. With this the mentioned resonance parameters can be extracted as

$$\nu_0 = \mathrm{Re}\,(v_2) \tag{4.82}$$

$$\nu_B = 2 \cdot \mathrm{Im}\,(v_2) \tag{4.83}$$

$$A = \frac{|v_1/\mathrm{Im}(v_2)|}{|v_3|}\,. \tag{4.84}$$

To find the insertion loss A of the resonator the relative amplitude of the resonance has to be calculated by calibrating the absolute of $\hat{A}$ by the offset v_3, as seen in (4.84).

It is crucial for a good fit to find well-enough initial starting parameters. They are determined from the absolute transmission spectrum $S_{21}(\nu)$ by taking the position of the local minimum as starting parameter for ν_0, the depth of the dip for A and the bandwidth at which $A/2$ is reached for ν_B.

4.9. DC-measurements

Apart from microwave data, which characterizes the samples at GHz-frequencies, the indium oxide samples in this work are also characterized by DC-measurements. This is especially useful since many properties of these highly disordered films show their characteristics already in the DC-conductivity such as e.g. the opening of a hard gap [8, 12, 14, 33], see section 3.5. The hard-gap activation gap in turn can also be used to determine the distance of the individual samples to the transition and give good possibility to characterize their location in the phase diagram.

There are some major challenges concerning the DC-measurements however, since excitation currents and voltages have to be very low, in the range of nA and µV. They have to be as low as possible, since the samples should be able to completely thermalize at mK-temperatures. High excitation energies can counteract this, since on the one hand imprinting a high current I to the sample can lead to a temperature increase of the whole sample including its surroundings. The heating-power follows

$$P = R \cdot I^2 \,, \tag{4.85}$$

with R the sample resistance. On the other hand, the electronic bath of the charge carriers can have a certain temperature, which can differ from thermal temperature of the lattice, meaning that electrons and phonons decouple [180, 181]. To minimize any difference between electron and phonon temperature, the excitation energies have to be as low as possible [181].

The DC-measurement setup overcoming these challenges that was used to characterize the indium oxide samples is shown schematically in Fig. 4.15. It includes a Stanford Research SR830 Lock-in amplifier, as well as some home-made filtering and an external current-voltage amplifier of type Femto Variable Gain Low Noise Current Amplifier DLPCA-200. The setup is used in two measuring configurations, one of them being a configuration for 2-point measurements and one for 4-point measurements. The 4-point measurement configuration is shown in Fig. 4.15 (c). The Lock-in amplifier creates an excitation current with the help of a 10 MΩ resistance. Following

$$R = \frac{U}{I} \quad \Rightarrow \quad I = \frac{U}{R} \,, \tag{4.86}$$

this creates an excitation current in the range of several 10 nA for typical Lock-in excitation voltages in the 100 mV-regime. The high resistance of 10 MΩ ensures, that the excitation voltage creates an excitation current dominated by the external resistance, since the resistance of the sample at room temperature

is typically less than 100 kΩ when measuring with the 4-point setup. The excitation current is then sent to the sample through twisted-pair cables, which ensures a minimum of noise pick-up from the environment of the experiment. The voltage occurring at the center contacts on the sample is then detected by the differential input of the Lock-in amplifier.

Naturally it would be desired to perform 4-point measurements in all conditions of the experiment in order to cancel out contact and cable resistances and have direct access to the resistance of the sample. However, this is not straightforwardly possible, since in some conditions the resistance of the sample increases by many magnitudes. Since the Lock-in amplifier has an input impedance of 10 MΩ, 4-point measurements become unreliable when the resistance of the sample becomes larger than a few MΩ. This is typically the case when samples get to an insulating regime at low temperatures. Using the 4-point setup would then lead to the excitation current running through the Lock-in instead of the sample, resulting in a maximum measurement range below 10 MΩ. The 4-point measurement method can therefore only be used for relatively low sample-resistances in the 100 kΩ-regime.

To measure large sample-resistances in the MΩ-regime, a 2-point measurement configuration is used, as shown in Fig. 4.15 (a). Here, the output of the Lock-in is connected to a shielded box containing a voltage divider, shown in detail in Fig. 4.15 (b). This divider reduces the voltage from the Lock-in, typically in the 100 mV-regime, by a factor of 1×10^3, down to the 100 µV-regime. This excitation voltage induces a current through the sample, which is in turn measured again by the Lock-in and is used for resistance calculation with (4.86). For accessibility and low noise the small measured current is converted by an external current-voltage amplifier to a voltage measurable by the Lock-in. Typical amplifications are in the range of $1 \times 10^7 - 1 \times 10^9$. To reduce the noise level further an additional RC-filter is included with $R = 5\,\text{k}\Omega$ and $C = 2\,\mu\text{F}$, giving a cut-off frequency of about 15 Hz, while the excitation frequency is in the range of a few Hz.

With this setup the excitation happens by imprinting a voltage to the sample and the response is measured by the resulting current. This is advantageous if samples are expected to have increasing resistance, since following equation (4.86) with fixed U, the excited current reduces and the heating-power decreases further as well, following (4.85). This prevents accidental heating of the sample. As an example, for a sample resistance of $1\,\mathrm{M\Omega}$ and an excitation voltage of $500\,\mu\mathrm{V}$, the heating-power which has to be dissipated is about $250\,\mathrm{pW}$. This is much less than the cooling power of the used dilution fridge in the relevant temperature-range and the sample will not heat up.

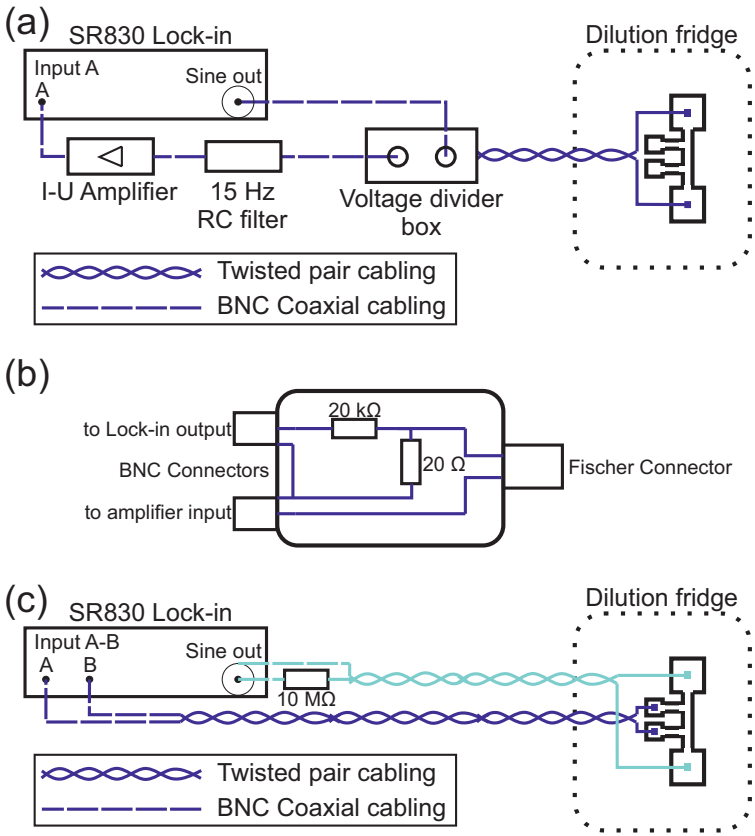

Fig. 4.15.: (a) Schematic depiction of the 2-point DC-measurement setup. A Lock-in amplifier, voltage divider, as well as an external amplifier is used. Cable types are indicated. (b) Voltage divider box detailed with the included resistances. (c) 4-point setup using the Lock-in and an additional resistance.

The depicted Hall-bar structure shown already in Fig. 4.15 on the right is shown in greater detail in Fig. 4.16 with typical dimensions. The Hall-bar

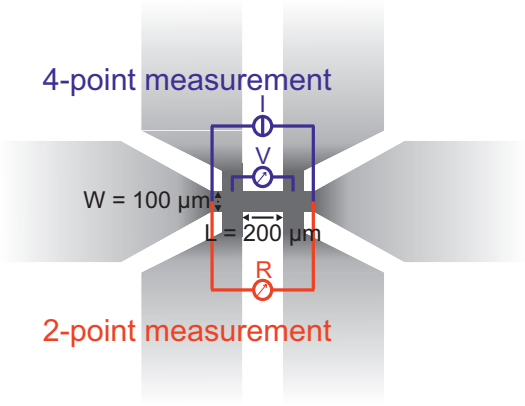

Fig. 4.16.: Schematic model of the Hall-bar used for DC-measurements. Configurations for 2-point and 4-point measurements are shown, measuring the resistance of the center strip. The large pads to each side are for easier contacting. Typical dimensions are indicated.

design is a commonly used design to measure DC transport properties of samples [28, 32], since it has a defined structure and dimension and sample-specific properties can directly be found. In the Hall-bar used here, the center strip has a length of 500 µm and a width of 100 µm. There are six pads for easy contacting of external wires, two of them located at the ends of the strip and two of them located to each side. The leads leading from the pads on the side to the center strip have a separation of 200 µm.

The measurement configurations mentioned before are indicated in the figure. The 2-point measurement is performed along the whole length of the strip, from one contacting pad to the other. Therefore, contributions from the contact resistance, the pads and the leads to the center strip are included. The 4-point measurement is performed using the pads at the ends of the

strip for imprinting the excitation current. The current is assumed to run uniformly from one end of the strip to the other, while the resulting voltage is measured between two pads on one side.

From the geometry of the Hall-bar, the sheet resistance R_s as well as the resistivity ρ of the sample can be calculated using the 4-point configuration. For the 4-point resistance $R_{4\mathrm{P}}$ along the film is holds

$$R_{4\mathrm{P}} = \rho\frac{L}{A} = \rho\frac{L}{t \cdot W} = R_s\frac{L}{W}\,, \tag{4.87}$$

with L the length of the center strip, A its cross-sectional area and ρ the resistivity of the sample. Since the film is homogeneous in thickness t and has defined width W, the area is $A = W \cdot t$. ρ is related to R_s as

$$\rho = R_s \cdot t\,. \tag{4.88}$$

From the 4-point measurement R_s can therefore be calculated using half of the measured resistance $R_{4\mathrm{P}}$, since here it is $L = 2W$, and afterwards equation (4.88) can be used to calculate the resistivity ρ of the sample.

Usually the samples measured in this work become insulating upon cooling to low temperatures. This increases the resistance strongly and leads to the aforementioned challenges. Since 4-point measurements cannot be performed for high resistance samples, 2-point measurements will be performed and calibrated by the 4-point measurements performed at room temperature. Fig. 4.17 (a) shows an exemplary temperature-dependence for R_s which has already been calibrated. It shows hard-gap activated behavior with an exponential increase of the form

$$R_s = R_0 e^{\frac{T_0}{T}}\,, \tag{4.89}$$

that can be fit with an activation temperature T_0 and a fit parameter R_0. Plotting the data in an Arrhenius-type form as a function of $1/T$ gives a

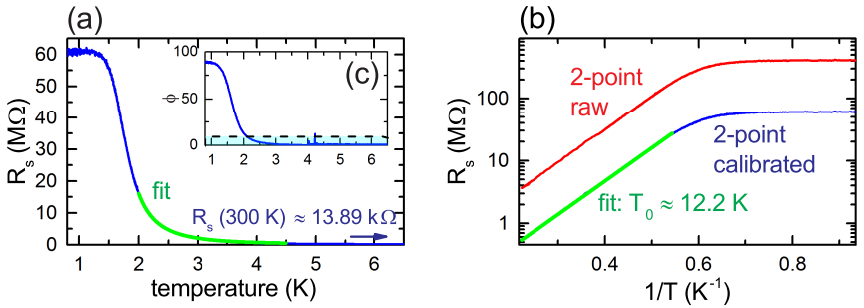

Fig. 4.17.: (a) Sheet resistance of a sample which gets insulating upon cooling. An activation law is fitted. (b) Arrhenius-plot of an insulating sample. The raw data from 2-point measurement is shown as well as the calibrated sheet resistance with activation fit following (4.89). (c) Phase of the Lock-in measurement upon cooling.

linear regime, shown in Fig. 4.17 (b), now also including the raw, uncalibrated data.

To calibrate the measured 2-point resistance $R_{2\mathrm{P}}$, both 2-point and 4-point measurements are performed before cooldown at room temperature, where also the 4-point measurement performs well (giving $R_s(300\,\mathrm{K})$), since sample resistance is in the kΩ-regime. The temperature-dependent sheet resistance $R_s(T)$ is then found as

$$\begin{aligned} R_s(T) &= R_{2\mathrm{P}}(T) \cdot \frac{R_s(300\,\mathrm{K})}{R_{2\mathrm{P}}(300\,\mathrm{K})} = (2R_s + R_r)\, e^{\frac{T_0}{T}} \cdot \frac{R_s e^{\frac{T_0}{300\,\mathrm{K}}}}{(2R_s + R_r)\, e^{\frac{T_0}{300\,\mathrm{K}}}} \\ &= R_s e^{\frac{T_0}{T}} \,. \end{aligned} \tag{4.90}$$

$R_{2\mathrm{P}}(T)$ consists of twice the sheet resistance R_s (due to the geometry $L = 2W$) and R_r is the resistance of contacts, pads, leads, etc. R_r can have contributions from temperature-dependent resistances, e.g. from the pads and the leads to

the strip, but also constant parts from the experimental wiring. The constant resistance from the experimental wiring is usually much smaller in value compared to the temperature-dependent parts, which is why it has been neglected in the above calculation. Naturally temperature-dependence other than activated behavior is also possible.

In Fig. 4.17 it can be seen that R_s saturates at some point for high values at low temperatures. This saturation is accompanied by an increase in the phase of the Lock-in measurement, which is shown in Fig. 4.17 (c). At lowest temperature the phase is 90°, meaning the measured signal is completely out of phase. This hints towards some kind of parasitic capacity between the wires connecting the measurement devices with the sample. Since in this case sample resistance and capacitance are both parallel, the capacitance becomes increasingly important when the resistance of the sample increases and at some point completely dominates the signal. To reduce this influence as much as possible, a low lock-in frequency is chosen, typically in the range of a few Hz. The experimental wiring is also chosen to be less susceptible to parasitic capacities by using twisted-pair cables and coaxial cables with BNC-connectors. All connections are shielded and the experimental devices, as well as the cryostat are grounded to the same potential. With this, high absolute values of resistances can be measured, to above 400 MΩ, which is in general enough to characterize the temperature-dependence of the insulating samples in this work. The activation behavior of the samples is then analyzed along the linear regime in the Arrhenius-plot (see Fig. 4.17 (b)), which corresponds to a lock-in phase change below about 10° (shaded area in Fig. 4.17 (c)).

5. Experimental application and feasibility

In this chapter the general idea of the experiment is detailed and its feasibility and performance are investigated. This is done by simulations using CST Microwave Studio [182] and by demonstration measurements, in order to show the applicability of previously shown techniques. First the practical application of the method will be detailed. Then simulations will be shown as a proof of concept as well as some demonstration experiments on known dielectric samples.

Part of the data in the following chapter has been published in the following publication:
Nikolaj Gabriel Ebensperger, Benedikt Ferdinand, Dieter Koelle, Reinhold Kleiner, Martin Dressel and Marc Scheffler.
"Characterizing dielectric properties of ultra-thin films using superconducting coplanar microwave resonators"
Rev. Sci. Instrum., **90**, 114701 (2019) [1]

5.1. Idea of the experiment

The goal of this work is to find ε of thin-film samples in the GHz-regime. Here, many materials show peculiar properties at low temperatures, especially indium oxide in the mK-regime [8, 28, 33, 39, 42]. In the GHz-regime the energies of the probing electromagnetic waves are still quite low, i.e. µeV,

meaning that it can be assumed to still be in the static limit. The GHz-frequencies also allow to go to ultra low cryogenic temperatures in the mK-regime, as the energies of the microwaves can be chosen to be lower then characteristic thermal energies of mK.

The general idea of the experiment is to take a coplanar waveguide resonator with known resonance characteristics such as frequency ν_0 and quality factor Q. Then, in a second step, a dielectric sample is added into the system with its material properties acting as perturbation to the resonator characteristics [1, 183]. This leads to a measurable change in ν_0 and Q. Since superconducting resonators made of Nb on a very low-loss substrate such as Al_2O_3 [170, 171, 184–186] usually have very high Q in the order of $1 \times 10^4 - 1 \times 10^5$ [1, 4, 136], their precision in ν_0 is exceptionally high and in turn allow for sensitive measurements of the resonance frequency shift.

The sample is added by deposition directly on top of the CPW resonator. This allows for simple creation of samples without any intermediate steps, which might alter sample properties. By adding a patterned photo-resist layer beforehand, the samples can be shaped at will with lift-off procedures. This can be utilized to form additional structures of the samples, which will also be done in this work, e.g. for Hall-bar structures.

Since the samples that can be investigated with this method are very thin, in the few nm to tens of nm-regime, thickness measurements are usually performed using microscopic measurement methods, such as profilometer or atomic force microscopy (AFM). A three dimensional visualization of a topographical map of an empty CPW and a CPW with deposited sample is shown in Fig. 5.1. The typical magnitudes are shown schematically in the figure and include the center conductor width S and its distance to ground planes W, which have typical sizes in the range of µm to tens of µm. The metallization thickness is usually in the range of several 100 nm, in this work it is always about 300 nm.

With the addition of a dielectric sample the effective dielectric constant of the CPW is changed and additional losses are introduced. This changes

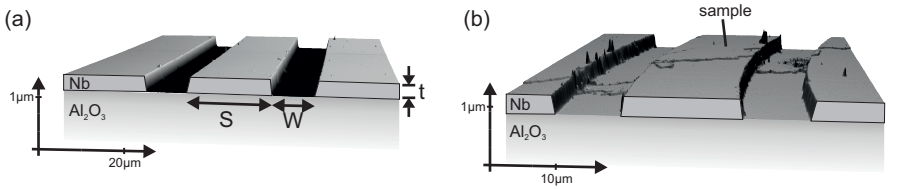

Fig. 5.1.: (a) Three dimensional visualization of a topography map of an empty CPW, measured with AFM. Schematically characteristic quantities in the crosssection are included showing typical geometry. Vertical dimensions are enhanced for clarity. (b) 3D visualization of a topography map of a CPW with partially covering thin-film sample. The sample thickness is much smaller than the metallization thickness.

the resonance frequency ν_0 of our resonator and its quality factor Q. A demonstration of this is shown in Fig. 5.2. The resonance shifts to lower frequencies and gets broader.

This procedure can be done for a large variety of dielectric samples in a wide frequency and temperature range. Since superconducting Nb is used as conductor for the resonator, temperature ranges from about $8 - 9\,\mathrm{K}$ down to mK can be accessed. With microwave resonators frequencies up to 50 GHz can possibly be accessed [137], typically in this work the dielectric properties of the sample materials are investigated up to about 30 GHz.

5.2. Probing thin-film samples with resonator-chips

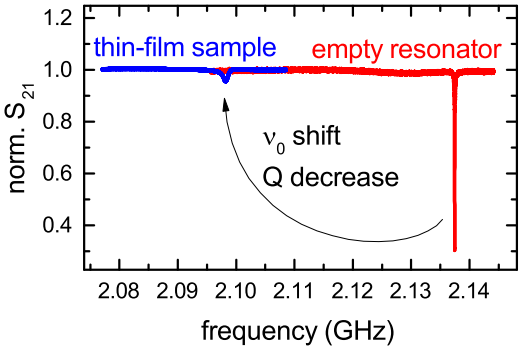

Fig. 5.2.: Transmission spectrum of a resonance in the case of an empty resonator and under the influence of a thin-film sample. The resonance shifts and broadens.

5.2.1. Resonator-chips

For practical applications, resonator chips have to be designed, which fit the experimental conditions but also the spatial limitations of the measurement setups. Usually the wavelengths of resonances at GHz-frequencies and in resonators with Al_2O_3 substrate are somewhere in the area of cm. This has to fit in a spatial area which is in the range of about $1\,cm^2$, which is the typical accessible space in the cryogenic setups. In order to be able to additionally fit multiple resonators in this space, they are meandered and coupled to a common feedline. Fig. 5.3 (a) shows a schematic representation of such meandered $\lambda/4$-resonator with parallel coupling to a feedline. (b) shows an example of a complete resonator-chip. Its total dimensions are $10 \times 12\,mm$ and it carries eight different resonators. The common feedline crosses the total length of the resonator-chip in the center and multiplexes the resonators, allowing for read out of all resonators with a single frequency sweep.

Since the resonators are independent on each other, they can each have different lengths and dimensions. In the example of Fig. 5.3 (b) the resonators

have different values for S and W and varying lengths, giving them fundamentals in the range of $2 - 8\,\mathrm{GHz}$. On this chip in particular the resonators are designed in the way that there are always two resonators of about the same length at either side of the feedline. They are only slightly different in length (few µm) for them to not have resonances at exactly the same but at slightly different frequencies to still be differentiable. The advantage of having pairs of very similar resonators is to have in-situ reference measurements. By covering only one half of the resonators with the sample, the other resonators are left empty and ensure the nominal performance of the resonator-chip even after the additional step of sample deposition. These type of dual resonator-chips are used frequently in this work, however resonator-chips, where all eight resonators have different lengths and frequencies are also regularly employed.

The resonators in Fig. 5.3 (b) also have different values of S and W. Since this resonator-chip is applied as a probe for thin-films, the filling factor q plays an important role in the sensitivity to the sample properties, see equation (4.28) and section 5.3.3. For thin-films in the range of few 10 nm thickness, the filling factors have magnitudes in the range of 1×10^{-3}. By varying S and especially W of the resonators for a given thin-film thickness, q can be varied. This gives a direct handle on the sensitivity of the resonator to the sample. Sometimes very high sensitivity is wanted, meaning W should be quite small, but sometimes also less sensitivity is desired, in particular when the losses in the sample are strong and start to suppress resonator oscillation. Here a larger W is employed. By having multiple different resonators with varying S and W on the same chip, the chip is more versatile to a multitude of samples.

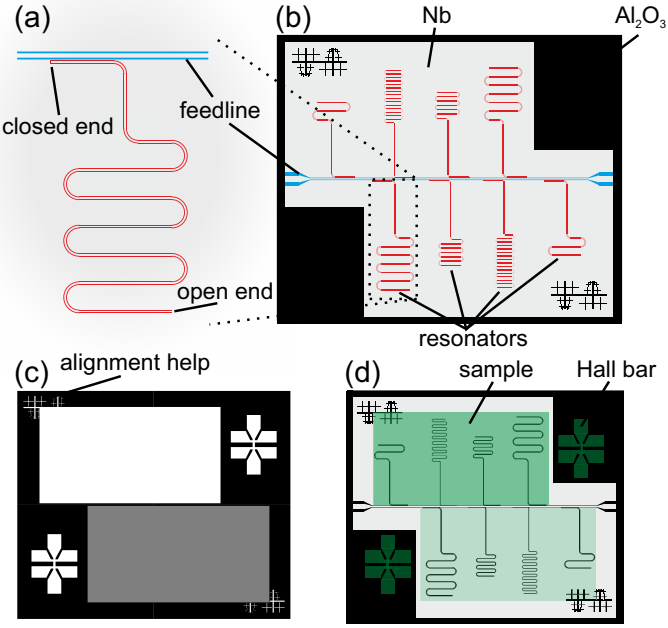

Fig. 5.3.: Mask design for a resonator-chip. (a) Single resonator coupled to a feedline. Parts have been shortened for clarity. (b) Design of the whole resonator-chip. The different parts are marked in the figure, resonators are shown in red, the common feedline in blue. The total dimensions of the resonator-chip are $10 \times 12\,\mathrm{mm}$. (c) Mask for sample deposition. White parts are transparent, this is where the sample will remain after lift-off. Grey can either be transparent or opaque, depending on desired sample distribution. (d) Sample (green) deposited on the resonator-chip.

5.2.2. Sample design

Sample deposition is preceded by a step which allows for shaping of the sample. In this step the resonator-chip is covered by photoresist. After performing optical lithography and developing the photoresist, the photoresist only exists in locations where the sample is not supposed to be deposited. At locations where the photoresist is gone, the sample accumulates directly on the resonator-chip as desired.

In order to deposit the sample only on the resonators and e.g. not on the areas necessary for microwave contacting at the ends of the feedline, a photo lithography mask is used. An example is shown in Fig. 5.3 (c). White parts are transparent. In these areas the sample will be deposited. Depending on the desired application, the sample can be deposited on both sides of the resonator-chip, or only on one (gray area in the figure is either completely transparent or opaque). After sample deposition onto the partially covered resonator-chip and subsequent lift-off of the photoresist and sample, the resonator is covered as shown in Fig. 5.3 (d).

In order to cover individual resonators only partially and not along their whole length, it is also possible to cover the resonators partially before sample deposition. Here Fixogum [187], a glue-like substance that also lifts off in the lift-off process, can be applied to the resonator-chip. Areas covered by this glue then are sample-free. This allows for the further reduction of the influence of losses in the sample on the resonator performance. Since only parts of the resonator are covered, the sample has less influence on the microwave properties as a whole. This however complicates the analysis of the data, as shown in section 4.5.

5.2.3. Mounting of resonator-chips

After deposition of the sample onto the chip, the resonator-chip is mounted into a box in order to contact microwave connectors to the feedline. A schematic model of such a box is featured in Fig. 5.4 (a) and a photo of the

mounted box on the cold-finger in (b). The box is made of brass and consists

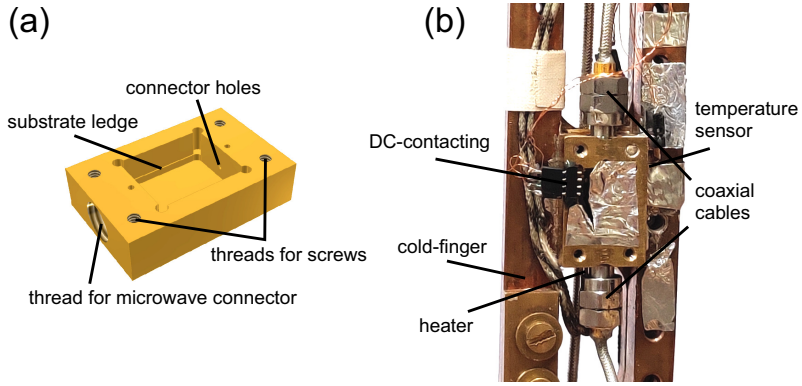

Fig. 5.4.: (a) Schematic model of a brass box used for mounting. It consists of a cavity for the resonator-chip and feedthroughs with threadings for connectors. (b) Photo of a brass box mounted to the cold-finger of the dilution refrigerator with attached connectors for DC-measurements and temperature sensing.

of a cavity for the resonator-chip and several threads for microwave connectors and screws. The chip is placed in the cavity and sits on the substrate ledge. At the bottom of the chip the brass box is closed and typically the top is also closed with aluminum tape, meaning that the CPWs can be assumed conductor-backed.

The microwave connectors are screwed into the threads to either side and their inner-conductor endings are pushed onto the endings of the feedline. For better contact these endings have been increased in size, to allow for a large contacting area (see Fig. 5.3 (b)). The connection of the coaxial connector to the feedline is then additionally improved with silver-paste.

This assembly is done ex-situ. The whole box with the chip is afterwards screwed to the cold-finger of the experimental setup and connected to coaxial cables. Any additional DC-connectors can be glued to the box and short

wires are used to connect the external circuitry to the sample directly (DC-contacting in Fig. 5.4 (b)).

5.3. Simulations

Simulations have been regularly employed to optimize resonator geometry as well as to validate analysis procedures. For this the commercial simulation software CST Microwave Studio [182] has been used. Here, various models fitting the investigated problems and challenges have been designed in a CAD environment, e.g. models shown in Fig. 4.4, and microwave parameters such as the transmission coefficient S_{21} have been evaluated. The analysis is done analogously to experimental measurements, although here an absolute Lorentzian fit to the absolute value of the transmission is sufficient. From this Q and the insertion loss can be acquired.

5.3.1. Resonator optimization

In order to optimize resonator performance for the experimental application, the coupling of the resonator to the feedline has been simulated in dependence of several geometry parameters. Since the resonators are in-plane with parallel coupling to the feedline, all parameters are situated in the lateral dimension of the CPW. Especially the length of the coupling arm l_c and the distance of the coupling arm to the feedline g_c are the most important parameters, see Fig. 5.5 (a). The larger l_c, the more of the resonator is parallel to the feedline and is directly excited. The closer the resonator is to the feedline, i.e. the smaller g_c, the larger is the magnitude of the electromagnetic fields of the feedline at the coupling arm, compare Fig. 4.3 in section 4.2, and consequently the coupling is larger. Varying both g_c and l_c and looking at both Q and the insertion loss A leads to the dependence shown in Fig. 5.5 (b) and (c). Here, a resonator with $S = 24\,\mu\text{m}$ and $W = 10\,\mu\text{m}$ has been simulated with a perfect conductor on a lossy Al_2O_3 substrate (limiting Q) with $\varepsilon_1 \approx 10$

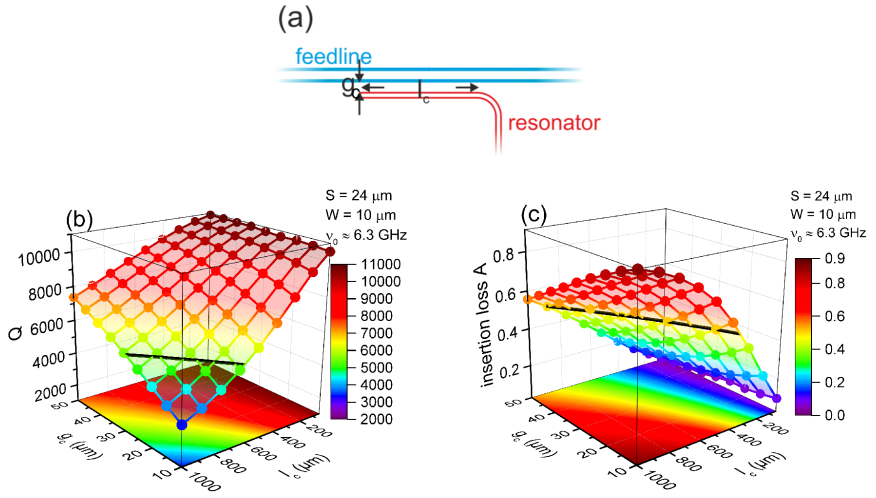

Fig. 5.5.: (a) Schematic depiction of a resonator arm coupled to a feedline with coupling parameters shown. (b,c) Simulation data for (b) Q and (c) A as a function of l_c and g_c. Smaller Q/Larger A means stronger coupling. The black line indicates critical coupling. (b,c) is also shown in [1].

($\varepsilon_{\text{eff}} \approx 5.5$). Q decreases with stronger coupling (larger l_c and smaller g_c), whereas A increases. This matches the theoretical prediction of CPW coupling from section 4.2.1, especially Fig. 4.6. The black lines in Fig. 5.5 (b) and (c) show the values of critical coupling [136], where both Q and A are half their maximum value. For Q values above the black line the resonator is undercoupled and below the line it is overcoupled (for A this is reversed, above the line being the overcoupled regime).

It is expected that some samples can induce significant losses to the resonators. In this case if A is low, resonator oscillation can quickly be suppressed completely. For high A however, an oscillation, although weaker, might still be possible. It is therefore of interest to still stay in the undercoupled regime,

so Q is predominantly dependent on the intrinsic resonator properties, while having a large enough coupling for A to be large. From Fig. 5.5 (b) and (c) reasonable values for g_c and l_c have been found as $l_c = 400\,\mu m$ and $g_c = 10\,\mu m$ for experimental resonator-chips.

5.3.2. Sensitivity to thin-film samples

The samples that should be able to be investigated with the presented method are thin-films with their thickness ranging in the regime of several nm up to about 100 nm [10, 11, 28, 32]. It is therefore on the one hand necessary to establish that the resonators are sensitive enough to detect weak influences of thin-film samples. On the other hand, it is necessary to show that the analysis methods using conformal mapping (section 4.3) are applicable. In order to demonstrate this simulations have been performed, with a CPW $\lambda/4$-resonator with parallel coupling to a feedline and an additional thin-film layer on top. The metallization thickness of the CPW is non-zero and has been kept at 300 nm, roughly corresponding to experimental CPWs. For S and W standard values of $S = 24\,\mu m$ and $W = 10\,\mu m$ have been used.

The crucial parameters of the thin-film sample are the complex dielectric constant ε with its real and imaginary values ε_1 and ε_2 and the film-thickness d. The resonance frequency ν_0 of the simulated resonator model as a function of both ε_1 and d is shown in Fig. 5.6 (a). Here ε_1 has been varied between $\varepsilon_1 = 1$ (vacuum) and $\varepsilon_1 = 1000$, and d in the range between 5 nm and 300 nm (up to the metallization thickness), which roughly corresponds to the expected limits in experimental applications. ν_0 is expected to decrease with an increase of both ε_1 and d. It is directly related with equation (4.1) to the effective dielectric constant ε_{eff} of the CPW, which in turn is directly affected by ε_1 of the sample via (4.27) from conformal mapping theory (section 4.3). d has influence on the filling factor q of the sample (equation (4.28)), which enhances the contribution of the sample to ε_{eff} (equation (4.27)).

Fig. 5.6 (a) shows that for the experimentally important region of relatively small values in d and ε_1 the simulated data fits the theoretical prediction quite well. Only for highest values of d and ε_1 small deviations from theory arise, which are less then a few percent. In the crucial regime at $d < 50\,\mathrm{nm}$ and values of ε_1 in the range of up to hundreds, corresponding to predicted values of experimental thin-film data, theory is well matched by the simulation data. In this regime the applicability of conformal mapping technique for the correlation of resonator parameters to the material parameters of the thin-film samples is given.

When going to larger film-thicknesses, larger than the metallization thickness, ν_0 continues to shift to lower values. This is seen in Fig. 5.6 (b). There is however a saturation of ν_0 towards even larger d. The point at which saturation sets in roughly corresponds in magnitude to the size of typical geometry parameters, such as S and W, here in the order of tens of µm. From this point on, larger thicker films can be considered bulk. When comparing theory to the simulation data, a good fit is possible only for slightly larger assumed ε_1 of the film compared to the set value in simulation (compare legends in Fig. 5.6 (b)). This deviation however will be neglected for the following work, since it occurs only for bulk-like samples, which are not the focus of the following experiments. Additionally for bulk samples other issues arise, such as the "air-gap"-issue [1, 2].

The third parameter that is important to investigate for the applicability of the method is the influence of the imaginary part of the dielectric constant ε_2. ε_2 predominantly enhances the losses in the system, as shown in section 4.4. This goes hand in hand with a reduction of the quality factor Q of the resonators and even suppresses resonances completely for very large losses. This can already be seen in the raw spectrum of the simulation in the inset of Fig. 5.6 (c). The main panel shows the *calculated* ε_2 from simulation data as a function of *set* ε_2. Note, that set ε_2 has not been given directly but rather $\tan\delta$ due to software limitations in CST Microwave Studio, but here it is $\tan\delta = \varepsilon_2$, since ε_1 is set to $\varepsilon_1 = 1$ (c.f. equation (4.48)). The simulation

data fits theory reasonably well. This means that also for the calculation of ε_2 conformal mapping and the previously mentioned procedure is applicable.

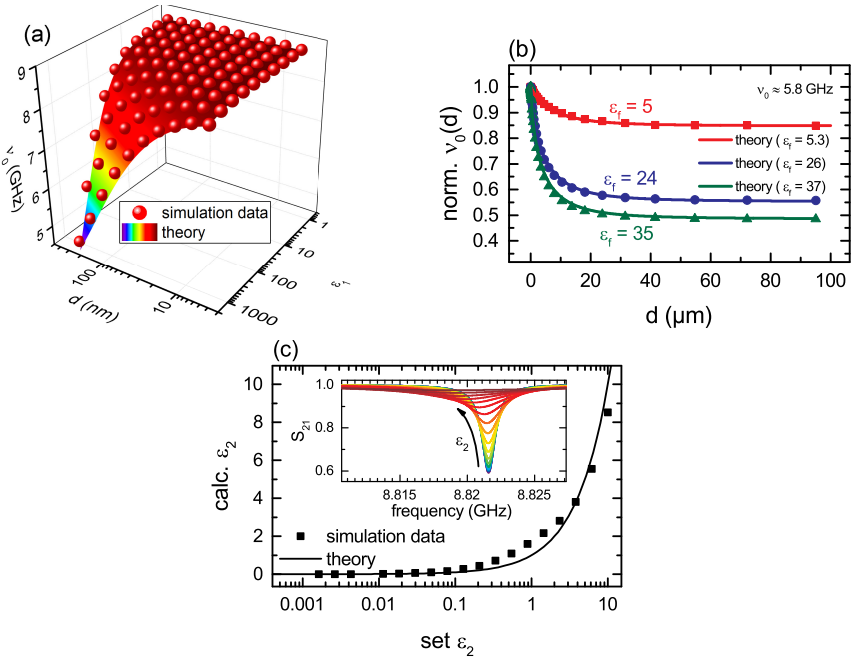

Fig. 5.6.: (a) ν_0 as a function of d and ε_1 for simulation data and theory from conformal mapping technique. The simulation replicates theory quite well. (b) Normalized ν_0 as a function of d for three different set values of ε_1. At large d, ν_0 saturates and the sample can be considered bulk [1]. (c) Calculated ε_2 as a function of set ε_2. Simulation data fits theory reasonably well. The inset shows raw spectra.

5.3.3. Role of sample location

In Fig. 4.3 (a) and 4.8 (a) it can be seen, that the finite metallization thickness of the conductor layer leads to an enhancement of the E-field between center conductor and ground planes, where the E-field is homogeneous. The resonator therefore has the highest field density in this gap and is most sensitive to properties of a thin-film sample in the space between center conductor and ground planes.

In order to compare the contributions from ε of the sample in the gap and on top of the conductor, simulations have been performed. The resulting resonance shifts are shown in Fig. 5.7. The dimensions of the simulation model were chosen to be similar to experimental geometry ($S = 24\,\mu\text{m}$, $W = 10\,\mu\text{m}$, $t = 0.3\,\mu\text{m}$, $d_s = 50\,\text{nm}$). The dielectric constant of the sample in the gap ε_g and on the conductor ε_c have been varied independently of each other.

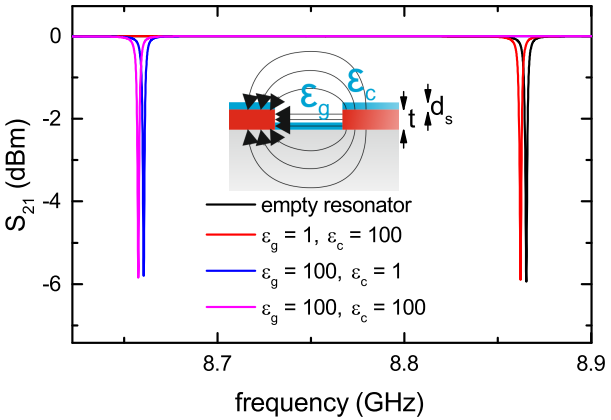

Fig. 5.7.: Spectra of a simulated resonator with a thin-film sample. The real part of ε has been changed individually depending on sample location, whether it is in the gap between center conductor and ground planes ε_g or on top of the conductor ε_c, see inset.

Increasing either ε_c or ε_g from 1 (vacuum) to 100 shifts the resonance to lower frequencies (the value of $\varepsilon_1 = 100$ here is taken as an order of magnitude value since it expected to be a typical value for a thin-film sample with high disorder [33, 188]). This shift however, is much larger when changing ε_g compared to changing ε_c with a shift of about 200 MHz compared to about 3 MHz. When changing both $\varepsilon_g = \varepsilon_c = 100$, meaning a fully covered resonator, both shifts add up.

The shift evoked by the film on top of the conductor is only about 1 % of the shift evoked by the sample in the gap. The properties of the sample on top the conductor only have minor influence. Upon thin-film deposition it might be possible that some differences in film-properties arise depending on whether it is deposited on the substrate or on the conductor. This however, is expected to only have little influence on the measured microwave data. Since the sample in the gap has predominant influence on the microwave propagation, any deviation of the dielectric constant or the film thickness or properties on top of the conductor compared to the sample on the substrate has negligibly small influence. Therefore, in the following no particular distinction between the film in the gaps compared to films on the conductor is performed.

This is of interest in particular because it could be possible that long-range Coulomb interactions are screened by nearby metallic interfaces [189–191]. Especially Ovadyahu [191] shows, that the spatial range of long-range Coulomb interactions in indium oxide can effectively be limited by a metallic electrode close to the indium oxide film. In this work, since the sample is deposited not only on the substrate but also on the metallic/superconducting Nb layer, the sample might also be screened on top of the conductor. The above simulations show however, that ε_c of the sample on the conductor only has marginally weak influence and the resonance properties are primarily influenced by ε_g. Therefore only the unscreened sample on the substrate but not on the conductor is investigated. Any possible screening of Coulomb interactions due to the metallic layer is only negligibly represented in the acquired data and can therefore be ignored.

5.3.4. Partially covering samples

In order to tune the magnitude of the sample influence on the resonator properties, e.g. in order to reduce induced losses and maintain resonator oscillation, samples can also be deposited partly of a single resonator. The calculation of the derived properties, i.e. ε, is then done by solving the frequency-dependent Helmholtz equation and finding the fitting resonance frequency for given ε-distribution, as has been shown in section 4.5. In order to validate this approach, simulations have been performed.

The simulation model with the sample covering only about half of the resonator is shown in Fig. 5.8 (a). Simulation parameters have again been

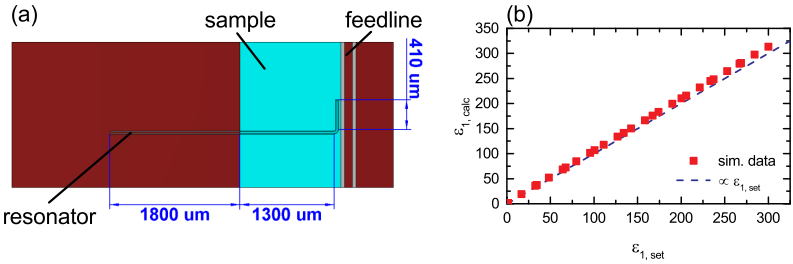

Fig. 5.8.: (a) Simulation model of a $\lambda/4$-resonator with parallel coupling to a feedline. The resonator is covered by a sample to about one half. (b) Calculated values $\varepsilon_{1,\mathrm{calc}}$ following the procedure in section 4.5 as a function of $\varepsilon_{1,\mathrm{set}}$ set in the simulation.

chosen close to possible experimental values ($S = 24\,\mu\mathrm{m}$, $W = 10\,\mu\mathrm{m}$, $t = 0.3\,\mu\mathrm{m}$ and $d = 0.1\,\mu\mathrm{m}$). Upon increasing $\varepsilon_{1,\mathrm{set}}$ set in the simulation, the resonances shift accordingly, allowing for the calculation of $\varepsilon_{1,\mathrm{calc}}$ from the resulting simulation data. The found values of $\varepsilon_{1,\mathrm{calc}}$ for a $\varepsilon_{1,\mathrm{set}}$-sweep from 1 to 300 are shown in Fig. 5.8 (b). A straight line $\propto \varepsilon_{1,\mathrm{set}}$ has been included representing theory. The calculated values for $\varepsilon_{1,\mathrm{calc}}$ show that the values match well to the set values $\varepsilon_{1,\mathrm{set}}$. The procedure described in section 4.5 therefore is suitable to find ε of samples covering only part of a resonator.

This can be extended not only to covering half a resonator but also much less, e.g. covering only one meander etc. In the following work this will therefore be used to acquire some of the ε data.

5.4. Sample thickness measurements

Knowing the thickness of the thin-film sample is of pivotal importance when an exact determination of ε_1 is desired. Since the thickness d goes in directly to the filling factor q, equation (4.28) (with (4.22)), it also goes in to the calculation of ε_1 of the layer directly, equation (4.30). This in turn leads to stronger influence of thicker samples on the CPW properties, as shown with simulations in section 5.3.2. It is therefore important to characterize the sample thickness precisely.

This is performed with atomic force microscopy (AFM), giving nm-resolution in lateral dimensions and profile. An exemplary AFM characterization measurement is shown in Fig. 5.9. Here, two layers of MgF_2 have been deposited on a resonator-chip, with the image in (a) showing the intersection of two boundaries of the individual layers on the Al_2O_3-substrate. They have been deposited with the second layer being deposited on the first one (the numbering "2" and "3" correspond to the films thickness changes in the coming analysis of ε of these films in section 5.6.1). The sharp boundaries are created by lift-off of glue or photo-resist after deposition of the thin-films (compare section 5.2.2 and Fig. 5.3).

From such an AFM-scan the thickness of the individual layers can be extracted. This can be done in two ways, one of them being the extraction from topographical profiles. This is done at the film boundaries, shown in (a) with the white dashed line, giving the profile in Fig. 5.9 (b). From this, the steps from substrate to layer and from one layer to the next can be seen and the difference in height can be found with which d is established.

A second way to determine layer thickness from AFM-scans is to look at the histograms showing height distribution. This is shown in Fig. 5.9 (c). Here, several peaks are visible, each corresponding to a different terrace-level, the peak at 0 nm being the substrate-floor. Each following peak corresponds to one layer and the last to their combined thickness. From the center peak location the layer thickness can directly be found.

This is the typical way the thin-film sample-thicknesses are found in this work. Another possibility is to use a Dektak profilometer, with which profiles such as in Fig. 5.9 (b) can also directly be measured.

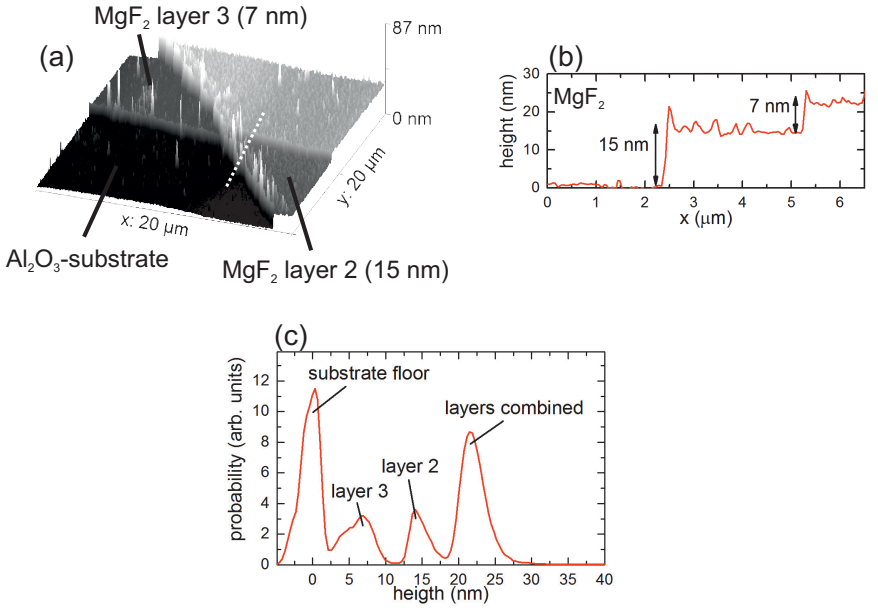

Fig. 5.9.: (a) Three-dimensional visualization of an AFM-scan of two MgF_2-layers subsequently deposited on Al_2O_3-substrate. The boundaries are created by subsequent lift-off. (b) Profile of the AFM-scan at the dashed line in (a). From the two steps the layer-thicknesses can be found. (c) Histogram of the height-distribution of the scan in (a). From the peaks in the distribution the layer-thicknesses can be found.

5.4.1. Uncertainty in sample thickness as an error source

Since precise determination of the sample thickness is crucial, any uncertainties are major contributions to errors in the determination of ε. Via the filling factor q, any error in the determination of d directly translates to an error in ε_1.

The determination of the proportionality between errors in d and errors in ε_1 is not trivial to do analytically. Especially when taking into account further corrections such as the correction for metallization thickness of the CPW (section 4.3.1), the derivative $\frac{\partial \varepsilon_1}{\partial d}$ gets very complex. However, numerically this can be done conveniently and evaluated at parameters corresponding to experimental geometry ($S = 24\,\mu\text{m}$, $W = 10\,\mu\text{m}$, $t = 0.3\,\mu\text{m}$ and $\nu_0 \approx 2\,\text{GHz}$). This is shown in Fig. 5.10 (a) for a number of values of d. For a relative

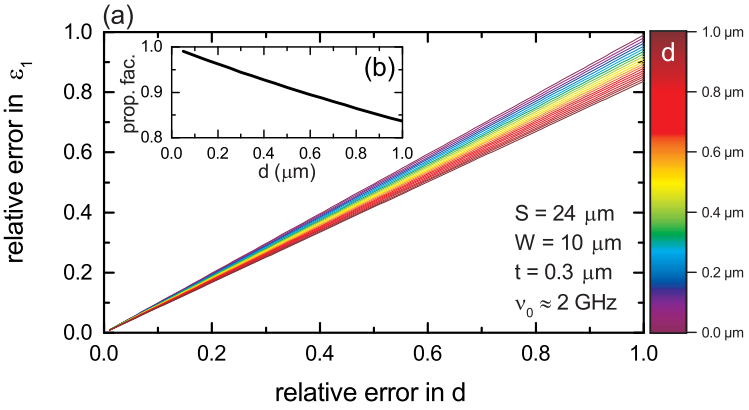

Fig. 5.10.: (a) Relative error in ε_1 as a function of the relative error in film-thickness d according conformal mapping technique (section 4.3). The slope of the linear dependence is shown in (b). For very thick films the influence of Δd on the calculation of ε_1 decreases slightly.

error in d ranging from $\Delta d = 0$ (absolute precision) to $\Delta d = 1$ (error in the range of d), the relative error in ε_1 increases linearly. For very thin films

the slope of the proportionality reaches ≈ 1. For larger film-thicknesses this decreases to an extent due to less concentration of the E-field in the thin-film, meaning that here Δd has less of an impact on the error in ε_1. The slope of the proportionality between Δd and $\Delta\varepsilon_1$ is shown in Fig. 5.10 (b). Usually the thin-film samples in this work have thickness values in to order of several 10 nm. In this regime it is therefore $\Delta\varepsilon_1 \propto \Delta d$, and knowledge about d is particularly important.

5.5. Properties of empty resonators

As detailed in section 5.1, measurements on thin-films are performed by comparing a resonator under the influence of the sample to the very same resonator without the sample. This necessitates comprehensive knowledge of the microwave properties of the empty resonator without sample (before deposition). On the one hand, the resonances of each individual resonator within the resonator-chip, with its fundamental and their harmonics, have to be measured precisely. Here resonance frequency ν_0 as well as the respective quality factors Q are the main quantities. On the other hand, it is also important to know how these quantities behave in varying temperature, since temperature-dependent determination of sample parameters such as $\varepsilon(T)$ are desired and therefore good reference data are needed. However, already the CPW resonator itself with its superconducting Nb-layer shows strong temperature-dependence, stemming from the temperature-dependent penetration depth (equation (4.75)), detailed in section 4.6.

A typical resonator-chip, as detailed in section 5.2.1 (Fig. 5.3), typically shows a spectrum as exemplary depicted in Fig. 5.11. (a) displays the transmission with the microwave parameter S_{21} up to 20 GHz at about 2 K. Many resonances are seen, belonging to different resonators on the same resonator-chip. Each color corresponds to an individual resonator with its fundamental at a few GHz and its harmonics at odd multiples. The enveloping

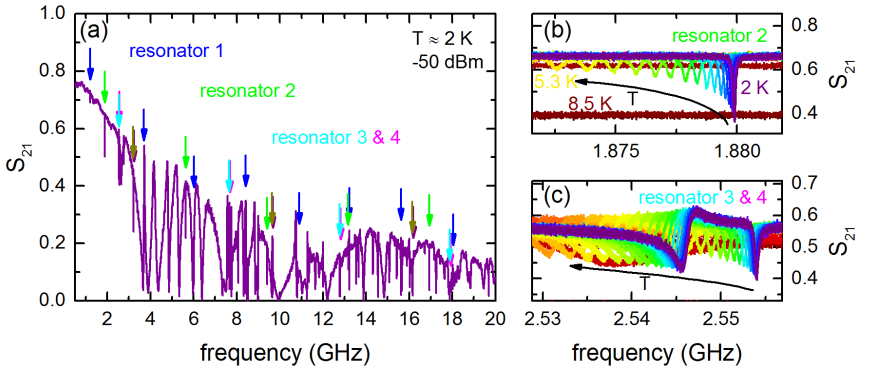

Fig. 5.11.: (a) Spectrum of a resonator-chip with its transmission parameter S_{21} up to 20 GHz measured at 2 K. Resonances of four different resonators are found (marked with colored arrows). (b) Fundamental resonance of a resonator at about 1.88 GHz for temperatures up to 8.5 K. The resonance shifts stem from $\lambda_L(T)$. (c) Fundamentals of two resonators. Both have similar geometry and frequency.

downtrend of S_{21} with increasing frequency originates from the attenuation in the cables of the experimental setup, since both skin depth and therefore resistance in the microwave regime increase [56]. Some of the resonances of the resonators in Fig. 5.11 (a) each form a pair with another resonator at roughly the same resonance frequency, leading to double-dips in the spectrum (e.g. resonators 3 & 4).

Fig. 5.11 (b) and (c) detail resonances for various temperatures up to 8.5 K. The resonances shift to lower frequency and their quality factor Q decreases continuously, which is due to the impedance of the CPW increasing with $\lambda_L(T)$, as detailed in section 4.6. Above T_c, here about $8.2 - 8.3$ K, superconductivity in Nb is lost, resonances vanish and the transmission decreases (red data in (b) and (c)). By fitting the resonances, following the procedure in section 4.8, $Q(T)$ and $\nu_0(T)$ can be extracted. Fig. 5.12 displays $Q(T)$ and $\nu_0(T)$ for several different resonators. In (a), $Q(T)$ is seen

in a temperature-range of $2 - 6\,\mathrm{K}$. Along the whole temperature range Q decreases with higher T, indicating increasing losses in the resonator with larger temperature. The exact shape of $Q(T)$ is strongly dependent on the quality of the Nb in the resonator. Even small amounts of impurities in the conducting Nb layer can have major impact on the performance of the resonator concerning superconducting transition temperature T_c as well as the maximum Q and its suppression [136].

At $2\,\mathrm{K}$ $Q(T)$ has values mostly above 1×10^4 for low frequencies, whereas for higher frequencies Q decreases. This can be seen in detail when looking at $Q(T = 2\,\mathrm{K})$ shown in Fig. 5.12 (e). With higher frequencies $Q(\nu)$ decreases, which is the typical behavior where $Q \propto 1/\nu$ [136] is expected due to the increase of losses stemming from the frequency-dependent microwave conductivity increasing with frequency [56, 192, 193].

Going to mK-temperatures reveals that $Q(T)$ saturates quickly below $2\,\mathrm{K}$, as seen in Fig. 5.12 (c). Here, two resonances from a resonator shown already in (a) are shown and additional resonances from a resonator of a different resonator-chip. Below about $1\,\mathrm{K}$ a maximum saturated value is reached, which is determined by the Nb quality and the quality of resonator structure. For the latter, the quality of the meander edges of the resonator structure can be a major loss contributor [144]. The conductor losses are represented by the attenuation constant α_c of equation (4.14). Additional losses by the substrate contribute to α_D, although they are very small for empty resonators, since $\tan\delta \ll 1 \times 10^{-6}$ for crystalline Al_2O_3-substrate [170, 171, 184–186]. The sum of all losses then limits the maximum Q, which here is on the order of 1×10^4, similar to comparable microwave resonators at low temperatures [136]. Since loss contributions limit Q, the $1/\nu$-behavior also does not have to apply when comparing individual resonators to each other. However, resonances within an individual resonators (fundamental and harmonics) typically follow this behavior.

Looking at the resonance frequency $\nu_0(T)$ of the resonances, a shift to lower frequencies with the increase in $\lambda_L(T)$ is seen, see Fig. 5.12 (b). Equa-

tion (4.77) can be fitted to the data at temperatures close to T_c, giving the zero-temperature $\lambda_L(T = 0)$ and T_c of the Nb-layer. Typical values of the fits in (b) are in the range $\lambda_L(T = 0) \approx 450 - 550\,\mathrm{nm}$ and $T_c = 7.8 - 8.6\,\mathrm{K}$. $\lambda_L(T = 0)$ seems high compared to the literature value of λ_L of Nb at about 39 nm [176], however the latter value is for bulk-material, whereas here thin-films with thicknesses of $t \approx 300\,\mathrm{nm}$ are used. Additionally, impurities in the Nb-layer quickly increase λ_L even at low concentrations [194]. The values for $\lambda_L(T = 0)$ and T_c are in range of what has been found before [2]. Below about 2 K, $\nu_0(T)$ does not change significantly (change below 1×10^{-4}), see Fig. 5.12 (d), with an even more constant $\nu_0(T)$ below 1 K (below 1×10^{-7}).

5.6. Demonstration measurements

The resonators designed in this work should be able to work as probes for the dielectric properties of thin-film samples. To demonstrate their proper operability and their application to thin-film samples, several measurement on thin-film samples with known properties have been performed.

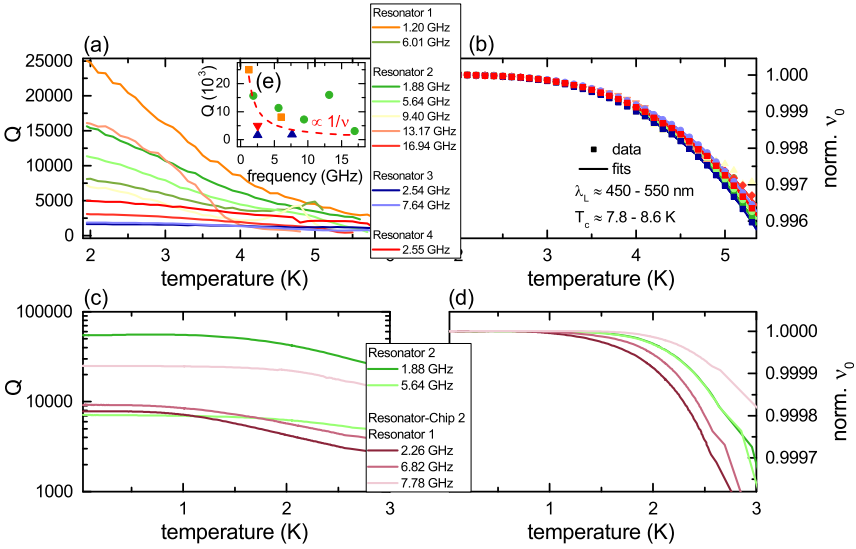

Fig. 5.12.: (a) Quality factor $Q(T)$ as a function of temperature for several resonators with fundamentals and harmonics. Decreasing Q comes from increasing losses with T. (b) Resonance frequency $\nu_0(T)$ as a function of temperature. Increasing $\lambda_L(T)$ shifts $\nu_0(T)$ to lower values. (c) $Q(T)$ in a temperature range down to 30 mK. $Q(T)$ saturates below 1 K. (d) $\nu_0(T)$ down to 30 mK. Below $1 - 2$ K $\nu_0(T)$ is mostly constant. (e) $Q(T = 1.95\,\mathrm{K})$ for all resonances in (a). A $1/\nu$-behavior is roughly seen.

5.6.1. Fully covered resonators

The typical application procedure is to cover the whole resonator with a thin-film sample and to compare resonance characteristics (ν_0, Q) to the ones of the resonance before sample-deposition. In order to demonstrate this procedure and the subsequent analysis, several thin-film samples have been deposited on resonator-chips, covering the resonators completely. The samples used are MgF_2 and SiO_2. Both form amorphous glasses, when depositing thin-films [195–199]. The respective ε_1 for MgF_2 and SiO_2 in the crystalline, bulk form are in the range of $4.9 - 5.5$ for MgF_2 [196–198, 200–203] and about 3.9 for SiO_2 [195, 199]. For MgF_2 the range between 4.9 and 5.5 depends on orientation [202, 203], for thin-films typically values of about 5 are found [196–198]. The films are deposited by thermal evaporation (e-beam evaporation in the case of SiO_2) in a single evaporation process and their thickness is afterwards characterized, as shown in section 5.4.

Several spectra of resonances of the empty resonators and of resonances under the influence of the 50 nm-thick SiO_2 sample are shown in Fig. 5.13 (a) - (d), with fits following section 4.8 for resonance characterization shown in yellow. The resonances under the influence of the sample always shift to lower frequencies when compared to the empty resonators. The quality factor Q also decreases, due to the losses induced by the sample, although not by much, since the losses in SiO_2 are relatively small with $\tan\delta \approx 1 \times 10^{-3} - 1 \times 10^{-4}$ [199, 204]. Since this is of similar order as the reciprocal value of Q of the empty resonator with about $Q \approx 1 \times 10^4$, such small losses can generally not be detected. For this to be possible any contribution $1/Q_{\text{losses}}$ have to be larger than $1/Q_{\text{empty}}$ of the empty resonator (compare equation (4.15)). It is therefore not possible to calculate ε_2 for these demonstration experiments.

Similarly also a resonator with deposited MgF_2-layers has been investigated. Here, the resonator has been covered by a first layer, followed by a second and a third layer, each of which was deposited on top of the preceding layers, adding approximately 13 nm, 15 nm and 7 nm respectively. The latter two

layers ("layer 2" and "layer 3") are shown in the AFM-scan in Fig. 5.9. The corresponding spectra are displayed in Fig. 5.13 (e), the labels corresponding to the sum of the total deposited layer thickness. Again it is seen that the resonance shifts to lower frequencies, yet Q stays mostly constant.

From the resonance-shifts and the Q-factors ε_1 can be calculated, following the procedure in section 4.4. The resulting values are shown in Fig. 5.13 (f) as a function of resonance-frequency up to about 27 GHz (16 GHz for MgF_2). For MgF_2 here only the thinnest sample is shown. No frequency-dependence is seen, which is expected, since compared to excitations and transitions giving rise to frequency-dependent effects in $\varepsilon_1(\omega)$ [56], the probing GHz-frequencies of the resonators used here are small and ε_1 can be considered static resulting in the same ε_1 for all used frequencies.

In Fig. 5.13 (g) the data is displayed as a function of film-thickness d. Additionally to the data plotted in (f), all three film-thicknesses of the measurement on MgF_2 are shown. The literature value of about $4.9 - 5.5$ for MgF_2 and 3.9 for SiO_2 are in the range of the error bars. They are estimated slightly than literature values, which however is due to uncertainty in the thickness of the layers. Since the layers are rather thin, down to about 13 nm in the case of the thinnest MgF_2-sample, the uncertainties weigh rather strong towards the error bars in ε_1, which in turn are linearly proportional to errors in d, as seen in section 5.4.1. An error of about 3 nm in the measurement of the film-thickness per layer is assumed here.

The errors in film thickness are the dominating error source in the calculation of ε_1, as can be seen in Fig. 5.13 (h), where the contributions to the error bars is detailed for a resonance probing MgF_2 at thickest configuration. Additionally to the errors in thickness Δd, also errors stemming from uncertainties in ν_0 determination, $\Delta\nu_0$ are expected. Their magnitude is in the order of the inverse of Q, which here is $Q \approx 1 \times 10^4$. Compared to Δd the contribution of $\Delta\nu_0$ is small, which guarantees the high sensitivity that is needed to probe the thin-films.

The measurements on thin-films of MgF_2 and SiO_2 show, that the measurement method presented in this work has the desired sensitivity to measure ε_1 of films with thicknesses in the nm and ε_1 in the single-digit regime. It should therefore be possible to investigate the dielectric properties of highly disordered thin-films near SIT.

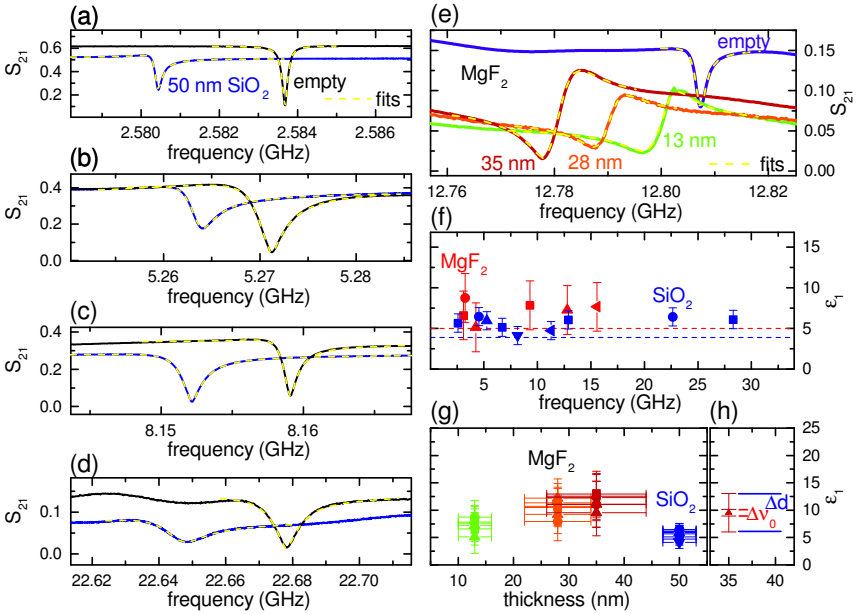

Fig. 5.13.: (a) - (d) Spectra of several resonances under the influence of a 50 nm-thin SiO_2-sample compared to the resonances of the empty resonators. Fits following section 4.8 are shown in yellow. Resonances shift to lower frequencies due to ε_1, yet Q stays mostly constant, since $\tan\delta$ of the sample is small. (e) Spectra of resonances for a MgF_2-sample. Layers were deposited on previous layers with the labels denoting the combined thickness. (f) ε_1 determined from resonance shift and Q, following section 4.4, as a function of frequency. Only the thinnest layer for MgF_2 is shown. (g) ε_1-data as a function of d. (h) ε_1 of one resonance probing the thickest MgF_2 with the different contributions to the error bar detailed.

5.6.2. Partially covered resonators

To test the possibility to find ε_1 of samples covering only parts of the resonators, a test sample has been investigated. Covering only parts of the resonators can have the advantage, that the sample has less influence on the resonator properties and can allow for resonator operation even if the losses are very high. Covering only parts of the individual resonators however, increases the complexity of the problem concerning the analysis and necessitates additional steps detailed in section 4.5. Here the Helmholtz equation for the resonator is solved, giving different E-field distributions for different harmonics.

In Fig. 5.14 (a) the resonator-chip is shown where the resonators have been covered partially by a MgF_2 sample. The partial covering has been achieved by covering the resonators with Fixogum-glue before deposition of the sample. Afterwards this glue was completely removed, leaving only the sample covering the resonators to some extend, which can be seen in (a). Most of the resonators are covered only partially, two of them almost completely and one has been left empty as a reference. The boundary where the sample ends typically has been chosen to be located in a bend of the meander structure, as is shown in Fig. 5.14 (b). Locating this boundary precisely is important since it defines the spatial extend of the sample. Typically this can be done down to a few µm.

Finding the solution of the Helmholtz equation is performed using a linear model of the resonators, as schematically depicted in Fig. 5.14 (c). This is done by comparing the resonator and the sample distribution to the lithography mask from which the resonator-chip has been produced. Here, the dimensions are known exactly and the model can be constructed. The different harmonics of the resonator are affected differently by the sample, since their E-field maxima are located at varying locations.

The resulting calculated ε_1 of the sample film is shown in Fig. 5.14 (d). Two different films with similar spatial distributions have been investigated,

one of them being 120 nm in thickness, the other 300 nm. The symbol shapes correspond to the individual resonators shown in (a) and show the fundamental and harmonics. Most of the measured values of ε_1 fit well to the literature value of about 5 [196–198] (dashed line). The deviations of some of the resonances are similar to the errors detailed in section 5.6.1 comprised of errors in thickness determination of the sample Δd, which is assumed to be about 10 nm here, uncertainty in resonance frequency $\Delta\nu_0$, as well as an additional contribution, the uncertainty in locating the sample boundary (shown in Fig. 5.14 (b)). Since some boundaries are located at some point along long linear parts of the resonators (see e. g. resonators ■ or ◀), locating the boundary is difficult and has to be approximated to some extend. Here the error is in the order of a few 10 µm. To reduce this error, when possible the boundary is chosen to be located in a bend of the meander for better locatability.

With these measurements it has been shown, that calculation of ε_1 is possible, if the resonators are only partially covered by the sample, following the procedure in section 4.5.

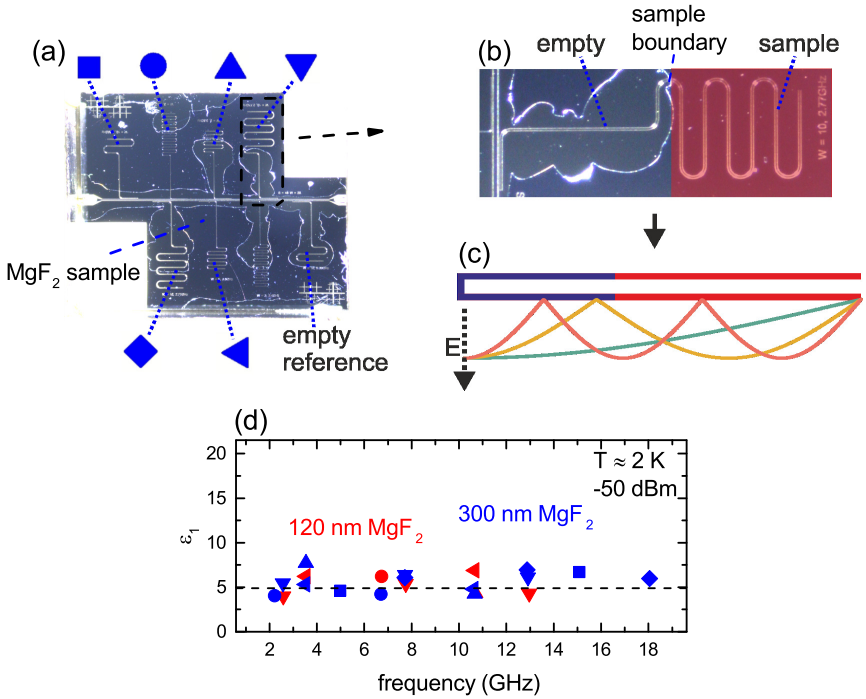

Fig. 5.14.: (a) Top-view on a resonator-chip, covered partially by a MgF_2 sample thin-film (darker color). The eight resonators are covered to varying extend, one being left empty as reference. Symbol shapes correspond to symbols in (d). (b) Single resonator covered partially by the sample. Red depicts the area where the resonator is covered. (c) Schematic linear representation of the resonator with the absolute value of the E-field. Colors represent covered/empty parts. (d) ε_1 as a function of frequency for all resonators. Different symbols correspond to different resonators with fundamentals and their harmonics. The dashed line indicates the literature value of about 5 [196–198].

6. Indium Oxide

6.1. State of the art and open questions

The material of interest in this work is strongly disordered amorphous indium oxide as thin-film samples. Disordered indium oxide consists of a random distribution of the elements indium and oxygen in a glass-like amorphous structure [10, 19]. Of particular importance is, that although they are very disordered and amorphous, the samples are completely homogeneous and do not show any granules or inclusions of e.g. free indium or crystalline In_2O_3 [10]. This has been shown in various diffraction experiments [10, 11, 18–20]. The fundamental phenomena, such as superconductivity or insulation, which will be discussed in the following, are most probably of different origin than for granular materials [15, 106] such as found e.g. in granular aluminum [90, 205]. The low-temperature properties of indium oxide are strongly disorder dependent. For very low disorder, indium oxide behaves like a regular BCS-superconductor [26, 33] with $T_c \sim 3.3\,\mathrm{K}$ [10, 26] (see later Fig. 6.3 (b)). However, when increasing disorder, T_c is suppressed and at some point reaches zero. At this point a prototypical quantum phase transition (QPT) occurs with a transition from a superconductor directly to an insulator without any intermediate metallic phase [8, 33]. While such QPT have also been observed in other materials and compounds [17, 206–210], the peculiar observation in indium oxide is, that global superconductivity is suppressed ($T_c \to 0$), while still the energy gap remains of finite size [8, 28, 32]. Apart from experiments probing the amorphous structure and the composition of amorphous indium

oxide mentioned above, there are only two general types of experimental methods, charge transport measurements and tunneling, that have been applied to disordered indium oxide and only charge transport measurements explicitly in the insulating state [8]. Probing the latter has been a challenging endeavour, as only resistance measurements are possible to certain extent. Here many studies exist probing the resistivity or the sheet resistance as a function of disorder, temperature or magnetic field, which will further be presented later in this section. Other methods, such as investigation of a possible (space-resolved [211]) Meissner-effect in the insulating but potentially local superconducting state or the investigations of possible effects of pairing on the magnetization via SQUID magnetometry have not been conducted for amorphous indium oxide thin-films. In this regard amorphous indium oxide still poses great potential for future experiments.

In highly disordered but still superconducting indium oxide samples, tunneling spectroscopy, in particular spatially resolved STM measurements [28] was performed, giving showing a finite gap (Cooper-pairing in k-space) with real-space localization in absence of global phase coherence. This gap is particularly prominent in tunneling spectra probing the single-particle density of states of weakly superconducting samples [28, 32]. Some seminal work published by Benjamin Sacépé [28] is shown in Fig. 6.1 (a) - (c), where tunneling spectra as a function of voltage and temperature are shown. In particular it can be seen that for two different samples with (a) low disorder and (b) high disorder, the spectra look different, as so-called coherence peaks are lost for highly disordered samples below T_c. As a function of location, shown in (c), this is even more pronounced, as both the coherence peaks and to lesser extend the energy gap vary with location. This shows that, while superconducting pairing happens in k-space, with electrons of opposite spin and momenta pairing to Cooper-pairs, in real-space superconductivity can vary and fluctuate, and can be confined to small areas of superconducting puddles [17].

The tunneling spectra show the normalized differential conductance (called G in Fig. 6.1), meaning dI/dU. Since a normal conducting tip is used [28], the differential conductance reflects the single-particle density of states (DOS) of the unpaired single electrons as a function of tunneling voltage. This means, that for a perfect superconductor a gap in the spectrum is expected, where $G = 0$ up to energies Δ where Cooper-pairs are broken and single-electrons again contribute to transport. The missing states in the regime $< \Delta$ reappear at the location of Δ leading to strong enhancement of G and the conservation of weight. This leads to peaks at the edge of the gap, which are so-called coherence peaks. They appear as a direct consequence of a *coherent* superconducting state, reflecting the diverging DOS at the edge of the energy gap in a globally coherent superconductor. Since measurements are performed at finite temperature and there is already disorder present in the measurements of Fig. 6.1 (a), there are some inter-gap states where $G > 0$ and the coherence peaks are finite in height. Nevertheless, the spectra found for low disorder are reminiscent of a typical BCS-superconductor with coherent phase.

For high disorder the spectra change significantly. Most strikingly, the so-called coherence peaks vanish completely, as can be seen in Fig. 6.1 (b). In direct consequence this means that the single-particle DOS is modified in a way that a pile-up of states at the edges of the gap (as given for the BCS-DOS) is gone, meaning that global phase-coherence is lost and a macroscopic superconducting state is suppressed [8, 28, 33, 46, 47]. This stresses the difference between the BCS-gap evoked by many-body correlations leading to a coherent state and the local pairing gap due to simple binding of two electrons even in the strongly disordered state [33]. For the latter, all paired electrons shift down in energy and are basically removed from participating in transport or tunneling (since the resulting Cooper-pairs are localized), leading to a (local pairing) gap in the DOS close to the Fermi-energy. This reduction of DOS, without reintroducing *coherent* Cooper-pairs to the system, effectively leads to a reduction of the total number states near

the Fermi-energy. Therefore, the spectral weight is not conserved and the so-called coherence peaks vanish [28, 33]. This happens on a local scale and is highly inhomogeneous, as can be seen spatially resolved as a function of location in Fig. 6.1 (c), forming what is sometimes dubbed "superconducting granularity" [8]. Similar superconducting granularity has been found in few other homogeneously disordered materials, e.g. in TiN [17] or NbN [92].

The gap found in tunneling experiments even exists to far above the critical temperature, up to $6 \cdot T_c$ [32] (T_c being defined as the temperature where the total system goes globally superconducting) and the ratio of T_c to the gap deviates strongly from the BCS-value for strong disorder [28]. Recent experiments by Dubouchet, Sacépé et al. [32] using Andreev-spectroscopy, directly show the formation of superconductivity only below T_c, while above T_c no global superconductivity but still a gap is observable, see Fig. 6.1 (d). This gap points towards the existence of Cooper-pairs, which are unable to condense into a macroscopic superconducting state above T_c. They form below characteristic temperatures of about $3 - 4\,\mathrm{K}$, which are typical onset temperatures for pairing [28]. Such pairs are often called "preformed" Cooper-pairs [8, 28, 32].

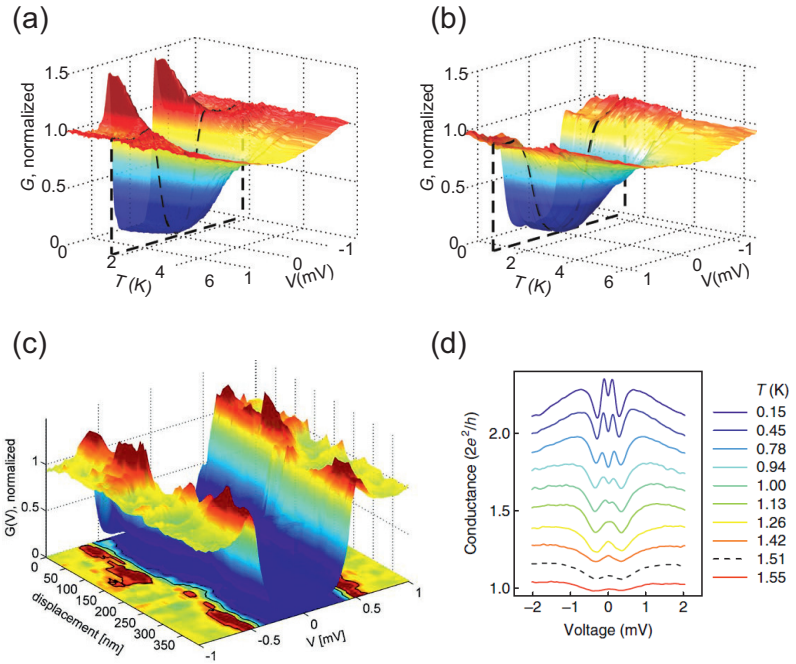

Fig. 6.1.: (a,b) Tunneling spectra as a function of excitation voltage and temperature for a (a) low (b) high disorder sample. Coherence peaks vanish, indicating lost macroscopic superconductivity, while the gap is still present. Even above T_c the gap is found. (c) Similar spectra as a function of location. (d) Andreev-spectroscopy at multiple temperatures, showing superconductivity below T_c and a residual gap above. Panels (a)-(c) from [28] (including suppl. material), panel (d) from [32].

Fig. 6.2 (a) [32] schematically shows a $R(T)$ resistance curve of an indium oxide film with preformed Cooper-pairs. $R(T)$ increases close to T_c, with the slope typically being found to be disorder-dependent, see Fig. 6.2 (b) [28]. In this range, $R(T)$ follows activated behavior [10, 40], which indicates that a hard-gap is found in the conductivity [12, 33] (see section 3.5). In this regime the single-electrons are assumed to pair already to preformed Cooper-pairs leading to a reduction of single-electrons contributing to charge transport [8, 28, 32, 33, 55]. It is also regularly found that maximum resistance values in the shoulder in $R(T)$ close to T_c increase up to a quantum resistance $\hbar/(2e)^2$ shortly before condensation [28, 32].

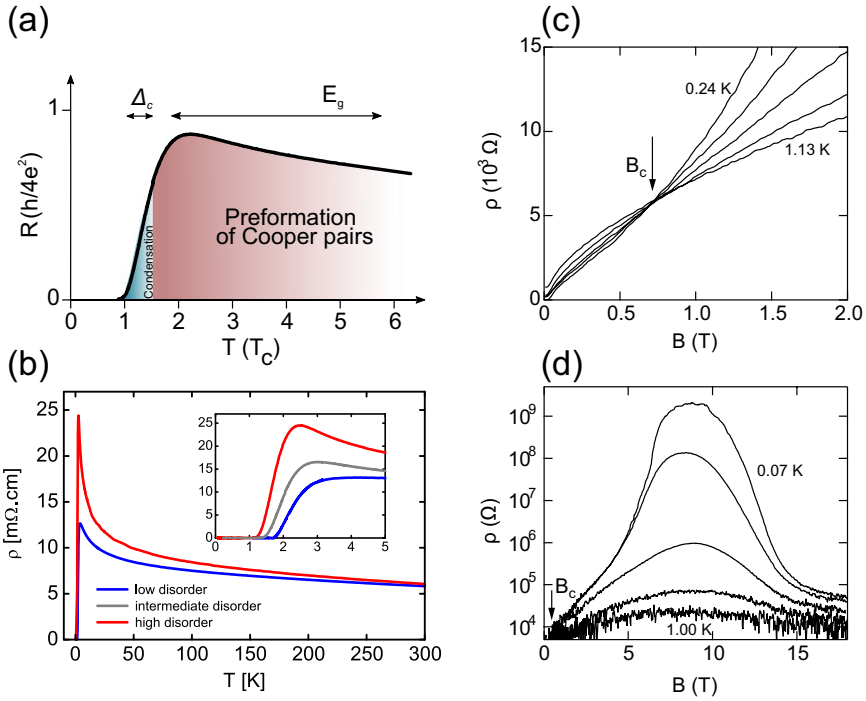

Fig. 6.2.: (a) Schematic resistance of a disordered amorphous indium oxide film in units of the quantum resistance $h/(2e)^2$ as a function of temperature. Cooper-pairs are preformed at $T > T_c$ which condense at $T < T_c$. (b) Measured resistivity data for three indium oxide samples of different disorder. (c) Resistance ρ isotherms as a function of magnetic field B. A crossingpoint is found close to $h/(2e)^2 \approx 6.5\,\mathrm{k\Omega}$, indicating B-driven SIT. (d) Giant magnetoresistance peak at several Tesla. Mechanisms behind this peak are largely unknown [8]. Panel (a) with modifications from [32], panel (b) from [28] (suppl. material), panels (c) and (d) with modifications from [25].

Activated behavior is not only found for weakly superconducting samples but in particular for completely insulating samples [10, 19, 25, 40], meaning that although the system does not get superconducting globally, the charge transport is equally affected by the existence of an energy gap. While in this regime tunneling experiments have not been conducted, defining characteristics of activated behavior are regularly found in transport [10, 11]. As an example, the slope of the resistivity in the Arrhenius-plot shown in Fig. 6.3 (a) depends on disorder, with more disorder leading to stronger increase. A characteristic parameter for this insulation strength is the activation energy T_0, which is directly related to $k_F l$ in a linear fashion [10, 11], the latter being a common indicator of the disorder in homogeneously disordered samples [10, 11, 33, 49, 212]. For strongly disordered indium oxide, $k_F l$ is found very small $k_F l < 0.3$ and reaches even lower values where T_0 increases [10, 11]. Maximum values for T_0 have been found in the range of $T_0 \sim 15\,\mathrm{K}$ [8, 33, 40]. Upon increasing disorder even further and/or increasing temperature, Mott variable range hopping is found [49, 54, 67], see e.g. Fig. 6.3 (c) [49], which can also transition to Efros-Shklovskii VRH [19, 54, 67], when a Coulomb gap opens at low temperatures.

Peculiar behavior is also found when studying disordered indium oxide in large magnetic field. Upon increasing magnetic field, first superconductivity is suppressed and the resistivity isotherms show a crossing point at the quantum resistance $h/(2e)^2 \approx 6.5\,\mathrm{k\Omega}$ [25, 213], seen exemplary in Fig. 6.3 (c) [25], indicating a magnetic-field driven SIT. Beyond this crossing point, at large magnetic fields the films are insulating, showing that magnetic field can also drive weakly superconducting films across the transition. There is a giant magnetoresistance peak found [25, 107, 213] at magnetic fields of several tesla, see Fig. 6.3 (d) [25], although the mechanisms behind this phenomenon are not well understood yet [8]. At finite magnetic fields also the concept of a superinsulator/finite-temperature insulator has been suggested [14] and indications for that have been found [42]. In this regard it is suggested that

the conductivity drops to exactly zero already at finite temperatures [14, 34, 42].

From a theoretical standpoint, these findings obtained experimentally in disordered indium oxide have attracted considerable interest [12, 13, 46, 47, 84, 214–216] describing the experimental evidence to varying extend. Most of the theories, however, themselves pose several major unsolved questions, which are under heavy debate [8]. The Finkel'stein mechanism [29, 30], with the general suppression of Cooper-pairing due to enhanced Coulomb interaction caused by slow electron diffusion [81], counterintuitively seems to not be active at all. The reason why this is the case however, could only be speculated before and there has not been any hard evidence as to why Coulomb interactions are effectively suppressed [8, 33]. The existence of local Cooper-pairs in turn points towards a phase-driven mechanism, however it is not settled which mechanism is at play [8, 14]. On the one hand, it has been spectulated in particular by V. Vinokur [34] and T. Baturina [14], that the nature of insulating indium oxide might be explained by BKT-physics with the structure of a Josephson-Junction-array network (see section 3.4), similar to granular materials. The importance of the quantum resistance $h/(2e)^2$ in various experiments and the possibility of a finite-T insulator lend support to the theory proposed by M. P. A. Fisher [35, 36, 85], where Cooper-pairs and anti-Cooper-pairs condense into a dipole state following BKT-physics. On the other hand however, it has been able to show, that Anderson localization by itself can be the main driving factor for emergent granularity [46, 47] and the vanishing of coherence peaks [46, 47, 215]. The problem with these studies is, however, that most methods are limited to strong coupling, whereas superconductivity is expected to be essentially a weak effect with weak coupling [8, 33]. In this regard the theory by Feigel'man et al. [12, 33] (section 3.5) delivers the most advanced theoretical approach. Feigel'man et al. propose in several works [12, 33], that indium oxide is an Anderson insulator, which shows fractal electronic eigenstates. On top of the fractal localization, the electrons can still form Cooper-pairs

via space-local weak-coupling attraction, which itself has various influences on conductivity and also on polarization [38, 39]. With this mechanism the variations of superconductivity on a microscopic scale of a few 10 nm, as well as the temperature-dependent conductivity found in both disorder-driven and magnetic field-driven insulating thin-film samples and the results from tunneling experiments can be explained, however direct evidence is lacking, that would support definitive predictions [38, 39] concerning in particular the dynamical properties of conductivity and polarization.

The question whether a BKT-driven or a purely Anderson localization-driven mechanism is more plausible in indium oxide, is mainly defined by the role of Coulomb interactions [8, 14, 33]. It is established, that there is an intricate interplay [8] between Coulomb interactions, Cooper-pairing and Anderson localization, where the strength of electron-electron interactions plays an important role, however it has not been clear yet as to how Coulomb interactions participate in the formation of pseudo-gapped insulating states [8]. Firstly, knowing the strength of polarization in indium oxide could give insight on electronic screening and therefore may explain why it is even possible to have active Cooper-pairing despite the possibility of the Finkel'stein mechanism looming (this will be detailed further in the next section 6.1.1). Secondly, knowing the polarization and also its scaling with disorder could give decisive insight [33, 38, 39] into the nature of electronic eigenstates in indium oxide, their possibly fractal structure and whether charge localization purely by Anderson localization itself can produce a pseudo-gapped insulator in disordered amorphous indium oxide.

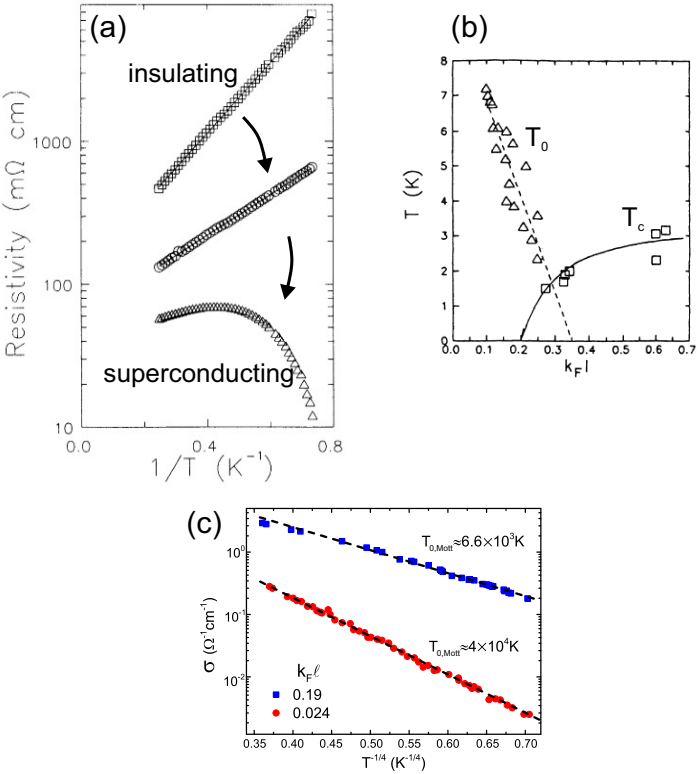

Fig. 6.3.: (a) Resistivity as a function of $1/T$ (Arrhenius-plot) for three indium oxide samples of different disorder showing the transition from insulator to superconductor. The activated behavior stems from a hard gap. (b) T_0 and T_c as a function of $k_F l$, a common parameter describing disorder, where for larger disorder $k_F l$ is smaller. T_0 increases with increasing disorder. (c) Conductivity as a function of Mott VRH $1/T^{1/4}$-behavior. High-disorder indium oxide samples show linear behavior. (a) and (b) with modifications from [10], (c) with modifications from [49].

6.1.1. Role of Coulomb interactions

The role of Coulomb interactions in insulating indium oxide is largely not well understood yet [8]. Many of the phenomena found in experiments detailed in the previous section 6.1, suggest that Cooper-pairing is possible in a wide range of disordered states in indium oxide, even in the insulating phase. This is highly unusual, as typically it is expected that the superconducting gap vanishes entirely when increasing disorder above a critical amount, following the Finkel'stein mechanism [29, 30] detailed in section 3.3. Generally it is expected that disorder decreases the diffusive motion of electrons substantially [81], decreasing their possibility to screen their Coulomb interaction potentials. This in turn leads to stronger electron-electron repulsion, which at some point is stronger than phonon-mediated Cooper-attraction and inhibits Cooper-pairing. Since in insulating indium oxide Cooper-pairs are expected to prevail without global superconductivity, the effective repulsive Coulomb interaction has to somehow be sufficiently suppressed even though disorder levels are very high [33].

It is suspected that the polarizability and the dielectric constant in indium oxide are still large even though disorder is large [33]. It has to be differentiated mainly between two contributions to the dielectric constant ε_1 quantifying this polarization. On the one hand, the contribution by immobile charges far from the Fermi-energy and the regular host lattice contribute a constant dielectric constant, called here $\varepsilon_{1,\mathrm{Host}}$ [54]. This part is thought to be quite sizable in indium oxide due to the low density of charge carriers $n \sim 1 \times 10^{21}\,\mathrm{cm}^{-3}$ [10, 33] and the large density of states distant from the Fermi-energy [33]. On the other hand, the localized electrons also contribute to the polarization of the total system. This contribution is expected to be disorder-dependent [39, 54], as the localization radii ξ, in which the electrons are localized, depend on the amount of disorder.

In insulating, but potentially pseudo-gapped indium oxide, the two parts, the one from electrons far away from the Fermi-energy and the one from

conduction electrons, both contribute to electronic screening [54]. The first part is independent of the conduction properties and equally contributes to screening, independent of the electrons being paired or unpaired. However, in the premise of existent localized Cooper-pairs, it might be argued that the second part stemming from the conduction electrons is sensitive to pairing, as coupling electrons to pairs might change relevant length scales and consequently alter the polarization. Cooper-pairing is indeed expected to have a certain effect on the polarization [38, 39], see section 3.5.5, however, it is not expected that the polarization is altered too strongly for Cooper-pairing to be inhibited. The reason for this is, that in insulating indium oxide the localization length ξ, defining the radius in which electrons are enclosed, is much smaller than the superconducting coherence length $\xi_{\mathrm{sc}} \gg \xi$ [123]. The latter relationship in turn is in close correlation to possible localized Cooper-pairs and implies their existence. It also means, that superconductivity in the context of localization is essentially a weak effect with weak coupling, which basically sits on top of the localization of electrons [8], meaning that it occurs in the spatially separate "puddles" of size ξ.

Since Cooper-pairing is expected to prevail in insulating indium oxide, the screening must be sufficiently strong to reduce the bare Coulomb repulsion of the electrons, although a self-consistent theory about the suppression of Coulomb repulsion and net-attraction by phonons is not yet constructed [123]. To quantify the strength of the Coulomb interaction and its screening, a dimensionless characterization parameter can be introduced as [33]

$$\frac{\xi_{\mathrm{sc}}^2}{\alpha_{\mathrm{scr}}^2 \varepsilon_1} \,. \tag{6.1}$$

It relates the coherence length of the superconductor ξ_{sc} to the Thomas-Fermi screening length α_{scr} and the dielectric constant ε_1. If $\xi_{\mathrm{sc}}^2/\alpha_{\mathrm{scr}}^2\varepsilon_1 \gg 1$ the effective screening is weak and the Coulomb interactions are strong [33]. This happens if both α_{scr} and ε_1 are small, meaning that the potential of the

Yukawa potential $\phi(r) = e/(\varepsilon_1 r)\exp(-\alpha_{\mathrm{scr}} r)$, equation (2.11), is only weakly suppressed since both the screening length α_{scr} and the polarization ε_1 are low, compare section 2.2. Then the effective Coulomb interaction is strong and the Finkel'stein mechanism is in process (section 3.3), where the effective Cooper-attraction, equation (3.15), is essentially negative and Cooper-pairs may not form [29, 30]. If however $\xi_{\mathrm{sc}}^2/\alpha_{\mathrm{scr}}^2\varepsilon_1 \ll 1$, screening is expected to be large, such that Coulomb interaction is weakened, leading to an effectively net-positive Cooper-attraction and the pairing of electrons to Cooper-pairs.

To make a quantitative estimation for this dimensionless Coulomb parameter for indium oxide samples, equation (6.1) will have to be related to well accessible characteristic material parameters. In order to accomplish this, formulas will be used in the following to relate ξ_{sc} and α_{scr} to quantities determined from sample deposition or subsequent experiments. All formulas will be assumed in their three dimensional form, as although the amorphous indium oxide films used in this work are indeed of relatively thin thickness d, they still are assumed to exhibit three dimensional properties. This can be inferred from looking at the maximum typical hopping distances $r_{\mathrm{hop}} \approx \frac{3}{8}\xi_{\mathrm{Mott}}\left[(T_{0,\mathrm{Mott}}/T)^{1/4}\right] < d$ [49, 54], which will be calculated for some samples in the following sections, finding that r_{hop} is smaller than d in the relevant temperature ranges, implying three dimensional properties. This is also a main requirement, as the theory presented in section 3.5 is restricted to three dimensional systems. The details of a crossover to the two dimensional limit is beyond the developed theory [33]. ξ_{sc} can be expressed as the localization length in a dirty superconductor with [217]

$$\xi_{\mathrm{sc}} = \sqrt{\frac{\hbar D}{2\pi k_B T_c}} = \sqrt{\frac{\hbar v_F l}{6\pi k_B T_c}}\,, \tag{6.2}$$

where $D = v_F l/d$ is the diffusion constant [218, 219] with v_F the Fermi-velocity, l the mean free path and the dimension $d = 3$. T_c is the critical temperature unaltered by disorder (equation (3.16)). α_{scr} can be expressed

as $\alpha_{\mathrm{scr}} = v_F/\omega_p = v_F\sqrt{m\varepsilon_0/Ne^2}$ with m the charge mass and N the particle density, see equation (2.10) in section 2.2. With this, equation (6.1) becomes

$$\frac{\xi_{\mathrm{sc}}^2}{\alpha_{\mathrm{scr}}^2\varepsilon_1} = \frac{\hbar v_F l}{2\pi k_B T_c} \cdot \frac{Ne^2}{m v_F^2 \varepsilon_0 \varepsilon_1} \tag{6.3}$$

$$= \frac{\hbar}{2\pi k_B T_c \varepsilon_0 \varepsilon_1} \cdot \frac{e^2 k_F}{3\pi^2\hbar} k_F l \tag{6.4}$$

$$= \frac{\hbar\sigma}{2\pi k_B T_c \varepsilon_0 \varepsilon_1}\,, \tag{6.5}$$

with $k_F = mv_F/\hbar$ the Fermi-vector and [56]

$$k_F = (3\pi^2 N)^{1/3} \tag{6.6}$$

$$\rightarrow N = k_F^3/3\pi^2\,. \tag{6.7}$$

σ is the residual conductivity [33], which is derived from the Drude DC-conductivity with [56, 220]

$$\sigma = \frac{Ne^2\tau}{m} = \frac{Ne^2}{\hbar k_F} l = \frac{e^2 k_F}{3\pi^2\hbar} k_F l\,, \tag{6.8}$$

with $\tau = l/v_F$ the scattering time.

From equations (6.1) and (6.5) it is clear that ε_1 is the crucial factor for the magnitude of the Coulomb interaction and decides whether Cooper-attraction exists or is inhibited. To give an estimate about the size of a critical value $\varepsilon_{1,\mathrm{c}}$ above which Cooper-attraction is positive, the Coulomb interaction parameter can be calculated with $\hbar\sigma/2\pi k_B T_c \varepsilon_0 \varepsilon_{1,\mathrm{c}} \approx 1 \Rightarrow \varepsilon_{1,\mathrm{c}} \approx \hbar\sigma/2\pi k_B T_c \varepsilon_0$. If ε_1 is smaller that this critical value, Cooper-attraction is inhibited, if it is larger, Cooper-attraction is possible. For the samples investigated in this work the Fermi-vector k_F can be calculated assuming a particle density $N \approx 1 \times 10^{21}\,\mathrm{cm}^{-3}$ [10, 33] with equation (6.6) to about $k_F \approx 3 \times 10^7\,\mathrm{cm}^{-1}$ and $k_F l$ can be estimated as $k_F l \approx 0.3$ [10], compare Fig. 6.3 (b). With the

unaltered critical temperature $T_c \approx 3.3\,\mathrm{K}$ [10, 26] (compare Fig. 6.3 (b) at large $k_F l$) the critical $\varepsilon_{1,\mathrm{c}}$ can then be calculated via equation (6.4) to*

$$\varepsilon_{1,\mathrm{c}} \approx 100\,. \tag{6.9}$$

One main goal of this work is therefore to measure the absolute value of ε_1 and determine whether the criteria of $\varepsilon_1 > \varepsilon_{1,\mathrm{c}}$ is met and the prerequisites for Cooper-pairing are fulfilled.

Note, that the above calculations with the assumptions $N = 1 \times 10^{21}\,\mathrm{cm}^{-3}$ and $k_F l \approx 0.3$ can be upper estimates depending on the disorder in indium oxide. For very disordered indium oxide samples, e.g. in the electron glass regime, it is possible that both N as well as $k_F l$ (compare Fig. 6.3 (b) [10]) can be smaller to some extend. This however does not change much in the general argumentation above and $\varepsilon_{1,\mathrm{c}} \approx 100$ is still a good estimation.

6.2. Sample preparation and annealing

Thin-film indium oxide samples have been grown in collaboration with Benjamin Sacépé and co-workers at the Institut Néel, CNRS Grenoble, France. The samples were deposited by evaporating high-purity (99.999 %) In_2O_3 with electron beam evaporation on liquid nitrogen cooled substrates, while keeping a constant oxygen partial pressure P_{O2} in the deposition chamber, resulting in amorphously disordered but homogeneously thick indium oxide films [10, 11, 28]. The sample thickness d was determined in-situ during deposition using a quartz-crystal thickness monitor. The deposition parameters d and P_{O2} of all samples investigated in this work are detailed in Tab. 6.1. The actual sample thickness might by slightly off from the set value shown, however, the actual sample thicknesses are determined afterwards ex-situ with AFM, as described in section 5.4 and shown exemplary for sample E in Fig. 6.4. Only

*Note that in Ref. [33] by Feigel'man et al. there was a calculation error [123], leading to their estimation of $\varepsilon_{1,\mathrm{c}} \sim 10$ being too small by a factor of ten.

small differences (few percent) to the set thickness are found (see measured thicknesses in Tab. 6.2). The RMS roughness of the samples has been found in the regime of about 1 nm, which is expected [28].

Tab. 6.1.: Deposition parameters, thickness d and oxygen partial pressure P_{O2}, of all samples investigated in this work.

Sample	d [nm]	P_{O2} [1×10^{-4} mbar]
A	18	3
B	20	2
C	20	2
D	25	0.7
E	25	0.7
F	28	0.8
G	42	0.9
H	30	0.5

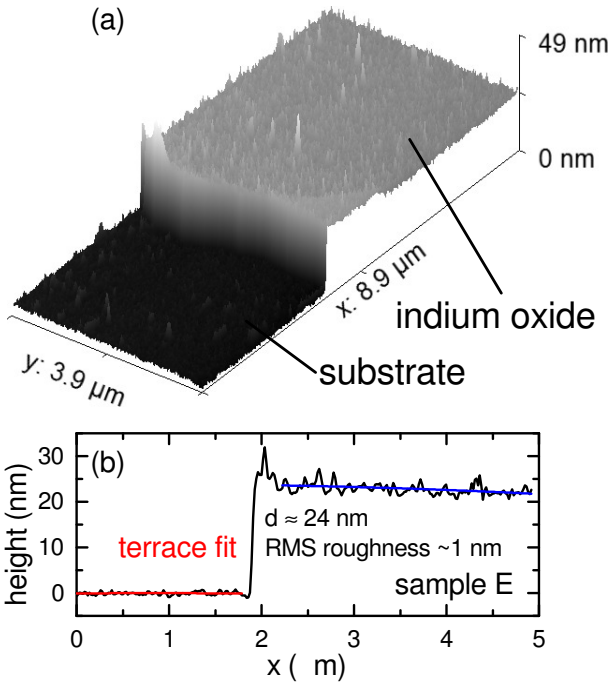

Fig. 6.4.: (a) AFM image of sample E on the substrate. (b) Profile across the step shown in (a). The thickness is determined by polynomial terrace fits. The RMS roughness of the indium oxide samples is typically found in the region $\sim 1\,\mathrm{nm}$.

With the above mentioned deposition procedure thin-films of amorphous indium oxide are created, which are much less dense than their crystalline counterpart In_2O_3 [45]. Their structure is amorphous and sponge-like with many microvoids and compositional variations [10, 11, 45]. Evaporating In_2O_3 by e-beam leads to a hot gaseous phase, which quench-condenses on the cooled substrate to form a spongy thin-film where long-range ordering is absent. As a result this structure includes many small cavities, meaning structural inhomogeneities and defects on the microscopic scale, which on the macroscopic scale are evenly distributed. This makes thin-films of amorphous indium oxide disordered but in a homogeneous fashion. These microvoids reduce the interatomic overlap [45] and lead to charge carrier density variations [10, 11]. Both of which lead to increased interatomic potential barriers for single electrons, which impede simple electron transport and promote hopping (section 3.1). This sponge-like amorphous structure is quite similar to rapidly chilled glasses [45, 221] and defines the "disorder" as it has been mentioned in this work. It is basis of the main properties and the peculiar phenomena found in amorphous indium oxide and is a driving parameter for SIT [8, 10, 28].

Disordered indium oxide thin-films are sensitive to thermal aging [45]. In general, the conductivity increases when the sample is exposed to room temperature or above. It is expected that an initially very insulating sample becomes less insulating with time [10, 45]. A sample that has been measured once will therefore have changed until the next measurement, if the sample is kept at room temperature between measurements. This will be utilized in the following procedures, as measurements are performed with temporal separation and the change in sample properties is used to sweep through the insulating phase. In some occasions however, the sample is driven faster through the phase diagram. To accomplish this, the sample is heated to about 50 °C. With this heat-treatment, its disorder decreases more rapidly, reducing resistivity substantially [222], meaning that the localization length ξ increases, while preserving the amorphous structure and chemical composition

[45]. The setup used for heating of the samples in-situ is shown schematically in Fig. 6.5 (b), where a heater is mounted in the cold-finger just below the resonator box carrying resonators and sample. R_s as a function of time during a typical annealing procedure is shown for sample E in (c). Starting from room temperature where the resistance has an initial value $R_{s,i}$, the sample is heated to 50 °C, where it is kept for the duration of 25 min. During this time the resistance gradually decreases. After set time of heating, the heater is turned off and the sample returns back to room temperature, where it is found that the ending room temperature resistance $R_{s,e}$ is less than the initial resistance $R_{s,i}$.

The mechanism behind the reduction of resistivity upon heat treatment and the temperature-dependence of $R_s(T)$ with its negative temperature coefficient, seen in Fig. 6.5 (c) upon initial temperature increase, is based on the fact that the spongy structure of the indium oxide films shrinks in volume [45, 223]. This densification of the sample is reminiscent of other amorphous systems exposed to increased pressure [221]. When exhibiting pressure their volume reduces considerably, mainly by interatomic densification, reducing microvoids. Analogous to this mechanical densification, the heat treatment of indium oxide is suggested to follow similar densification with increasing temperature [45, 223]. It has been found that film thicknesses change in the range of up to $\lesssim 20\,\%$ [45, 223] (note, that this is found during extensive heating of the sample over very long durations ($> 10\,000$ s), where resistivity changes over several orders of magnitudes, while in the experiments of the present work only less extensive treatments are performed, which makes repeated thickness-measurements of the sample unnecessary within given error bars). During an increase of temperature, this densification occurs rapidly, leading to a rapid decrease in resistivity, which is seen also for the exemplary heat treatment cycle in Fig. 6.5 (c). Z. Ovadyahu explains the mechanisms behind these phenomena and its partially permanent character heuristically with the simple model shown in Fig. 6.5 (a) [45]. It describes two states, one called the spongy state “S” and one called the dense state “D”.

Two potential wells are shown as a function of interatomic distance r. For the spongy state the potential S(2) is lower in energy than S(1), meaning that the system tends to prefer a larger interatomic distance, while for the dense state D(1) is lower than D(2) and a smaller distance is preferred. The total system of the macroscopic film consist of many of such systems, each for neighboring atoms. The overall strength of disorder in the whole system then depends on the compositional ratio between states of type S and D. If more states of type S are present, as it is the case for freshly deposited indium oxide samples [45, 223], then the system has larger disorder (more distance between most atoms, weaker interatomic overlap between neighbors). While if more states of type D are present the sample has less disorder (atoms closer together), it is more dense and the disorder has reduced in comparison to the initial state. It is now argued that with time many S-type states convert to D-type states [45, 223], thus disorder decreases with time.

When increasing temperature above a certain threshold (found to be roughly $\gtrsim 10\,\mathrm{K}$ above room temperature [223]), thermally excited electrons in state S follow Boltzmann statistics and can traverse the potential barrier 3 to go from potential well S(2) to S(1), meaning that the atoms move closer together and densify. This is the reason for the rapid decrease of $R_s(T)$ with the initial increase of temperature $23\,^\circ\mathrm{C} \rightarrow 50\,^\circ\mathrm{C}$ seen in Fig. 6.5 (c). This process is partially reversible, leading to the increase of $R_s(T)$ again after heating (the potential barrier is traversed back from S(1) to S(2)). In part, however, this densification is also irreversible and permanent, which is utilized in the present work for the permanent change of the samples by annealing. The permanent contribution of the annealing process is suggested [223] to originate from the induced dense state S(1), where possibly reconstruction processes occur, rearranging many surrounding atoms permanently. This reconstruction then possibly leads potential S(2) increasing in energy, making the S-type state a D-type state, again in turn changing compositional ratio between states of type S and D, making the system less disordered. This can be repeated to anneal an initially less dense, freshly deposited indium oxide sample to

become more dense and less disordered. Such heat treatment protocols have been used extensively in previous studies on amorphous indium oxide [10, 11, 28, 45, 223] and will also be used in this work.

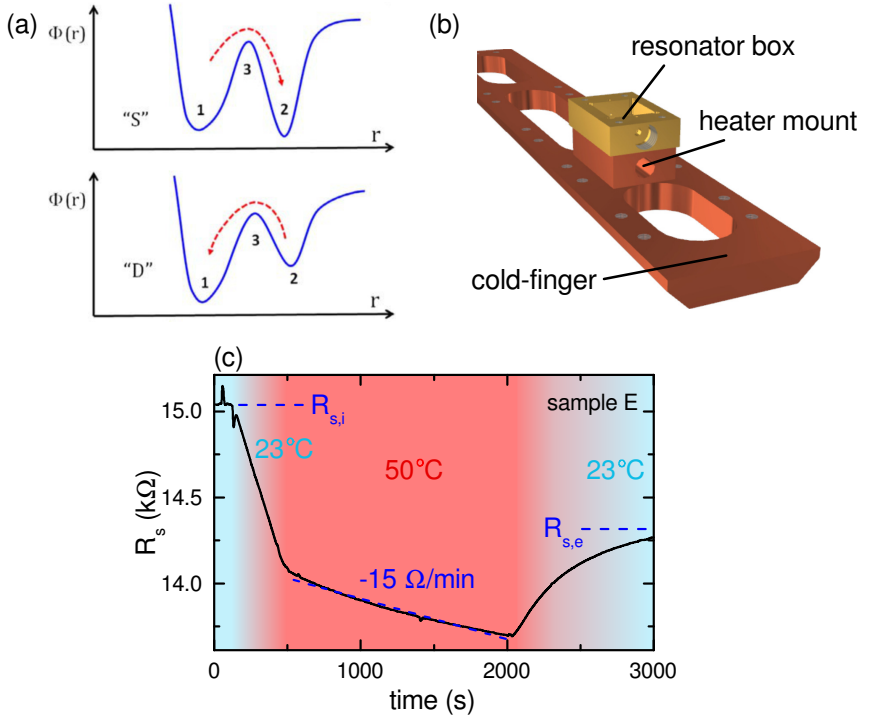

Fig. 6.5.: (a) Simple model heuristically describing the two densification states in amorphous indium oxide. Two potential wells are shown as a function of interatomic distance r with the spongy state "S" preferring large r and the dense state "D" preferring smaller r. Their ratio defines the amount of disorder in amorphous indium oxide. (b) Schematic depiction of the annealing setup, where a heater in the cold-finger heats the resonator box with sample. (c) R_s as a function of time for a typical annealing procedure. After annealing $R_{s,e}$ is smaller than initial resistance $R_{s,i}$. Panel (a) with modifications from [45].

6.3. Samples investigated in this work and their regime of insulation

In this work a total of eight different indium oxide samples of varying amount of disorder have been investigated to cover a wide range in the insulating regime. The samples have been deposited with varying thickness, ranging from 16 nm for the most insulating samples up to 42 nm for the sample closest to transition and in oxygen atmosphere of varying pressure. The thickness has been recorded during deposition using a quartz crystal (as described in section 6.2) and afterwards confirmed or corrected using AFM (shown in section 5.4). Sample characterization has been performed during each cooldown using DC-measurements, as shown in section 4.9. For all samples one exemplary sheet-resistance R_s measurement is shown in Fig. 6.6.

There are three different regimes, indium oxide samples can be in, depending on the amount of disorder. For very high disorder the samples are in the electron glass regime (samples A to C). Here it is expected that the electrons are extremely localized, such that not even local pairing can occur. For moderately disordered samples local pairing but no condensation to a superconducting state will occur (samples D to G). For even less disorder (sample H), at first resistive behavior is found followed by superconductivity at very low temperatures.

From the Arrhenius-plot in Fig. 6.6 it is obvious that only samples in the local pairing regime show distinct simple activated behavior. This is expected since activated behavior requires the existence of a hard gap. This is given in the local pairing regime with the formation of local Cooper-pairs and the resulting suppression of both Cooper-pair hopping and single-particle transport (see section 3.5.2). The required localization of the single-electrons still has to be sufficiently large, so that Cooper-pairs do not form a coherent superconducting state, but not too large as to inhibit Cooper-pair formation itself. This is met if the energy splitting, equation (3.25),

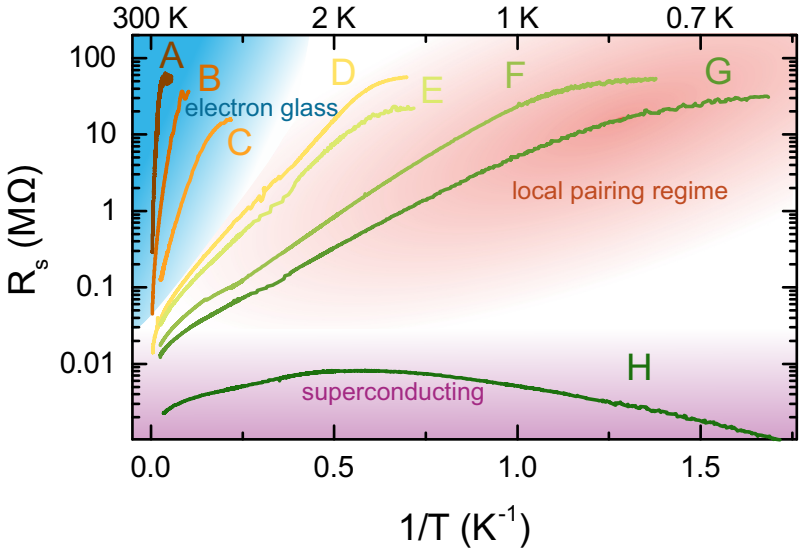

Fig. 6.6.: Sheet-resistance R_s of all samples measured in this work. There are three regimes, the electron glass regime without local pairing, the local pairing regime and the superconducting regime. The latter is not investigated further in this work.

$\delta = 1/\left(\nu_0 \xi^3\right)$, with ν_0 the single-particle density of states at the Fermi-energy, is $\Delta_p \ll \delta \ll \hbar\omega_D$, being larger than the superconducting gap Δ_p but smaller than the energy $\hbar\omega_D$. In this case, phonons can still mediate attractive Cooper-interaction between electrons and consequently Cooper-pairs can form locally, yet they cannot form a condensate. If however, $\Delta_p \ll \hbar\omega_D \ll \delta$ the energy splitting exceeds the phonon-energy and Cooper-attraction cannot be mediated, resulting in a state of localized single-electrons, the electron glass regime. This results in three distinct regimes, that can be visualized in a proposed phase diagram, as depicted in Fig. 6.7, showing typical energy scales as a function of disorder represented by energy level splitting δ. All important phases are shown with corresponding typical magnitudes of the relevant energy

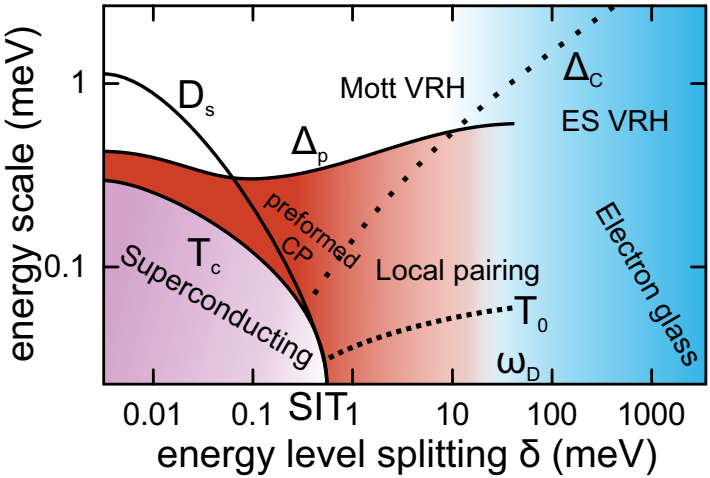

Fig. 6.7.: Proposed phase diagram for amorphous insulating indium oxide thin-films. Typical energy scales are given as a function of the energy level splitting δ, representing disorder (k_B and $\hbar$ have been omitted).

scales. The superconducting state is suppressed upon inducing disorder due to the decreasing superconducting stiffness D_s, forming preformed CP at $T_c < T < \Delta_p/k_B$. At the SIT the local pairing regime is reached, where both Δ_p and T_0 increase to some extent (equation (3.29)). At even higher disorder with $\delta > \hbar\omega_D$, the system traverses to the electron glass regime. A Coulomb gap Δ_C separates Mott variable range hopping (VRH) from Efros-Shklovskii (ES) variable range hopping.

In Fig. 6.6 the sheet-resistance R_s is shown. The resistivity ρ of the samples can also be calculated by factoring in the sample thickness t, following equation (4.88) (section 4.9) with $\rho = R_s t$. An overview of the resistivity of all samples measured is shown in Fig. 6.8. Typical values of ρ match well to what has previously been found in insulating indium oxide samples [10, 224]. As the temperature-dependence of $\rho(1/T)$ and $R_s(1/T)$ are equal and

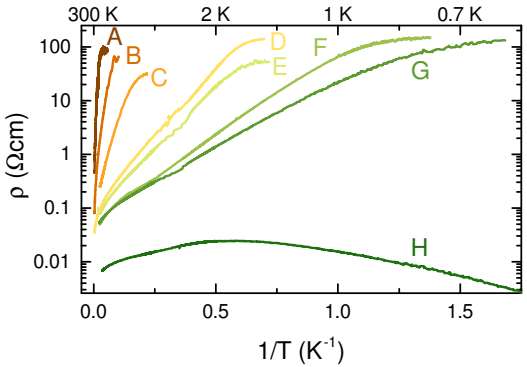

Fig. 6.8.: Resistivity $\rho(1/T)$ as a function of $1/T$ (Arrhenius plot) for all samples measured in this work. It is obvious that the temperature-dependence of $\rho(1/T)$ and $R_s(1/T)$ (Fig. 6.6) are equal.

derived parameters can equally be extracted from either magnitude, ρ and R_s are entirely interchangeable for the determination of temperature-dependent scaling parameter. The following analysis therefore focuses on R_s, since here typically more phenomena can be seen, such as e.g. the quantum critical value of $h/(2e)^2$ [8, 32] shortly above the onset of superconductivity (e.g. section 6.3.1).

To find the magnitude of the localization length ξ and the energy splitting δ, the DC-data can be plotted as a function of $1/T^{1/4}$, corresponding to a Mott-type variable-range-hopping (VRH) behavior in three dimensions with its temperature-dependence following equation (3.1). This is shown in Fig. 6.9. At high enough temperatures all of the samples show Mott VRH seen as linear behavior in the figure. This is expected, since at some point the temperature exceeds all relevant energy scales, which could modify hopping conductivity. Apart from the hard gap (pseudo gap) due to local pairing Δ_p, which forms below temperatures in the range of a few K [26, 28], the formation of a Coulomb-gap Δ_C [54, 67] is also possible due to electron-electron interaction

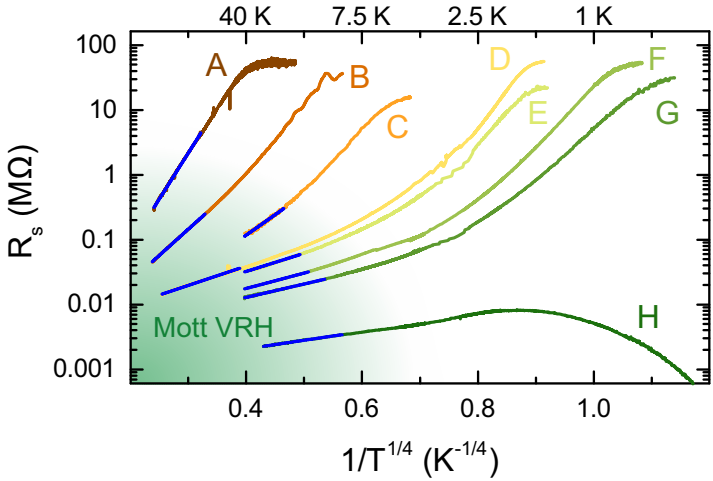

Fig. 6.9.: R_s as a function of $1/T^{1/4}$. All samples show Mott VRH at high enough temperature which can be fitted (blue) to extract $T_{0,\mathrm{Mott}}$.

leading to a Coulomb-glass state with Efros-Shklovskii-type VRH. As shown later in section 6.3.1, this crosses over to Mott-type VRH at temperatures of several 10 K. Since the high-temperature data shown in Fig. 6.9 for all samples corresponds well to the Mott VRH with $d = 3$ but not to $d = 2$, all samples in this work can be seen as three-dimensional. Fits to the data (blue) then give the characteristic Mott-temperature $T_{0,\mathrm{Mott}}$. For all samples measured in this work typical values of $T_{0,\mathrm{Mott}}$ are given in Tab. 6.2.

Tab. 6.2.: Overview of all indium oxide samples S of thickness d measured in this work with corresponding characteristic Mott-temperature $T_{0,\mathrm{Mott}}$, localization length ξ_{Mott}, the resulting energy splitting δ and the resistivity $\rho(4\,\mathrm{K})$ at 4 K. Samples in the electron glass regime where no local pairing is expected are denoted with *. For the latter $\rho(4\,\mathrm{K})$ exceeded experimental capabilities.

S	d [nm]	$T_{0,\mathrm{Mott}}$ [1×10^3 K]	ξ_{Mott} [nm]	δ [eV]	$\rho(300\,\mathrm{K})$ [Ω cm]	$\rho(4\,\mathrm{K})$ [Ω cm]
A*	16	948	1.07	5.11	0.56	-
B*	18	181 − 65.9	1.86 − 2.64	0.97 − 0.34	0.12 − 0.061	-
C*	20	84.9 − 45.5	2.39 − 2.94	0.46 − 0.24	0.083 − 0.045	-
D	25	5.37 − 3.50	6.00 − 6.92	0.029 − 0.019	0.036 − 0.033	7.8 − 2.9
E	24	2.29 − 1.81	7.97 − 8.61	0.012 − 0.010	0.036 − 0.034	2.6 − 1.4
F	28	3.31 − 2.03	7.05 − 8.30	0.018 − 0.011	0.019 − 0.018	0.68 − 0.56
G	42	0.600 − 0.531	12.5 − 13.0	0.0032 − 0.0029	0.029 − 0.028	0.38 − 0.25
H	30	0.058	27.1	0.000 31	0.0028	0.015

Using $T_{0,\mathrm{Mott}}$, the localization length can be calculated following equation (3.2),

$$T_{0,\mathrm{Mott}} = \frac{16}{k_B \nu_0 \xi^3} \quad \Rightarrow \quad \xi = \sqrt[3]{\frac{16}{\nu_0 k_B T_{0,\mathrm{Mott}}}}\,. \tag{6.10}$$

The factor 16 stems from the dimensionality [52, 54, 212] but leaves room for uncertainty. For the density of states at the Fermi energy an order of magnitude of about $\nu_0 \approx 1\times10^{45}\,\mathrm{J^{-1}\,m^{-3}}$ [54, 212, 225] with an electron density of about $1\times10^{19} - 1\times10^{20}\,\mathrm{cm^{-3}}$ [49, 225, 226] is assumed. Note that ν_0 is taken constant in the analysis for all samples [49, 54, 212, 225]. This however might induce additional uncertainties since ν_0 is expected to change for different amounts of disorder in indium oxide [226] with less disordered samples having larger ν_0 than more insulating samples. However, giving quantitative magnitudes on the variation of ν_0 in insulating indium oxide is difficult as studies are lacking. This is why most studies on insulating indium oxide simply assume a constant value of ν_0 [49, 54, 212, 225] typically in the range of $\nu_0 \approx 1\times10^{45}\,\mathrm{J^{-1}\,m^{-3}}$ [54, 212, 225]. With this, the values found for δ shown in Tab. 6.2 correspond well to transport studies on insulating indium

oxide with respect to the absolute values [49, 225]. The value of sample A with $\xi_{\mathrm{Mott}} \approx 1.07\,\mathrm{nm}$ even is in good agreement to what is expected for the full localization of the single-particle states, as this value comes close to the Bohr radius of indium oxide ($\sim 1\,\mathrm{nm}$) [10, 49], while it is expected that the electrons localize within the area of the Bohr radius upon very strong localization [49].

In particular when looking at the scaling behavior of $\varepsilon_1(\xi)$ or $\sigma_1(\omega)$ as a function of ξ presented later in this chapter, the density of states ν_0 usually enters formulas as a certain factor, see e.g. equations (3.11) and (3.33) (typically $\propto \nu_0^2$). However, its real influence is masked, as it does not only enter directly, but also indirectly via the localization length ξ, which is factored in simultaneously. ξ itself is a function of $\xi \propto \nu_0^{1/3}$, see equation (6.10). In combination, the scaling behaviors of $\varepsilon_1(\xi)$ and $\sigma_1(\omega)$ finally relate to ν_0 with $\varepsilon_1(T_{0,\mathrm{Mott}}) \propto \nu_0^{1/3}$ and $\sigma_1(\omega) \propto \nu_0^{1/3}$ (see e.g. later equations (6.15) and (6.25)). These scaling relations therefore have a strongly reduced dependence on variations in ν_0. It is suspected that the magnitude of the factor by which ν_0 might change from completely localized samples to superconducting samples is in the order of maybe $2-3$ [123, 226]. This would translate into an uncertainty of less than 20 %. In reality when investigating the scaling of each sample individually or comparing neighboring samples (in disorder), the error is certainly much less than this upper estimate. This is why due to lack of better knowledge on disorder-dependent ν_0, in the following analysis ν_0 will have to be kept constant across all samples.

Other characteristic parameters are either measured directly such as $T_{0,\mathrm{Mott}}$ and $\rho(4\,\mathrm{K})$, the resistance at 4 K, or are immediately derived from measured properties such as the energy level splitting $\delta = \frac{1}{\nu_0 \xi_{\mathrm{Mott}}^3} \propto k_B T_{0,\mathrm{Mott}}$ (equations (3.25) and (3.2)). They will therefore not be affected by uncertainties in ν_0.

For most samples there are ranges given for each parameter in Tab. 6.2, since most samples have been measured multiple times at different states of disorder and insulation strength. This is utilized to cover a wider range

in disorder states and to have many measurements in between. It has been accomplished on the one hand by letting the sample rest at room temperature (in vacuum) between individual measurements (separated by days to months), leading to glassy aging processes reducing disorder [10, 40, 45]. On the other hand, in some cases the samples have additionally been annealed in-situ in vacuum at $\sim 50\,^{\circ}\mathrm{C}$, where the sample decreases in insulation strength on a shorter time-scale on the order of minutes [11, 45, 223] (see section 6.2). It has been found that either case preserves the amorphous structure of the indium oxide thin-films [40, 45] and does not lead to crystallization if too high temperatures are avoided ($T < 60 - 100\,^{\circ}\mathrm{C}$ [45]). It has also been found in literature [40] and during the experimental work of this project, that room-temperature storage and annealing both have equal effects on the composition of the samples and its insulation properties. In both cases the resistivity typically reduces with time, when stored or annealed in vacuum [40] and contact with air is reduced to a minimum. Since the characterizing parameters (e.g. $T_{0,\mathrm{Mott}}$) of each sample are measured during each cooldown simultaneously to the desired observables (i.e. ε_1 and σ_1) tightly linking them, the actual means of the change of disorder between individual measurements are irrelevant. The ranges given in Tab. 6.2 therefore include both changes in disorder due to time in room temperature storage and by purposeful annealing. Equally, in the following chapters it will not be distinguished between either way.

$T_{0,\mathrm{Mott}}$ ranges from several 10 K in the superconducting regime via several 100 K in the local pairing regime up to almost 1×10^6 K for the most disordered/most localized sample, covering more then three orders of magnitude in localization strength. The absolute values of $T_{0,\mathrm{Mott}}$ are in good agreement to values found in previous studies of strongly insulating indium oxide samples [49, 54, 67, 212]. The energy level splitting shown in Tab. 6.2, calculated with equation (3.25) from ξ_{Mott}, ranges from µeV for the superconducting sample via a few meV in the local pairing regime up to the range of several hundred meV to even above 1 eV in the electron glass regime. The superconducting

energy gap in indium oxide is expected to be about $0.5\,\mathrm{meV} - 1\,\mathrm{meV}$ [26, 28] (see also the tunneling-gaps in Fig. 6.1), meaning that for all samples except sample H it holds $\Delta_p \ll \delta$. All samples except for sample H therefore will not become globally superconducting even at arbitrarily low temperatures since condensation of the Cooper-pairs to a macroscopic condensate is not possible. The energy level splitting of sample H, however, with about 0.3 meV is slightly lower than Δ_p, which in turn means that it is superconducting but very close to the transition. This is confirmed in DC-measurements since sample H goes superconducting below 0.5 K (shown in section 6.3.1).

For the upper limit of the local pairing regime the condition $\delta \ll \hbar\omega_D$ holds. Naturally, finding a well defined Debye energy in amorphous indium oxide is not possible due to its disordered and amorphous nature [227]. However, typical Debye-energies have been reported and are expected to be in the range of about $\omega_D \approx 420 - 800\,\mathrm{K}$ [12, 33, 227, 228]. For lack of better knowledge about the Debye energy of the specific samples in this work, in the following analysis a typical value of roughly $\omega_D \approx 500$ [12, 33] is therefore assumed, corresponding to phonon-frequencies in the range of $\sim 1 \times 10^{13}\,\mathrm{Hz}$. For the above condition it then follows $\delta \lesssim 50\,\mathrm{meV}$. Note that this is only a rough estimate and should be taken as an order of magnitude comparison. $\delta \lesssim 50\,\mathrm{meV}$ is met for samples D-H, however for samples A-C it is clearly $\delta > 50\,\mathrm{meV}$, meaning that for the latter not even local Cooper-pairing can be established. This is also confirmed by DC-data, since for samples A-C no simple activated behavior is found in the accessible measurement range. Samples A-C therefore show electron glass [49] behavior.

It is found both in literature [54, 67] and in this work, that characterizing disorder and the insulating strength of insulating indium oxide samples can be done conveniently and reliably by $T_{0,\mathrm{Mott}}$ and parameters derived from it, such as the energy level splitting $\delta \propto T_{0,\mathrm{Mott}}$ and the localization length $\xi \propto 1/T_{0,\mathrm{Mott}}^{1/3}$. This works for all samples independent of whether Cooper-pairing is present or not, as $T_{0,\mathrm{Mott}}$ is extracted at temperatures above relevant values for Cooper-pairing. It will therefore be the main

characterization parameter for all electron glass samples and when comparing all samples to each other including both electron glass samples and local pairing samples. For local pairing samples a second quantity comes in handy, the activation energy T_0. It is linearly related to $k_F l$. The latter is a common parameter for disorder [10, 11] (see Fig. 6.3) but is inconvenient to determine in this work, which is why T_0 is the most convenient and reliable parameter for the low-temperature characterization of disorder in local pairing samples. Additionally, several predictions in theory concerning the fractal nature of electronic eigenstates are expressed as a function of T_0 (see section 3.5, e.g. equation (3.34)) and it is therefore desirable to find T_0-dependent data.

In the following, microwave measurements are performed at low temperatures. At mK-temperatures the power used for the microwave frequency typically has to be tightly controlled as to not heat up the sample due to power-dissipation in the resonator. For this a power-sweep is performed at base temperature and investigated for each resonance individually. Typically it is found that at powers $> -50\,\mathrm{dBm}$ the power-dissipation has detrimental impact on the resonator performance, decreasing Q. This is due to the resonator heating locally, enhancing losses. At the lower end of the power-range $< -70\,\mathrm{dBm}$ however, the signal-to-noise ratio decreases strongly. Therefore typically powers in the range of roughly $\sim -60\,\mathrm{dBm}$ are used which give good compromise of low noise but still negligible heating. The exact power is determined individually for each resonance, so that each resonance operates at its optimum. Any other power-dependence stemming from sample properties or from the interaction with the amorphous indium oxide samples is not found.

Sections 6.4 and 6.5 discuss the electron glass regime and the local pairing regime independently. Due to the different conduction/hopping mechanisms and energy scales, comparing electron glass samples to local pairing samples will first be done separately, and afterwards a direct comparison of all samples will be done in section 6.6.2. Where in the local pairing regime very low temperatures in the mK-region are necessary to reduce losses induced by

the sample, in the electron glass regime typically temperatures accessible with ^{4}He-systems are sufficient. Sample H will not be discussed in terms of dielectric constant measurements, since it is not possible to acquire microwave data of a superconducting sample with the current measurement method as it shortcuts the microwave resonators when directly deposited on top of the resonator-chip and eliminates their operation.

6.3.1. Crossover of hopping mechanisms in DC-measurements

In Fig. 6.6 and 6.9 it could already be seen that samples of different disorder show different resistive behavior. Depending on their disorder they can show activated behavior at low temperatures and hopping conduction at higher temperatures. Diffusive behavior will typically not be found. This is due to the localization length with characteristic energy δ being smaller then the diffusion length with energy k_BT. For most samples investigated here the typical temperature where $\delta \approx k_BT$ is $\gg 300\,\mathrm{K}$. For samples close to the transition it can get in the range of 100 K to several 10 K, however here also the investigated temperature range is lower. The remaining hopping conductivity, as shown in section 3.1 can vary depending on whether long-range Coulomb interaction between electrons lead to an opening of a Coulomb gap Δ_C [54, 67] or not. With finite Δ_C consequently the hopping is of Efros-Shklovskii (ES)-type VRH ("Coulomb-glass") [53, 54], without Δ_C it is Mott-type VRH [52, 56, 65] without electron-electron interactions ("Fermi-glass"). The finite size of Δ_C leads to a crossover in hopping conductivity from ES-type to Mott-type when raising the temperature, since if the temperature-assisted hopping energy exceeds Δ_C mostly states outside the Coulomb-gap contribute to transport and Δ_C does not play a role for the participating electrons. The characteristic temperature where this crossover occurs is called T_{co}.

Δ_C is the characteristic quantity of the ES VRH. For low-enough temperature, when only states within the gap contribute to the hopping transport,

$\sigma(T)$ acquires $\sigma(T) \propto \exp\left(-1/T^{1/2}\right)$-behavior (equation (3.3)). This can exemplary be seen in Fig. 6.10 (a) for a temperature-dependent sheet resistance R_s measurement of sample B as a function of $1/T^{1/2}$. Two regimes are visible with ES VRH below a cross-over temperature of about $T_{\mathrm{co}} \approx 80\,\mathrm{K}$ and Mott VRH above $T_{\mathrm{co}} \approx 80\,\mathrm{K}$. From the latter, $T_{0,\mathrm{Mott}}$ can be acquired as has been done before in section 6.3. At temperatures below T_{co}, $T_{0,\mathrm{ES}}$ can be acquired. Values for both $T_{0,\mathrm{Mott}}$ and $T_{0,\mathrm{ES}}$ of all samples (except for sample H) are displayed in Tab. 6.3.

Tab. 6.3.: Characteristic temperatures for Mott VRH $T_{0,\mathrm{Mott}}$ and ES VRH $T_{0,\mathrm{ES}}$ of all samples, determined as in Fig. 6.10 (a) at different temperature ranges. For each sample the crossover-temperature T_{co} and the size of the Coulomb gap Δ_C have been calculated.

S	$T_{0,\mathrm{Mott}}$ $[1 \times 10^3\,\mathrm{K}]$	$T_{0,\mathrm{ES}}$ [K]	T_{co} [K]	Δ_C [K]	Δ_C [meV]
A	948	1832	57	81	6.9
B	181 - 65.9	616 - 543	92 - 26	60 - 30	5.1 - 2.6
C	84.9 - 45.4	390 - 386	52 - 29	36 - 26	3.1 - 2.3
D	11.5 - 5.29	186 - 90	48 - 25	24 - 12	2.0 - 1.0
E	2.29 - 1.82	65 - 56	29 - 28	11 - 9.8	0.94 - 0.85
F	2.98 - 2.02	33 - 27	5.9 - 5.7	3.5 - 3.1	0.30 - 0.27
G	0.600 - 0.531	29 - 26	22 - 20	6.3 - 5.6	0.54 - 0.48

T_{co} directly follows from values of $T_{0,\mathrm{Mott}}$ and $T_{0,\mathrm{ES}}$ when the mean hopping energy difference between sites is equal for both Mott and ES VRH [54]. From this it can be found [54, 67]

$$T_{\mathrm{co}} = 16 \left(\frac{T_{0,\mathrm{ES}}^2}{T_{0,\mathrm{Mott}}} \right) . \tag{6.11}$$

Calculated values of T_{co} for all samples are also shown in Tab. 6.3 and correspond well to values found in insulating samples by Rosenbaum [54] and

Kim et al. [67]. The calculated values found with (6.11) also correspond well to the behavior found when looking directly at the temperature-dependence of R_s (Fig. 6.10 (a)). The value of $T_{co} \approx 80\,\mathrm{K}$ for sample B in the particular disordered state shown in the figure has been calculated with (6.11) and with the values for $T_{0,\mathrm{Mott}}$ and $T_{0,\mathrm{ES}}$ given in the figure. Around the temperature $T \approx T_{co}$, R_s clearly shows a transition from a curved behavior corresponding to Mott VRH (is $1/T^{1/2}$-dependence) to a linear behavior indicating ES VRH.

Values of $T_{0,\mathrm{Mott}}$ and $T_{0,\mathrm{ES}}$ also give the possibility to estimate the expected Coulomb gap evoked by long-range electron-electron interaction. It can be calculated following equation (3.5), $\Delta_C = k_B \left(T_{0,\mathrm{ES}}^3/T_{0,\mathrm{Mott}}\right)^{1/2}$ [67]. The resulting values are displayed in Tab. 6.3 (in meV as well as in K with Δ_C/k_B). Resulting values in the range of several 10 K down to a few K are in good correspondence to values found by Rosenbaum [54] and Kim et al. [67] for insulating indium oxide samples. It is found, that for almost all samples Δ_C is much larger than the expected pseudogap due to local pairing, which should be in the range of about $\sim 0.5\,\mathrm{meV}$ (see e.g. Fig. 6.1 in section 6.1). This shows that the effects of a gap found in later section 6.5 can only be evoked by the pseudogap, since the energy scale of the Coulomb gap is much larger [33]. Only very close to SIT (sample F) Δ_C is of similar size to the pseudogap, however it is expected that it only has weak effects ($\sigma(T) \propto \exp(-1/T^{1/2})$ vs. activated behavior).

All samples shown in Tab. 6.3 show both Mott and ES VRH. Sample H however, which is the sample going superconducting at low temperatures, does not show ES VRH. It only shows Mott VRH crossing over directly to activated behavior. This is expected, since T_{co} decreases continuously towards smaller disorder and it is expected to be at one point smaller than the onset-temperature where local pairing begins and Cooper-pairs preform. R_s then transitions directly from Mott VRH to activated behavior. R_s as a function of T and as a function of $1/T$ (Arrhenius) is shown in Fig. 6.10 (b) and (c) respectively. For indium oxide it is found that the preformation of

Cooper-pairs typically starts at around $3.5 - 4\,\mathrm{K}$ [28, 32], which is confirmed by the data shown in Fig. 6.10 (b), where R_s goes from Mott VRH to activated at roughly $\sim 4\,\mathrm{K}$. For $T < 4\,\mathrm{K}$ Cooper-pairs start to form, the pseudogap opens and R_s increases stronger. Below about $1.5\,\mathrm{K}$ condensation starts to occur, where the Cooper-pairs start to form a macroscopic phase-coherent superconducting state. The transition is relatively broad and T_c can be derived by the linear $R_s \to 0$ extrapolation [32] to about $T_c \approx 0.46\,\mathrm{K}$, which is comparably small [28, 32], meaning that the sample is still very close to the transition. This also means that the pseudogap where Cooper-pairs start to preform is much larger than the condensation energy corresponding to the superconducting state, which is found to be on the order of T_c [32]. With the rough estimate of T_c from above, the pseudogap ranges up to about $7T_c - 8T_c$ in this sample, estimated a little larger compared to known results [28, 32].

The curve of $R_s(T)$ of sample H is relatively smooth without any shoulders, kinks or any kind of reentrance behavior. This indicates that the sample is relatively homogeneous in disorder distribution and there are no macroscopic inhomogeneities [10]. It is also found that R_s rises up to roughly the quantum resistance of $h/(2e)^2 \approx 6.5\,\mathrm{k\Omega}$ close to the onset of condensation. This is also expected [28, 32] and shows that Cooper-pairs are main contributors to the properties of critical indium oxide ($2e$ in the quantum resistance).

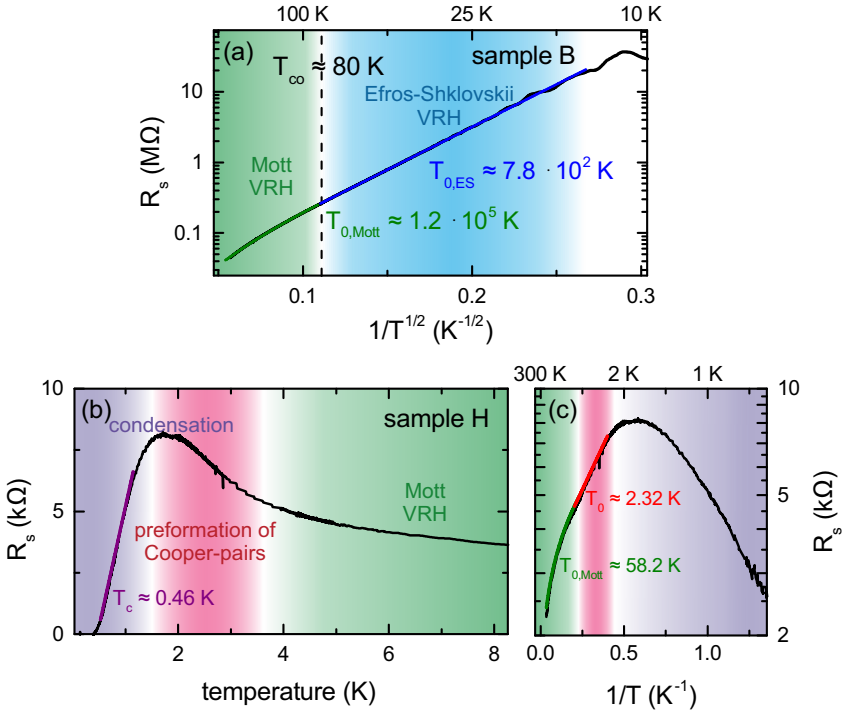

Fig. 6.10.: (a) Sheet resistance R_s of one particular disorder-state of sample B as a function of ES-type $1/T^{1/2}$ temperature-dependence. A transition from Mott VRH to ES VRH at T_{co} is seen upon lowering T. (b,c) R_s of sample H as a function of (b) T and (c) $1/T$ (Arrhenius). Three regimes, Mott VRH, Cooper-pair preformation and condensation are found.

6.4. The electron glass regime

In the electron glass regime it is expected that no local pairing occurs, since the single-electrons are strongly localized with the resulting energy level splitting exceeding Debye energies $\delta \gg \hbar\omega_D$, meaning that phonons cannot mediate any Cooper-attraction. As a consequence, in this regime the single-particle electrons are localized and no signs of Cooper-pairing are expected, whatsoever. Conductivity takes place by variable range hopping (VRH) of Mott-type or Efros-Shklovskii-type (compare section 3.1 and 6.3.1), depending on disorder and temperature.

It has been found [41, 49, 181] that strongly disordered indium oxide samples in the electron glass regime can show excess conductance upon excitation with very long relaxation times (several $\sim 1000\,\mathrm{s}$ [181]) corresponding to glassy properties of the samples. This excess conductance is due to the electron-temperature being essentially warmer than the lattice temperature. Such relaxation processes however, will not be excited with the experimental setup in this work and will not have interfering influence on the acquired data. Typical excitation energies where this excess conductivity can be observed, e.g. during the "stress protocol" of Ovadayhu [181], are orders of magnitudes larger than typical excitation voltages used in this work. Excitations with microwaves are expected to result in very weak excess conductivity ($< 10\,\%$ [181]). In the following measurements, no time-dependence of ε_1 or σ_1 has been found following initial cooldown or during a single measurement run, which could last up to several days during which the sample is kept at low temperatures. Also no difference in DC-properties comparing cool-down to warm-up has been found which could also be separated by up to several days. This means that the relaxation processes found in extremely insulating indium oxide upon strong excitation do not play a role in this work.

The samples have been deposited directly onto the resonator-chips. As an example, a top-view of sample B deposited directly on its resonator-chip is shown in Fig. 6.11. As detailed in section 5.2.2, especially Fig. 5.3, the

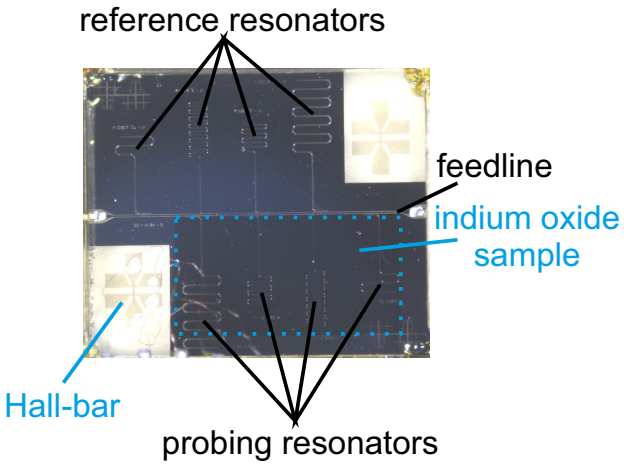

Fig. 6.11.: Top-view of sample B deposited on its resonator-chip. One half of the resonators is covered, the other half of equal lengths is left empty as reference. One Hall-bar is connected to external circuitry allowing for DC-measurements.

sample covers half of the resonators, leaving the other half of the eight resonators as reference. In this particular case the reference and the probing resonators have pair-wise equal length and are therefore expected to show similar resonance frequencies. In two corners Hall-bars are deposited directly on the Al_2O_3-substrate, one of which is connected to external circuitry, as detailed in section 4.9 and Fig. 4.15.

In the following section, samples A-C will be investigated. First the transport properties will be studied in more detail and afterwards the dielectric properties and microwave conductivity will be investigated. The dielectric properties will be discussed first as a function of DC localization length ξ_{Mott}. This will give the possibility to infer the nature of polarization in the electron glass regime of small localization length. As a function of temperature, Austin-Mott behavior is found. From fits to this behavior,

the localization length measured with DC-measurements can be confirmed by microwave measurements. The frequency-dependent conductivity can be described by Mott behavior, although smaller amplitude is found. This is expected however, due to the extreme localization of the charge carriers leading to reduced contributions of Mott resonances.

Data of sample B has been measured by Paul Kugler in his Bachelor's project [229].

6.4.1. Transport

The temperature-dependent sheet resistance $R_s(T)$ has been measured performing DC-measurements on the indium oxide Hall-bar. All three electron glass samples A-C show very strong insulating behavior. This is shown in Fig. 6.12 as a function of (a) $1/T$ (Arrhenius-plot), (b) $1/T^{1/2}$ (ES VRH) and (c) $1/T^{1/4}$ (Mott VRH). (f) shows the resistivity ρ in Mott VRH, where equal scaling to (c) is found. None of the samples show activated behavior, which is expected since $\delta \gg \hbar\omega_D$ meaning that no local pairing occurs [12, 33]. It is found however, that the samples show clear hopping behavior, where samples B and C show Mott VRH at higher temperatures and ES VRH at lower temperatures. The corresponding crossover temperature T_{co} has been calculated in the previous section 6.3.1 corresponding well to the temperatures at which the curvature of $R_s(T)$ in Fig. 6.12 (b) and (c) changes. T_{co} of sample A with about $T_{\mathrm{co}} \approx 57\,\mathrm{K}$ (see Tab. 6.3) also explains why for this sample ES VRH is never found in the given experimental circumstances. At about 50 K, $R_s(T)$ of sample A is already too large ($> 100\,\mathrm{M\Omega}$) to be measured by the current experimental setup.

Samples B and C have been measured multiple times with time in between individual measurements. Typical timescales of this resting time were in the range of several days. During this time the samples where kept at room temperature, which resulted in glassy aging processes reducing the disorder gradually. Consequently their insulating strength reduces. This is exemplary

shown for sample B in Fig. 6.12 (d) and (e). The legend shows the accumulated resting time t starting from the first cool-down. It is found that $R_s(T)$ overall decreases in value. However more strikingly, the slope of $R_s(1/T^{1/2})$ and $R_s(1/T^{1/4})$ reduces as well. This indicates that with accumulating resting time at room temperature, the hopping conductivity continuously enhances with the hopping distance lengthening more and more. From linear fits to $R_s(1/T^{1/2})$ and $R_s(1/T^{1/4})$ the characteristic temperatures $T_{0,\mathrm{ES}}$ and $T_{0,\mathrm{Mott}}$ can be extracted. For sample B this is shown in Fig. 6.13 (a) as a function of t. Starting from values $T_{0,\mathrm{ES}}(0) \approx 1000\,\mathrm{K}$ and $T_{0,\mathrm{Mott}}(0) \approx 190 \times 10^3\,\mathrm{K}$ they reduce to approximately half in value for ES and a third for Mott respectively over the duration of the total measurement time. It is found that $T_{0,\mathrm{ES}}(t)$ decreases roughly linearly, while $T_{0,\mathrm{Mott}}(t)$ is found to decrease very roughly with $T_{0,\mathrm{Mott}} \sim 1/t^3$ plus an offset c. From $T_{0,\mathrm{Mott}}(t)$ the localization length ξ_{Mott} can be found with equation (6.10). $\xi_{\mathrm{Mott}}(t)$ as a function of t is depicted in Fig. 6.13 (b). It is found that $\xi_{\mathrm{Mott}}(t)$ increases linearly with t. This means that the sample changes at a fixed rate roughly linear with the resting time. In turn this gives the possibility to cover a wide range on the insulating side of the transition.

$T_{0,\mathrm{Mott}}$ as well as derived parameters $\xi \propto 1/T_{0,\mathrm{Mott}}^{1/3}$ and the energy level splitting $\delta \propto T_{0,\mathrm{Mott}}$ will be regularly and interchangeably be used to characterize the disorder and insulation strength of the electron glass samples. These parameters have been found to be good indicators for the level of disorder [54, 67] allowing to compare samples to each other quite well. This is done for comparison of all electron glass samples with each other but additionally also for comparison of the electron glass samples to the local pairing samples which will be done in a later section 6.6.2.

Both $T_{0,\mathrm{ES}}$ and $T_{0,\mathrm{Mott}}$ are directly dependent on the localization length ξ. $T_{0,\mathrm{ES}}$ however, is additionally dependent on the dielectric constant ε, with [53]

$$T_{0,\mathrm{ES}} = \frac{3e^2}{\varepsilon_0 \varepsilon_{1,\mathrm{ES}} k_B \xi} \tag{6.12}$$

$$\Rightarrow \varepsilon_{1,\mathrm{ES}} = \frac{3e^2}{\varepsilon_0 k_B T_{0,\mathrm{ES}} \xi}\,, \tag{6.13}$$

see equation (3.4), with k_B the Boltzmann constant and ε_0 the vacuum permittivity. The prefactor is on the order of 3 [54, 65, 67]. Using (6.13) and $\xi_{\mathrm{Mott}}(t)$ determined from $T_{0,\mathrm{Mott}}(t)$, $\varepsilon_{1,\mathrm{ES}}(t)$, which is the dielectric constant estimated by ES VRH can be calculated, as performed for sample B in Fig. 6.13 as a function of (c) t and (d) ξ_{Mott}. The values in the range of about $\varepsilon_{1,\mathrm{ES}} \approx 300 - 450$ are large but correspond well to estimations of $\varepsilon_{1,\mathrm{ES}}$ by Rosenbaum [54] on insulating indium oxide samples. $\varepsilon_{1,\mathrm{ES}}(t)$ increases roughly monotonously with t and as a function of ξ_{Mott}. To compare to the expected $\varepsilon_{1,\mathrm{ES}}(\xi) = \alpha \frac{e^2 \nu_0}{\varepsilon_0} \xi^2$ behavior [39] (equation (3.33), with $\nu_0 \approx 1 \times 10^{45}\,\mathrm{J}^{-1}\,\mathrm{m}^{-3}$ [49, 54, 212]) a guide to the eye is plotted in the figure. $\varepsilon_{1,\mathrm{ES}}(\xi_{\mathrm{Mott}})$ seems to somewhat follow ξ^2_{Mott} for larger values of ξ_{Mott}.

Although absolute values of $\varepsilon_{1,\mathrm{ES}}$ are consistent to what has been found before [54], they are much larger than what is found by direct measurements, see section 6.4.2. Values found by ES VRH are about a factor of 10 larger. This is also reflected in the slope of $\varepsilon \propto \xi^2$ in Fig. 6.13 (d), where the numerical coefficient α has been set to about $\alpha \approx 24$ roughly an order of magnitude larger than what is expected for the three dimensional case with $\alpha \approx 3$ [39]. The method to estimate $\varepsilon_{1,\mathrm{ES}}$ from hopping characteristics is therefore not sufficient to estimate dielectric properties of insulating indium oxide, yet it has been one crude way to estimate ε_1 up to now. The direct measurements of ε_1 shown in the coming sections however, offer more insight into the actual dielectric properties and the conductivity at low temperatures.

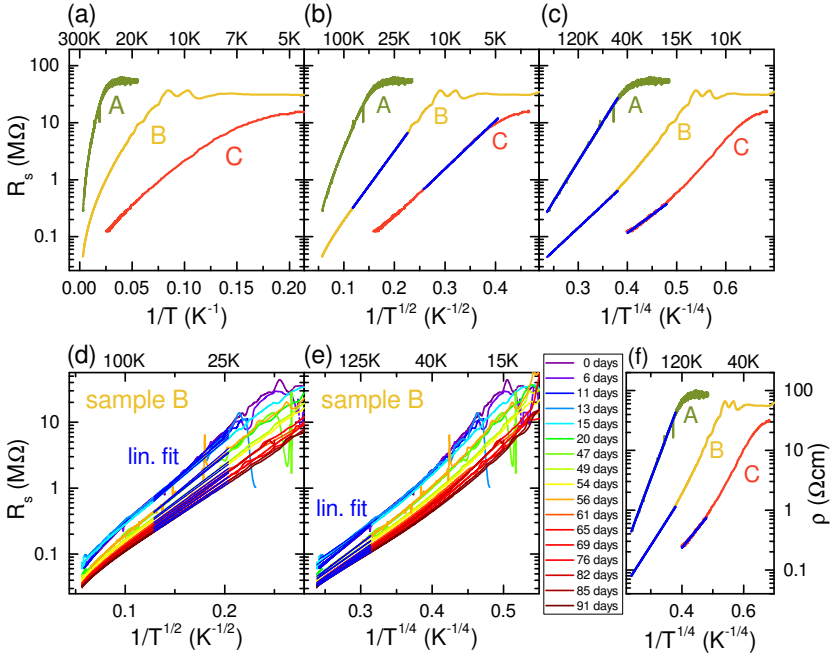

Fig. 6.12.: (a-c) Sheet resistance R_s of electron glass samples A-C as a function of (a) $1/T$ (Arrhenius-plot), (b) $1/T^{1/2}$ (ES VRH) and (c) $1/T^{1/4}$ (Mott VRH). None of the samples show activated behavior, since no local pairing occurs, but VRH is prominent. (d,e) $R_s(1/T^{1/x})$ ((d) $x = 2$, (e) $x = 4$) of several measurements with intermediate resting time at room temperature between each measurement as detailed in the main text. Both (d) ES VRH and (e) Mott VRH is found, indicated by linear fits which can be used to acquire characteristic parameters $T_{0,\mathrm{ES}}$ and $T_{0,\mathrm{Mott}}$. (f) Resistivity ρ as a function of Mott VRH. Scaling of $\rho(1/T^{1/4})$ with $1/T^{1/4}$ is equal to (c).

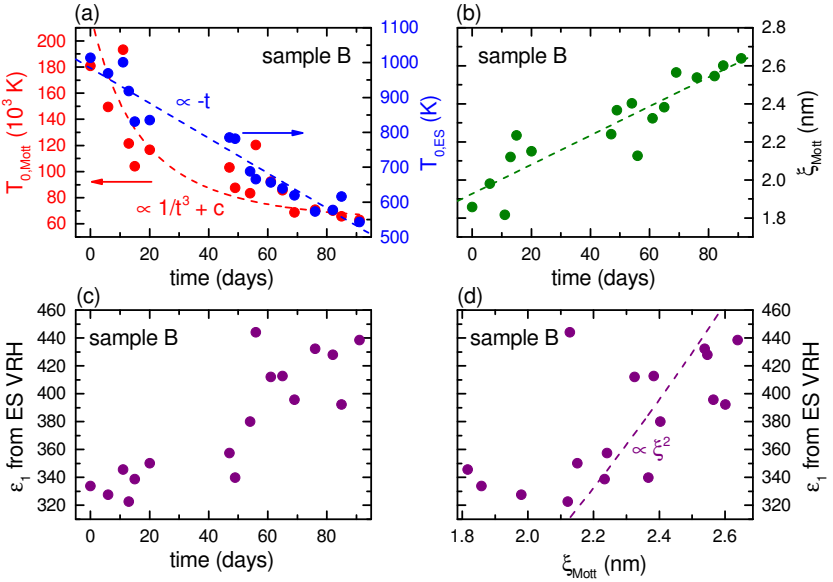

Fig. 6.13.: (a) $T_{0,\mathrm{Mott}}(t)$ and $T_{0,\mathrm{ES}}(t)$ fitted from Fig. 6.12 (d) and (e) as a function of resting time t. Both $T_{0,\mathrm{Mott}}(t)$ and $T_{0,\mathrm{ES}}(t)$ decrease, although with different t-dependence. (b) Localization length $\xi_{\mathrm{Mott}}(t)$ calculated from $T_{0,\mathrm{Mott}}(t)$. $\xi_{\mathrm{Mott}}(t)$ increases linearly with t. (c,d) $\varepsilon_{1,\mathrm{ES}}$ determined from $T_{0,\mathrm{ES}}$ with equation (6.13) as a function of (c) t and (d) ξ_{Mott}. $\varepsilon_{1,\mathrm{ES}} \propto \xi^2$ is shown as guide to the eye.

6.4.2. Dielectric constant as a function of static localization length

From the perturbative interaction of the sample with the resonator, the dielectric constant as well as the conductivity (section 6.4.3) of the thin-film electron glass indium oxide samples could be measured. For this, spectra of resonances have been measured as a reference beforehand, without the sample and after deposition of the sample. Some representative spectra for sample B and C are shown in Fig. 6.14 (a,b) and (e,f) respectively. Spectra of the resonances under the influence of the sample are shown for all stages of the glassy aging process. The spectra of sample B have been measured in a VTI cryostat at the base temperature of about 1.9 K, the spectra of sample C in the dilution refrigerator at about 25 mK (compare section 4.7). Since with decreasing disorder the conductivity increases (resistance decreases, see Fig. 6.12), losses will increase for less insulating samples. Due to the close spatial vicinity of the sample to the resonators, this will at some point lead to strong suppression of the resonances making it hard or even impossible to acquire resonance parameters. For sample B, however, already at $T < 5\,\mathrm{K}$ the losses are low enough for resonances to be distinctly measurable since here the resistance is already very large, making it possible to acquire microwave data already at VTI-temperatures. For sample C this is not given. Here losses decrease only at smaller T making the use of the dilution refrigerator preferable.

From the spectra in Fig. 6.14 it is already seen, that the reference resonance initially sits at higher resonance frequency with high Q. Upon applying the sample to the resonator, the resonance shifts to lower frequencies and Q decreases. This is a direct consequence of the additional sample-layer with $\varepsilon_1 > 1$ and σ_1. (b) shows a harmonic resonance of the fundamental shown in (a). The shift for the harmonic, although higher in absolute values is equal to the shift of the fundamental in relative terms, which implies that the influence of the sample has equal influence on all resonances of this particular

resonator. This can also be seen for sample C in (e) and (f) respectively. The resonances in the spectrum can be fitted with a complex Lorentzian model as detailed in section 4.8 and as exemplary demonstrated by the green fits in Fig. 6.14 (a) and (e) each for the largest and smallest resonance shift. For sample B the resonance frequency and Q of the fundamental shown in (a) are shown in (c) as a function of $T_{0,\mathrm{Mott}}$ and in (d) as a function of ξ_{Mott} from DC-measurements. For sample C the same quantities of the harmonic shown in (e) are shown in (g) and (h).

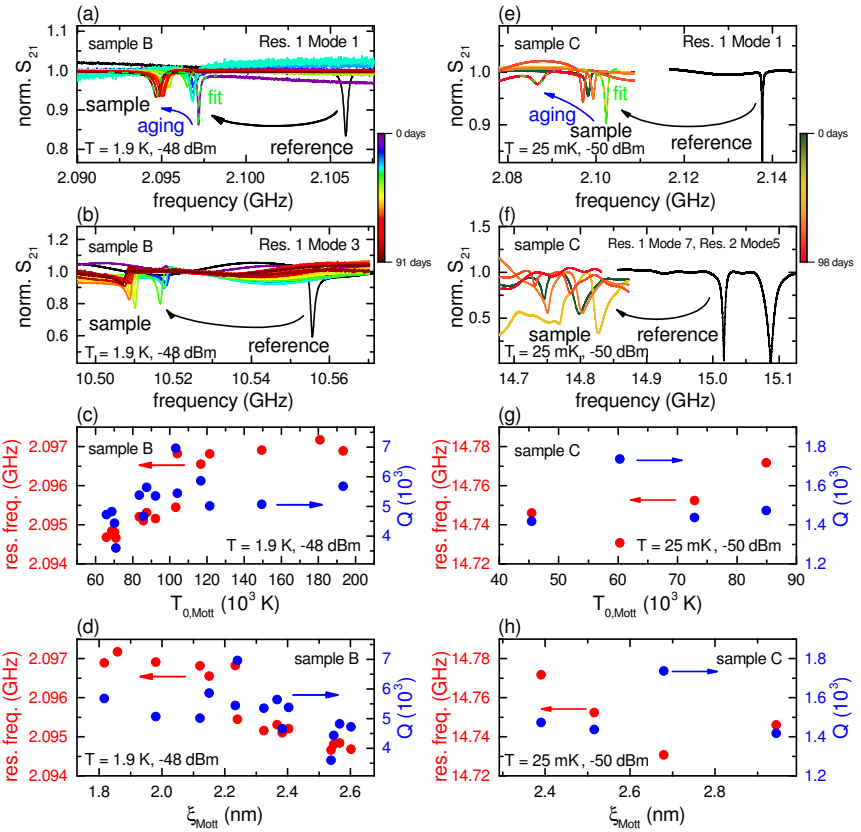

Fig. 6.14.: (a,b) Spectra of a resonance of a resonator with (a) its fundamental and (b) a harmonic under the influence of sample B of all aging stages and for an empty reference. The resonances shift to lower frequencies and Q is reduced. Exemplary complex Lorentzian fits to the data are shown in green. (c,d) Resonance frequencies and Q of the resonance shown in (a) as a function of (c) $T_{0,\mathrm{Mott}}$ and (d) ξ_{Mott} from DC-measurements. Both quantities are found to decrease with increasing $T_{0,\mathrm{Mott}}$ and ξ_{Mott}. (e,f) Similar spectra for sample C. (g,h) derived quantities for the harmonic shown in (f).

It is found that with decreasing $T_{0,\mathrm{Mott}}$, meaning with decreasing insulation strength and increasing localization length ξ_{Mott}, the resonance frequency decreases mostly monotonically. This is in turn a direct consequence from ε_1 of the sample, being the main contribution to the shift in frequency (c.f. section 4.4). From the resonance frequency shift and the change in Q, the dielectric constant ε_1 can be calculated following the procedure described in section 4.4. Resulting values for $\varepsilon_1(T_{0,\mathrm{Mott}})$ of all three samples in the electron glass regime as a function of $T_{0,\mathrm{Mott}}$ from DC-measurements are shown in Fig. 6.15 (a) and as a function of ξ_{Mott} in (b). Values are in the range between about 10 for sample A up to slightly above 100 for sample C. Values for sample A have quite large uncertainty, which is due to additional steps which had to be undertaken in the analysis in the data, including reattaining reference data by removing the already deposited sample. The whole procedure is explained in appendix A.2. Consequently values of ε_1 range in the area of about $10 - 30$ with large uncertainty, rendering this measurement more an order of magnitude estimate. Values of $\varepsilon_1 \approx 10$ would fit well to ε_1-values for crystalline indium oxide, which could on the one hand be derived from indirect high-frequency measurements [230] to about $\varepsilon_1 \approx 10.55$. On the other hand they could also be measured in preliminary low-temperature measurements on In_2O_3-samples in the low-frequency regime with THz frequency-domain and time-domain spectroscopy to about $\varepsilon_1 \approx 9.5 - 10.5$ [231]. This shows that ε_1 possibly approaches the values of the crystalline form upon complete localization, although from the presented data this is not unambiguously determined and might be expected to be higher [123]. Complete localization is mostly given since for sample A, ξ_{Mott} with $\xi_{\mathrm{Mott}} \approx 1.07\,\mathrm{nm}$ is quite similar to the expected Bohr radius of very strongly localized indium oxide in the range of $\sim 1\,\mathrm{nm}$ [10, 49].

Values for each individual measurement at fixed $T_{0,\mathrm{Mott}}$ (or fixed ξ_{Mott}) seem to vary from one resonance to the other, reaching differences in measured ε_1 of up to about 15 %. This can be explained by spatial variances in sample properties depending on location. Since each resonator probes a

different location of the macroscopic sample, as can be seen e.g. in Fig. 6.11, the properties an individual resonator probes can differ from the others, since properties of the indium oxide can vary macroscopically from one resonator to the next. This is confirmed by looking at all resonances from one individual resonator, meaning fundamental mode as well as its harmonics. This is depicted in Fig. 6.15 (c) for a measurement of one cool-down of sample C with fixed $T_{0,\mathrm{Mott}}$ or ξ_{Mott} (marked by the dashed rectangle in (b)). Here, ε_1 determined from all resonances of each resonator are plotted as a function of the mode number n (compare equation (4.1)). ε_1-values of individual resonators clearly separate from each other, but ε_1-values measured by resonances of the same resonator roughly fit together. This shows that each resonator is influenced as a whole by the properties of the indium oxide sample, which is expected to vary from one resonator to the next on the macroscopic scale of a few millimeter by which the resonators are separated [11]. Differences in ε_1-values measured by resonances of the very same resonator are in turn stemming from the fact that each harmonic also itself probes different locations along the resonator, as can be seen e.g. in the E-field distribution along the resonator in Fig. 4.10 (e) (section 4.5). This again shows that variations in disorder along the indium oxide sample on the size of few mm reflect in varying ε_1. Similar variations as found in ε_1 both from one resonator to the next as well as within one resonator, are also expected to be found in Q and σ_1 respectively.

It has been expected that the dielectric constant of indium oxide is quite large [33, 39, 54] (at least above $\varepsilon_1 > 30$ [33]), although direct measurements of ε_1 so far were not possible [14, 33]. With the data of direct measurements of ε_1 acquired in this work it can now be confirmed that ε_1 is indeed quite large even at the very strong localization limit, the electron glass regime.

In section 6.1.1 a critical value for the dielectric constant $\varepsilon_{1,\mathrm{c}} \approx 100$ has been determined. $\varepsilon_{1,\mathrm{c}}$ decides whether the Coulomb interactions in indium oxide are expected to be larger or smaller then attractive Cooper-interactions mediated by phonons [33]. If $\varepsilon_1 > \varepsilon_{1,\mathrm{c}}$ then Coulomb interactions are

expected to be sufficiently screened so Cooper-pairs can form. However, if $\varepsilon_1 < \varepsilon_{1,c}$, as it is the case for almost all samples and disorders in the samples measured in this section, then Coulomb interactions cannot be assumed negligibly small. This means that the absolute values found for ε_1 in the electron glass regime presented in this section give evidence that Coulomb interactions indeed exceed Cooper-attraction and Cooper-pairs cannot form, following the Fermi-mechanism detailed in section 3.3. This also corresponds to $\delta > \hbar\omega_D$. For very strongly insulating indium oxide samples with very high disorder it is therefore found that electron interaction inhibits the formation of Cooper-pairs and local pairing is not possible.

It has to be kept in mind, that the density of states at the Fermi-energy ν_0 is kept constant across all samples with $\nu_0 \approx 1 \times 10^{45}\,\mathrm{J}^{-1}\,\mathrm{m}^{-3}$ as suggested by Ovadyahu [54, 212, 225] corresponding to an electron density of about $1 \times 10^{19} - 1 \times 10^{20}\,\mathrm{cm}^{-3}$ [49, 225, 226]. For the data shown in Fig. 6.15 (a) this does not play a role, as all quantities shown (ε_1 and $T_{0,\mathrm{Mott}}$) are directly measured in the experiment. For (b) however, the values on the horizontal axis are themselves dependent on ν_0 with $\xi_{\mathrm{Mott}} \propto \nu_0^{-1/3}$, meaning that here uncertainties in the value of ν_0 are reflected directly in the data, although uncertainties are mitigated to some extend due to the small exponent of $-1/3$. Comparing the relative relation of $\varepsilon_1(T_{0,\mathrm{Mott}})$ and $\varepsilon_1(\xi_{\mathrm{Mott}})$ of the different samples towards each other in (a) and (b) also shows that uncertainties in ν_0 probably are rather small, since the horizontal separation of the individual samples stays relatively constant.

Looking at the overall trend of ε_1-values including all electron glass samples shown in Fig. 6.15 (a) and (b), it is found that $\varepsilon_1(T_{0,\mathrm{Mott}})$ increases with

decreasing $T_{0,\mathrm{Mott}}$ and increases with ξ_{Mott}. This is expected, with the behavior following section 3.5.3, equation (3.34) [39]

$$\varepsilon_1 = a \cdot \alpha \frac{e^2 \nu_0}{\varepsilon_0} \xi^2 + \varepsilon_{1,\mathrm{Host}} \tag{6.14}$$

$$\text{and} \quad \varepsilon_1 = a \cdot \alpha \frac{e^2}{\varepsilon_0} \nu_0^{1/3} \left(\frac{16}{k_B} \right)^{2/3} T_{0,\mathrm{Mott}}^{-2/3}, \tag{6.15}$$

with $\varepsilon_{1,\mathrm{Host}}$ an additional offset value stemming from constant contributions of the "host"-material, meaning the positive ions of the background and the immobile valence electrons far from the Fermi energy, which could have sizable magnitude [33, 39, 54]. Note that equation (6.15) only depends on $\nu_0^{1/3}$, while (6.14) depends on ν_0 and $\xi_{\mathrm{Mott}}^2 \propto \nu_0^{-2/3}$. Uncertainties in ν_0 might again be more pronounced in the latter dependence while they are strongly mitigated in the first. Yet, since there seems to be no large difference between the data shown in Fig. 6.15 (a) and (b) both cases will be discussed interchangeably. Equations (6.15) and (6.14) are plotted in Fig. 6.15 (a) and (b) respectively. The dimension-dependent prefactor α is set here to $\alpha \approx 3$ corresponding to a three-dimensional system [39]. Additionally a constant offset of $\varepsilon_{\mathrm{Host}} \approx 10$ is introduced, which is of reasonable size being similar to the possible ε_1 of crystalline In_2O_3 [230, 231]. a denotes an additional prefactor to account for a possible suppression of ε_1.

The data is expected to follow three-dimensional dependence as the electronic properties of the samples are assumed to be three-dimensional. This is given since the hopping distance is smaller than the sample thickness with $r_{\mathrm{hop}} \approx \frac{3}{8}\xi_{\mathrm{Mott}} \left[(T_{0,\mathrm{Mott}}/T)^{1/4} \right] < d$ [49, 54] at least down to temperatures of several 100 mK (calculated with values from Tab. 6.2). At least below 1 K, $\varepsilon_1(T)$ is found constant (shown in later section 6.4.3), making the assumption of a three-dimensional system reasonable, since there is no distinct feature found in $\varepsilon_1(T)$ which would hint towards a change in dimensionality. The 3D behavior shown in Fig. 6.15 (a) and (b) fits well to the high-$T_{0,\mathrm{Mott}}$/low-

ξ_{Mott}-values of sample B, however values of sample C show slight vertical offset (better correspondence is found when extracting ξ directly from microwave data, detailed later in section 6.4.3). To explain the discrepancy, it has to be kept in mind that the horizontal axes are determined purely from DC-measurements. In this case it is assumed that the sample is uniform both at the location of the resonator as well as the Hall-bar. This however, might not be given to full extend, as already in ε_1 between resonators differences have been found (Fig. 6.15 (c)) and differences between transport properties at the location of the Hall-bar and the resonators cannot be excluded. It will be shown in section 6.4.3, that this can be circumvented with pure microwave measurements. Nevertheless it is confirmed that strongly localized indium oxide in the electron glass regime in general follows $\varepsilon_1 \propto \xi^2$ behavior expected for Anderson insulators [39, 232, 233], corresponding to the polarization of non-interacting electrons. Since no clear deviation from $\varepsilon_1 \propto \xi^2$ is found it is also possible to argue that the electrons in the samples interact neither by Coulomb repulsion nor by Cooper-attraction since e.g. for the latter this would inevitably lead to suppression of ε_1 [39] expected to a factor of about $2-3$ [119], compare section 3.5.3. While this suppression is not found in the electron glass samples, it is found in the local pairing samples, shown in section 6.5.2.

To catch this offset, an additional $\varepsilon_1 \propto \xi^2_{\mathrm{Mott}}$ has been fitted to the data of sample C, as shown in Fig. 6.15 (b) (dashed blue line), but with the additional scaling prefactor $a > 1$. It is found that the data is best described, when $a \approx 1.3$. This prefactor will be important in the later section 6.6.2, especially when compared to the local pairing samples, where smaller a is expected. For sample B, a is found to match the red dashed line for its highest disorder values, setting the prefactor to be $a \approx 1$. Here only the highest disorder values measured for sample B can be considered, as further data behaves unexpectedly, when evolving with decreasing disorder. With decreasing disorder (decreasing $T_{0,\mathrm{Mott}}$, increasing ξ_{Mott}), ε_1 of sample B does not match $\varepsilon_1 \propto \xi^2_{\mathrm{Mott}}$ with the expected scaling prefactors ($a = 1$,

$\alpha \approx 3$, $\nu_0 \approx 1 \times 10^{45}\,\mathrm{J}^{-1}\,\mathrm{m}^{-3}$). A slight increase is seen, but it is much weaker than expected (compare to red dashed line). An explanation for this might be, that the polarization is predominantly governed by $\varepsilon_{1,\mathrm{Host}}$ of the sample. It might be possible that the host polarization $\varepsilon_{1,\mathrm{Host}}$ is fixed during initial deposition of the sample, the further evolution of $\varepsilon_1(\xi_{\mathrm{Mott}})$ however, is then mostly dominated by the localized electrons close to the Fermi-energy. Additionally to this increase of localization length with the corresponding $\varepsilon_1 \propto \xi^2_{\mathrm{Mott}}$ however, there might be another process going on, as $\varepsilon_1(\xi_{\mathrm{Mott}})$ does not increase as strongly as expected but about half as quickly as expected for a three dimensional system. It is possible that $\varepsilon_1(\xi_{\mathrm{Mott}})$ is rather rigid even when ξ_{Mott} increases strongly. The reason for this is unclear as of yet, with the hope for clarification in future studies both experimentally and theoretical. The possibility that the reason for ε_1 staying relatively constant might be a variation of ν_0 is unrealistic, as ν_0 would have to decrease with aging, meaning it would have to decrease with less disorder and weaker insulation. While this is already unrealistic since it is expected to actually increase in this situation [226], this would have to be a very strong effect (on the order of $\Delta\nu_0 \propto \Delta T^2_{0,\mathrm{Mott}}$).

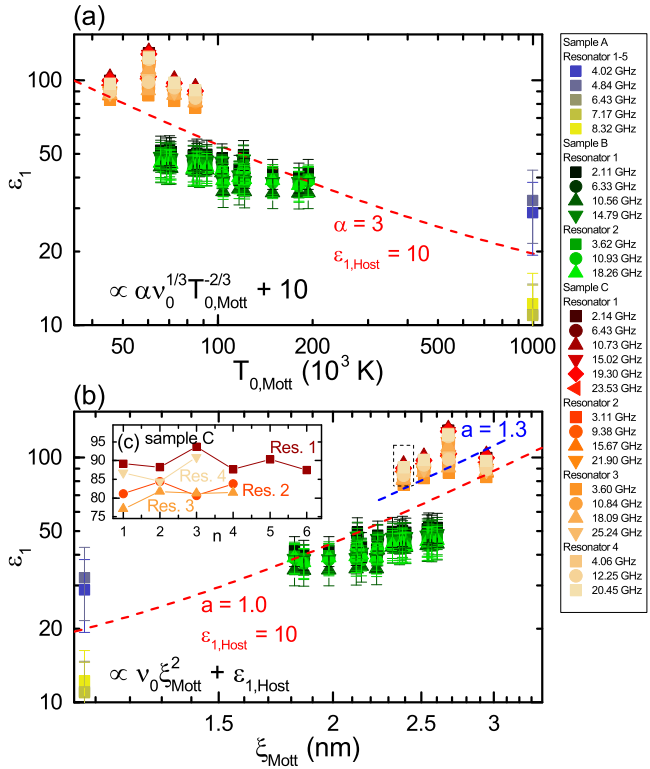

Fig. 6.15.: (a) $\varepsilon_1(T_{0,\mathrm{Mott}})$ of samples A-C as a function of the characteristic temperature $T_{0,\mathrm{Mott}}$ extracted from Mott VRH in DC-measurements. The dependence $\varepsilon_1(T_{0,\mathrm{Mott}}) = \alpha\frac{e^2}{\varepsilon_0}\left(\frac{16}{k_B}\right)^{2/3}\nu_0^{1/3}T_{0,\mathrm{Mott}}^{-2/3} + \varepsilon_{1,\mathrm{Host}}$ is shown in three dimensions (red, $\alpha \approx 3$), describing the data reasonably well. (b) $\varepsilon_1(\xi_{\mathrm{Mott}})$ as a function of the localization length ξ_{Mott}. The same fit is shown. Additionally, blue shows $\varepsilon_1(\xi_{\mathrm{Mott}}) = a \cdot \alpha\frac{e^2\nu_0}{\varepsilon_0}\xi_{\mathrm{Mott}}^2 + \varepsilon_{1,\mathrm{Host}}$ for sample C ($a \approx 1.3$). (c) $\varepsilon_1(n)$ as a function of mode number n for the measurement indicated in (b). ε_1 measured with resonance of the same resonator fit to each other, different resonators differ due to local sample differences.

6.4.3. Temperature-dependent conductivity

From the extracted values of resonance frequency and quality factor Q shown in Fig. 6.14 not only ε_1 can be calculated, but also the conductivity $\sigma_1 \propto \omega\varepsilon_2$, which is directly connected to the imaginary part of the complex dielectric constant ε_2, equation (4.55). This can be done as a function of temperature using temperature-dependent resonance frequency and $Q(T)$. An example of each is shown in Fig. 6.16 (a) and (b) respectively for the fundamental frequency of a resonator probing sample B. Upon initial deposition of the sample the resonance shifts to lower frequency as already seen before in the raw spectra of Fig. 6.14 (a). For higher temperatures, the resonance frequency under the influence of the sample follows the resonance frequency of the empty resonator very analogously. The form of which can be traced back to the increase of the penetration depth $\lambda_L(T)$ (equation (4.75)) and consequently the impedance Z with the resulting temperature dependence following equation (4.77) (a fit with corresponding parameters is shown with blue color in the figure).

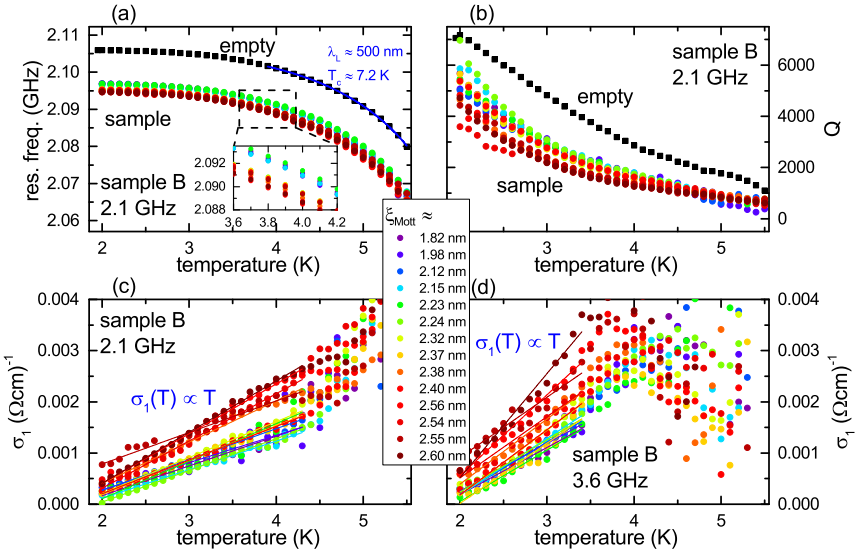

Fig. 6.16.: (a) Resonance frequency as a function of temperature of a resonator under the influence of sample B at different stages of aging. Black data shows the empty resonator. The resonance frequency is mainly influenced by the temperature-dependent change in penetration depth into conductor Nb, leading to an increase in impedance of the resonator (fitted in blue with parameters given). The inset shows a magnified region, in order to differentiate the data sets. (b) Quality factor $Q(T)$. $Q(T)$ is suppressed under the influence of the sample. (c,d) Conductivity $\sigma_1(T)$ for (c) the above resonance and (d) the fundamental of a second resonator. Linear Austin-Mott behavior $\sigma_1(T) \propto T$ is found.

$Q(T)$ (Fig. 6.16 (b)), shows more prominent differences between empty resonator and the resonator under influence of the sample. Where $Q_e(T)$ of the empty resonator decreases roughly linearly, $Q_s(T)$ under sample-influence decreases stronger than linear, which is a direct consequence of finite $\varepsilon_2(T)$ and conductivity $\sigma_1(T)$. From section 4.4 it is clear, that while the resonance frequency is largely affected by ε_1, Q_s is predominantly affected by ε_2 (for large Q_e, which is given here). From both the resonance frequency, as well as $Q_e(T)$ and $Q_s(T)$, the conductivity $\sigma_1(T)$ can therefore be calculated following the procedure detailed in section 4.4 with equations (4.53), (4.51) and (4.55). This is done for each temperature individually by comparing the resonator under the influence of the sample to the empty resonator. $\sigma_1(T)$ determined from values shown in (a) and (b) is shown in Fig. 6.16 (c). In Fig. 6.16 (d), $\sigma_1(T)$ for a resonance of another resonator on the same resonator-chip probing sample B is shown. In the temperature range above 2 K, $\sigma_1(T)$ is perfectly linear up to temperatures where the measurement precision gets too weak (due to diminishing Q of the Nb-conductor). This linearity in $\sigma_1(T)$ can perfectly be described with Austin-Mott behavior, equation (3.13), with $\sigma(\omega, T) = \frac{\pi^4}{384} e^2 \xi_{\mathrm{GHz}}^{d+2} \nu_0^2 k_B T \omega \ln^4\left(\frac{\nu_{\mathrm{ph}}}{\omega}\right)$ [43, 74, 75]. Here, the system is again assumed to be three dimensional $d = 3$, the full single-particle density of states is taken as $\nu_0 \approx 1 \times 10^{45}\,\mathrm{J}^{-1}\,\mathrm{m}^{-3}$ [54, 212, 225] and typical phonon frequencies are taken as $\nu_{\mathrm{ph}} \approx 1 \times 10^{13}\,\mathrm{Hz}$ ($\omega_D \approx 500\,\mathrm{K}$ [12, 33, 227, 228]). For given frequencies ω of the resonances this leaves ξ_{GHz}, the localization length, as the only fit parameter. Fig. 6.16 (c) and (d) show that Austin-Mott behavior describes the data very well. The fitted ξ_{GHz} are in the range $\xi_{\mathrm{GHz}} \approx 1.86\,\mathrm{nm} - 2.56\,\mathrm{nm}$ in very close range to ξ_{Mott} determined by DC-measurements showing very good agreement between microwave conductivity and DC-conductivity. ξ_{GHz} of each resonance will be shown as values on the horizontal axis in Fig. 6.18.

Good correspondence between microwave conductivity and DC-conductivity is also seen when looking at $\sigma_1(T)$ of sample C. This is shown in Fig. 6.17. (a) shows a temperature-range from 40 K down to 40 mK. It is expected

that $\sigma_1(T)$ decreases with decreasing temperature. At some point however the energy induced to the sample by the probing microwaves is larger than the thermal energy $\hbar\omega > k_B T$. When entering this regime, $\sigma_1(T)$ levels off, with the saturation value being frequency-dependent [65, 73]. In the regime $\hbar\omega \gg k_B T$ the transport in the sample is mainly consisting of photon-assisted hopping, whereas phonon-assisted hopping is negligibly small. This is the so-called zero-phonon regime [43, 44], where σ_1 is found to be temperature-independent. When comparing the guide to the eye of the DC-conductivity from Fig. 6.17 (a) to $\sigma_1(T)$ of the microwave measurements it is also apparent, that σ_1 measured at finite frequency is many orders of magnitudes larger than σ_1 measured by DC (suggested by extrapolation). This is expected [65, 73] since σ_1 at GHz-frequencies is completely dominated by photon contributions. The frequency dependence will be discussed later in section 6.4.6.

Fig. 6.17 (b) shows $\sigma_1(T)$ measured by microwaves for some selected resonances of (a) with (c) showing a magnified version of the low-frequency resonances. It is found, similar to sample B in Fig. 6.16, that above a certain temperature, where $\hbar\omega \ll k_B T$, $\sigma_1(T)$ again enters Austin-Mott behavior with linear dependence $\sigma_1(T) \propto T$ as expected (indicated by the green fits in the figure). This again can be used to extract ξ_{GHz} with equation (3.13).

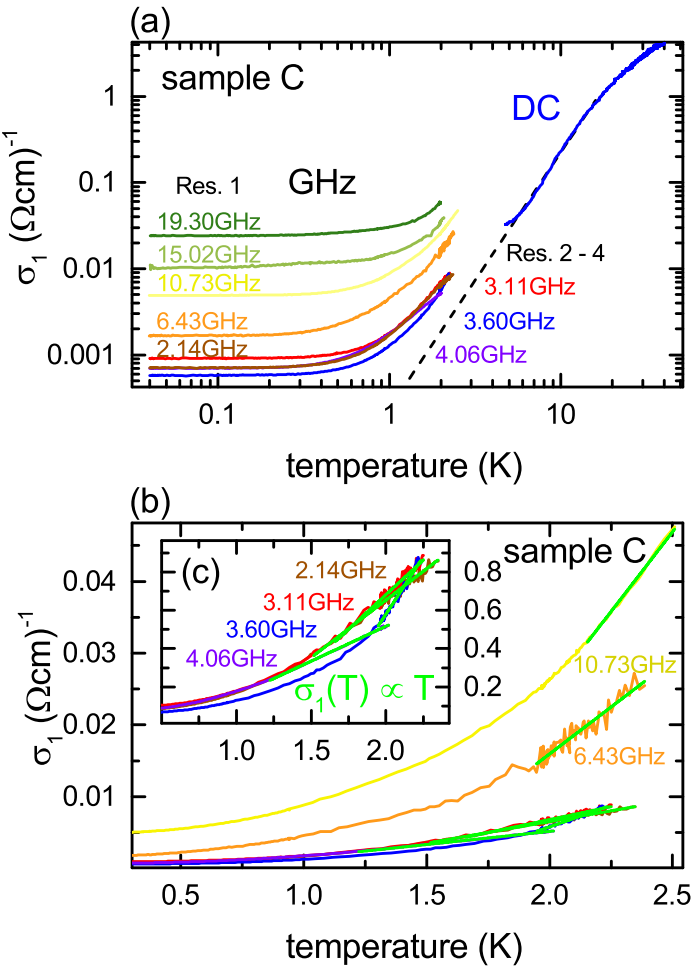

Fig. 6.17.: (a) $\sigma_1(T)$ measured by microwave resonances at several different frequencies as well as $\sigma_1(T)$ determined from DC-measurements. $\sigma_1(T)$ measured at GHz frequencies approaches $\sigma_1(T)$ measured by DC when going to larger temperatures, where $\hbar\omega \ll k_B T$, following Austin-Mott behavior. At $\hbar\omega \gg k_B T$ the zero-phonon regime with temperature-independent σ_1 is found. (b,c) Data of selected resonances from (a) with linear Austin-Mott fits.

6.4.4. Dielectric constant as a function of dynamic localization length

With the extracted ξ_{GHz} from $\sigma_1(T)$ from samples B and C in section 6.4.3, the localization length-dependent dielectric constant $\varepsilon_1(\xi_{\mathrm{GHz}})$ can be replotted, as shown in Fig. 6.18. Data from Fig. 6.15, as a function of ξ_{Mott} is plotted again

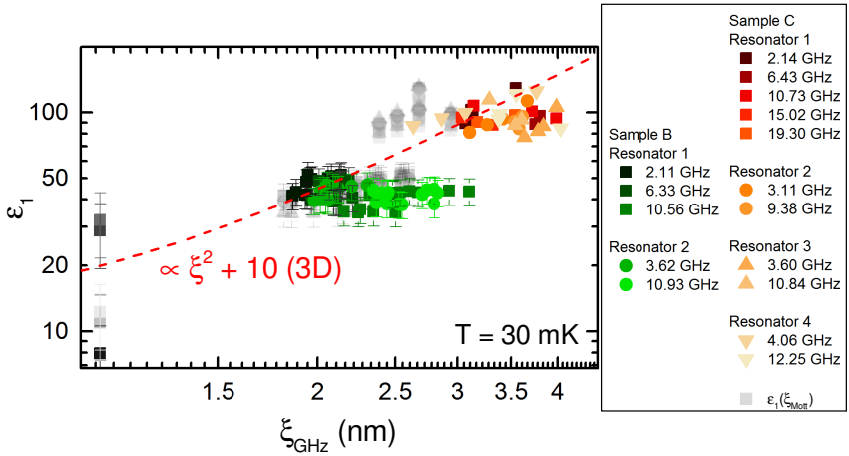

Fig. 6.18.: Dielectric constant $\varepsilon_1(\xi_{\mathrm{GHz}})$ as a function of localization length ξ_{GHz} determined from $\sigma_1(T)$. $\varepsilon_1(\xi_{\mathrm{Mott}})$-data with ξ_{Mott} from DC-measurements are shown in gray. $\varepsilon_1(\xi_{\mathrm{GHz}})$ of low ξ_{GHz}-values are well described by $\varepsilon_1 \propto \xi^2_{\mathrm{GHz}} + \varepsilon_{\mathrm{Host}}$-behavior.

in gray for comparison. It is found that for sample B, $\xi_{\mathrm{GHz}} \approx \xi_{\mathrm{Mott}}$, meaning that both microwave data and DC-data align well concerning the localization length. For sample C, ξ_{GHz} has been found larger than ξ_{Mott} to some extent, for most resonances. This shifts $\varepsilon_1(\xi_{\mathrm{GHz}})$ data to larger localization length, which makes $\varepsilon_1(\xi_{\mathrm{GHz}})$ align better with the three dimensional $\varepsilon_1 \propto \alpha\xi^2 + \varepsilon_{1,\mathrm{Host}}$ behavior, as it has been given before already, with $\alpha \approx 3$. Considering values of $\varepsilon_1(\xi_{\mathrm{GHz}})$ each for the lowest values of ξ_{GHz}, the data is well described by 3D scaling behavior of the dielectric constant, taking into account an

offset of about $\varepsilon_{\mathrm{Host}} \approx 10$. With this method it was therefore possible to acquire complete $\varepsilon_1(\xi_{\mathrm{GHz}})$-dependence entirely from microwave measurements. Direct comparison of ε_1-data to the localization length extracted directly at the resonator is possible giving the possibility to omit DC-measurements measured at spatial distance to the resonators. The measurement of ξ_{GHz} is performed directly at the region of the sample, where ε_1 is measured as well, reducing the influence of location dependent disorder variations on the data. This variation seems to be particularly prominent in the data of sample C, where the strongest change in localization length was found. Additionally it was found that during the aging the sample evolved differently at the location of the resonators compared to the location of the Hall-bars, since with ξ_{GHz} extracted from $\sigma_1(T)$ the data follows the trend $\varepsilon_1 \propto \xi^2_{\mathrm{GHz}}$ better, see e.g. resonances of resonator 3 and 4 following the red line, while for $\varepsilon_1(\xi_{\mathrm{Mott}})$ this was less clear.

However, it is again found that the variation between resonances and for different aging-stages can be quite large for some individual resonances. This again leads to large horizontal spread in the figure. This is particularly prominent for resonances with high frequencies ($> 10\,\mathrm{GHz}$). For these frequencies the zero-phonon regime ranges to higher temperatures, compare Fig. 6.17 (a), where the onset of the increase in $\sigma_1(T)$ for larger frequencies shifts to higher temperatures since $\sigma_1(T)$ saturates at larger value. This effectively limits the accessible temperature-range at which $\sigma_1(T)$ can successfully be fitted with Austin-Mott behavior. It is therefore found that the determination of ξ_{GHz} is more prone to errors at larger frequencies where establishing a clear linear dependence for Austin-Mott behavior is more difficult. This probably explains the spread of ξ_{GHz} for sample C where the temperature-range is additionally limited by losses increasing at temperatures only merely larger than the onset of the Austin-Mott-regime. For data of sample B this is found as well. Resonances in the single-digit GHz-regime correspond very well to each other and to the expected $\varepsilon_1(\xi_{\mathrm{GHz}}) \propto \xi^2_{\mathrm{GHz}}$ behavior. For resonances $> 10\,\mathrm{GHz}$ however an increase of ξ_{GHz} is found exceeding expected values,

whereas ε_1 stays roughly constant. Compared to ξ_{Mott}, it is found that resonances below 10 GHz shift less while resonances above 10 GHz shift stronger. Another interpretation of this could again be that $\varepsilon_{1,\mathrm{Host}}$ is fixed upon deposition. While the localization length increases upon aging, ε_1 stays rigid, being mostly defined by the background positive ions and valence electrons, which are not influenced by the localization length. However, at this point this is merely of speculative nature, since it is only found in one particular sample. To further investigate this on a systematic level, additional samples in similar disorder regimes could be investigated in the future.

6.4.5. Temperature-dependent dielectric constant

The dielectric constant $\varepsilon_1(T)$ can also be determined as a function of temperature. For this the resonance frequencies as well as the quality factors of both the resonator under influence of the sample, see e.g. Fig. 6.16 (a) and (b), as well as the empty resonator are again compared for each temperature individually, following the procedure shown in section 4.4. For samples B and C the resulting values of $\varepsilon_1(T)$ are shown for multiple resonances in Fig. 6.19 (a) and (b) and for different aging-stages in (c) and (d) respectively. Error-bars as shown in Fig. 6.15 are omitted here for clarity. It is found that for sample C, $\varepsilon_1(T)$ varies only little over the temperature range of mK up to 2 K. (b) and (c) show that $\varepsilon_1(T)$ is roughly constant and only increases above 2 K. The vertical offset in (b) corresponds to the difference between ε_1-values for different resonances shown in Fig. 6.15 and 6.18, which mainly stems from the difference in sample properties at the different resonator locations. This separation between ε_1-values of individual resonances remains about constant over the total temperature range. $\varepsilon_1(T)$ for one resonance at different stages of aging, shown in (d) shows that the temperature-dependence of $\varepsilon_1(T)$ changes with increasing localization length. Towards larger ξ the onset of the slight increase of $\varepsilon_1(T)$ shift to lower temperatures. For sample B (Fig. 6.19 (a) and (c)) the temperature range $2 - 5$ K is covered. It is

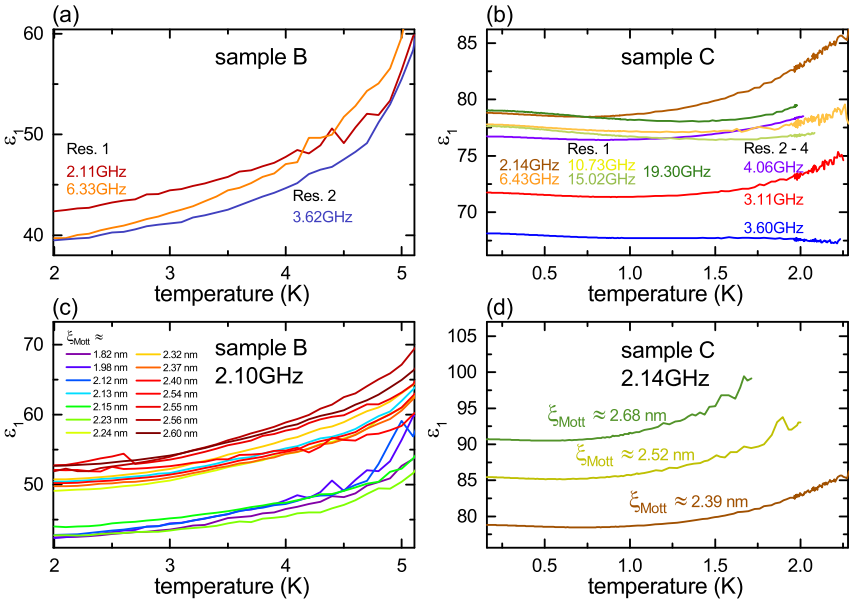

Fig. 6.19.: (a,c) $\varepsilon_1(T)$ of sample B for (a) several different resonances of two separate resonators and for (c) different stages of aging of the sample. An increase in $\varepsilon_1(T)$ is found. (b,d) $\varepsilon_1(T)$ of sample C respectively. In the mK-regime $\varepsilon_1(T)$ is mostly constant with a slight increase above 1.5 K.

found that $\varepsilon_1(T)$ increases towards higher temperatures with a first moderate increase of about 20 % up to $4 - 4.5$ K followed by a more steep increase above, similar to what is found in sample C. The temperature-dependence is quite rigid with the shape of $\varepsilon_1(T)$ staying about the same for all stages of aging.

The increasing $\varepsilon_1(T)$ towards larger temperatures might be explained by increasing relaxation processes due to phonons [65]. Another striking feature, however, is $\varepsilon_1(T)$ of sample C forming a minimum in the temperature range of about 1 K. It is only found for electron glass samples at low temperatures

$< 2\,\mathrm{K}$, but not for local pairing samples, where such a minimum is absent with $\varepsilon_1(T)$ being mostly constant below 1 K (see later section 6.5.4). Similar features have been seen before [65, 234] in a Fermi-glass/electron glass system although in a different compound, namely in (bulk) Phosphorous-doped Si [65, 234]. It might be an inherent property of electron glass systems at low temperatures, although an explanation is missing. Hering et al. [65] find the location of the minimum to be localization-dependent, shifting to larger temperatures for stronger disorder. This is apparent also in the data shown in Fig. 6.19 (d), where with larger disorder also the minimum shifts to larger temperature. Sample B might show the minimum just at the edge but outside the temperature-range for the low-ξ_{Mott} states. So the minimum found in the temperature-dependent dielectric constant $\varepsilon_1(T)$ might be inherent to electron glass samples, however, no explanation of the origin of this phenomenon is currently known [65], yet further study in this direction might be worthwhile.

6.4.6. Frequency-dependent conductivity

In Fig. 6.17 (a) it could already be seen, that the conductivity σ_1 increases for higher frequencies at fixed temperature. At the base temperature of 25 mK however, sample C is in the zero-phonon regime [43, 44] (where $\sigma_1(T)$ is constant [65, 73]), meaning that here thermally excited phonons do not contribute to the conductivity but only photon-assisted hopping processes enhance σ_1. Lowest temperatures for sample B are about 2 K. Here the zero-phonon might not entirely be established, which makes the following analysis for sample B more of an upper estimate calculation. At base temperature the frequency-dependent conductivity $\sigma_1(\nu)$ is extracted for each resonance. Resulting values are displayed in Fig. 6.20 (a). $\sigma_1(\nu)$ increases strongly with ν, which is expected from hopping mechanisms enhanced by hybridized Mott

resonances, see section 3.1. The general trend follows $\sigma_1(\omega) \propto \omega^2 \ln^4(\delta/\omega)$ very well. This is shown by the dashed lines, which are fits of the form

$$\sigma_1(\omega) = a \cdot \frac{\pi^2}{3} e^2 \xi^5 \nu_0^2 \hbar\omega^2 \ln^4\left(\frac{\delta}{\hbar\omega}\right) \tag{6.16}$$

$$\Rightarrow \sigma_1(\omega) = a \cdot \frac{\pi^2}{3} e^2 \left(\frac{16}{k_B T_{0,\mathrm{Mott}}}\right)^{5/3} \nu_0^{1/3} \hbar\omega^2 \ln^4\left(\frac{k_B T_{0,\mathrm{Mott}}}{16\hbar\omega}\right). \tag{6.17}$$

following Mott-behavior, equation (3.11). The localization length ξ has been expressed with the directly measured value of $T_{0,\mathrm{Mott}}$ via $\xi = [16/(\nu_0 k_B T_{0,\mathrm{Mott}})]^{1/3}$ (equation (3.2)) and the energy level splitting by $\delta = k_B T_{0,\mathrm{Mott}}/16$ (via equation (3.25)).

For the samples in the electron glass regime it holds, that the energy level splitting δ is in the range of several 100 meV. Compared to the maximum frequencies used here, which are in the range of about 25 GHz, corresponding to an energy of about 0.1 meV, this is much greater by more than three orders of magnitude. In this strong $\delta \gg \hbar\omega$-regime it is expected, that contributions to hopping by Mott resonances are additionally suppressed compared to simple Mott arguments [33, 39]. This has been derived and motivated in section 3.5.4, where numerical studies [33] show that contributions to $\sigma_1(\omega)$ are found smaller if $\delta \gg \hbar\omega$ by many orders of magnitude. To account for this, equation (6.17) has been extended by an additional prefactor a. This prefactor will be the only fit parameter left, as $T_{0,\mathrm{Mott}}$ is taken from DC-measurements and $\nu_0 \approx 1 \times 10^{45}\,\mathrm{J}^{-1}\,\mathrm{m}^{-3}$ [54, 212, 225] is taken constant.

The sample-dependent factor a is displayed in Fig. 6.20 (a) for samples B and C. In the case of sample C, a has been found similar for all stages of disorder and a mean value is displayed. For sample B a mean value of the first several stages of aging is taken, as the sample develops slightly unexpected for later stages of disorder (discussed below). The fitted prefactor amounts to about $a_C \approx 0.33$ (sample C) and $a_B \approx 0.2$ (sample B) and shows that $\sigma_1(\omega)$ is indeed reduced compared to the values expected by simple Mott

behavior. It is therefore confirmed that the conductivity follows regular Mott behavior with $\sigma_1(\omega) \propto \omega^2 \ln^4(\delta/\hbar\omega)$ although with reduced contributions by the hybridized Mott resonances. Since $a_B < a_C$ it can be assumed that this effect enhances with larger ratios of $\delta/\hbar\omega$, meaning that for stronger localization also the suppression increases. This holds even when assuming the value of $a_B \approx 0.2$ to be an upper estimate.

Unfortunately there are no exact numerical studies on the magnitude and the predicted values for this suppression as of yet [123]. Theoretical predictions are limited to qualitative descriptions of this suppression [33, 39]. The experiments shown here may therefore give food for further quantitative numerical studies.

As a function of disorder, σ_1 is shown in Fig. 6.20 (c). The vertical spread for each state of disorder here is the strong frequency-dependence discussed above. The data is expected to follow $\sigma_1(T_{0,\mathrm{Mott}}) \propto T_{0,\mathrm{Mott}}^{-5/3} \ln^4(T_{0,\mathrm{Mott}}/\mathrm{const.})$, from equation (6.17). This might be found to weak extent in the data when comparing similar frequencies across the two samples as done in (b) for selected resonances in the range $2.1 - 4\,\mathrm{GHz}$ (sample B deviates for lower disorders, so only larger disorders can be considered). However, the dependence on the disorder is only very weak with small exponent $T_{0,\mathrm{Mott}}^{-5/3}$ (plus logarithmic contributions) and is therefore hard to clearly establish in the given data. Additionally the factor a cannot be accounted for quantitatively. It is also seen that sample B does not show an increase of $\sigma_1(T_{0,\mathrm{Mott}})$ with decreasing disorder, which is unexpected, with the reasons being currently unknown. The sample not being completely in the zero-phonon regime is not a valid reason for this phenomenon, as Austin-Mott behavior (equation (3.13)) is dependent both on temperature and disorder and a decrease in disorder therefore affects σ_1 at all temperatures equally (this is shown for local pairing samples in a later section 6.5.4). Sample B is the only sample that shows this less-then-expected dependence on disorder and the current understanding is lacking. It may be worth to study a similar sample in future experiments to gain insight into this issue.

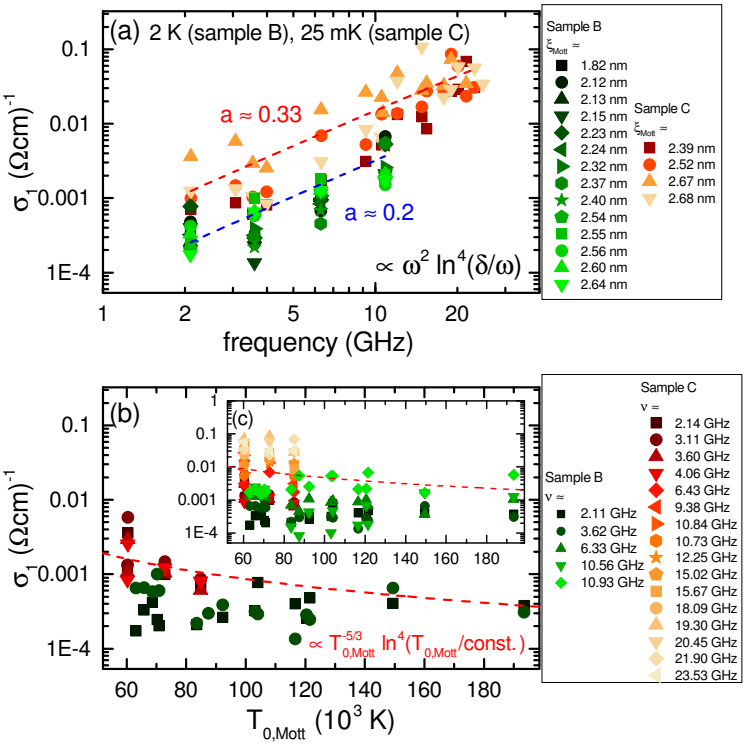

Fig. 6.20.: (a) Conductivity $\sigma_1(\nu)$ as a function of frequency ν for many resonances probing electron glass samples B and C at different stages of disorder. $\sigma_1(\nu)$ shows good correspondence to Mott-behavior $\sigma_1(\omega) \propto \omega^2 \ln^4(\delta/\hbar\omega)$ although with reduced prefactor, indicating hopping of non-interaction single-electrons with smaller contribution of the hybridized Mott resonances. Fits are shown as dashed lines, with the suppression factor a given in the plot. (b) $\sigma_1(T_{0,\mathrm{Mott}})$ as a function Mott activation temperature $T_{0,\mathrm{Mott}}$ for selected resonances in the range $2.1 - 4\,\mathrm{GHz}$. Only weak dependence is expected $\sigma_1(T_{0,\mathrm{Mott}}) \propto T_{0,\mathrm{Mott}}^{-5/3} \ln^4(T_{0,\mathrm{Mott}}/\mathrm{const.})$ which might be seen across samples (sample B deviates strongly). (c) $\sigma_1(T_{0,\mathrm{Mott}})$ for all resonances and a guide to the eye for resonances at $\sim 10\,\mathrm{GHz}$.

6.4.7. Summary

In this section 6.4, the electron glass regime has been of prime interest. For these samples, the charge carriers are confined to very small areas of $< 3\,\mathrm{nm}$, resulting in very high energy level splitting exceeding any possible pairing gap. Three different samples have been investigated as a function of disorder, temperature and frequency. The main result is that these highly disordered indium oxide samples can perfectly be described as Fermi-glass with their behavior mostly predicted by (simple) Mott arguments. Mott variable range hopping is found in charge transport measurements, which crosses over to Efros-Shklovskii variable range hopping upon cooling, indicating the opening of a Coulomb soft-gap. This hopping behavior continues down to lowest accessible temperatures with no sign of a crossover to potential activated behavior evoked by a hard gap.

The dielectric constant as a function of disorder is reminiscent of typical electron glass behavior with the expected $\varepsilon_1 \propto \xi^2$ dependence. The prefactor is found to fit three dimensional systems with no suppression, pointing towards the lack of electronic pairing (which would otherwise lead to reduced values of ε_1) and the localization of individual single-electrons. The low-temperature microwave conductivity $\sigma_1(\omega)$ shows typical Mott behavior where Mott resonances are the main contributors to photon-induced conductivity. Due to very strong localization, the contributions by these resonances are somewhat reduced, however. As a function of temperature, Austin-Mott behavior is found confirming simple hopping, successfully bridging the gap between microwave conductivity and DC-transport.

Concluding, samples A-C are electron glass samples with very strong localization, which behave like typical Mott Fermi-glass systems. No sign of a pairing gap is found whatsoever.

6.5. Local pairing regime

In this section, samples of the local pairing regime will be discussed. This includes samples D-G, see section 6.3. All of these samples show simple activated behavior at low temperatures in DC. The derived energy level splitting for these samples is smaller than the Debye-energy $\delta \ll \hbar\omega_D$ with δ being calculated from the localization length ξ_{Mott} determined by DC-measurements (section 6.3). The activated behavior found and the size of the energy level splitting point towards the possibility that in these samples local pairing occurs. This means that the electrons pair together forming immobile Cooper-pairs localized in space [12, 33]. At first the DC-transport will be discussed in the next section after which the dielectric properties and the conductivity are discussed in the following sections.

6.5.1. Transport

For all local pairing samples, DC-measurements were performed using the procedure detailed in section 4.9. Compared to the electron glass samples, the local pairing samples D-G reach high resistance values only at lower temperatures, which is expected since their amount of disorder is smaller compared to the electron glass samples. Typical temperature ranges for the following evaluation of transport properties are $1\,\mathrm{K} < T < 40\,\mathrm{K}$. At temperatures of about $> 15\,\mathrm{K}$ variable range hopping (VRH) behavior is found as Mott VRH with $T^{1/4}$-dependence. This is seen in Fig. 6.21 (a), where for all local pairing samples (at one fixed aging state) the sheet resistance $R_s(1/T^{1/4})$ as a function of Mott VRH $1/T^{1/4}$-behavior is shown with linear fits performed in the hopping regime. From the fits, characteristic temperatures $T_{0,\mathrm{Mott}}$ can be extracted. The localization length ξ_{Mott} can be found using equation (3.2) with $\xi_{\mathrm{Mott}} = \left(\frac{16}{\nu_0 k_B T_{0,\mathrm{Mott}}}\right)^{1/3}$. Typical values have been shown in section 6.3 in Tab. 6.2, where it is seen that for the local pairing samples D-G, $T_{0,\mathrm{Mott}}$ is in the range of thousands down to hundreds of K and consequently ξ_{Mott}

is in the range up to above 10 nm. However, here again it has to be kept in mind, that ξ_{Mott} in Tab. 6.2 is calculated using constant density of states at Fermi-energy $\nu_0 = 1 \times 10^{45}\,\mathrm{J}^{-1}\,\mathrm{m}^{-3}$ [49, 225, 226]. For samples close to the transition, ν_0 is expected to increase [226]. For the calculation of ξ_{Mott} these effects will not be considered however, as the specific development of ν_0 of the samples investigated is unknown. Nevertheless the acquired magnitudes of ξ_{Mott} seem reasonable, when comparing the samples to each other.

At temperatures of a few K, VRH transitions over to simple activated behavior, as depicted in an Arrhenius-plot in Fig. 6.21 (b). This activated behavior found in all local pairing samples is evoked by the emergence of the pseudogap Δ_p, leading to a hard-gap insulator (c.f. section 3.5.2) and might therefore be a first indication for single-electrons pairing to immobile, localized Cooper-pairs. Typical temperatures at which the VRH transitions to activated behavior are found to be about 4 K. This corresponds well to typical onset-temperatures at which Cooper-pair formation begins, as seen e.g. with the preformation of Cooper-pairs shortly before the onset of global superconductivity in tunneling experiments (section 6.1, Fig. 6.1 [28, 32]). Opposed to the samples studied in tunneling experiments however, the samples shown in this chapter will not transition to a globally superconducting state since $\Delta_p < \delta$, yet the fingerprints of Cooper-pairing are still seen in $R_s(1/T)$.

The temperature-dependence found for R_s already gives clear indication that although the single-electrons in the disordered amorphous thin-film sample are further and further restricted in their conduction and transport the lower the temperature goes, they can still form localized Cooper-pairs without global coherence [8, 33]. These Cooper-pairs are spatially confined to certain areas or "puddles" [28, 47] with their size being on the order of the localization length ξ. This ξ is the same length scale, which is also responsible for Mott VRH found at higher temperatures ($T > 15\,\mathrm{K}$). The reason for this length scale being universal both for VRH but also for the confinement of Cooper-pairs is the fact that superconductivity in indium

oxide (either local (high disorder) or global (low disorder)) is mediated by relatively weak BCS coupling [8, 12, 33]. This makes it a relatively weak effect [8] without modifying the spatial dependence strongly. This would be different if the coupling is assumed to be strong, where ξ might be different depending on whether the system is in the VRH regime (high-T) or in the (local) superconducting regime (low-T).

Fig. 6.21 (c) shows the resistivity $\rho(1/T)$ for all samples at fixed stages of aging as a function of $1/T$ (Arrhenius-plot). From this, the resistivity $\rho(4\,\mathrm{K})$ at fixed temperature of 4 K can be extracted as shown in the figure. It is found that $\rho(4\,\mathrm{K})$ is strongly sample and aging dependent and can be used well as a parameter to characterize the disorder state. Typical values have been given in Tab. 6.2 and are in agreement with previous studies [10, 224]. From Fig. 6.21 (c) it is also obvious that the temperature-dependence of $\rho(1/T)$ behaves equal to that of the sheet resistance $R_s(1/T)$ (since they are connected only by the sample thickness, equation (4.88)) giving equal slope of the linear fit.

Fig. 6.21 (a)-(c) only show one particular state of aging of each local pairing sample measured. However, similar to the sample in the electron glass regime, the disorder in the local pairing samples also changes between individual measurements. On the one hand, they age with storage time at room temperature, where repeated measurements with resting time in between typically give continuous decrease of disorder and insulation strength. On the other hand, they age when being annealed at 50 °C, with the procedure detailed in section 6.2. Both methods, leaving the samples to rest at room temperature in between measurements and purposely annealing them at higher temperatures have been employed for the samples shown here. With this, the samples typically became less insulating with time and a wide range in different amounts of disorders, localization length and insulation strengths could be covered. An example for such a decrease in insulation strength is shown in Fig. 6.21 (d), where $R_s(1/T)$ is shown for sample E at different stages of aging. Fitted values of T_0 are given in the legend and show the

Tab. 6.4.: Activation energy T_0 of all local pairing samples S. Ranges are given, since each sample has been measured multiple times at different stages of aging.

S	T_0 [K]
D	15.3 - 12.2
E	17.3 - 10.0
F	9.6 - 8.2
G	6.5 - 5.8

sample continuously getting more conductive. This is mainly due to the localization length ξ increasing, see equation (3.31) (section 3.5.2).

In total, including all samples, T_0 reaches from about about 17 K (sample E) down to about 6 K (sample G), as detailed in Tab. 6.4, meaning that it covers a very large range of insulation strength on the insulating side of the SIT. The largest values of $T_0 \sim 15 - 17\,\mathrm{K}$ are at the very edge of the local pairing regime shortly before entering the electron glass regime. In previous studies maximum values in the range of $T_0 \approx 15\,\mathrm{K}$ have been found [8, 19, 40]. For even higher disorder the energy level splitting would be larger than the Debye energy $\delta > \hbar\omega_D$ and even local pairing would not be possible anymore (Tab. 6.2 shows already that for some stages of sample D, $\delta \lesssim \hbar\omega_D \sim 50\,\mathrm{meV}$). On the lower end, $T_0 \approx 6\,\mathrm{K}$ is already quite close to the transition, although it is not clear how low T_0 could go before the samples become globally superconducting. As a comparison, sample H was already globally superconducting with $T_c \approx 0.5\,\mathrm{K}$ and an onset of coherent superconductivity around 2 K, see Fig. 6.10 in section 6.3.1. Shortly above the global superconducting transition sample H still showed activated behavior with $T_0 \approx 2.3\,\mathrm{K}$. This has also been shown in earlier works [10], where samples with $T_0 \sim 2\,\mathrm{K}$ still go superconducting when the temperature is low enough, as shown e.g. in Fig. 6.3 (b). The extrapolated curve in

Fig. 6.3 (b) also suggest that samples with activation energies up to $T_0 \approx 4\,\mathrm{K}$ might still become superconducting at mK-temperatures. The extend of the extrapolated curve estimating these T_0-values is probably not entirely correct (especially since it is usually applicable only for larger values of $k_F l$ [10]), however, combined with the data of sample H it means that the SIT does not necessarily have to be at $T_0 \approx 0\,\mathrm{K}$ as one might initially assume, but at finite T_0 somewhere $T_0 > 2.3\,\mathrm{K}$. Sample G therefore might not be too far from the transition to the (global) superconductor regime.

From the data shown in Fig. 6.21 (a) and (b) it is clear, that both $T_{0,\mathrm{Mott}}$ and T_0 are a good characterization parameters for the amount of disorder in the sample and its insulation strength. In the following, both will therefore be used to characterize and compare the samples to each other and to find relevant scaling predictions.

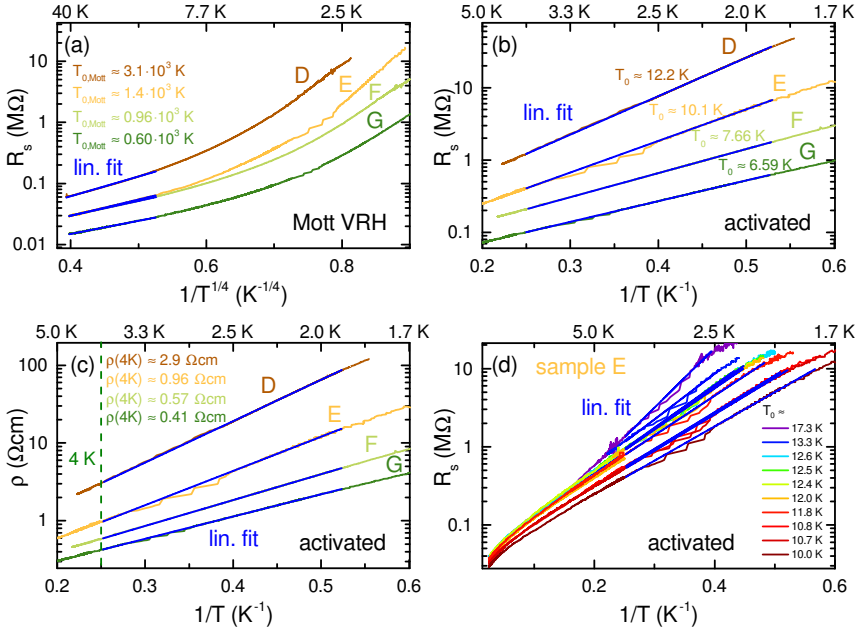

Fig. 6.21.: (a,b) Sheet resistance R_s as a function of (a) $1/T^{1/4}$ (Mott VRH) and (b) $1/T$ (Arrhenius plot). Mott VRH is found for temperatures $T > 15\,\mathrm{K}$, whereas simple activated behavior is found below $4\,\mathrm{K}$. Characteristic parameters can be extracted from linear fits. (c) Resistivity $\rho(1/T)$ as a function of $1/T$. $\rho(1/T)$ shows activated behavior as well. $\rho(4\,\mathrm{K})$ can be extracted at $4\,\mathrm{K}$ (dashed line) as a characterizing parameter of the sample. (d) $R_s(1/T)$ of sample E for several different stages of aging. T_0 is found as the characterizing parameter.

6.5.2. The insulator with (multi-)fractal local superconductivity

The goal of this section is to investigate the dielectric constant and the conductivity of amorphous indium oxide samples in the local pairing regime with the aim to find indications of multifractality of the localized electronic eigenstates. As shown from a theoretical standpoint in sections 3.5 and from the experimental side in section 6.1, indium oxide is expected to have local pairing of the electrons to localized Cooper-pairs, for which the electronic eigenstates have to be (multi-)fractal (section 3.5.1). As a consequence, the resulting electronic state should have strong inhomogeneity (section 3.5.2) although the structural form of the underlying indium oxide (the "host lattice") is homogeneous. While tunneling experiments on conducting samples (section 6.1, Fig. 6.1) indeed show granular electronic structure [28], with the possibility to infer that this might be evoked by multifractality, although this is not unambiguously settled [8, 14, 34]. Further evidence for the fractality of the electronic eigenstates could be obtained by looking at the influence of fractality via its fractal dimension D_2 on the scaling of some physical observables such as ε_1 and σ_1. This will be shown in the following.

Another long standing question in insulating indium oxide is the role of Coulomb interactions [8], see section 6.1.1. While for other materials not only the global superconductivity but also the superconducting gap itself are continuously suppressed on increasing the disorder (Finkelstein mechanism [29, 30], section 3.3), which is due to the Coulomb interactions between electrons increasing with increasing disorder, in indium oxide only the global superconductivity is suppressed while Cooper-pairing remains active. Whether Coulomb interactions are effectively weakened enough so the Cooper-attraction still remains dominant depends predominantly on the strength of the screening and consequently on the magnitude of the dielectric constant. Absolute values of ε_1 therefore will also give valuable insight into the mechanisms at play in indium oxide.

To measure ε_1 and σ_1 indium oxide samples have again been deposited on top of coplanar waveguide resonators. From the resulting resonance shift and the decrease in Q, ε_1 and σ_1 of the samples can be evaluated, as detailed in section 4. Spectra of two of such resonators are detailed in Fig. 6.22. (a) and (b) show resonances of a total of four resonators from two twin pairs of different geometry (different S and W, given in the figure), where each one resonator probes sample D. The inset of Fig. 6.22 (b) shows a top-view of the resonator-chip with the sample marked in blue covering half of the resonators leaving the other half uncovered. This is reflected in the spectra in (a) and (b), where black shows the spectra before deposition of the sample. Both resonances of the two twin resonators each have roughly similar frequency and quality factor Q. Slight differences are due to small imperfections remaining from the lithography process or the etching of the Nb conductor layer. Upon applying the sample, the resonance of the resonator covered by the sample shifts to lower frequencies and loses Q, while the uncovered twin resonator remains constant throughout the total life cycle of the sample. This ensures, that the reference data stays valid even if the sample ages with time. The resonator in (a) here shows larger relative shift than the one in (b). This is due to the difference in geometry, where the first has smaller geometry than the latter, resulting in larger sensitivity to the sample properties.

As a function of T_0 determined by DC-measurements, the resonance frequency and Q are plotted in Fig. 6.22 (c). It is found that for lower T_0, meaning a more conductive sample, the resonance frequency as well as Q tend to decrease. At some point Q even decreases below 1×10^3. In this regime the resonances get very broad and the fits with a complex Lorentzian (c.f. section 4.8) get unreliable. This is why for most samples at some point measurements on the very same but aged sample stop to work, as resonances vanish, as can be seen in particular in Fig. 6.22 (a), where for $T_0 = 12.2\,\mathrm{K}$ no resonance is seen anymore. This can be mitigated to some extend by making resonators with larger dimensions (S and W), since then effectively the losses of the sample on the resonators are reduced. However, with larger dimensions

also the sensitivity to the sample properties strongly reduces due to the filling factor of the sample getting smaller (c.f. section 4.3, equation (4.28)). It is therefore necessary to balance both effects. This is also one reason why it is technically not possible to measure properties of a single indium oxide sample that starts very strongly disordered and moves towards the SIT until it gets superconducting, but rather multiple samples have to be measured.

Fig. 6.22 (d) shows example spectra of two resonators on a different resonator-chip probing sample G. Since sample G is expected (due to the deposition parameters) to be quite close to the SIT, where σ_1 might be large, losses have to be strongly reduced. This is achieved by taking resonators with very large dimensions ($W = 50\,\mu\text{m}$) and covering it only partially with the sample. The covered part being at the tail end of the resonator, where the electric field is low (c.f. section 4.5.2, Fig. 4.10). This again reduces sensitivity, which is also reflected in (d), where the resonator which is completely covered by the sample shifts much further than the sample which is covered only partially. (f) shows the resonance frequency and Q for both resonators. It is again seen that with decreasing T_0 both resonance frequency and Q in general tend to lower values. For the resonator at 2.48 GHz there are also the directly measured quality factors Q_{pc} of the partially covered resonator shown and Q_{cov} the hypothetical quality factor if the sample would cover the total resonator (c.f. section 4.5), which is necessary for further calculations. Naturally, Q_{cov} is much smaller than Q_{pc}.

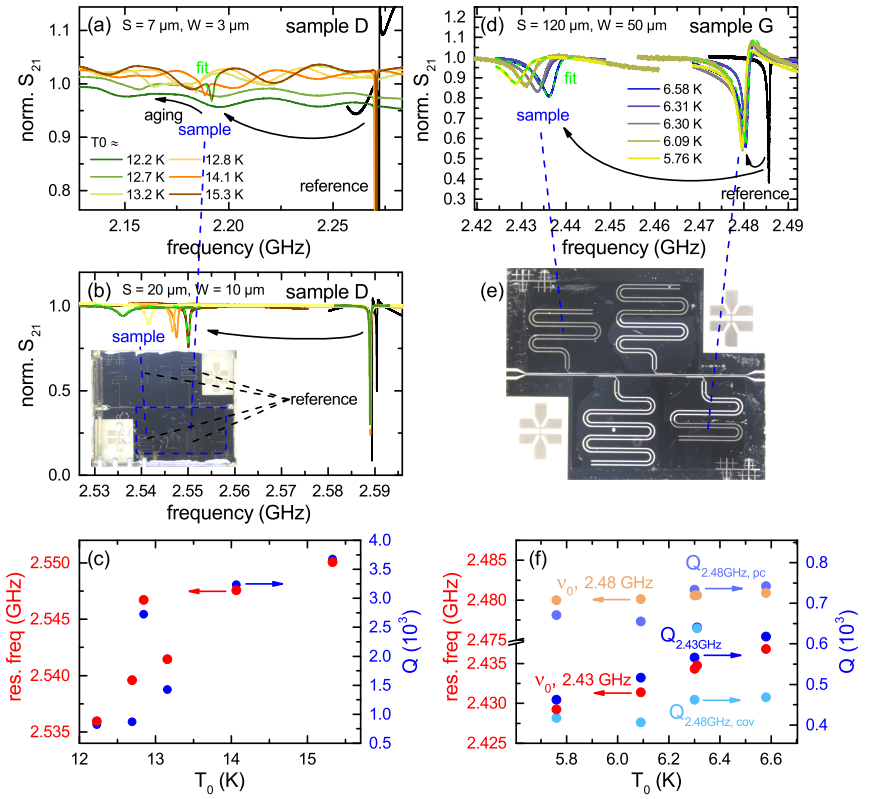

Fig. 6.22.: (a,b) Spectra each of one resonator under the influence of sample D and a twin reference resonator. The influence of the sample shifts the resonances and reduces Q. The inset in (b) shows a top-view on the resonator-chip. (c) Resonance frequency and Q of the resonator shown in (b). Both tend to decrease with a more conductive sample (smaller T_0). (d) Spectra of two resonators covered by sample G. One is covered completely, one partially, compare to (e). (f) Resonance frequency and Q of the two resonators shown in (e) as a function of T_0. Again both decrease with a more conductive sample.

From the shift in resonance frequency and the change in quality factor Q, both ε_1 and σ_1 can be calculated, as shown in section 4.4. This has been done for all local pairing samples at the different stages of aging and with multiple resonators. The results are shown in Fig. 6.23. The values of ε_1 cover a wide range from about 100 to about 600 and increase towards smaller T_0. Each set of data points at a fixed value of T_0 is an individual cool-down of the sample, where all shown resonances have been measured. The data shown has been acquired at base temperature of about 30 mK. (c) shows the very same data but with a range down to $T_0 = 2\,\mathrm{K}$ and an extrapolation of the fit that will be discussed in the following. Since it is possible that almost critical indium oxide might go globally superconducting only at values of T_0 in the range slightly above $T_0 \sim 2\,\mathrm{K}$ (see section 6.3.1 and Fig. 6.3 (b)) it might be possible that $T_0 \gtrsim 2\,\mathrm{K}$ are lowest possible disorder values where ε_1 could be extracted, although this is beyond the experimental range in this work. In order to give an idea as to how large ε_1 might possibly grow, the data from Fig. 6.23 (a) is replotted in (c), if it would continue following the scaling behavior that has been found. It shows that it might possibly grow up to $\varepsilon_1 \sim 2000$. This will further become important in the discussion on the possibility of a Josephson-junction-array superinsulator in section 6.6.1.

The vertical spread of the measured ε_1 data in (a) again stems from spatial variance of the sample properties across the macroscopic dimensions of the resonator-chip. Since the sample has quite large lateral dimension and each resonator is spatially separated from neighboring resonators by up to a few mm, see e.g. Fig. 6.22 (e), the sample properties each resonator is subjected to can vary from resonator to resonator. This is supported by the fact that each resonator roughly measures similar values ε_1 with both its fundamental and its higher harmonic, as shown in Fig. 6.23 (b) where values of ε_1 measured by the three different resonators probing sample G separate in bundles from each other. Differences between the different harmonics in turn can be explained by the varying field distribution of the standing waves in the resonator depending on the mode number n, see e.g. Fig.4.10 (e). These different distributions in

turn probe different areas along the resonator to varying extend, leading to varying influence of the sample on each resonance accordingly. Furthermore, the spatial separation of the Hall-bar measuring DC-conductivity from which T_0 is acquired, also leads to additional uncertainties in particular in values of T_0. The aforementioned uncertainties in ε_1 and T_0 however, are hard to quantize. The uncertainties are not only sample-dependent but also resonator and even harmonic-dependent, leading to a random error without quantitative systematic properties. This is why error-bars are omitted in Fig. 6.23.

The vertical spread seen in $\sigma_1(T_0)$, Fig. 6.23 (e), directly stems from a strong frequency-dependence of $\sigma_1(\omega) \propto \omega^2 \ln^4(\text{const.}/\omega)$, as will be discussed in further detail in section 6.5.3. In the plot shown here, this leads to σ_1-values measured by resonances of higher frequency to be much larger than for resonances at lower frequencies. Only $\sigma_1(T_0)$-values at roughly the same frequency can be compared to one another, such as e.g. values measured by resonances at about $2.4 - 4\,\text{GHz}$ as detailed in Fig. 6.23 (d).

Since the dielectric constant shown in Fig. 6.23 (a) covers a wide range from about 100 to about 600, depending on the insulation strength, it is obvious that for all ε_1-data measured in the local pairing regime it holds $\varepsilon_1 > \varepsilon_{1,\text{c}}$, meaning that the absolute value of the dielectric constant is larger than the critical value $\varepsilon_{1,\text{c}} \approx 100$ determined in section 6.1.1. $\varepsilon_{1,\text{c}}$ has been estimated to be a lower boundary for the dielectric constant at which Coulomb interactions are sufficiently screened, such that Cooper-attraction can overcome the electron-electron repulsion and localized Cooper-pairs can form. For all local pairing samples investigated here, it is therefore found that the requirements for strong screening of the Coulomb interactions are strongly fulfilled. The absolute values of ε_1 with $\varepsilon_1 > \varepsilon_{1,\text{c}}$ suggest that the effective Coulomb interaction strength is suppressed to smaller values than possible Cooper-attraction, making potential phonon-mediated Cooper-pairing localized in space possible.

That the lower ε_1-values measured for the local pairing samples with large $T_0 \sim 15 - 17\,\text{K}$ are in the range of a roughly $\varepsilon_1 \sim 100$ is certainly no

coincidence. The formation of Cooper-pairs leading to the emergence of a pseudogap Δ_p (with the activated behavior in DC as a consequence) is tightly linked to $\varepsilon_1 > \varepsilon_{1,\mathrm{c}}$. For samples with even stronger disorder where smaller ε_1-values are expected, the critical value is not met and the samples will not form a pseudogap, see the electron glass regime in section 6.4. This means that the local pairing regime is limited by $\varepsilon_{1,\mathrm{c}} \approx 100$ which is found here to correspond to T_0-values in the region of $T_0 \sim 15 - 17\,\mathrm{K}$, which in turn corresponds to typical values found for T_0 of samples at the most insulating end of the local pairing regime [8, 40]. In this regime it also holds $\delta \sim \hbar\omega_D$, the energy level splitting being only slightly smaller than the Debye energy.

Together with the electron glass samples the critical value of $\varepsilon_{1,\mathrm{c}} \approx 100$ is well confirmed as the value determining whether bosonic or fermionic localization mechanisms are present in disordered amorphous indium oxide. The experiments shown here estimate the critical value to be well in the region of $\varepsilon_{1,\mathrm{c}} \approx 100$ as suggested by theory (section 6.1.1).

$\varepsilon_1(T_0)$ and $\sigma_1(T_0)$ are predicted to increase when the samples get less insulating, meaning that they will increase with decreasing T_0. This is given due to the localization length ξ increasing. This consequently leads to an increase in polarization, see equation (3.33) in section 3.5.3, where $\varepsilon_1 \propto \xi^2$ [39]. Similarly the conductivity is found to scale with ξ as $\sigma_1 \propto \xi^5$ [38, 43, 71] (Mott-behavior) in three dimensions, see equation (3.11) in section 3.1. As a function of T_0 the dielectric constant and the conductivity are expected to scale with equation (3.34) and (3.36) as [33]

$$\varepsilon_1 \propto \nu_0 T_0^{-2/D_2} \approx \nu_0 T_0^{-1.54} \tag{6.18}$$

$$\sigma_1 \propto \nu_0^2 T_0^{-5/D_2} \approx \nu_0^2 T_0^{-3.85}\,, \tag{6.19}$$

since $\xi \propto T_0^{-1/D_2}$, equation (3.31) [33], and $D_2 \approx 1.3$ [33, 116, 117]. D_2 is the fractal dimension giving a quantity on the magnitude of the fractality of the electronic wavefunctions, see section 3.5.1. Equations (6.18) and (6.19)

are shown as guides to the eye in Fig. 6.23 (a), (c) and (d), with an additional $\varepsilon_{1,\mathrm{Host}} \approx 10$ estimated from the electron glass samples in section 6.4.2 (ν_0 is again kept constant with $\nu_0 = 1 \times 10^{45}\,\mathrm{J}^{-1}\,\mathrm{m}^{-3}$ [54, 212, 225]). $\varepsilon_1(T_0)$ in (a) follows the predicted scaling behavior reasonably well. This is given not only comparing individual samples to each other but also $\varepsilon_1(T_0)$-data within one sample measured by a single resonance upon aging of the sample. Note, that in the case of $\sigma_1(T_0)$ again only values measured by resonances at similar frequencies can directly be compared to each other. This is done here by the dashed line in Fig. 6.23 (d) for resonances at about $2.4 - 4\,\mathrm{GHz}$. The scaling of $\sigma_1(T_0)$ is well described by (6.19), again both for the individual development of each sample, as well as comparing the samples.

The scaling behavior found in $\varepsilon_1(T_0)$ and $\sigma_1(T_0)$ hint towards fractal eigenstates governing the polarization and the microwave conductivity. This further support to the theory developed by Feigel'man et al. [12, 33, 39], section 3.5, where the electronic wave functions are assumed strongly localized in space, occupying only a fraction of the typical volume of a delocalized state [37, 114]. In this conglomerate of localized electronic states, Cooper-pairs can form within a space-local state with two single electrons of opposite spin making one pair. Indications for a pseudogap that probably stems from electrons indeed pairing together to form localized Cooper-pairs, is seen already in its influence on the DC-conductivity as shown in section 6.5.1. The absolute value of both ε_1 and σ_1 give further indications that will be investigated in section 6.5.3. Nevertheless the scaling behavior found for $\varepsilon_1(T_0)$ and $\sigma_1(T_0)$ as a function of the activation energy T_0 and the large size of the absolute value of ε_1, lend strong support to the suggestion that there indeed exist localized Cooper-pairs in insulating indium oxide, which are situated in fractal localized eigenstates.

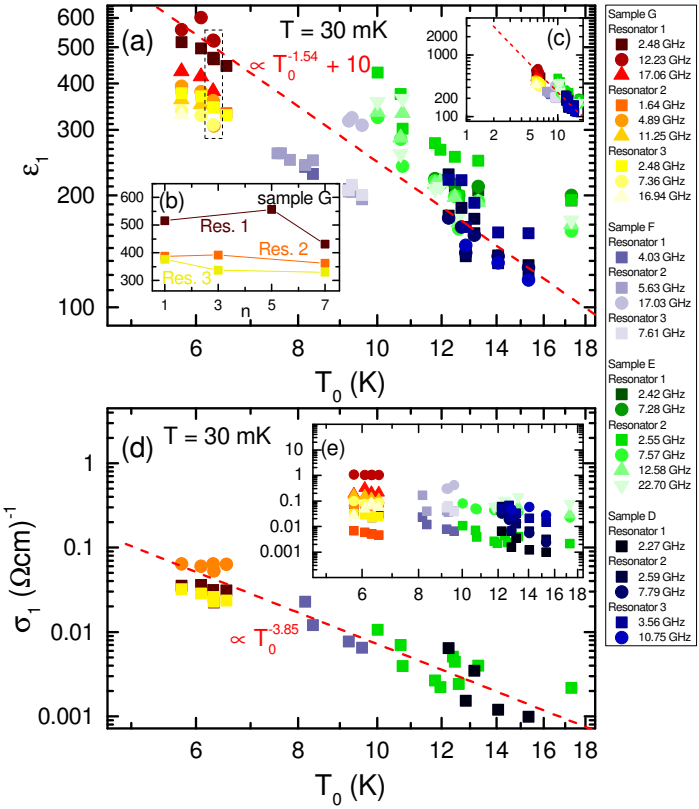

Fig. 6.23.: (a) Dielectric constant $\varepsilon_1(T_0)$ of all local pairing samples measured by several resonances each as a function of activation energy T_0. The predicted $\varepsilon_1 \propto T_0^{-1.54}$ behavior indicating fractal eigenstates is shown as guide to the eye. (b) $\varepsilon_1(n)$ data as a function of mode number n for sample G at a fixed T_0 (indicated by the dashed rectangle in (a)). (c) data from (a) with range down to $T_0 = 2\,\mathrm{K}$. (d) Conductivity $\sigma_1(T_0)$ as a function of T_0 for resonances in the regime $2.4 - 4\,\mathrm{GHz}$. Only similar frequencies can be compared due to strong frequency dependence. The predicted $\sigma_1(T_0) \propto T_0^{-3.85}$ behavior is shown as a guide to the eye. (e) $\sigma_1(T_0)$ for all measured resonances. Some resonances are missing due to the inability of proper resonance fitting.

6.5.3. Suppression of dielectric constant and conductivity by the pseudogap

While the focus of the previous section was set on the absolute values in terms of the Coulomb interaction and the scaling stemming from fractal eigenstates, in this section the focus lies on the absolute values of both ε_1 and σ_1 in comparison to theoretical predictions when pairing of single electrons to localized Cooper-pairs and the emergence of a pseudogap Δ_p comes into play. Main predictions are that both ε_1 and σ_1 are suppressed [38, 39] to some extent (section 3.5.5), so they show smaller values than they would without pairing. One key requirement for the possibility to measure the influence of the pseudogap Δ_p on dielectric and conductive properties, is for the probing energies to be lower than the gap Δ_p itself, so possible localized Cooper-pairs are not broken up. This requirement is fulfilled for all frequencies used in this work, since maximum frequencies used here are $\nu < 25\,\mathrm{GHz}$. Corresponding maximum energy of the microwaves then is $\hbar\omega \approx 0.1\,\mathrm{meV} \ll \Delta_p \approx 0.5\,\mathrm{meV}$. So for all resonances used in this work the energies are always smaller than the pseudogap energies and possible Cooper-pairs will stay intact. The key theory has mostly been derived by M. V. Feigel'man and D. A. Ivanov [33, 38] and was presented in sections 3.1 and 3.5.5.

Suppression of the dielectric constant

As a first quantity, ε_1 is shown in Fig. 6.24 (a) for all local pairing samples each probed by multiple resonances as a function of $T_{0,\mathrm{Mott}}$ and in (b) as a function of ξ_{Mott} for all stages of disorder. $T_{0,\mathrm{Mott}}$ is the activation energy determined from DC-measurements at high temperatures $T > 15\,\mathrm{K}$, see section 6.5.1 Fig. 6.21 (a) and gives direct access to the localization length ξ_{Mott} with [41, 52, 54, 56, 65]

$$\xi_{\mathrm{Mott}} = \left(\frac{16}{k_B \nu_0 T_{0,\mathrm{Mott}}}\right)^{1/3} \tag{6.20}$$

from equation (6.10) [52, 54, 65]. As discussed already in section 6.4.2 the density of states at the Fermi-energy is kept constant with $\nu_0 \approx 1 \times 10^{45}\,\mathrm{J}^{-1}\,\mathrm{m}^{-3}$ [54, 212, 225] although it might change between samples, where a change of about a factor of $2-3$ might be expectable [123]. By calculating ξ_{Mott} with equation (6.20) there are already assumptions taken about ν_0 being constant, which in turn might reflect in errors on the horizontal axis of Fig. 6.24 (b). However, the general shape of the data, especially the relation between different samples is very consistent between Fig. 6.24 (a) and (b), which indicates that ν_0 must not change by a massive amount between samples.

$\varepsilon_1(T_{0,\mathrm{Mott}})$ increases with decreasing $T_{0,\mathrm{Mott}}$ and increasing ξ_{Mott} respectively. This is reminiscent of $\varepsilon_1(T_0)$ from Fig. 6.23 (a) and means that the polarization grows with decreasing disorder. This can be explained by the polarization increasing with the size of the localized states to which the localized Cooper-pairs are confined. The predicted dependence follows equation (3.33) [39]

$$\varepsilon_1 = a \cdot \alpha \frac{e^2 \nu_0}{\varepsilon_0} \xi^2 \tag{6.21}$$

$$\varepsilon_1 = a \cdot \alpha \frac{e^2}{\varepsilon_0} \nu_0^{1/3} \left(\frac{16}{k_B}\right)^{2/3} T_{0,\mathrm{Mott}}^{-2/3}\,. \tag{6.22}$$

Note that again in equation (6.22) possible variation of ν_0 is strongly suppressed due to the small exponent $\nu_0^{1/3}$ and variations in ν_0 therefore are neglected. In addition to the dimension-dependent prefactor $\alpha \approx 3$ (in $d = 3$) [39] a second prefactor a has been introduced. This second prefactor is used to account for a possible reduction of ε_1 by Δ_p. Equation (6.22) has been fitted to the $\varepsilon_1(T_{0,\mathrm{Mott}})$-data individually for each resonance as shown in Fig. 6.24 (a) with dashed lines. It is seen that data measured by each resonance fall on a line $\varepsilon_1 \propto T_{0,\mathrm{Mott}}^{-2/3}$ (or $\varepsilon_1 \propto \xi^2$ respectively), following Anderson localization-like behavior [39].

From the fits in Fig. 6.24 (a) the suppression factor a is found and displayed in Fig. 6.24 (c). Theory predicts, section 3.5.5, that the polarization χ is suppressed by a relative factor $\delta\chi/\chi$, equation (3.42) [38, 39]

$$\frac{\delta\chi}{\chi} \propto -\frac{\Delta_p}{\delta} \ln^4\left(\frac{\delta}{\Delta_p}\right) = \frac{1}{a}\,, \tag{6.23}$$

which is the inverse value of the factor a given in Fig. 6.24 (c). From $\varepsilon_1 = \varepsilon_0(\chi + 1)$ equal suppression is also expected for the dielectric constant ε_1 (see also section 3.5.5). It depends on the energy level splitting δ and the pseudogap Δ_p. For Δ_p values are expected to be roughly about $\Delta_p \approx 0.5\,\mathrm{meV}$ [28, 32], see e.g. tunneling-spectra in Fig. 6.1, while δ is in the range of about a few meV to several 10 meV, as given for all samples in Tab. 6.2 in section 6.3. Resulting values of $\delta\chi/\chi$ therefore are in the range of about $\delta\chi/\chi \approx 2 - 4.5$ depending on the sample and its disorder state. The values of $a = (\delta\chi/\chi)^{-1}$ calculated from δ and Δ_p are additionally plotted as empty symbols in Fig. 6.24 (c) as comparison to measured data. Note that for the calculation of the theoretical value of $\delta\chi/\chi = 1/a$, a mean value of δ across all stages of disorder of each individual sample is taken. This has to be done in order to reach a comparison with values of a determined from the fits in Fig. 6.24 (a), since the latter are themselves acquired as a mean value across all stages of disorder. The experimental values found in Fig. 6.24 (c) are of the same magnitude as predicted values and are therefore in good agreement with the theory. However, for samples D-F values of a are determined larger (smaller suppression) than predicted values and for sample G they are smaller. This deviation from theory is not surprising, since on the one hand equation (6.23) is only determined up to a numerical factor of order unity [38, 39] and on the other hand spatial separation between the resonators probing ε_1 and the Hall-bar probing $T_{0,\mathrm{Mott}}$ can again lead to local variations in sample properties, so deviations such as they are found here can be expected.

The experimental ε_1-data shown here directly show that there is a finite pseudogap in insulating amorphous indium oxide close to SIT. $\varepsilon_1(T_{0,\mathrm{Mott}})$ is suppressed by a certain factor, well in agreement with predictions by theory [38, 39]. This suppression has not been found for highly disordered samples in the electron glass regime and therefore points towards a mechanism that opens a gap Δ_p only close to the SIT. Given the vicinity to the superconducting state, where a gap in the single-particle DOS emerges due to Cooper-pairing and existing tunneling experiments show that this gap is rather rigid on strong disorder increase [28, 32] (see Fig. 6.1), as well as absolute values $\varepsilon_1 > \varepsilon_{1,\mathrm{c}}$ suggesting diminishing Coulomb interactions, it is likely that the gap found in the experiments of this work is the superconducting pseudogap surviving deep into the insulating regime.

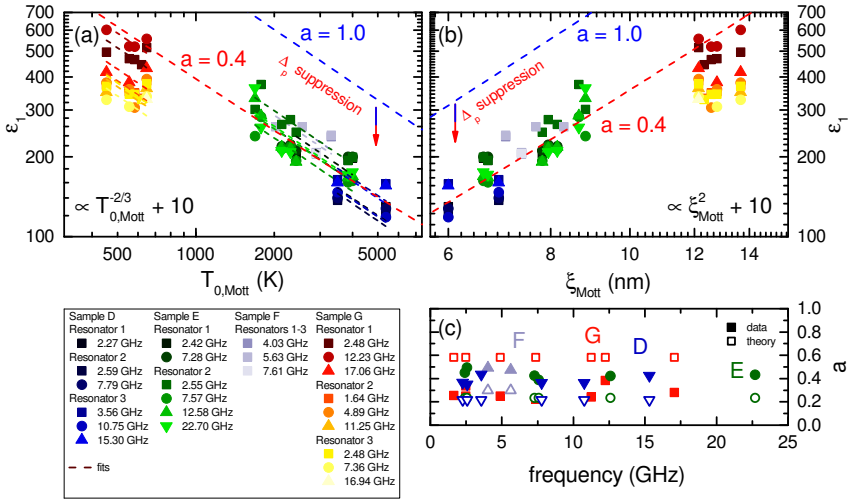

Fig. 6.24.: (a) Dielectric constant $\varepsilon_1(T_{0,\mathrm{Mott}})$ as a function of Mott activation energy $T_{0,\mathrm{Mott}}$ determined from DC-measurements. The data is fitted with $\varepsilon_1 \propto a \cdot T_{0,\mathrm{Mott}}^{-2/3}$, equation (6.22), from which the prefactor a is determined. ε_1-data is suppressed in amplitude by the pseudogap Δ_p. The red dashed line shows $\varepsilon_1 \propto a \cdot T_{0,\mathrm{Mott}}^{-2/3}$ across all samples with a factor of $1/a = 2.5$ (blue shows $a = 1$). (b) $\varepsilon_1(\xi_{\mathrm{Mott}})$ as a function of localization length ξ_{Mott}. (c) Suppression factor a for all resonances. $\varepsilon_1(\xi_{\mathrm{Mott}})$ is suppressed by a factor of about $1/a \approx 2 - 4.5$, in agreement to theory.

Suppression of the frequency-dependent conductivity

Additional to the dielectric constant ε_1, the conductivity σ_1 is also expected to show prominent effects of the pseudogap Δ_p with a general, sample-independent suppression in value [38]. This results from the energy reduction of the paired states compared to that of the unpaired single-electron states by the amount Δ_p, which in turn leads to a strong reduction of hopping between individual localized states [33, 38], as described in section 3.5.5. Hopping is strongly suppressed since transitions from one localized state to the other can occur only via single-electron states hybridizing to Mott-resonances [33, 38] (Fig. 3.9 (a)), which in turn are higher in energy due to the electrons being unpaired. This energetically unfavorable transition results in a massively reduced number of hopping events. The theoretical details are discussed in section 3.1 and 3.5.5.

In Fig. 6.25, $\sigma_1(\nu)$ is plotted as a function of frequency ν for all local pairing samples and all stages of disorder. (a) shows a compilation of all data, where it is seen that the general trend exhibits an increase of $\sigma_1(\nu)$ with increasing ν. As a guide to the eye, typical Mott-behavior, equation (3.11), $\sigma_1(\omega) \propto \omega^2 \ln^{d+1}(\delta/\omega)$ [38, 43, 70, 71] is plotted. The slope of the data follows Mott-behavior well with an exponent of the logarithm of $d + 1 = 4$ and its argument being defined by the energy level splitting δ. It is therefore found that Mott resonances play the dominating role in the hopping conductivity between localized states [33, 38]. Photon-induced hopping transport thus consists of the hopping of charges between localized states separated by a distance larger than their localization length $r > \xi$, with the difference in energy levels between the states being equal to the energy of the incoming photon $\hbar\omega$ [33, 38].

Now this hopping however is strongly reduced in magnitude compared to simple Mott arguments. This is due to the pairing of electrons to localized pairs [38]. To quantify this suppression of the amplitude and the scaling of

the data with frequency, Mott-behavior has been fitted to the data following equation (3.11) [38, 43, 70, 71]

$$\sigma_1(\omega) = a \cdot \frac{\pi^2}{3} e^2 \xi^5 \nu_0^2 \hbar\omega^2 \ln^4\left(\frac{\delta}{\hbar\omega}\right) \tag{6.24}$$

$$\Rightarrow \sigma_1(\omega) = a \cdot \frac{\pi^2}{3} e^2 \left(\frac{16}{k_B T_{0,\mathrm{Mott}}}\right)^{5/3} \nu_0^{1/3} \hbar\omega^2 \ln^4\left(\frac{k_B T_{0,\mathrm{Mott}}}{16\hbar\omega}\right). \tag{6.25}$$

Here, the localization length ξ and energy splitting δ are extracted from DC-hopping conductivity following equation (6.20) as $\xi = [16/(k_B \nu_0 T_{0,\mathrm{Mott}})]^{1/3}$ [41, 52, 54, 56, 65] and equation (3.25) [33], $\delta = k_B T_{0,\mathrm{Mott}}/16$. The additional prefactor a is again included, through which the suppression of $\sigma_1(\omega)$ is quantified. $T_{0,\mathrm{Mott}}$ is taken from DC-measurements of each individual cool-down of the samples at each individual disorder state, and the density of states at the Fermi-energy is taken constant as $\nu_0 \approx 1 \times 10^{45}\,\mathrm{J}^{-1}\,\mathrm{m}^{-3}$ [54, 212, 225]. This leaves a as the only fit parameter. The resulting fits of (6.25) to the data are shown as lines in Fig. 6.25 (b), (c) and (d) for each of the local pairing samples[†]. $\sigma_1(\omega)$ is indeed found smaller than it would be expected from simple single-electron Mott-resonances hopping. This is true for all fits performed. This leads to a quite small factor a across all samples and disorder states, which is shown in Fig. 6.25 (e) for each of the disorder states of each sample.

The theoretically predicted conductivity with active electron coupling interaction is found as $\sigma_1(\omega \ll \delta) = C(\omega/\Delta_p)\frac{\omega}{\omega+\Delta_p}\sigma_1\left(\sqrt{\omega(\omega+\Delta_p)}\right)_{\mathrm{nonint}}$ (equation (3.40) in section 3.5.5) from which the theoretically predicted value for a can be calculated [38]. The prefactor $C(\omega/\Delta_p)$ is found numerically as a function of the frequency ω in units of the pseudogap Δ_p, see Fig. 3.9 (b) [38]. In the limit of small frequencies, as it is given here, a is then found as $a = 0.446(1/2)^{d+1} \approx 0.028$, equation (3.41) (for $d = 3$) [38]. Note that this

[†]Note, that for sample D not all disorder states could be fitted as for some measurements the high temperature data was erroneous, so $T_{0,\mathrm{Mott}}$ could not be extracted.

theoretical value is a numerical constant independent on any sample properties as long as local pairing is expected. The only condition being that the energy of the incoming photons is small compared to the size of the pseudogap $\hbar\omega \ll \Delta_p$ so Cooper-pairs will not break and the limit of low frequencies for $C(\omega/\Delta_p)$ in Fig. 3.9 (b) is given [38]. $\hbar\omega \ll \Delta_p$ again is given even for highest frequencies used here ($\sim 25\,\mathrm{GHz}$), $\hbar\omega \approx 0.1\,\mathrm{meV} \ll \Delta_p \approx 0.5\,\mathrm{meV}$. The theoretically predicted value of $a \approx 0.028$ is additionally plotted in Fig. 6.25 (e) as a dashed line across all samples.

The fitted values of a from the experiments match the theoretically predicted value perfectly. This is given across all disorder states of all local pairing samples. Deviations from the theoretically predicted value are only marginal[‡]. There is no sample or disorder dependence found, in agreement to the predicted sample-independent suppression of $\sigma_1(\omega)$. Compared to $\sigma_1(\omega)$ of electron glass samples in section 6.4.6, where a suppression of $\sigma_1(\omega)$ has not been found to this extend, the data in Fig. 6.25 (e) give strong evidence for the existence of a pseudogap Δ_p in insulating indium oxide close to the SIT, where the electrons form localized Cooper-pairs that do not contribute to a macroscopic superconductivity.

[‡]Note, that for sample F the deviation is larger, yet $\sigma_1(\omega)$ is still strongly suppressed. The deviation probably stems from slight uncertainties in ξ or $T_{0,\mathrm{Mott}}$ respectively due to the spatial distance of Hall-bar and resonators.

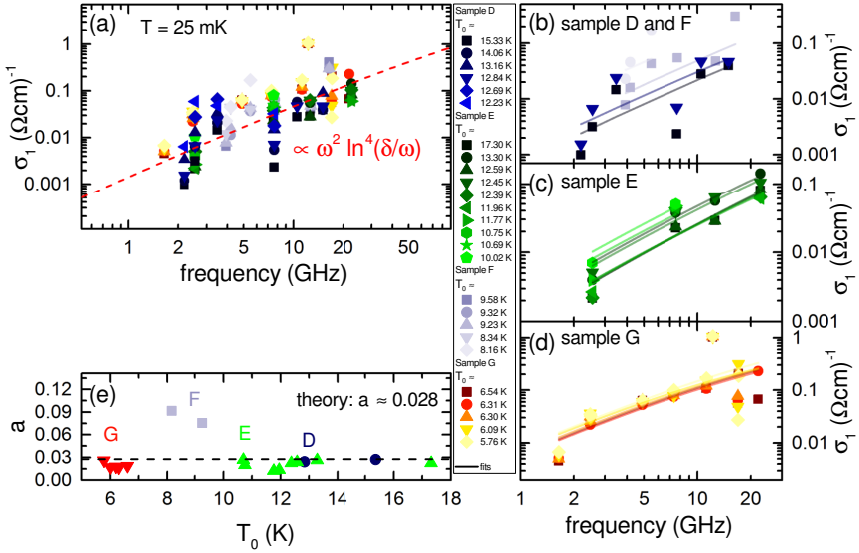

Fig. 6.25.: (a) Microwave conductivity $\sigma_1(\nu)$ as a function of frequency ν for all local pairing samples at varying stages of disorder. Mott-behavior $\sigma_1(\omega) \propto \omega^2 \ln^4(\delta/\hbar\omega)$ is shown as guide to the eye. (b)-(d) $\sigma_1(\nu)$ of each sample with individual Mott-behavior fits to each state of disorder. From the fits the suppression prefactor a is extracted. (e) Suppression prefactor a across all samples. Found values are perfectly in agreement with the theoretically predicted value of $a \approx 0.028$ giving strong evidence for the existence of a pseudogap Δ_p in the samples emerging from the local pairing of single electrons to localized Cooper-pairs.

6.5.4. Temperature-dependent conductivity and dielectric constant

The measurements performed on the dielectric and conductive properties of indium oxide samples in this work are not limited to measurements at base temperature, but are also performed as a function of temperature. For this, spectra are continuously recorded during cool-down of the sample from liquid He temperatures ($\sim 4\,\mathrm{K}$) down to mK-temperatures. This is done in addition to the DC-measurements that are also performed continuously during sample cool-down. Examples of two resonances under influence of indium oxide samples are shown in Fig. 6.26 (a) and (b), the one in (b) being a higher harmonic probing sample E and the one in (a) being a fundamental probing sample G. For the latter a top-view of the resonator-chip has already been shown in Fig. 6.22 (e). Apart from the resonance originating from the resonator under influence of the sample, Fig. 6.26 (a) also shows the resonance of an empty reference resonator at similar frequency. With increasing temperature the resonances decrease in amplitude and shift to lower frequencies, which is a direct consequence of the microwave conductivity $\sigma_{1,\mathrm{GHz}}$ changing with temperature. By fitting the raw spectra in Fig. 6.26 (a) and (b) with complex Lorentzian fits (see procedure in section 4.8), the temperature-dependent resonance frequency and $Q(T)$ can be extracted, as shown in (c) and (e) for the resonance in (a) and in (d) and (f) for the resonance in (b) respectively. Additionally the resonance frequency and $Q(T)$ of the reference resonances are shown in red with equal relative axis-ranges.

From both the spectra as well as the derived quantities it is found that the resonances decrease in amplitude and even vanish when approaching 1 K. This is due to the large losses introduced by $\sigma_{1,\mathrm{GHz}}$ of the samples with its temperature-dependence, where $\sigma_{1,\mathrm{GHz}}$ is expected to increase with temperature. In contrast to the resonances under influence of the samples, the reference resonances are only very marginally affected within the given temperature-range up to 4 K and even less so in the relevant temperature

range up to 1 K. It shows typical behavior of an empty Nb resonator on Al_2O_3-substrate, see section 5.5. Their resonance frequencies as well as the quality factor are both effectively constant. This simplifies the following analysis, as the resonance frequency and $Q(T)$ of the resonance under influence of the sample can be compared to constant values of the reference resonator instead of having to be compared for each temperature individually. In case of resonators which are only partially covered by the sample, $Q_{\mathrm{pc}}(T)$ is measured directly and $Q_{\mathrm{cov}}(T)$ is derived from the mode-dependent electric field distribution of the standing wave in the resonator, see section 4.5.2. $Q_{\mathrm{cov}}(T)$ is the quality factor of a hypothetically completely covered resonator and is necessary for further calculation. This is done for each temperature individually and resulting values for $Q_{\mathrm{cov}}(T)$ are also shown in Fig. 6.26 (e) and (f).

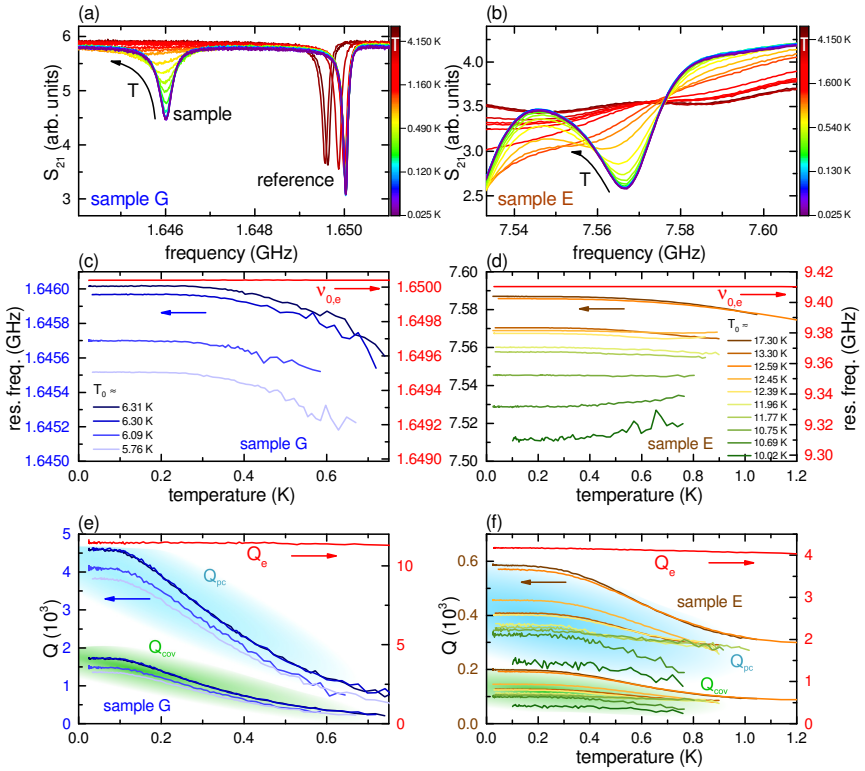

Fig. 6.26.: (a) Spectra of resonances at about 1.65 GHz for temperatures from base temperature up to 4 K. One resonance is probing sample G while the other is an empty reference. The one probing the sample vanishes at $T > 0.8$ K. (b) Spectra of a resonance probing sample E at temperatures up to 4 K. (c) Resonance frequency and (e) quality factor $Q(T)$ for both the sample resonance and the reference shown in (a) at different stages of disorder. The reference stays constant across the relevant temperature range and for all stages of aging. In (e) both $Q_{\mathrm{pc}}(T)$ of the partially covered resonator measured directly and $Q_{\mathrm{cov}}(T)$ of the hypothetically completely covered resonator (c.f. section 4.5.2) are shown. (d,f) Same quantities for the resonance shown in (b) and a reference.

With both the temperature-dependent resonance frequency and $Q_{\mathrm{cov}}(T)$ the temperature-dependent conductivity $\sigma_1(T)$ can be calculated, following the procedure detailed in section 4.4. The resulting values are shown in Fig. 6.27 (a) for one individual state of each local pairing sample, each probed with several different resonances and in (b) for sample E at several different stages of aging. $\sigma_{1,\mathrm{DC}}(T)$ measured by DC-measurements is additionally shown, calculated from the resistivity $\rho(T)$ (e.g. from Fig. 6.21 (c)). Both $\sigma_{1,\mathrm{GHz}}$ as well as $\sigma_{1,\mathrm{DC}}$ connect well to each other. It is expected that upon increasing the temperature $\sigma_{1,\mathrm{GHz}}$ approaches $\sigma_{1,\mathrm{DC}}$ and at some point goes over into $\sigma_{1,\mathrm{DC}}$ [65]. This is seen well in the data, although for most resonances the amplitude vanishes before a complete transition from $\sigma_{1,\mathrm{GHz}}$ to $\sigma_{1,\mathrm{DC}}$ is finished. $\sigma_{1,\mathrm{DC}}(T)$ decreases strongly with decreasing temperature giving the typical activated behavior, which is additionally extrapolated towards lower temperatures with dashed lines as guide to the eye. $\sigma_1(T)$ determined from microwave resonance measurements however, does not decrease indefinitely but saturates at certain values towards low temperatures. Here the samples enter the zero-phonon regime where $k_B T \ll \hbar\omega$ [43, 44]. In this regime no thermal excitation of hopping transport remains but only photon assisted hopping and σ_1 becomes independent of temperature [43, 71]. Here, incoming photons aid in the transition of electrons from one localized state to the other [38, 57], but absorption and emission of phonons by the electrons is strongly suppressed, see section 3.1. As expected and seen already in section 6.5.3, σ_1 shows strong frequency-dependence, which reflects in the vertical offsets of the saturation of $\sigma_1(T)$ towards base temperature. This means that with larger photon energy also the hopping conductivity is enhanced as expected.

Fig. 6.27 (b) shows $\sigma_1(T)$ of sample E measured by three different resonances (colored background) for several different stages of aging. It is found that overall values of $\sigma_1(T)$ increase with decreasing T_0, i.e. with decreasing disorder and insulation strength of the sample. This already been seen before at base temperature in Fig. 6.23 (b) where it has been found that $\sigma_1(T_0) \propto T_0^{-3.85}$. Now it is found that this behavior also holds across all

temperatures up to 1 K, as the relative distance between the curves of $\sigma_1(T)$ in Fig. 6.27 (b) stays mostly constant for different T_0. This is expected, as the Mott hopping, equation (3.11), responsible for the temperature-independent σ_1 at low temperatures and the Austin-Mott behavior, equation (3.13), responsible for the increase of $\sigma_{1,\mathrm{GHz}}(T)$ towards larger temperatures both depend on the localization length ξ following $\sigma_1 \propto \xi^5$ (aside from logarithmic corrections) [43]. With decreasing disorder, ξ increases (T_0 decreases with $T_0 \propto \xi^{-D_2}$) and consequently $\sigma_1(T)$ increases across the whole temperature-range.

That photon-assisted microwave conductivity $\sigma_{1,\mathrm{GHz}}$ dominates completely at mK-temperatures can be shown by comparing $\sigma_{1,\mathrm{GHz}}$ to expected values of $\sigma_{1,\mathrm{DC}}(T)$ at low temperatures. The latter is many orders of magnitude smaller than $\sigma_{1,\mathrm{GHz}}$ [65, 73], which can be seen when following the extrapolation of $\sigma_{1,\mathrm{DC}}(T)$ down to low temperatures (dashed lines). At temperatures of about $T \approx 30\,\mathrm{mK}$, values in the range of $\sigma_{1,\mathrm{DC}} \sim 1 \times 10^{-9} - 1 \times 10^{-13}\,\Omega^{-1}\,\mathrm{cm}^{-1}$ would be expected from the extrapolation (depending on the sample). This is vastly smaller than $\sigma_{1,\mathrm{GHz}}(30\,\mathrm{mK})$ determined by microwave resonances and it can safely be assumed that photon-assisted hopping is the main contributor to $\sigma_1(30\,\mathrm{mK})$ at base temperature for the frequencies used here. When now extrapolating the frequency-dependence of $\sigma_1(\nu)$ shown in section 6.5.3, Fig. 6.25, down to values that match $\sigma_{1,\mathrm{DC}} \sim 1 \times 10^{-9} - 1 \times 10^{-13}\,\Omega^{-1}\,\mathrm{cm}^{-1}$, then frequencies in the range of 5−500 kHz are expected where $\sigma_{1,\mathrm{GHz}} \approx \sigma_{1,\mathrm{DC}}$. Only below these frequencies the conductivity would again be dominated purely by the DC-part and the frequency-dependent $\sigma_1(\nu)$ would therefore saturate in this regime. Conversely this means, that the DC-conductivity $\sigma_{1,\mathrm{DC}}$ which is measured at finite frequency of a few Hz in this work (see section. 4.9), is far from the photon-assisted region, measured at much lower frequencies by at least three orders of magnitude. This means that the used DC-measurements indeed only probe $\sigma_{1,\mathrm{DC}}$ but no photon-assisted hopping.

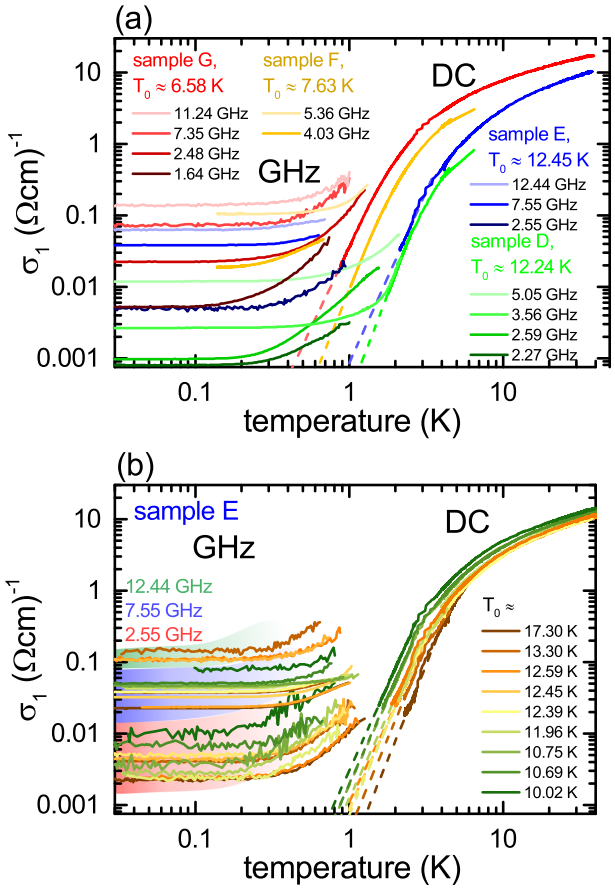

Fig. 6.27.: (a) Conductivity $\sigma_1(T)$ as a function of temperature T for all local pairing samples at fixed T_0 each probed by several different resonances. Additionally the DC-conductivity is shown with guide to the eye extrapolations to low T. Values of σ_1 determined from either method connect well. $\sigma_1(T)$ saturates at low T in the zero-phonon regime due to photon-induced hopping. (b) $\sigma_1(T)$ of sample E at several different stages of aging measured by three different resonances. The corresponding DC-conductivity is shown as well.

As mentioned before, above a certain temperature where $k_B T > \hbar\omega$ the conductivity enters the Austin-Mott regime with linear temperature-dependence [43, 74, 75]. This is detailed in Fig. 6.28 for some exemplary resonances, where $\sigma_1(T)$ is plotted linearly. In the Austin-Mott regime the hopping con-

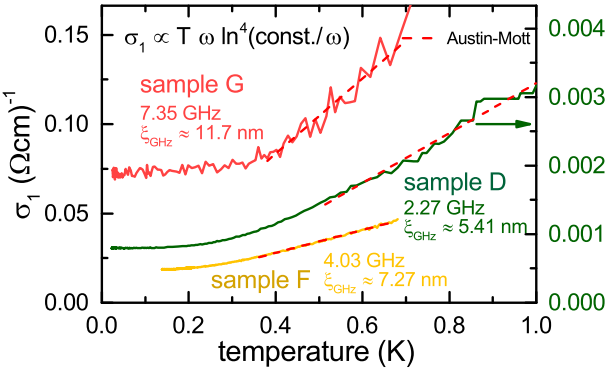

Fig. 6.28.: Linear plot of $\sigma_1(T)$ as a function of temperature. The samples enter the Austin-Mott regime at $k_B T > \hbar\omega$, where phonon-induced hopping contributes as well. From linear fits (shown in red) a localization length ξ_{GHz} can be extracted, following equation (6.26).

ductivity is again driven by the absorption and emission of phonons, where the conductivity follows equation (3.13) [43, 74, 75]

$$\sigma_1(T) = a \cdot \frac{\pi^4}{384} e^2 \xi_{\mathrm{GHz}}^5 \nu_0^2 k_B T \omega \ln^4\left(\frac{\nu_{\mathrm{ph}}}{\omega}\right) , \tag{6.26}$$

with typical phonon frequencies $\nu_{\mathrm{ph}} \approx\sim 1 \times 10^{13}\,\mathrm{Hz}$ (from typical Debye energy $\omega_D \approx 500\,\mathrm{K}$ [12, 33, 227, 228]), the density of states at the Fermi energy $\nu_0 \approx 1 \times 10^{45}\,\mathrm{J}^{-1}\,\mathrm{m}^{-3}$ [54, 212, 225] and in three dimensions $d = 3$. Additionally the suppression a of σ_1 due to the emergence of the pseudogap Δ_p has to be taken into account, with values for a taken from section 6.5.3, Fig. 6.25 (e). Equation (6.26) can be fitted to the data as shown in Fig. 6.28

as red lines. The only fit parameter left is the localization length ξ_{GHz} with the resulting values given in the figure. They compare well to the localization length ξ_{Mott} given in Tab. 6.2 derived from Mott VRH determined at $T > 15\,\mathrm{K}$ (Fig. 6.21 (a)). In contrast to samples in the electron glass regime however, with $\sigma_1(T)$ shown in section 6.4.3, where fits could be performed to the data in order to extract the localization length ξ_{GHz} quantitatively as a characterization parameter for most resonances, using ξ_{GHz} as a resonance-dependent characterization parameter cannot be done for the local pairing samples. This is on the one hand due to the suppression of σ_1 by the pseudogap Δ_p. As seen in Fig. 6.25 (e) this suppression is mostly constant, however slight differences in the suppression a of the prefactor of σ_1 are found which themselves introduce uncertainties, which magnify since $\sigma_1 \propto \xi_{\mathrm{GHz}}^5$. On the other hand, for many resonances probing the local pairing samples, fitting the Austin-Mott dependence is not feasible, since due to increasing losses they do not enter the Austin-Mott regime clearly in a large enough temperature-range for linear fits to correctly describe the data. Features like kinks or steps, which would hint towards the breaking of Cooper-pairs or suppression of pairing are absent within the given temperature-range, pointing towards the robustness of the Cooper-pairs up to temperatures, where the conductivity is already too high and the resonator operation ceases.

From the fits in Fig. 6.28 it is shown that $\xi_{\mathrm{GHz}} \approx \xi_{\mathrm{Mott}}$. This means, that the characteristic localization length defining properties such as hopping transport, dielectric properties and conductivity is consistent across the whole temperature range from very large temperatures $k_B T \gg \Delta_p$ ($T > 15\,\mathrm{K}$), where the electrons are unpaired, down to mK-temperatures where mostly localized Cooper-pairs are present. This shows that Cooper-pairing in disordered indium oxide is only a weak effect [8, 33], which is basically sitting on top of the localization of electrons and does not alter characteristic length scales.

Apart from the temperature-dependent microwave conductivity $\sigma_1(T)$ also the temperature-dependent dielectric constant $\varepsilon_1(T)$ is calculated. This is

shown for some exemplary resonances in Fig. 6.29 (a) and in Fig. 6.29 (b) for one resonance probing sample E at different stages of disorder. It is found that $\varepsilon_1(T)$ does not show any significant temperature-dependence and stays mostly constant over the temperature-range accessible here. The vertical offsets stem from the sample and resonator-dependent properties, as has been shown in section 6.5.2, Fig. 6.23 (a). Only very close to the vanishing of the resonances at about 1 K do the values of $\varepsilon_1(T)$ change, though this shift is inconsistent across the resonances and relatively small (typically only a few percent). It is probably caused by slight uncertainties in the fitting procedure of the resonances close to their vanishing point, where their amplitude gets very small and the signal-to-noise ratio is weak. A pronounced minimum at low temperatures is not found, as it has been for the electron glass samples around 1 K, see section 6.4.5, which further supports the possibility that this minimum might be an intrinsic property to electron glasses.

In Fig. 6.30 (a) the low-temperature dielectric constant $\varepsilon_1(30\,\mathrm{mK})$ and in (b) the low-temperature conductivity $\sigma_1(30\,\mathrm{mK})$ are displayed as a function of the conductivity at 4 K, $\sigma_1(4\,\mathrm{K})$. It is phenomenologically found that ε_1 follows $\sigma_1(4\,\mathrm{K})$ with $\varepsilon_1 \propto \sigma_1(4\,\mathrm{K})^{1/3}$ and $\sigma_1(30\,\mathrm{mK}) \propto \sigma_1(4\,\mathrm{K})$ linearly. The origin of the scaling of the first is unknown as of yet, the latter shows that the conductivity linearly decreases with temperature (up to the saturation where $\hbar\omega > k_B T$), confirming Austin-Mott behavior, equation (6.26), with constant ξ.

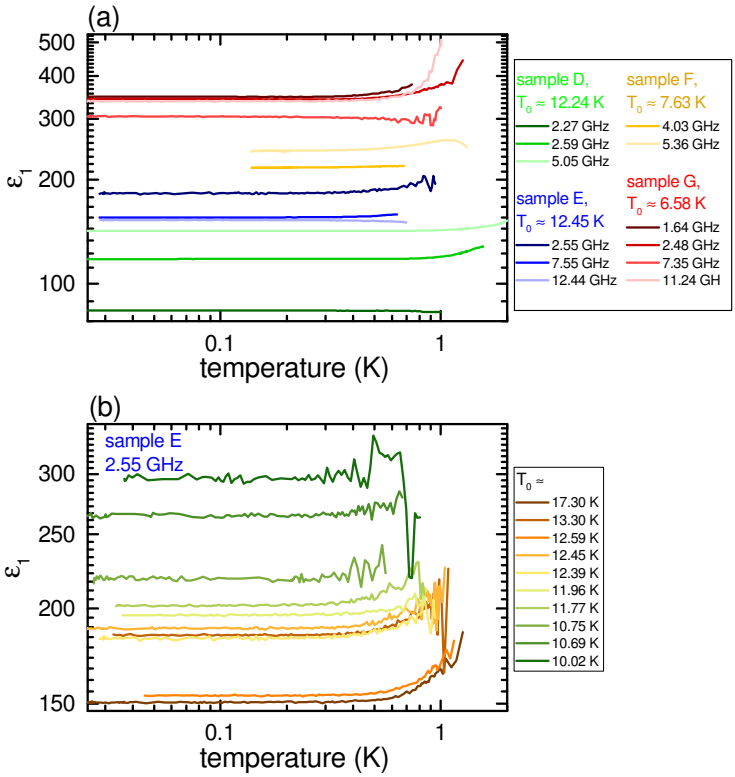

Fig. 6.29.: (a) $\varepsilon_1(T)$ for all local pairing samples each at a fixed T_0 and probed by several resonances. (b) $\varepsilon_1(T)$ probed by one resonance for multiple stages of aging. In both cases no particular temperature-dependence is visible, $\varepsilon_1(T)$ is found to be constant.

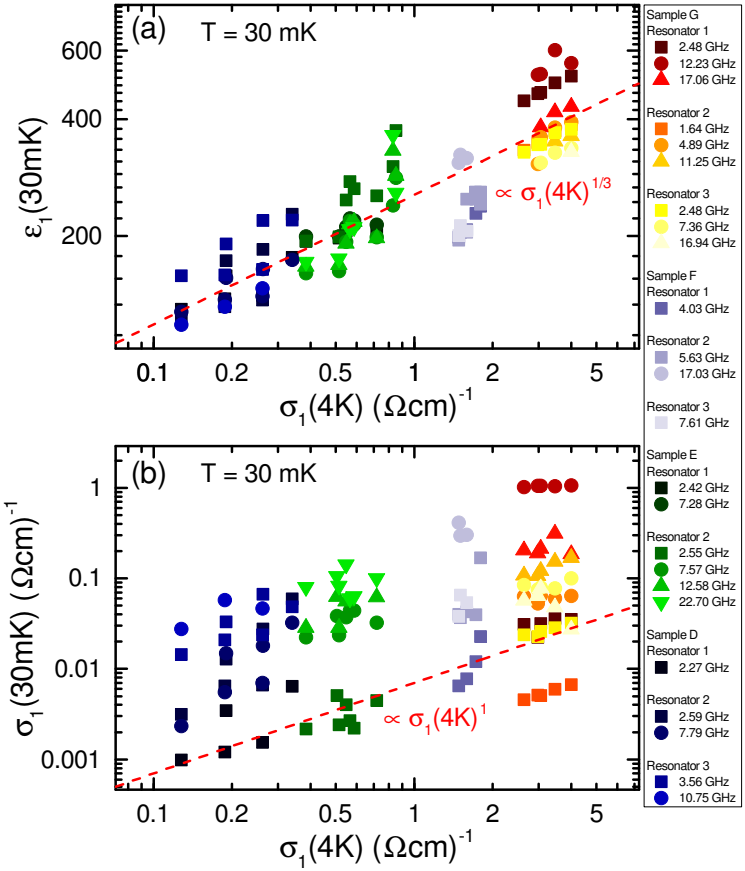

Fig. 6.30.: (a) Low-temperature $\varepsilon_1(30\,\mathrm{mK})$ as a function of 4 K-conductivity $\sigma_1(4\,\mathrm{K})$. The proportionality $\varepsilon_1 \propto \sigma_1(4\,\mathrm{K})^{1/3}$ is found. (b) Low-temperature $\sigma_1(30\,\mathrm{mK})$ as a function of $\sigma_1(4\,\mathrm{K})$. Linear proportionality is found, corresponding to Austin-Mott behavior.

6.6. Comparing all samples and concluding discussions

6.6.1. On the possibility of a JJA-superinsulator in indium oxide

In section 3.4 the possibility of a Josephson-junction-array network (JJA) consisting of superconducting islands separated by insulating barriers has been presented, which either goes superconducting or insulating depending on the ratio between Coulomb charging energy E_C and Josephson energy E_J, where for $E_C < E_J$ the system goes superconducting and for $E_C > E_J$ it goes insulating [14]. In section 3.4.2 it was speculated that this could even lead to an exotic state, the "superinsulator", with full duality to a superconductor [14, 36, 85], meaning that even at finite temperature $\sigma(0 < T < T_{\mathrm{CBKT}}) \equiv 0$ [34, 42, 94]. In the following, the main requirements for insulation based on JJA-networks are detailed and compared to the acquired data, in order to find decisive arguments on the nature of insulation in disordered indium oxide.

Some results found are indeed ambiguous and could also be explained by JJAs. Such as the emergence of a universal quantum resistance $\hbar/(2e)^2 \approx 6.5\,\mathrm{k\Omega}$ close to the transition [22, 85, 102, 104, 105], which is said to occur due to the competition of Cooper-pairs and vortices, which each tend to condense into a macroscopic state. This quantum resistance has also been found for the superconducting sample H in this work, where $R_s(T)$ roughly increased to a maximum shoulder of similar value shortly before going superconducting, see section 6.3.1 and Fig. 6.10 (b) and (c). Also the emergence of activated behavior in the conductivity of the samples $\sigma_1(T) \propto \exp(-T_0/T)$ is predicted [14, 34], which has been found in this work as well, see section 6.5.1. So some of the DC-data acquired could be explained by disordered indium oxide consisting of a JJA network.

One requirement for insulators made up of JJA networks however, is the fact that the superconducting lattice sites have to be large and separated by more or less homogeneous tunneling barriers [8, 14]. While the results presented in this work do not give answers to the questions whether the superconducting puddles found in disordered indium oxide [28] are indeed smaller than what is required for a typical JJAs and whether the tunneling barriers are too inhomogeneous in coupling strength [8], the direct measurement in particular of ε_1, which has been desired already previous to this work [14], gives strong indications about the nature of the insulating state. For the superinsulator to emerge, Cooper-pairs and "anti-Cooper-pairs" bind together to form neutral dipoles, which then do not form a superconducting state. A crucial requirement for this is that the interaction potential between Cooper-pair and anti-Cooper-pair becomes logarithmic in distance r [14, 110] so it exactly matches the energy contribution by entropy in the Helmholtz free energy [14, 83] (equation (3.18) for the vortex BKT-transition, which is dual to the charge BKT-transition). This however, is only given if the electrostatic screening length is larger than r and therefore larger then the total system size [34]. This results in the requirement $\varepsilon_1 d/(\varepsilon_{1,\mathrm{s}}+1) \gg r$ [14, 110], with d the sample thickness and $\varepsilon_{1,\mathrm{s}}$ the substrate dielectric constant. A lower estimate can be calculated for the minimum ε_1 that would be required for a typical sample in this work to be considered a JJA network. For this estimate it is assumed that the distance between center conductor and the ground plane W of a typical resonator defines the system size and is here roughly $r = W \sim 10\,\mu\mathrm{m}$. The maximum thickness is assumed $d \sim 40\,\mathrm{nm}$. This gives a lower limit of $\varepsilon_1 \sim 3000$ ($\varepsilon_{1,\mathrm{s}} \approx 10$). Such high values are certainly not reached, compare Fig. 6.23 (a). Even when considering a possible extrapolation down to $T_0 = 2\,\mathrm{K}$, possibly the lowest possible disorder before superconductivity sets in, see the inset Fig. 6.23 (c), $\varepsilon_1 \sim 2500$, still below the limit. Realistically the dimensions are even more restrictive, e.g. for the resonator probing sample G, $W \approx 50\,\mu\mathrm{m}$, meaning the limit of ε_1 is even larger by a factor of five. It is therefore safe to assume that one

fundamental requirement [14, 110] for the argument of amorphous disordered indium oxide thin-films consisting of a JJA network going superinsulating at low temperatures, is certainly not given.

Another phenomenon that has been found in other experiments, is the dependence of certain parameters on the system-size [14, 34, 111–113]. In these experiments e.g. the activation energy T_0 found in DC-conductivity is strongly size-dependent, with T_0 increasing with the array length [111]. However, in the results presented in the present work, no size-dependence of the microwave conductivity or the polarization is found whatsoever. This does not exclude possible size-dependence in DC-conductivity, as the Hall-bars used in this work all had equal dimensions, however there is no indication of any size-dependence when comparing GHz-properties between differently sized resonator structures. Various sizes of resonators from $W \sim 10\,\mu\text{m}$ up to $W \approx 50\,\mu\text{m}$ have been used, but the resulting values have all been found consistent with Anderson insulation.

Concluding, the results found in this work give major indications, that the nature of the insulator of disordered indium oxide at low temperatures is indeed not made up of a Josephson-Junction-array network, but is rather a fractal Anderson insulator with additional, space-local Cooper-pairing.

6.6.2. Main results

In this section all samples studied in this work will be compared. Two regimes have been found, the electron glass regime without Cooper-pairing and the local pairing regime with localized Cooper-pairs. Levels of disorder cover several orders of magnitude in energy level splitting δ, giving insight into a wide range of different insulation strengths. The main results concerning the dielectric constant and its scaling are summarized in Fig. 6.31. The two regimes are indicated to either side of the Debye energy $\hbar\omega_D$, which is the parameter deciding whether phonons can mediate a possible Cooper-attraction between electrons or not [12, 33]. For $\hbar\omega_D$ a quite broad range is indicated,

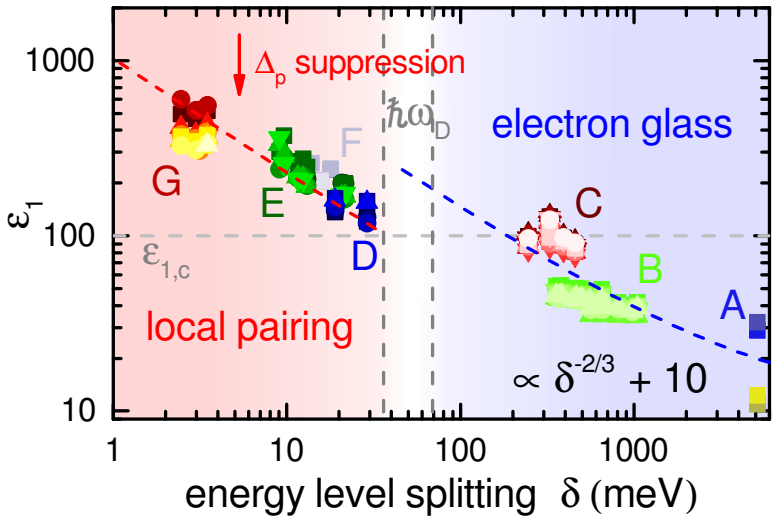

Fig. 6.31.: Real part of the dielectric constant ε_1 as a function of energy level splitting δ for all samples measured in this work. Two regimes are found, the electron glass regime and the local pairing regime. $\varepsilon_{1,c} \approx 100$ is confirmed as a critical value, determining whether electron-electron interaction is attractive (Cooper-attraction) or repulsive (Coulomb repulsion). Upon local pairing, ε_1 is suppressed by the pseudogap Δ_p.

as exact values of ω_D in the samples investigated are unknown but can be considered in the range $\omega_D \approx 420 - 800\,\mathrm{K}$ [12, 33, 227, 228]. For electron glass samples the energy level splitting is much larger than typical phonon energies $\delta > \hbar\omega_D$ [33], inhibiting Cooper-attraction by phonon exchange. For lower energy level splitting $\delta < \hbar\omega_D$ however, local pairing with a pseudogap Δ_p is expected.

A boundary of $\varepsilon_{1,c} \approx 100$ is found, separating ε_1-values of electron glass and local pairing samples. While for electron glass samples $\varepsilon_1 \approx 100$ are maximum values reached at the least disordered end of the electron glass

regime, $\varepsilon_1 \approx 100$ is found as the lower minimum value found for local pairing samples at the most disordered end of the local pairing regime. This perfectly confirms theoretical assumptions of a critical $\varepsilon_{1,c}$-value, which determines whether Coulomb interactions suppress pairing or are themselves screened enough for Cooper-attraction to dominate. In disordered indium oxide thin-films, the theoretical prediction of $\varepsilon_{1,c}$ is estimated to about $\varepsilon_{1,c} \approx 100$ (section 6.1.1) perfectly in line with experimental data.

The scaling of $\varepsilon_1(\delta) \propto \delta^{-2/3} + \varepsilon_{1,\mathrm{Host}}$ as a function of disorder [39] additionally confirms the existence of the two regimes and gives clear evidence for the existence of a pseudogap when pairing is present. The scaling shown in Fig. 6.31 follows the data very well (with a constant contribution $\varepsilon_{1,\mathrm{Host}} \approx 10$). For electron glass samples the full, non-suppressed dependence is shown, which describes the data as a three dimensional Anderson insulating material of single, non-interacting electrons [39]. In the local pairing regime however, $\varepsilon_1(\delta)$ is suppressed across all samples. This suppression amounts to a factor of about $2-4$, well in agreement with theoretical predictions [38, 39]. It is therefore found that the opening of a pseudogap Δ_p due to Cooper-pairing directly affects ε_1, suppressing it by quite some extent. This leads to a transition region between electron glass and local pairing regime around $\hbar\omega_D$, where it might be speculated that $\varepsilon_1 \approx 100$. This region might be of further interest for future experiments.

Fig. 6.32 details the suppression evoked by Δ_p for both the dielectric constant ε_1 and the conductivity σ_1. a_ε and a_σ are the prefactors found in front of the scaling behavior of $\varepsilon_1(\delta)$ and $\sigma_1(\omega)$ respectively. In ε_1 no suppression is found for electron glass samples ($a_\varepsilon \approx 1$). For local pairing samples however, the suppression is about $a_\varepsilon \approx 0.25 - 0.5$, fitting well to the theoretical prediction. The suppression of σ_1 is constant across all local pairing samples and perfectly fits to the theoretically predicted value of about $a_\sigma \approx 0.028$ [38]. For the electron glass samples there is also a suppression found, however, it is weaker (larger a_σ) and enhances for stronger disorder. This suppression is in agreement to the qualitative prediction by

theory, which expects that for very strong localization, contributions to the hopping conductivity by Mott resonances decrease [33, 39]. The suppression of both ε_1 and σ_1 in both regimes perfectly fit to theoretical predictions and demonstrate that a pseudogap Δ_p opens in insulating indium oxide when electrons attractively interact and form localized Cooper-pairs [38, 39].

Indium oxide has been found to be a disordered, amorphous, insulating thin-film material, in which electrons are localized to small localization volumina. Cooper-attraction does not lead to superconductivity, but has the opposite effect, as it drives the material to an even stronger insulating state by opening a pseudogap, which in turn shows various fingerprints in polarization and conductivity. The main results of this work are

- Coulomb interactions between electrons are strongly suppressed for insulating indium oxide films close to the superconductor to insulator transition. ($\varepsilon_1 > \varepsilon_{1,\mathrm{c}} \approx 100$)
- The nature of the electronic states is found fractal close to SIT. (Scaling of $\varepsilon_1(T_0)$ and $\sigma_1(T_0)$ with fractal dimension $D_2 \approx 1.3$)
- Evidence for the opening of a pseudogap Δ_p is found close to, but on the insulating side of SIT. (Suppression of ε_1 and σ_1)

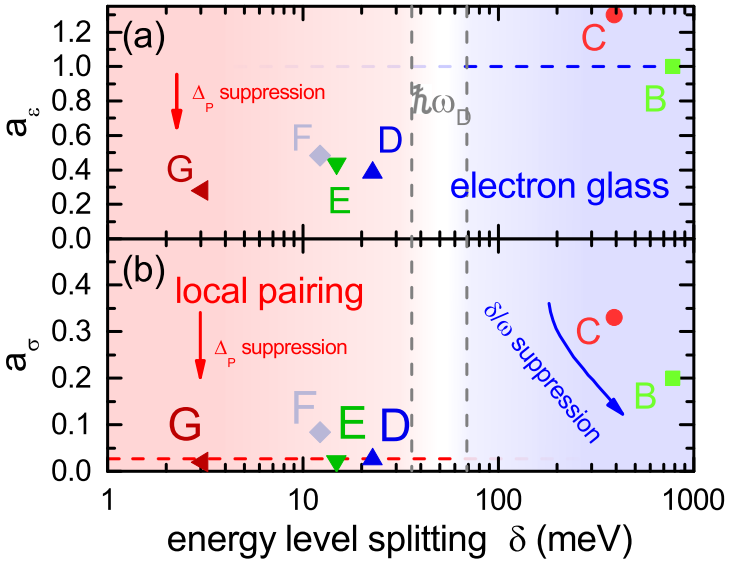

Fig. 6.32.: Suppression factors a_ε and a_σ extracted from the scaling behavior of (a) $\varepsilon_1(\delta)$ and (b) $\sigma_1(\omega)$. a_ε in (a) shows no suppression for electron glass samples ($a_\varepsilon \approx 1$). However, in the local pairing regime values of $\varepsilon_1(\delta)$ are suppressed by the emergence of a pseudogap Δ_p. This suppression is also found in (b) $\sigma_1(\omega)$, where Δ_p leads to a suppression down to the theoretically expected value of $a_\sigma \approx 0.028$. For electron glass samples a weaker suppression in $\sigma_1(\omega)$ is found, which even enhances with stronger localization. This suppression stems from reduced Mott resonance contributions.

7. Main conclusions from this work

In this work amorphous indium oxide thin-films samples with various amounts of disorder have been investigated. For this an experimental approach has been detailed [1], optimized and demonstrated, which allows for the investigation of the complex dielectric constant, including ε_1 and the microwave conductivity σ_1. It is based on coplanar waveguide (CPW) resonators and can be applied to ultra-thin film samples in the nm thickness regime, which act as perturbative element by being deposited on top of the resonators. It can be applied at temperatures below 8 K down to mK-temperatures. This allows for temperature-dependent measurements of $\varepsilon_1(T)$ and $\sigma_1(T)$, as well as frequency-dependent measurements from few GHz up to ~ 25 GHz.

With this, a wide range of disordered amorphous indium oxide samples on the insulating side of the superconductor-insulator-transition (SIT) has been investigated, ranging from samples close to the transition up to extremely localized samples very far away. Two regimes have been found. One being the electron glass regime far away from the transition, where single electrons are localized individually. Here, strong, only weakly screened Coulomb interactions act between the electrons, repelling them from each other, so that no attractive interaction prevails and single electrons are localized [29, 30]. Closer to SIT however, a second regime, the local pairing regime, exists, where Coulomb interactions are effectively screened such that Cooper-attraction surpasses Coulomb interactions and the localized electrons form localized Cooper-pairs [12, 33]. These localized Cooper-pairs are themselves confined

within their given localization volume and do not generate superconductivity. This state is then an insulating state, although Cooper-pairs prevail in the system. The magnitude of localization is characterized by the energy level splitting evoked by confinement of electrons to small areas [33]. This energy level splitting in turn categorizes the samples into the two above mentioned regimes, depending on its size in comparison to the Debye energy [12]. When the energy level splitting is smaller than the Debye energy, phonons will mediate Cooper-attraction, while if it is larger, Cooper-attraction cannot be mediated.

In the electron glass regime, good correspondence of the dielectric constant ε_1 to the localization length ξ is found as a function of disorder. This fits theoretical predictions well [39], which predict extremely localized amorphous indium oxide to be a three dimensional Anderson insulator, where $\varepsilon_1 \propto \xi^2$. As a function of temperature, Austin-Mott behavior is found, showing linear temperature dependence. Below a certain temperature, the conductivity is entirely dominated by photon-assisted Mott resonance hopping. At these low temperatures the frequency dependence confirms Mott behavior based on Mott resonances with the prefactor being found to be reduced due to the extreme localization, as predicted qualitatively by theory [33, 39].

At the transition from electron glass regime to local pairing regime a critical value of the dielectric constant of about $\varepsilon_1 \approx 100$ has been found, which perfectly matches quantitative theoretical predictions [33], assigning this value to be the critical value upon which electronic screening reduces Coulomb interactions to equal size of Cooper-attraction. In the electron glass regime it is $\varepsilon_1 < 100$ and Cooper-pairs cannot form. Closer to the transition, $\varepsilon_1 > 100$ is found and Cooper-attraction surpasses Coulomb repulsion. Here, localized Cooper-pairs are formed and the local pairing regime is established. This directly leads to a pseudogap Δ_p. Effects of Δ_p have directly been found in the frequency-dependent microwave conductivity $\sigma_1(\omega)$ and in disorder-dependent $\varepsilon_1(\xi)$, which show large suppressions in amplitude. The factor of suppression found, again perfectly matches quantitative theoretical predictions [38, 39]

and therefore gives direct evidence for the existence of a pseudogap even in entirely insulating amorphous indium oxide samples.

Scaling of $\varepsilon_1(T_0)$ with the activation temperature T_0 found from DC-measurements at low temperatures, where local pairing and therefore a pseudogap is found, shows $\varepsilon_1(T_0) \propto T_0^{-2/D_2} \approx T_0^{-1.54}$ and $\sigma_1(T_0) \propto T_0^{-5/D_2} \approx T_0^{-3.85}$. This confirms the scaling predicted by theory [33] with $D_2 \approx 1.3$ being the fractal dimension and shows that the electronic eigenstates close to the SIT are indeed (multi-)fractal, meaning that they occupy a fraction of the volume of a delocalized state.

Within this work, the dielectric constant ε_1 as well as the microwave conductivity σ_1 of insulating disordered amorphous indium oxide could be measured directly for the first time. It has been found that measured values of ε_1 are not in agreement with theories of indium oxide becoming insulating due to Coulomb blockade in analogy to a Josephson-junction array [14]. All of the above findings directly give very strong evidence, that insulating disordered amorphous indium oxide close to the transition is perfectly described as a fractal Anderson insulator with localized Cooper-pairs, as predicted by M. V. Feigel'man et al. [12, 33]. Within this work, crucial experiments could be performed and pivotal results have been gathered, giving an important contribution to the understanding of superconductivity in disordered thin-films.

Outlook To further establish the existence of a pseudogap Δ_p in insulating amorphous disordered indium oxide even better, the magnetic-field-dependence of ε_1 and σ_1 in strong magnetic field could be investigated in future experiments, since the suppression a of ε_1 and σ_1 is expected to also be magnetic field dependent due to the magnetic field affecting Δ_p [39]. For this, resonators would have to be designed, which are capable of operating even in very strong magnetic fields of several Tesla. With the current Nb-based resonators this is not possible due to the strong magnetic-field dependence of

Nb itself. However, e.g. with the help of high-T_c superconducting layers this might be possible in future experiments.

TiN forms amorphous thin-film layers, comparable to indium oxide [14, 17, 34], which may be of further interest to look for similar phenomena as found in this work for indium oxide. In TiN a high dielectric constant is expected as well [14], yet here also direct measurements have not been performed.

Acknowledgments

Finally I would like to thank everyone who contributed to this work and made this thesis possible. Many great people supported me and I would like to give my humble gratitude to everyone involved. Some people stand out, which I would like to thank in particular.

- Prof. Martin Dressel for the opportunity to work at the 1. Physikalisches Institut, University of Stuttgart and the possibility to do experimental work in a highly active and relevant topic.
- Prof. Jörg Wrachtrup for being my second examiner.
- Dr. Marc Scheffler for the continuous and very fruitful cooperative work in the microwave/high frequency-group. Thank you for many years of guidance, support and for the responsibilities that you trusted me with.
- Our close collaborator Benjamin Sacépé from Intitut Néel, CNRS Grenoble, France, for the outstanding indium oxide samples, as well as very fruitful discussions both online and in person at Grenoble.
- Our second close collaborator Mikhail Feigel'man from the Landau Institut, Moskau, Russia, for the formulation of the basic theories and the very helpful discussions. Thank you for answering all my questions.
- Gabriele Untereiner for the continuous support over many years and the assembling and treatment of resonators and samples, as well as all the friendly discussions.

- Agnieszka Cienkowska-Schmidt for the support concerning all organizational aspects and the very friendly help.
- The microstructure lab ob the 4. Physikalisches Insitut. In particular Monika Ubl for the fabrication and etching of the resonators as well as Philipp Karl and Ahmed Farag for the deposition of the Nb layers.
- Paul Kugler for the great collaboration and the measurements on sample B as well as many helpful discussions.
- Cenk Beydeda, Konstantin Nikolaou and Marius Tochtermann for the fruitful discussions, our cooperation and your contributions to the understanding and analysis of coplanar waveguide resonators.
- My PhD-colleagues Markus Thiemann, Björn Miksch and Anastasia Bauernfeind for the very good collaboration and friendly atmosphere.
- My student colleagues Alessandro D'Arnese, Mario Zinßer, Lars Wendel and Desirée Rausch for the good cooperative work.
- Vincent Engl for the very close collaboration and very friendly discussions.
- The low-temperature workshop, in particular Dario Profetto, Frank Wahl and Bernd Schobel, for the continuous supply of helium and nitrogen.
- Everyone involved at the 1. Physikalisches Insitut for the very friendly and cooperative atmosphere.

A. Appendix

A.1. Percolation theory

Percolation theory describes phenomena that occur if a larger system has randomly distributed small (compared to the total system) sub-structures (e.g. sites of a lattice) that interact with their nearest neighbors [235]. Each site has their own probability to be either of two states, e.g. conducting of non-conducting [236]. Then clusters can be formed consisting of multiple neighboring sites with the same state. These clusters are separated by areas with the opposing state. Within a cluster long-range interaction is possible from one end of the cluster to the other [235]. A system percolates, if a cluster gets as large as the system itself, meaning that a continuous path exists from one end of the system to the other, without having to hop between clusters. The driving property, which determines the size of the clusters is the probability distribution to be either state [235, 237]. In the conductive/non-conductive example, if the probability to be conductive is higher than to be non-conductive, large clusters will form. When one cluster spans the whole system it becomes macroscopically conductive. Percolation theory, however, is not limited to problems in solid state physics and can for example also describe the propagation of forest fires or the exploitation of oil fields [235], but due to obvious reasons the focus in this section will be placed on networks of conductive/less-conductive structures.

In a system with randomly distributed sites of well-conducting and less/non-conducting areas, a system will form as schematically shown in Fig. A.1 (a)

and (b) [14]. The white parts show conducting clusters separated by colored barriers. In this example (a) there are already two very large clusters that each connect to one electrode to either side. A possible path upon breaking one more insulating barrier (circled) is shown (dashed line), that would connect both electrodes and lead to macroscopic transport. Two smaller clusters separating the bigger clusters are shown in gray. Going closer to the percolation transition in (b), barriers separating the smaller clusters from the bigger ones break, incorporating the smaller ones to the latter. The system is now one step before percolation. This model shows, that by approaching the percolation transition the length of the barrier separating the two critical clusters (shown in green in (a) and (b)) increases further and further. This in turn leads to a characteristic critical scaling behavior of the system properties close to the transition [14, 236, 237].

In particular the dielectric constant ε shows critical behavior when approaching the transition [236, 237], leading to a divergence sometimes called the "polarization catastrophe" [238, 239]. The reasons for this divergence of ε get apparent when looking at the capacitance C of the clusters in Fig. A.1 (a) and (b). C is directly proportional to the length of the barrier b separating the clusters (shown in green), such as $C \propto b^{1+\psi}$ [14, 235], with ψ being a critical exponent > 0 (here ψ is only an exponent to show that C increases with b faster than linear). The dielectric constant in turn is directly proportional to the capacitance with $\varepsilon \propto C/b$ (equal to a simple plate capacitor), leading to $\varepsilon \propto b^{\psi}$ [14, 235]. Since the length of the barrier between clusters diverges upon approaching percolation, ε also diverges [236, 237, 240].

To find quantitative behavior of experimentally accessible quantities as a function of the distance to the percolation the general quantity ξ can be introduced as [235]

$$\xi \propto |p - p_c|^{-\nu} \ . \tag{A.1}$$

ξ is the correlation length of the system, defined as the average distance of two sites belonging to the same cluster. ν is the critical exponent depending only on the dimensionality of the system (universality hypothesis), but not its type (metallic/superconducting clusters, insulators etc.). p is the probability with which a site is one state (e.g. conductive), while $(1-p)$ is the probability of it being the other state (less-conductive). p_c is its critical value, where the system is percolating at $p > p_c$ [235]. With this, the scaling of the conductivity σ and of ε can be found as [237]

$$\sigma(p) = \begin{cases} \sigma_0 \left(p - p_c\right)^t & p > p_c \\ \sigma_d \left(p_c - p\right)^{-q} & p < p_c \end{cases} \tag{A.2}$$

$$\varepsilon(p) = \varepsilon_d \left(p - p_c\right)^{-q} . \tag{A.3}$$

σ_0 is the conductivity of the system where all sites are conducting ($p = 1$) and σ_d the (residual) conductivity where all states are less-conductive ($p = 0$). If the less-conductive state is in fact insulating then $\sigma_d = 0$ and $\sigma(p) = 0$ for $p < p_c$. ε_d is the dielectric constant of the insulating parts. Note that $\varepsilon(p)$ (A.3) only applies at $p < p_c$ (system not percolating). Both $\sigma(p)$ and $\varepsilon(p)$ diverge when approaching the percolation respectively from the conducting side and the insulating side. If $\sigma_d > 0$, $\sigma(p)$ diminishes at the percolation transition. In reality there is a smooth crossover of $\sigma(p)$ from $p < p_c$ to $p > p_c$ [237].

The critical exponents ν, t and q introduced above only depend on the dimension d of the system but not on the type of percolation [235, 237]. They can in part be derived analytically but mostly have to be found in numerical fashion [235, 241, 242], simulating e.g. resistor-capacitor networks [236] as shown exemplary in Fig. A.1 (c). The following values therefore have a certain uncertainty and can vary depending on the underlying analysis, especially in three dimensions [235]. Typically ν, the critical exponent for the correlation length is found as $\nu \approx 4/3 \approx 1.33$ ($d = 2$) and $\nu \lesssim 0.9$ ($d = 3$)

[235, 241]. For t it follows $t = (d-1)\nu$ [241]. The other exponents can then be derived following $q = t\,(1/s - 1)$ [237], with s being a critical exponent $s = 1/2$ ($d = 2$) and $s \approx 0.62$ ($d = 3$). With this it is found for $d = 2$, $t = q = \nu \approx 1.3$ [237] and in $d = 3$, $t \approx 1.6 - 2$ [237, 241], $q \approx 1$ [237].

In reality the divergence of the dielectric constant may be somewhat limited. This is dependent on the frequency ω of the electromagnetic waves probing $\varepsilon(p, \omega)$ and leads to a maximum value of $\varepsilon(p_c, \omega) = \varepsilon_d \left(\frac{4\pi\sigma_0}{\omega\varepsilon_d}\right)^{1-s}$ (cgs units) [188, 237]. Equation (A.3) can also be expressed as a function of thickness of percolating thin-films, with similar exponential behavior [188].

In solid state physics systems showing percolative behavior are manifold. Prime examples are granular thin-films, such as Au [188], Pb [243], Sn [5, 244] or Al [245, 246]. Also the previously discussed (section 3.4) Josephson-junction arrays, in most instances being the fundamental system of granular thin-films, can be described by percolative behavior [14, 247–250]. But also composite polymers can show percolative behavior [251, 252] and percolation can also lead to phase coexistence e.g. at the first order Mott transition [253–255].

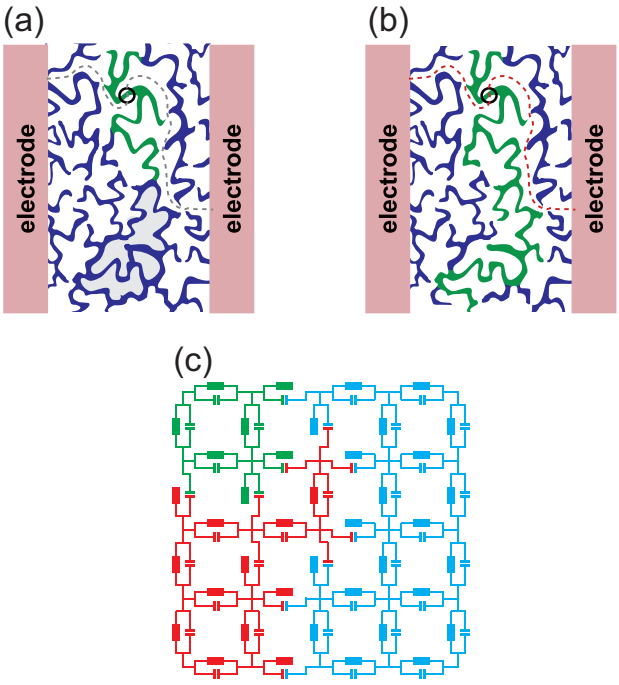

Fig. A.1.: (a,b) System consisting of metallic clusters (white), separated by insulating barriers (colored) connected to electrodes to both sides. (a) Shows a non-percolating structure, with two large clusters to the left and right and some smaller clusters (gray) in between. Green barriers denote the barrier between the two largest clusters. (b) Same system one step before percolation. Upon breaking the encircled barrier a path connecting the electrodes (red) is possible. (c) Network consisting of resistors (⎓) and capacitors (⏚) for numerical studies. Connections at resistors are randomly broken, leading to three big clusters (colors). Figure (a) and (b) with modifications from [14].

A.2. Calculation of the dielectric constant in electron glass sample A

Unfortunately, for sample A no proper reference data (before deposition of the sample to the resonator-chip) has been obtained. This means, that a direct comparison of reference resonance to resonance under the influence of the sample has not been possible. Due to these circumstances, the resonators have been measured once with applied sample, after which the sample has been removed by acetone from one of the resonators, as shown in Fig. A.2 (a). This lead to the resonance shift, as shown in (b). The shape of the resonance changes quite significantly as well. This however, can be expected, since the removal of the sample necessitates a cleaning procedure included disassembling of the resonator-chip from the mounting box and the subsequent refitting following successfully removal of the sample. The contacting of the feedline to the external circuitry therefore had to be redone and transmission properties could slightly change. This repeated contacting however, does not have any influence on either Q nor the resonance frequency, as can be exemplary seen for an untreated resonator in Fig. A.2 (c), where both Q and the resonance frequency are constant. The treatment of the resonator in (b) however, leads to a resonance shift compared to the background and might change shape of the resonance. From the resonance shift and the change in Q of the treated resonator, ε_1 can be calculated directly. For the other resonators however, the reference data has to be extrapolated from the frequency shift shown in (b). This is exemplary shown in (c), where a neighboring resonator shows no effective change in the two spectra before and after treatment (solid lines). The dashed line however, shows the resonance extrapolated from the shift in (b), which has been acquired by scaling the frequency shift to the whole spectral range. From this, ε_1 can be estimated for the other resonators. Naturally however, this leads to some substantial uncertainties, since the true reference value is unknown (estimated as error bars in section 6.4.2).

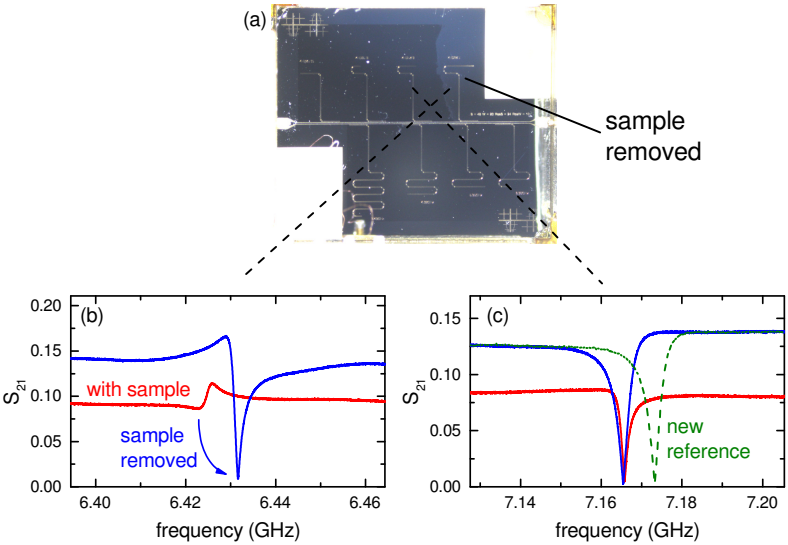

Fig. A.2.: (a) Sample A covering its resonator-chip. The sample has been removed from one resonator, after the initial measurement. (b) Spectra of the treated resonator with sample and with removed sample. Reference data is recovered. (c) Spectra of an untreated resonator. The dashed line shows a spectrum extrapolated from the shift in (b).

A.3. Error-bars of electron glass sample B

During the repeated measurements of sample B an unexpected shift in resonance frequency has been found, which is not stemming from the sample. This can be seen when comparing spectra of a resonator under the influence of the sample, shown in Fig. A.3 (a) and an empty resonator shown in (b). The empty resonator is expected to stay constant across all stages of aging. However it is seen, that there is a slight shift at some point during the repeated measurements over few months. The origin of this shift is unknown, but it probably stems from slight changes in the Nb conductor layer. It

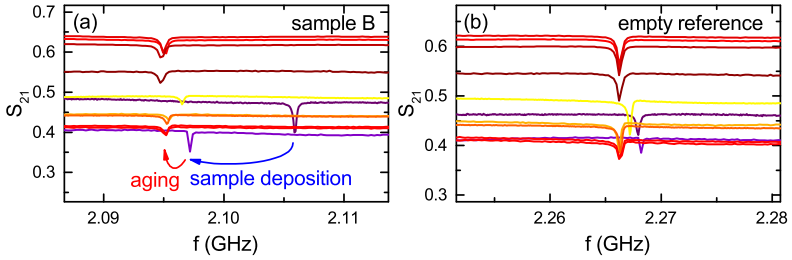

Fig. A.3.: (a) Spectra of a resonance under the influence of sample A. An unexpected additional shift is seen at some point during the repeated measurements. This unexpected shift is also seen for an empty resonator, shown in (b).

has never been observed for other resonator-chips probing the other samples. However, compared to the shift evoked by ε_1 of the sample, shown in (a), this unexpected shift is small ($< 15\,\%$), meaning that it only leads to small uncertainty. While it has not been included in the calculation of ε_1, since the exact magnitude of the underlying shift for each individual resonator is unknown, it has been respected by estimated error bars in section 6.4.2.

A.4. Original sample names and annealing steps

In Tab. A.1 the original sample names are given connected to the sample names used in this work. In Tab. A.2 the characteristic activation energies are given for all measurement steps as well as an indication whether this step was reached by annealing.

Tab. A.1.: Sample names used in this work and original names during measurements.

Sample name	Original sample name
A	NE012
B	NE011
C	NE007
D	NE003
E	NE010
F	NE002
G	NE013
H	NE006

Tab. A.2.: Characteristic activation temperatures of all measurement steps.

S	$T_{0,\mathrm{Mott}}$ [K]	$T_{0,\mathrm{ES}}$ [K]	T_0 [K]	Annealing
A	9.97E+05	1.84E+03	-	-
B	1.49E+05	9.70E+02	-	+
	1.93E+05	1.00E+03	-	+
	1.22E+05	9.19E+02	-	+
	1.04E+05	8.31E+02	-	+
	1.17E+05	8.35E+02	-	+
	1.03E+05	7.85E+02	-	+
	8.75E+04	7.82E+02	-	+
	8.35E+04	6.89E+02	-	+
	1.20E+05	6.66E+02	-	+
	9.23E+04	6.56E+02	-	+
	6.87E+04	6.20E+02	-	+
	7.09E+04	5.73E+02	-	+
	7.02E+04	5.77E+02	-	+
	6.59E+04	6.16E+02	-	+
	6.31E+04	5.43E+02	-	+
C	4.54E+04	3.86E+02	-	-
	8.49E+04	3.90E+02	-	-
	7.29E+04	4.33E+02	-	-
	6.03E+04	3.36E+02	-	+
	6.04E+04	4.02E+02	-	+
D	5.37E+03	-	15.33	-
	-	-	14.06	-
	3.50E+03	-	12.84	-
	-	-	13.16	-
	-	-	12.69	-
	-	-	12.23	-
E	2.34E+03	-	12.39	+
	-	-	12.45	+
	2.43E+03	-	13.30	+
	3.84E+03	-	17.30	+
	3.99E+03	-	12.59	+
	2.31E+03	-	11.77	+
	2.14E+03	-	11.96	+
	1.78E+03	-	10.69	-
	-	-	10.02	-
	1.69E+03	-	10.75	-
F	-	-	9.58	-
	-	-	9.32	-
	6.57E+03	-	9.23	-
	-	-	8.34	-
	3.31E+03	-	8.16	-
	1.19E+03	-	-	-
	6.89E+02	-	7.82	-
	-	-	7.63	-
	-	-	7.55	-
G	6.20E+02	3.18E+01	6.54	-
	5.83E+02	2.97E+01	6.31	-
	5.56E+02	3.04E+01	6.30	-
	4.54E+02	2.58E+01	6.09	-
	6.47E+02	2.36E+01	5.76	-

Schriftliche Bestätigung der eigenständig erbrachten Leistung gemäß § 6 Absatz 2 der Promotionsordnung der Universität Stuttgart

Die eingereichte Dissertation zum Thema
Dielectric properties on the insulating side of the superconductor-insulator transition
stellt meine eigenständig erbrachte Leistung dar.
Ich habe ausschließlich die angegebenen Quellen und Hilfsmittel benutzt. Wörtlich oder inhaltlich aus anderen Werken übernommene Angaben habe ich als solche kenntlich gemacht.
Die Richtigkeit der hier getätigten Angaben bestätige ich und versichere, nach bestem Wissen die Wahrheit erklärt zu haben.

Stuttgart, den

Erklärung zur Übereinstimmung der digitalen Version mit der vorgelegten Printversion der Dissertation

Hiermit erkläre ich, Nikolaj Gabriel Ebensperger, geboren am 29.12.1991, dass das von mir eingereichte pdf-Dokument zur Dissertation mit dem Thema *Dielectric properties on the insulating side of the superconductor-insulator transition*
in Inhalt und Wortlaut der ebenfalls eingereichten Printversion meiner Dissertationsschrift entspricht.

Stuttgart, den

References

[1] N. G. Ebensperger, B. Ferdinand, D. Koelle, R. Kleiner, M. Dressel, and M. Scheffler, "Characterizing dielectric properties of ultra-thin films using superconducting coplanar microwave resonators", *Rev. Sci. Instrum.* **90**, 114701 (2019).

[2] L. Wendel, V. T. Engl, G. Untereiner, N. G. Ebensperger, M. Dressel, A. Farag, M. Ubl, H. Giessen, and M. Scheffler, "Microwave probing of bulk dielectrics using superconducting coplanar resonators in distant-flip-chip geometry", *Rev. Sci. Instrum.* **91**, 054702 (2020).

[3] V. T. Engl, N. G. Ebensperger, L. Wendel, and M. Scheffler, "Planar GHz resonators on SrTiO3: suppressed losses at temperatures below 1 K", *arXiv* **cond-mat.supr-con**, 1911.11456 (2019).

[4] N. G. Ebensperger, M. Thiemann, M. Dressel, and M. Scheffler, "Superconducting pb stripline resonators in parallel magnetic field and their application for microwave spectroscopy", *Supercond. Sci. Technol.* **29**, 115004 (2016).

[5] M. H. Beutel, N. G. Ebensperger, M. Thiemann, G. Untereiner, V. Fritz, M. Javaheri, J. Nägele, R. Rösslhuber, M. Dressel, and M. Scheffler, "Microwave study of superconducting sn films above and below percolation", *Supercond. Sci. Technol.* **29**, 085011 (2016).

[6] A. M. Goldman and N. Marković, "Superconductor-insulator transitions in the two-dimensional limit", *Phys. Today* **51**, 39 (1998).

[7] V. F. Gantmakher and V. T. Dolgopolov, "Superconductor–insulator quantum phase transition", *Phys. Usp.* **53**, 1 (2010).

[8] B. Sacépé, M. Feigel'man, and T. M. Klapwijk, "Quantum breakdown of superconductivity in low-dimensional materials", *Nat. Phys.* **16**, 734 (2020).

[9] S. L. Sondhi, S. M. Girvin, J. P. Carini, and D. Shahar, "Continuous quantum phase transitions", *Rev. Mod. Phys.* **69**, 315 (1997).

[10] D. Shahar and Z. Ovadyahu, "Superconductivity near the mobility edge", *Phys. Rev. B* **46**, 10917 (1992).

[11] U. Givan and Z. Ovadyahu, "Compositional disorder and transport peculiarities in the amorphous indium oxides", *Phys. Rev. B* **86**, 165101 (2012).

[12] M. V. Feigel'man, L. B. Ioffe, V. E. Kravtsov, and E. A. Yuzbashyan, "Eigenfunction fractality and pseudogap state near the superconductor-insulator transition", *Phys. Rev. Lett.* **98**, 027001 (2007).

[13] M. V. Feigel'man, L. B. Ioffe, and M. Mézard, "Superconductor-insulator transition and energy localization", *Phys. Rev. B* **82**, 184534 (2010).

[14] T. I. Baturina and V. M. Vinokur, "Superinsulator–superconductor duality in two dimensions", *Ann. Phys.* **331**, 236 (2013).

[15] I. S. Beloborodov, A. V. Lopatin, V. M. Vinokur, and K. B. Efetov, "Granular electronic systems", *Rev. Modern Phys.* **79**, 469 (2007).

[16] A. F. Hebard and M. A. Paalanen, "Pair-breaking model for disorder in two-dimensional superconductors", *Phys. Rev. B* **30**, 4063 (1984).

[17] B. Sacépé, C. Chapelier, T. I. Baturina, V. M. Vinokur, M. R. Baklanov, and M. Sanquer, "Disorder-induced inhomogeneities of the superconducting state close to the superconductor-insulator transition", *Phys. Rev. Lett.* **101**, 15 (2008).

[18] S. Muranaka, H. Hirooka, and Y. Bando, "Influence of oxygen pressure on the structure of reactively deposited indium oxide films", *J Mater Chem* **3**, 237 (1993).

[19] D. Kowal and Z. Ovadyahu, "Disorder induced granularity in an amorphous superconductor", *Solid State Commun.* **90**, 783 (1994).

[20] D. B. Buchholz, Q. Ma, D. Alducin, A. Ponce, M. Jose-Yacaman, R. Khanal, J. E. Medvedeva, and R. P. H. Chang, "The structure and properties of amorphous indium oxide", *Chem. Mater.* **26**, 5401 (2014).

[21] D. B. Haviland, Y. Liu, and A. M. Goldman, "Onset of superconductivity in the two-dimensional limit", *Phys. Rev. Lett.* **62**, 2180 (1989).

[22] A. F. Hebard and M. A. Paalanen, "Magnetic-field-tuned superconductor-insulator transition in two-dimensional films", *Phys. Rev. Lett.* **65**, 927 (1990).

[23] A. Yazdani and A. Kapitulnik, "Superconducting-insulating transition in two-dimensionala-MoGe thin films", *Phys. Rev. Lett.* **74**, 3037 (1995).

[24] T. I. Baturina, D. R. Islamov, J. Bentner, C. Strunk, M. R. Baklanov, and A. Satta, "Superconductivity on the localization threshold and magnetic-field-tuned superconductor-insulator transition in TiN films", *JETP Lett.* **79**, 337 (2004).

[25] G. Sambandamurthy, L. W. Engel, A. Johansson, and D. Shahar, " Superconductivity-related insulating behavior", *Phys. Rev. Lett.* **92**, 10 (2004).

[26] D. Sherman, G. Kopnov, E. Farber, D. Shahar, and A. Frydman, "Tunneling density of states of indium oxide films through the superconductor to insulator transition", *J Supercond Nov Magn* **26**, 1473 (2013).

[27] P. W. Anderson, "Theory of dirty superconductors", *J. Phys. Chem. Solids* **11**, 26 (1959).

[28] B. Sacépé, T. Dubouchet, C. Chapelier, M. Sanquer, M. Ovadia, D. Shahar, M. Feigel'man, and L. Ioffe, "Localization of preformed cooper pairs in disordered superconductors", *Nat. Phys.* **7**, 239 (2011).

[29] A. M. Finkel'stein, "Superconducting transition temperature in amorphous films", *JETP Lett.* **45**, 46 (1987).

[30] A. M. Finkel'stein, "Suppression of superconductivity in homogeneously disordered systems", *Phys. B: Condens. Matter* **197**, 636 (1994).

[31] J. M. Graybeal and M. R. Beasley, "Localization and interaction effects in ultrathin amorphous superconducting films", *Phys. Rev. B* **29**, 4167 (1984).

[32] T. Dubouchet, B. Sacépé, J. Seidemann, D. Shahar, M. Sanquer, and C. Chapelier, "Collective energy gap of preformed Cooper pairs in disordered superconductors", *Nat. Phys.* **15**, 233 (2019).

[33] M. V. Feigel'man, L. B. Ioffe, V. E. Kravtsov, and E. Cuevas, "Fractal superconductivity near localization threshold", *Ann. Phys.* **325**, 1390 (2010).

[34] V. M. Vinokur, T. I. Baturina, M. V. Fistul, A. Y. Mironov, M. R. Baklanov, and C. Strunk, "Superinsulator and quantum synchronization", *Nature* **452**, 613 (2008).

[35] M. P. A. Fisher, P. B. Weichman, G. Grinstein, and D. S. Fisher, "Boson localization and the superfluid-insulator transition", *Phys. Rev. B* **40**, 546 (1989).

[36] M. P. A. Fisher, "Quantum phase transitions in disordered two-dimensional superconductors", *Phys. Rev. Lett.* **65**, 923 (1990).

[37] E. Cuevas and V. E. Kravtsov, "Two-eigenfunction correlation in a multifractal metal and insulator", *Phys. Rev. B* **76**, 235119 (2007).

[38] D. A. Ivanov and M. V. Feigel'man, "Low-energy dynamical response of an anderson insulator with local attraction", *Phys. Rev. B* **95**, 045147 (2017).

[39] M. V. Feigel'man, D. A. Ivanov, and E. Cuevas, "Dielectric response of anderson and pseudogapped insulators", *New J. Phys.* **20**, 053045 (2018).

[40] V. F. Gantmakher and M. V. Golubkov, "Giant negative magnetoresistance of semi-insulating amorphous indium oxide films in strong magnetic fields", *JETP* **82**, 951 (1996).

[41] Z. Ovadyahu, "Suppression of inelastic electron-electron scattering in anderson insulators", *Phys. Rev. Lett.* **108**, 156602 (2012).

[42] M. Ovadia, D. Kalok, I. Tamir, S. Mitra, B. Sacépé, and D. Shahar, "Evidence for a finite-temperature insulator", *Sci. Rep.* **5**, 1 (2015).

[43] B. I. Shklovskii and A. L. Efros, "Zero-phonon ac hopping conductivity of disordered systems", *JETP* **54**, 218 (1981).

[44] L. P. Gor'kov, O. N. Dorokhov, and F. V. Prigara, "Structure of wave functions and ac conductivity in disordered one-dimensional conductors", *Zh. Eksp. Teor. Fiz.* **85**, 1470 (1983).

[45] Z. Ovadyahu, "Structural dynamics in thermal treatment of amorphous indium oxide films", *Phys Status Solidi B* **257**, 1900310 (2019).

[46] A. Ghosal, M. Randeria, and N. Trivedi, "Role of spatial amplitude fluctuations in highly disordereds-wave superconductors", *Phys. Rev. Lett.* **81**, 3940 (1998).

[47] A. Ghosal, M. Randeria, and N. Trivedi, "Inhomogeneous pairing in highly disordereds-wave superconductors", *Phys. Rev. B* **65**, 014501 (2001).

[48] D. Sherman, G. Kopnov, D. Shahar, and A. Frydman, "Measurement of a superconducting energy gap in a homogeneously amorphous insulator", *Phys. Rev. Lett.* **108**, 177006 (2012).

[49] Z. Ovadyahu, "Electron glass in a three-dimensional system", *Phys. Rev. B* **90**, 054204 (2014).

[50] M. V. Feigel'man and L. B. Ioffe, "Microwave properties of superconductors close to the superconductor-insulator transition", *Phys. Rev. Lett.* **120**, 037004 (2018).

[51] J. Bardeen, L. N. Cooper, and J. R. Schrieffer, "Theory of superconductivity", *Phys. Rev.* **108**, 1175 (1957).

[52] N. F. Mott, "Conduction in glasses containing transition metal ions", *J. Non-Cryst. Solids* **1**, 1 (1968).

[53] A. L. Efros and B. I. Shklovskii, "Coulomb gap and low temperature conductivity of disordered systems", *J. Phys. C: Solid State Phys.* **8**, L49 (1975).

[54] R. Rosenbaum, "Crossover from Mott to Efros-Shklovskii variable-range-hopping conductivity in In_xO_y films", *Phys. Rev. B* **44**, 3599 (1991).

[55] L. B. Ioffe and M. Mézard, "Disorder-driven quantum phase transitions in superconductors and magnets", *Phys. Rev. Lett.* **105**, 037001 (2010).

[56] M. Dressel and G. Grüner, *Electrodynamics of solids: optical properties of electrons in matter* (Cambridge University Press, Cambridge, UK, 2011).

[57] D. A. Ivanov, M. A. Skvortsov, P. M. Ostrovsky, and Y. V. Fominov, "Hybridization of wave functions in one-dimensional localization", *Phys. Rev. B* **85**, 035109 (2012).

[58] L. N. Cooper, "Bound electron pairs in a degenerate Fermi gas", *Phys. Rev.* **104**, 1189 (1956).

[59] D. S. Inosov, J. T. Park, A. Charnukha, Y. Li, A. V. Boris, B. Keimer, and V. Hinkov, "Crossover from weak to strong pairing in unconventional superconductors", *Phys. Rev. B* **83**, 214520 (2011).

[60] F. London and H. London, "The electromagnetic equations of the supraconductor", *Proc. Roy. Soc. A* **149**, 71 (1935).

[61] M. Tinkham, *Introduction to superconductivity* (Dover Publications, 2004).

[62] N. W. Ashcroft and N. D. Mermin, *Solid state physics* (Holt, Rinehart and Winston, New York, USA, 1976).

[63] T. Ando, A. B. Fowler, and F. Stern, "Electronic properties of two-dimensional systems", *Rev. Mod. Phys.* **54**, 437 (1982).

[64] C. H. Seager and G. E. Pike, "Percolation and conductivity: a computer study. II", *Phys. Rev. B* **10**, 1435 (1974).

[65] M. Hering, M. Scheffler, M. Dressel, and H. v. Löhneysen, "Signature of electronic correlations in the optical conductivity of the doped semiconductor Si:P", *Phys. Rev. B* **75**, 205203 (2007).

[66] J. G. Massey and M. Lee, "Direct observation of the coulomb correlation gap in a nonmetallic semiconductor, Si:B", *Phys. Rev. Lett.* **75**, 4266 (1995).

[67] J.-J. Kim and H. J. Lee, "Observation of a nonmagnetic hard gap in amorphous In/InOx films in the hopping regime", *Phys. Rev. Lett.* **70**, 2798 (1993).

[68] M. Hornung and H. v. Löhneysen, "Crossover from Mott to Efros-Shklovskii variable range-hopping in Si:P", *Czechoslovak J. Phys.* **46**, 2437 (1996).

[69] P. N. Butcher, "Calculation of hopping transport coefficients", *Philos. Mag. B* **42**, 799 (1980).

[70] N. F. Mott, "Conduction in non-crystalline systems i", *Philos. Mag.* **17**, 1259 (1968).

[71] N. F. Mott, "Conduction in non-crystalline systems iv", *Philos. Mag.* **22**, 7 (1970).

[72] E. Helgren, N. P. Armitage, and G. Grüner, "Electrodynamics of a Coulomb glass in n-type Silicon", *Phys. Rev. Lett.* **89**, 246601 (2002).

[73] M. Pollak and T. H. Geballe, "Low-frequency conductivity due to hopping processes in Silicon", *Phys. Rev.* **122**, 1742 (1961).

[74] A. L. Efros, "On the theory of a.c. conduction in amorphous semiconductors and chalcogenide glasses", *Philos. Mag. B* **43**, 829 (1981).

[75] R. N. Bhatt, "Dielectric constant of an Anderson insulator", *J. Phys. C: Solid State Phys.* **18**, L537 (1985).

[76] A. I. Larkin and A. A. Varlamov, "Fluctuation phenomena in superconductors", *arXiv* **cond-mat.supr-con**, 0109177 (2001).

[77] A. Larkin, "Superconductor-insulator transitions in films and bulk materials", *Ann. Phys.* **8**, 785 (1999).

[78] P. B. Weichman, "Dirty bosons: twenty years later", *Modern Phys. Lett. B* **22**, 2623 (2008).

[79] S. Maekawa, H. Ebisawa, and H. Fukuyama, "Upper critical field in two-dimensional superconductors", *J. Phys. Soc. Japan* **52**, 1352 (1983).

[80] B. L. AItshuler and A. G. Aronov, "Contribution to the theory of disordered metals in strongly doped semiconductors", *JETP* **50**, 968 (1979).

[81] B. L. Altshuler, A. G. Aronov, and P. A. Lee, "Interaction effects in disordered fermi systems in two dimensions", *Phys. Rev. Lett.* **44**, 1288 (1980).

[82] V. L. Berezinskii, "Destruction of long-range order in one-dimensional and two-dimensional systems having a continuous symmetry group I. classical systems", *Sov. Phys. JETP* **32**, 493 (1971).

[83] J. M. Kosterlitz and D. J. Thouless, "Ordering, metastability and phase transitions in two-dimensional systems", *J. Phys. C: Solid State Phys.* **6**, 1181 (1973).

[84] Y. Dubi, Y. Meir, and Y. Avishai, "Nature of the superconductor–insulator transition in disordered superconductors", *Nature* **449**, 876 (2007).

[85] M. P. A. Fisher, G. Grinstein, and S. M. Girvin, "Presence of quantum diffusion in two dimensions: universal resistance at the superconductor-insulator transition", *Phys. Rev. Lett.* **64**, 587 (1990).

[86] K. B. Efetov, "Phase transition in granulated superconductors", *JETP* **51**, 1015 (1980).

[87] B. Srinivasan, G. Benenti, and D. L. Shepelyansky, "Transition to an insulating phase induced by attractive interactions in the disordered three-dimensional hubbard model", *Phys. Rev. B* **66**, 172506 (2002).

[88] P. W. Anderson, "Random-phase approximation in the theory of superconductivity", *Phys. Rev.* **112**, 1900 (1958).

[89] A. Gerber, A. Milner, G. Deutscher, M. Karpovsky, and A. Gladkikh, "Insulator-superconductor transition in 3D granular Al-Ge films", *Phys. Rev. Lett.* **78**, 4277 (1997).

[90] U. S. Pracht, N. Bachar, L. Benfatto, G. Deutscher, E. Farber, M. Dressel, and M. Scheffler, "Enhanced cooper pairing versus suppressed phase coherence shaping the superconducting dome in coupled aluminum nanograins", *Phys. Rev. B* **93**, 100503 (2016).

[91] F. Levy-Bertrand, T. Klein, T. Grenet, O. Dupré, A. Benoît, A. Bideaud, O. Bourrion, M. Calvo, A. Catalano, A. Gomez, J. Goupy, L. Grünhaupt, U. v. Luepke, N. Maleeva, F. Valenti, I. M. Pop, and A. Monfardini, "Electrodynamics of granular aluminum from superconductor to insulator: observation of collective superconducting modes", *Phys. Rev. B* **99**, 094506 (2019).

[92] M. Mondal, A. Kamlapure, M. Chand, G. Saraswat, S. Kumar, J. Jesudasan, L. Benfatto, V. Tripathi, and P. Raychaudhuri, "Phase fluctuations in a strongly disordereds-wave NbN superconductor close to the metal-insulator transition", *Phys. Rev. Lett.* **106**, 047001 (2011).

[93] M. Chand, G. Saraswat, A. Kamlapure, M. Mondal, S. Kumar, J. Jesudasan, V. Bagwe, L. Benfatto, V. Tripathi, and P. Raychaudhuri, "Phase diagram of the strongly disordereds-wave superconductor NbN close to the metal-insulator transition", *Phys. Rev. B* **85**, 014508 (2012).

[94] T. I. Baturina, A. Y. Mironov, V. M. Vinokur, M. R. Baklanov, and C. Strunk, "Hyperactivated resistance in TiN films on the insulating side of the disorder-driven superconductor-insulator transition", *JETP Lett.* **88**, 752 (2008).

[95] B. Spivak and F. Zhou, "Mesoscopic effects in disordered superconductors near H_{c2}", *Phys. Rev. Lett.* **74**, 2800 (1995).

[96] M. A. Skvortsov and M. V. Feigel'man, "Superconductivity in disordered thin films: giant mesoscopic fluctuations", *Phys. Rev. Lett.* **95**, 057002 (2005).

[97] M. V. Feigel'man, A. I. Larkin, and M. A. Skvortsov, "Quantum superconductor-metal transition in a proximity array", *Phys. Rev. Lett.* **86**, 1869 (2001).

[98] R. Fazio and H. van der Zant, "Quantum phase transitions and vortex dynamics in superconducting networks", *Phys. Rep.* **355**, 235 (2001).

[99] D. J. Resnick, J. C. Garland, J. T. Boyd, S. Shoemaker, and R. S. Newrock, "Kosterlitz-thouless transition in proximity-coupled superconducting arrays", *Phys. Rev. Lett.* **47**, 1542 (1981).

[100] R. Fazio and G. Schön, "Charge and vortex dynamics in arrays of tunnel junctions", *Phys. Rev. B* **43**, 5307 (1991).

[101] N. M. Zimmerman, W. H. Huber, B. Simonds, E. Hourdakis, A. Fujiwara, Y. Ono, Y. Takahashi, H. Inokawa, M. Furlan, and M. W. Keller, "Why the long-term charge offset drift in Si single-electron tunneling transistors is much smaller (better) than in metal-based ones: two-level fluctuator stability", *J. Appl. Phys.* **104**, 033710 (2008).

[102] M. Wallin, E. S. Sorensen, S. M. Girvin, and A. P. Young, "Superconductor-insulator transition in two-dimensional dirty boson systems", *Phys. Rev. B* **49**, 12115 (1994).

[103] V. Gurarie, L. Pollet, N. V. Prokof'ev, B. V. Svistunov, and M. Troyer, "Phase diagram of the disordered Bose-Hubbard model", *Phys. Rev. B* **80**, 214519 (2009).

[104] M.-C. Cha, M. P. A. Fisher, S. M. Girvin, M. Wallin, and A. P. Young, "Universal conductivity of two-dimensional films at the superconductor-insulator transition", *Phys. Rev. B* **44**, 6883 (1991).

[105] G. Sambandamurthy, A. Johansson, E. Peled, D. Shahar, P. G. Björnsson, and K. A. Moler, "Power law resistivity behavior in 2D superconductors across the magnetic field-tuned superconductor-insulator transition", *Europhys. Lett.* **75**, 611 (2006).

[106] I. S. Beloborodov, K. B. Efetov, and A. I. Larkin, "Magnetoresistance of granular superconducting metals in a strong magnetic field", *Phys. Rev. B* **61**, 9145 (2000).

[107] V. F. Gantmakher, M. V. Golubkov, V. T. Dolgopolov, A. Shashkin, and G. E. Tsydynzhapov, "Observation of the parallel-magnetic-field-induced superconductor-insulator transition in thin amorphous InO films", *JETP Lett.* **71**, 473 (2000).

[108] M. Ovadia, D. Kalok, B. Sacépé, and D. Shahar, "Duality symmetry and its breakdown in the vicinity of the superconductor–insulator transition", *Nat. Phys.* **9**, 415 (2013).

[109] M. V. Burdastyh, S. V. Postolova, I. A. Derbezov, A. V. Gaisler, M. C. Diamantini, C. A. Trugenberger, V. M. Vinokur, and A. Y. Mironov, "Dimension effects in insulating NbTiN disordered films and the asymptotic freedom of cooper pairs", *JETP Lett.* **109**, 795 (2019).

[110] L. V. Keldysh, "Coulomb interaction in thin semiconductor and semimetal films", *JETP Lett.* **29**, 658 (1979).

[111] M. V. Fistul, V. M. Vinokur, and T. I. Baturina, "Collective cooper-pair transport in the insulating state of Josephson-junction arrays", *Phys. Rev. Lett.* **100**, 086805 (2008).

[112] D. Kowal and Z. Ovadyahu, "Scale dependent superconductor–insulator transition", *Physica C: Supercond.* **468**, 322 (2008).

[113] D. Kalok, A. Bilusic, T. I. Baturina, V. M. Vinokur, and C. Strunk, "Intrinsic non-linear conduction in the super-insulating state of thin tin films", *arXiv* **cond-mat.supr-con**, 1004.5153 (2010).

[114] A. Mirlin, "Statistics of energy levels and eigenfunctions in disordered systems", *Phys. Rep.* **326**, 259 (2000).

[115] B. Kramer and A. MacKinnon, "Localization: theory and experiment", *Rep. Progr. Phys.* **56**, 1469 (1993).

[116] D. A. Parshin and H. R. Schober, "Distribution of fractal dimensions at the anderson transition", *Phys. Rev. Lett.* **83**, 4590 (1999).

[117] A. Mildenberger, F. Evers, and A. D. Mirlin, "Dimensionality dependence of the wave-function statistics at the anderson transition", *Phys. Rev. B* **66**, 033109 (2002).

[118] K. A. Matveev and A. I. Larkin, "Parity effect in ground state energies of ultrasmall superconducting grains", *Phys. Rev. Lett.* **78**, 3749 (1997).

[119] M. V. Feigel'man, *private communication* (2018).

[120] T. Ohtsuki, K. Slevin, and T. Kawarabayashi, "Review of recent progress on numerical studies of the anderson transition", *Ann. Phys.* **8**, 655 (1999).

[121] T. I. Baturina, A. Y. Mironov, V. M. Vinokur, M. R. Baklanov, and C. Strunk, "Localized superconductivity in the quantum-critical region of the disorder-driven superconductor-insulator transition in TiN thin films", *Phys. Rev. Lett.* **99**, 25 (2007).

[122] A. A. Abrikosov and I. A. Ryzhkin, "Conductivity of quasi-one-dimensional metal systems", *Adv. Phys.* **27**, 147 (1978).

[123] M. V. Feigel'man, *private communication* (2021).

[124] J. Zmuidzinas, "Superconducting microresonators: physics and applications", *Annu. Rev. Condens. Matter Phys.* **3**, 169 (2012).

[125] A. Blais, R.-S. Huang, A. Wallraff, S. M. Girvin, and R. J. Schoelkopf, "Cavity quantum electrodynamics for superconducting electrical circuits: an architecture for quantum computation", *Phys. Rev. A* **69**, 062320 (2004).

[126] A. Wallraff, D. I. Schuster, A. Blais, L. Frunzio, R.-S. Huang, J. Majer, S. Kumar, S. M. Girvin, and R. J. Schoelkopf, "Strong coupling of a single photon to a superconducting qubit using circuit quantum electrodynamics", *Nature* **431**, 162 (2004).

[127] G. Wendin, "Quantum information processing with superconducting circuits: a review", *Rep. Progr. Phys.* **80**, 106001 (2017).

[128] R. H. Hadfield, "Single-photon detectors for optical quantum information applications", *Nat. Photonics* **3**, 696 (2009).

[129] B. Dober, D. T. Becker, D. A. Bennett, S. A. Bryan, S. M. Duff, J. D. Gard, J. P. Hays-Wehle, G. C. Hilton, J. Hubmayr, J. A. B. Mates, C. D. Reintsema, L. R. Vale, and J. N. Ullom, "Microwave SQUID multiplexer demonstration for cosmic microwave background imagers", *Appl. Phys. Lett.* **111**, 243510 (2017).

[130] N. Casali, C. Bellenghi, M. Calvo, L. Cardani, G. Castellano, I. Colantoni, C. Cosmelli, A. Cruciani, S. Di Domizio, J. Goupy, M. Martinez, A. Monfardini, G. Pettinari, H. le Sueur, and M. Vignati, "Cryogenic light detectors for background suppression: the CALDER project", *J. Low Temp. Phys.* **200**, 206 (2020).

[131] D. Hafner, M. Dressel, and M. Scheffler, "Surface-resistance measurements using superconducting stripline resonators", *Rev. Sci. Instrum.* **85**, 014702 (2014).

[132] M. Thiemann, M. H. Beutel, M. Dressel, N. R. Lee-Hone, D. M. Broun, E. Fillis-Tsirakis, H. Boschker, J. Mannhart, and M. Scheffler, "Single-gap superconductivity and dome of superfluid density in nb-doped SrTiO3", *Phys. Rev. Lett.* **120**, 237002 (2018).

[133] Y. Wiemann, J. Simmendinger, C. Clauss, L. Bogani, D. Bothner, D. Koelle, R. Kleiner, M. Dressel, and M. Scheffler, "Observing electron spin resonance between 0.1 and 67 GHz at temperatures between 50 mK and 300 K using broadband metallic coplanar waveguides", *Appl. Phys. Lett.* **106**, 193505 (2015).

[134] B. Miksch, A. Pustogow, M. J. Rahim, A. A. Bardin, K. Kanoda, J. A. Schlueter, R. Hübner, M. Scheffler, and M. Dressel, "Gapped magnetic ground state in quantum-spin-liquid candidate κ-(BEDT-TTF)$_2$-Cu$_2$(CN)$_3$", *Science* **372**, 276 (2021).

[135] M. Thiemann, M. Dressel, and M. Scheffler, "Complete electrodynamics of a BCS superconductor with μeV energy scales: microwave spectroscopy on titanium at mK temperatures", *Phys. Rev. B* **97**, 214516 (2018).

[136] M. Göppl, A. Fragner, M. Baur, R. Bianchetti, S. Filipp, J. M. Fink, P. J. Leek, G. Puebla, L. Steffen, and A. Wallraff, "Coplanar waveguide resonators for circuit quantum electrodynamics", *J. Appl. Phys.* **104**, 113904 (2008).

[137] D. S. Rausch, M. Thiemann, M. Dressel, D. Bothner, D. Koelle, R. Kleiner, and M. Scheffler, "Superconducting coplanar microwave resonators with operating frequencies up to 50 GHz", *J. Phys. D: Appl. Phys.* **51**, 465301 (2018).

[138] J. J. A. Baselmans, J. Bueno, S. J. C. Yates, O. Yurduseven, N. Llombart, K. Karatsu, A. M. Baryshev, L. Ferrari, A. Endo, D. J. Thoen, P. J. de Visser, R. M. J. Janssen, V. Murugesan, E. F. C. Driessen, G. Coiffard, J. Martin-Pintado, P. Hargrave, and M. Griffin, "A kilo-pixel imaging system for future space based far-infrared observatories using microwave kinetic inductance detectors", *Astron Astrophys* **601**, A89 (2017).

[139] S. Beldi, F. Boussaha, J. Hu, A. Monfardini, A. Traini, F. Levy-Bertrand, C. Chaumont, M. Gonzales, J. Firminy, F. Reix, M. Rosticher, S. Mignot, M. Piat, and P. Bonifacio, "High Q-factor near infrared and visible Al_2O_3-based parallel-plate capacitor kinetic inductance detectors", *Opt. Express* **27**, 13319 (2019).

[140] M. Scheffler, M. M. Felger, M. Thiemann, D. Hafner, K. Schlegel, M. Dressel, K. S. Ilin, M. Siegel, S. Seiro, C. Geibel, and F. Steglich, "Broadband corbino spectroscopy and stripline resonators to study the microwave properties of superconductors", *ACTA IMEKO* **4**, 47 (2015).

[141] Y. Liu, L. Chen, C. Y. Tan, H. J. Liu, and C. K. Ong, "Broadband complex permeability characterization of magnetic thin films using shorted microstrip transmission-line perturbation", *Rev. Sci. Instrum.* **76**, 063911 (2005).

[142] M. Scheffler, C. Fella, and M. Dressel, "Stripline resonators for cryogenic microwave spectroscopy on metals and superconductors", *J. Phys. Conf. Ser.* **400**, 052031 (2012).

[143] S. M. Anlage and D.-H. Wu, "Magnetic penetration depth measurements in cuprate superconductors", *J. Supercond.* **5**, 395 (1992).

[144] M. Javaheri Rahim, T. Lehleiter, D. Bothner, C. Krellner, D. Koelle, R. Kleiner, M. Dressel, and M. Scheffler, "Metallic coplanar resonators optimized for low-temperature measurements", *J. Phys. D: Appl. Phys.* **49**, 395501 (2016).

[145] K. C. Gupta, *Microstrip lines and slotlines 2nd ed.* (Artech House, Inc., 1996).

[146] R. E. Collin, *Foundations for microwave engineering*, 2nd ed. (Wiley-IEEE Press, Hoboken, New Jersey, USA, 2001).

[147] R. N. Simons, *Coplanar waveguide circuits, components, and systems* (Wiley-IEEE Press, 2001).

[148] C. P. Wen, "Coplanar waveguide, a surface strip transmission line suitable for nonreciprocal gyromagnetic device applications", *IEEE MTTS Int Microw Symp* **1**, 1 (1969).

[149] S. Gevorgian, L. J. P. Linner, and E. L. Kollberg, "CAD models for shielded multilayered CPW", *IEEE Trans. Microw. Theory Tech.* **43**, 772 (1995).

[150] D. M. Pozar, *Microwave engineering* (John Wiley & Sons, Inc., 2011).

[151] M. Scheffler, K. Schlegel, C. Clauss, D. Hafner, C. Fella, M. Dressel, M. Jourdan, J. Sichelschmidt, C. Krellner, C. Geibel, and F. Steglich, "Microwave spectroscopy on heavy-fermion systems: probing the dynamics of charges and magnetic moments", *physica status solidi (b)* **250**, 439 (2013).

[152] I. Besedin and A. P. Menushenkov, "Quality factor of a transmission line coupled coplanar waveguide resonator", *EPJ Quantum Technology* **5**, 2 (2018).

[153] G. A. Garcia and C. T. Chang, "Crosstalk between two coplanar waveguides", *Kurzberichte - Letters, AEU* **43**, 1 (1989).

[154] J. Papapolymerou, G. E. Ponchak, E. Dalton, A. Bacon, and M. M. Tentzeris, "Crosstalk between finite ground coplanar waveguides over polyimide layers for 3-D MMICs on Si substrates", *IEEE Trans. Microw. Theory Techn.* **52**, 1292 (2004).

[155] D. F. Williams, F.-J. Schmuckle, R. Doerner, G. N. Phung, U. Arz, and W. Heinrich, "Crosstalk corrections for coplanar-waveguide scattering-parameter calibrations", *IEEE Trans. Microw. Theory Techn.* **62**, 1748 (2014).

[156] G. Ghione and C. U. Naldi, "Coplanar waveguides for MMIC applications: effect of upper shielding, conductor backing, finite-extent ground planes, and line-to-line coupling", *IEEE Trans. Microw. Theory Techn.* **35**, 260 (1987).

[157] E. Yamashita, "Variational method for the analysis of microstrip-like transmission lines", *IEEE Trans. Microw. Theory Techn.* **16**, 529 (1968).

[158] E. Yamashita and K. Atsuki, "Strip line with rectangular outer conductor and three dielectric layers", *IEEE Trans. Microw. Theory Techn.* **18**, 238 (1970).

[159] J. B. Knorr and K. Kuchler, "Analysis of coupled slots and coplanar strips on dielectric substrate", *IEEE Trans. Microw. Theory Techn.* **23**, 541 (1975).

[160] T. Itoh and R. Mittra, "Spectral-domain approach for calculating the dispersion characteristics of microstrip lines (short papers)", *IEEE Trans. Microw. Theory Techn.* **21**, 496 (1973).

[161] M. Houdart, *Coplanar lines : application to broadband microwave integrated circuits* (6th European Microwave Conference, IEEE, 1976).

[162] N. K. Das and D. M. Pozar, "A generalized spectral-domain Green's function for multilayer dielectric substrates with application to multilayer transmission lines", *IEEE Trans. Microw. Theory Techn.* **35**, 326 (1987).

[163] H. A. Wheeler, "Transmission-line properties of parallel wide strips by a conformal-mapping approximation", *IEEE Trans. Microw. Theory Techn.* **12**, 280 (1964).

[164] H. A. Wheeler, "Transmission-line properties of parallel strips separated by a dielectric sheet", *IEEE Trans. Microw. Theory Techn.* **13**, 172 (1965).

[165] J. Svacina, "Analysis of multilayer microstrip lines by a conformal mapping method", *IEEE Trans. Microw. Theory Techn.* **40**, 769 (1992).

[166] T. Kitazawa, Y. Hayashi, and M. Suzuki, "A coplanar waveguide with thick metal-coating", *IEEE Trans. Microw. Theory Techn.* **24**, 604 (1976).

[167] T. Kitazawa and Y. Hayashi, "Quasistatic characteristics of a coplanar waveguide with thick metal coating", *IEE Proceedings H Microwaves, Antennas and Propagation* **133**, 18 (1986).

[168] K. Wu, R. L. Vahldieck, J. L. Fikart, and H. Minkus, "The influence of finite conductor thickness and conductivity on fundamental and higher-order modes in miniature hybrid MIC's (MHMIC's) and MMIC's", *IEEE Trans. Microw. Theory Techn.* **41**, 421 (1993).

[169] A. K. Rastogi and S. Mishra, "Coplanar waveguide characterization with thick metal coating", *Int. J. Infrared Millimeter Waves* **20**, 505 (1999).

[170] J. Krupka, R. G. Geyer, M. Kuhn, and J. H. Hinken, "Dielectric properties of single crystals of Al_2O_3, $LaAlO_3$, $NdGaO_3$, $SrTiO_3$, and MgO at cryogenic temperatures", *IEEE Trans. Microw. Theory Tech.* **42**, 1886 (1994).

[171] J. Krupka, K. Derzakowski, M. Tobar, J. Hartnett, and R. G. Geyer, "Complex permittivity of some ultralow loss dielectric crystals at cryogenic temperatures", *Meas. Sci. Technol.* **10**, 387 (1999).

[172] C. Beydeda, "Superconducting flip-chip microwave resonators on materials with high dielectric constant" (1. Physikalisches Institut, University of Stuttgart, 2020).

[173] Compugraphics Jena GmbH, `https://www.compugraphics-photomasks.com`, Accessed: 2021-07-27, 2021.

[174] H. A. Wheeler, "Formulas for the skin effect", *Proceedings of the IRE* **30**, 412 (1942).

[175] A. T. A. M. de Waele, "Basic operation of cryocoolers and related thermal machines", *J. Low Temp. Phys.* **164**, 179 (2011).

[176] C. Kittel, *Introduction to solid state physics* (John Wiley & Sons, Inc., 2004).

[177] M. Zinßer, K. Schlegel, M. Dressel, and M. Scheffler, "Role of non-linear effects and standing waves in microwave spectroscopy: corbino measurements on superconductors and VO2", *Rev. Sci. Instrum.* **90**, 034704 (2019).

[178] T. J. Balle and W. H. Flygare, "Fabry–perot cavity pulsed fourier transform microwave spectrometer with a pulsed nozzle particle source", *Rev. Sci. Instrum.* **52**, 33 (1981).

[179] J. M. Raimond, M. Brune, and S. Haroche, "Manipulating quantum entanglement with atoms and photons in a cavity", *Rev. Mod. Phys.* **73**, 565 (2001).

[180] M. Ovadia, B. Sacépé, and D. Shahar, "Electron-phonon decoupling in disordered insulators", *Phys. Rev. Lett.* **102**, 176802 (2009).

[181] Z. Ovadyahu, "Thermalization processes in interacting anderson insulators", *Phys. Rev. B* **91**, 035113 (2015).

[182] Dassault Systèmes Simulia Corp., `https://www.3ds.com/de/produkte-und-services/simulia/produkte/cst-studio-suite/`, Accessed: 2021-07-27, 2021.

[183] D. S. Wisbey, M. R. Vissers, J. Gao, J. S. Kline, M. O. Sandberg, M. P. Weides, M. M. Paquette, S. Karki, J. Brewster, D. Alameri, I. Kuljanishvili, A. N. Caruso, and D. P. Pappas, "Dielectric loss of boron-based dielectrics on niobium resonators", *J. Low Temp. Phys.* **195**, 474 (2019).

[184] T. Konaka, M. Sato, H. Asano, and S. Kubo, "Relative permittivity and dielectric loss tangent of substrate materials for high-T_c superconducting film", *J. Supercond.* **4**, 283 (1991).

[185] N. McN Alford, J. Breeze, X. Wang, S. J. Penn, S. Dalla, S. J. Webb, N. Ljepojevic, and X. Aupi, "Dielectric loss of oxide single crystals and polycrystalline analogues from 10 to 320 K", *J. Eur. Ceram. Soc.* **21**, 2605 (2001).

[186] X. Aupi, J. Breeze, N. Ljepojevic, L. J. Dunne, N. Malde, A.-K. Axelsson, and N. M. Alford, "Microwave dielectric loss in oxides: theory and experiment", *J. Appl. Phys.* **95**, 2639 (2004).

[187] Marabu, `https://www.marabu-creative.com`, Accessed: 2021-07-27, 2021.

[188] M. Hövel, B. Gompf, and M. Dressel, "Dielectric properties of ultrathin metal films around the percolation threshold", *Phys. Rev. B* **81**, 3 (2010).

[189] B. Hadley, M. Green, M. Pollak, R. Chicon, and M. Ortuno, "Low energy excitations of interacting anderson localized electrons", *J. Non-Cryst. Solids* **97**, 233 (1987).

[190] D. Sherman, B. Gorshunov, S. Poran, N. Trivedi, E. Farber, M. Dressel, and A. Frydman, "Effect of Coulomb interactions on the disorder-driven superconductor-insulator transition", *Phys. Rev. B* **89**, 3 (2014).

[191] Z. Ovadyahu, "Screening the coulomb interaction and thermalization of anderson insulators", *Phys. Rev. B* **99**, 184201 (2019).

[192] K. Steinberg, M. Scheffler, and M. Dressel, "Quasiparticle response of superconducting aluminum to electromagnetic radiation", *Phys. Rev. B* **77**, 21 (2008).

[193] U. S. Pracht, D. Sherman, B. Gorshunov, K. S. Il'in, D. Henrich, M. Siegel, E. Heintze, C. Clauss, D. Hafner, R. Bek, D. Werner, S. Gelhorn, M. Scheffler, and M. Dressel, "Electrodynamics of the superconducting state in ultra-thin films at THz frequencies", *IEEE Trans. on THz Sci. Technol.* **3**, 269 (2013).

[194] M. Martinello, A. Grassellino, M. Checchin, A. Romanenko, O. Melnychuk, D. A. Sergatskov, S. Posen, and J. F. Zasadzinski, "Effect of interstitial impurities on the field dependent microwave surface resistance of niobium", *Appl. Phys. Lett.* **109**, 062601 (2016).

[195] G. Siddall, "Vacuum deposition of dielectric films for capacitors", *Vacuum* **9**, 274 (1959).

[196] M.-C. Liu, C.-C. Lee, M. Kaneko, K. Nakahira, and Y. Takano, "Microstructure of magnesium fluoride films deposited by boat evaporation at 193 nm", *Appl. Opt.* **45**, 7319 (2006).

[197] T. Pilvi, T. Hatanpää, E. Puukilainen, K. Arstila, M. Bischoff, U. Kaiser, N. Kaiser, M. Leskelä, and M. Ritala, "Study of a novel ALD process for depositing MgF_2 thin films", *J. Mater. Chem.* **17**, 5077 (2007).

[198] T. Pilvi, E. Puukilainen, U. Kreissig, M. Leskelä, and M. Ritala, "Atomic layer deposition of MgF_2 thin films using TaF_5 as a novel fluorine source", *Chem. Mater.* **20**, 5023 (2008).

[199] Crystran Ltd., *Silica glass (SiO2) optical material*, `https://www.crystran.co.uk/optical-materials/silica-glass-sio2` (visited on 02/16/2021).

[200] J. Fontanella, C. Andeen, and D. Schuele, "Low-frequency dielectric constants of α-quartz, sapphire, MgF_2, and MgO", *J. Appl. Phys.* **45**, 2852 (1974).

[201] R. G. Geyer, J. Baker-Jarvis, and J. Krupka, "Dielectric craracterization of single-crystal LiF, CaF_2, MgF_2, BaF_2 and SrF_2 at microwave frequencies", in The 17th annual meeting of the IEEE lasers and electro-optics society, 2004. LEOS 2004. (2004).

[202] M. V. Jacob, J. Mazierska, and J. Krupkac, "Low temperature complex permittivity of MgF_2 at microwave frequencies from TE-modes", in 2005 asia-pacific microwave conference proceedings (2005).

[203] M. V. Jacob, J. Krupka, J. Mazierska, and G. S. Woods, "Cryogenic complex anisotropic permittivity of magnesium fluoride", *Mater. Sci. Eng.* **427**, 175 (2006).

[204] A. Mandal and R. Sen, "Microwave absorption of barium borosilicate, zinc borate, Fe-doped alumino-phosphate glasses and its raw materials", *Technologies* **3**, 111 (2015).

[205] N. Bachar, U. S. Pracht, E. Farber, M. Dressel, G. Deutscher, and M. Scheffler, "Signatures of unconventional superconductivity in granular aluminum", *J. Low Temp. Phys.* **179**, 83 (2014).

[206] N. Marković, C. Christiansen, A. M. Mack, W. H. Huber, and A. M. Goldman, "Superconductor-insulator transition in two dimensions", *Phys. Rev. B* **60**, 4320 (1999).

[207] T. I. Baturina, J. Bentner, C. Strunk, M. R. Baklanov, and A. Satta, "From quantum corrections to magnetic-field-tuned superconductor–insulator quantum phase transition in TiN films", *Phys. B: Condens. Matter* **359**, 500 (2005).

[208] T. I. Baturina, A. Bilušić, A. Y. Mironov, V. M. Vinokur, M. R. Baklanov, and C. Strunk, "Quantum-critical region of the disorder-driven superconductor–insulator transition", *Phys. C: Supercond.* **468**, 316 (2008).

[209] T. I. Baturina, S. V. Postolova, A. Y. Mironov, A. Glatz, M. R. Baklanov, and V. M. Vinokur, "Superconducting phase transitions in ultrathin TiN films", *Europhys. Lett.* **97**, 17012 (2012).

[210] T. Schneider and S. Weyeneth, "Gate voltage tuned quantum superconductor to insulator transition in an ultrathin bismuth film revisited", *J Supercond Nov Magn* **26**, 3423 (2013).

[211] D. Rohner, L. Thiel, B. Müller, M. Kasperczyk, R. Kleiner, D. Koelle, and P. Maletinsky, "Real-space probing of the local magnetic response of thin-film superconductors using single spin magnetometry", *Sensors* **18**, 3790 (2018).

[212] Z. Ovadyahu, "Absorption of ac fields in amorphous indium-oxide films", *AIP Conf. Proc.* **1610**, 3 (2014).

[213] N. P. Breznay, M. A. Steiner, S. A. Kivelson, and A. Kapitulnik, "Self-duality and a hall-insulator phase near the superconductor-to-insulator transition in indium-oxide films", *Proc. Natl. Acad. Sci.* **113**, 280 (2015).

[214] M. Ma and P. A. Lee, "Localized superconductors", *Phys. Rev. B* **32**, 5658 (1985).

[215] K. Bouadim, Y. L. Loh, M. Randeria, and N. Trivedi, "Single- and two-particle energy gaps across the disorder-driven superconductor–insulator transition", *Nat. Phys.* **7**, 884 (2011).

[216] M. V. Feigel'man and M. A. Skvortsov, "Universal broadening of the bardeen-cooper-schrieffer coherence peak of disordered superconducting films", *Phys. Rev. Lett.* **109**, 147002 (2012).

[217] V. S. Stolyarov, T. Cren, C. Brun, I. A. Golovchanskiy, O. V. Skryabina, D. I. Kasatonov, M. M. Khapaev, M. Y. Kupriyanov, A. A. Golubov, and D. Roditchev, "Expansion of a superconducting vortex core into a diffusive metal", *Nat Commun* **9**, 2277 (2018).

[218] M. Mondal, A. Kamlapure, S. C. Ganguli, J. Jesudasan, V. Bagwe, L. Benfatto, and P. Raychaudhuri, "Enhancement of the finite-frequency superfluid response in the pseudogap regime of strongly disordered superconducting films", *Sci. Rep.* **3**, 1357 (2013).

[219] V. Palenskis, "Drift mobility, diffusion coefficient of randomly moving charge carriers in metals and other materials with degenerated electron gas", *World J. Condens. Matter Phys.* **03**, 73 (2013).

[220] X. D. Liu, E. Y. Jiang, and D. X. Zhang, "Electrical transport properties in indium tin oxide films prepared by electron-beam evaporation", *J. Appl. Phys.* **104**, 073711 (2008).

[221] P. W. Bridgman and I. Šimon, "Effects of very high pressures on glass", *J. Appl. Phys.* **24**, 405 (1953).

[222] Z. Ovadyahu, "Slow dynamics of electron glasses: the role of disorder", *Phys. Rev. B* **95**, 134203 (2017).

[223] Z. Ovadyahu, "Memory versus irreversibility in the thermal densification of amorphous glasses", *Phys. Rev. B* **95**, 214207 (2017).

[224] M. R. Graham, C. J. Adkins, H. Behar, and R. Rosenbaum, "Experimental study of the ioffe-regel criterion for amorphous indium oxide films", *J. Phys.: Condens. Matter* **10**, 809 (1998).

[225] Z. Ovadyahu, "Anisotropic magnetoresistance in a fermi glass", *Phys. Rev. B* **33**, 6552 (1986).

[226] J. E. Medvedeva, D. B. Buchholz, and R. P. H. Chang, "Recent advances in understanding the structure and properties of amorphous oxide semiconductors", *Adv. Electron. Mater.* **3**, 1700082 (2017).

[227] L. Xu, B. Fauqué, Z. Zhu, Z. Galazka, K. Irmscher, and K. Behnia, "Thermal conductivity of bulk In_2O_3 single crystals", *Phys. Rev. Materials* **5**, 014603 (2021).

[228] N. Preissler, O. Bierwagen, A. T. Ramu, and J. S. Speck, "Electrical transport, electrothermal transport, and effective electron mass in single-crystalline In_2O_3 films", *Phys. Rev. B* **88**, 085305 (2013).

[229] P. Kugler, "Microwave permittivity of superconductor thin films with strong disorder" (1. Physikalisches Institut, University of Stuttgart, 2021).

[230] M. Stokey, R. Korlacki, S. Knight, A. Ruder, M. Hilfiker, Z. Galazka, K. Irmscher, Y. Zhang, H. Zhao, V. Darakchieva, and M. Schubert, "Optical phonon modes, static and high frequency dielectric constants, and effective electron mass parameter in cubic In_2O_3", *arXiv* **cond-mat.mtrl-sci**, 2104.14611 (2021).

[231] C. Beydeda, F. Bolle, P. Kugler, J. Jakschik, Z. Galazka, S. Roh, and M. Scheffler, *private communication* (2021).

[232] Y. Imry, Y. Gefen, and D. J. Bergman, "Dielectric anomalies near the anderson metal-insulator transition", *Phys. Rev. B* **26**, 3436 (1982).

[233] Y. Imry and Y. Gefen, "Interaction effects in disordered conductors near the metal–insulator transition", *Philos. Mag. B* **50**, 203 (1984).

[234] H. S. Tan and T. G. Castner, "Piezocapacitance measurements of phosphorous- and antimony-doped silicon: uniaxial strain-dependent donor polarizabilities", *Phys. Rev. B* **23**, 3983 (1981).

[235] D. Stauffer and A. Aharony, *Introduction to percolation theory* (Taylor & Francis, 2018).

[236] V. E. Dubrov, M. E. Levinshtein, and M. S. Shur, "Permittivity anomaly in metal-dielectric transitions. theory and simulation", *J. Exp. Theor. Phys.* **43** (1976).

[237] A. L. Efros and B. I. Shklovskii, "Critical behaviour of conductivity and dielectric constant near the metal-non-metal transition threshold", *Phys. Status Solidi (b)* **76**, 475 (1976).

[238] M. Capizzi, G. A. Thomas, F. DeRosa, R. N. Bhatt, and T. M. Rice, "Observation of the approach to a polarization catastrophe", *Phys. Rev. Lett.* **44**, 1019 (1980).

[239] O. Cheshnovsky, U. Even, and J. Jortner, "The polarization catastrophe and the metal–non-metal transition in disordered materials", *Philos. Mag. B* **44**, 1 (1981).

[240] D. J. Bergman and Y. Imry, "Critical behavior of the complex dielectric constant near the percolation threshold of a heterogeneous material", *Phys. Rev. Lett.* **39**, 1222 (1977).

[241] M. E. Levinshtein, B. I. Shklovskii, M. S. Shur, and A. L. Efros, "The relation between the critical exponents of percolation theory", *JETP* **42**, 197 (1975).

[242] I. Webman, J. Jortner, and M. H. Cohen, "Numerical simulation of electrical conductivity in microscopically inhomogeneous materials", *Phys. Rev. B* **11**, 2885 (1975).

[243] A. Frydman and R. C. Dynes, "Granular superconductors and ferromagnets: a proximity-effect-based analogue", *Philos. Mag. B* **81**, 1153 (2001).

[244] B. G. Orr, H. M. Jaeger, and A. M. Goldman, "Local superconductivity in ultrathin Sn films", *Phys. Rev. B* **32**, 7586 (1985).

[245] K. Yamada, H. Fujiki, B. Shinozaki, and T. Kawaguti, "Superconducting properties in granular aluminum films near percolation threshold", *Phys. C Supercond.* **355**, 147 (2001).

[246] J. Mayoh and A. M. García-García, "Strong enhancement of bulk superconductivity by engineered nanogranularity", *Phys. Rev. B* **90**, 134513 (2014).

[247] D. C. Harris, S. T. Herbert, D. Stroud, and J. C. Garland, "Effect of random disorder on the critical behavior of Josephson junction arrays", *Phys. Rev. Lett.* **67**, 3606 (1991).

[248] A.-L. Eichenberger, J. Affolter, M. Willemin, M. Mombelli, H. Beck, P. Martinoli, and S. E. Korshunov, "Dynamic measurement of percolative critical exponents in disordered Josephson junction arrays", *Phys. Rev. Lett.* **77**, 3905 (1996).

[249] Y.-J. Yun, I.-C. Baek, and M.-Y. Choi, "Phase transition and critical dynamics in site-diluted Josephson-junction arrays", *Phys. Rev. Lett.* **97**, 215701 (2006).

[250] R. M. Fernandes and J. Schmalian, "Complex critical exponents for percolation transitions in josephson-junction arrays, antiferromagnets, and interacting bosons", *Phys. Rev. Lett.* **106**, 067004 (2011).

[251] J. C. Grunlan, W. W. Gerberich, and L. F. Francis, "Lowering the percolation threshold of conductive composites using particulate polymer microstructure", *J. Appl. Polym. Sci.* **80**, 692 (2001).

[252] A. Katunin and K. Krukiewicz, "Electrical percolation in composites of conducting polymers and dielectrics", *J Polym Eng* **35**, 731 (2015).

[253] A. Pustogow, R. Rösslhuber, Y. Tan, E. Uykur, A. Böhme, M. Wenzel, Y. Saito, A. Löhle, R. Hübner, A. Kawamoto, J. A. Schlueter, V. Dobrosavljević, and M. Dressel, "Low-temperature dielectric anomaly arising from electronic phase separation at the mott insulator-metal transition", *npj Quantum Mater.* **6**, 9 (2021).

[254] R. Rösslhuber, A. Pustogow, E. Uykur, A. Böhme, A. Löhle, R. Hübner, J. A. Schlueter, Y. Tan, V. Dobrosavljević, and M. Dressel, "Phase coexistence at the first-order mott transition revealed by pressure-dependent dielectric spectroscopy of κ-(BEDT-TTF)$_2$-Cu$_2$(CN)$_3$", *Phys. Rev. B* **103**, 125111 (2021).

[255] Y. Saito, R. Rösslhuber, A. Löhle, M. S. Alonso, M. Wenzel, A. Kawamoto, A. Pustogow, and M. Dressel, "Chemical tuning of molecular quantum materials κ-[(BEDT-TTF)$_{1-x}$(BEDT-STF)$_x$]$_2$Cu$_2$(CN)$_3$: from the Mott-insulating quantum spin liquid to metallic Fermi liquid", *J. Mater. Chem. C*, `10.1039/d1tc00785h` (2021).